



UNIVERSITÀ DEGLI STUDI DELL'AQUILA  
DIPARTIMENTO DI SCIENZE FISICHE E CHIMICHE  
Dottorato di Ricerca in Scienze Fisiche e Chimiche

XXXIII CICLO

SSD FIS/03

# Electronic properties of novel low-dimensional systems

*Dottorando:*

Giovanni Marini

*Coordinatore:*

Prof. Antonio Mecozzi

*Relatore:*

Prof. Gianni Profeta

# Contents

<b>I</b>	<b>Graphene intercalation compounds</b>	<b>8</b>
<b>1</b>	<b>Origin of the Flat Band in Heavily Cs-doped Graphene</b>	<b>10</b>
1.1	Presentation of the scientific investigation . . . . .	10
1.1.1	What is a flat band? . . . . .	10
1.1.2	Flat band in graphene . . . . .	11
1.1.3	Zone-folding effects as a route to the observation of the flat band . . . . .	13
1.1.4	A tight binding model for $(2\times 2)$ Cs/graphene . . . . .	14
1.1.5	A realistic model . . . . .	18
1.2	Discussion . . . . .	19
1.2.1	System preparation and LEED . . . . .	19
1.2.2	Density functional theory description of the system . . . . .	20
1.2.3	Angle-resolved photoemission spectroscopy . . . . .	25
1.2.4	Comparison between theory and experiment . . . . .	31
<b>2</b>	<b>Coexistence of massive and massless charge carriers in an epitaxially strained alkali metal quantum well on bilayer graphene</b>	<b>35</b>
2.1	Experimental characterization . . . . .	37
2.1.1	Characterization of epitaxial bilayer graphene . . . . .	37
2.1.2	Cesium-derived quantum well states . . . . .	38
2.2	Structural characterization . . . . .	41
2.2.1	General considerations . . . . .	41
2.2.2	Ground state identification . . . . .	43
2.2.3	Physics of the Cs growth on graphene . . . . .	46
2.2.4	A tight binding model for the Cs/bilayer graphene system . . . . .	50
2.2.5	Methods . . . . .	53

<b>II</b>	<b>Transition metal dichalcogenides</b>	<b>58</b>
<b>3</b>	<b>Study of NiTe<sub>2</sub> electronic and superconducting under pressure</b>	<b>60</b>
3.1	Introduction . . . . .	60
3.2	Methods . . . . .	61
3.3	Enthalpy-pressure phase diagram of NiTe <sub>2</sub> . . . . .	63
3.4	Lifshitz transition in NiTe <sub>2</sub> under high pressure . . . . .	65
3.5	Superconductivity in bulk NiTe <sub>2</sub> . . . . .	67
<b>4</b>	<b>Characterization of the charge density wave in 1T-VSe<sub>2</sub></b>	<b>71</b>
4.1	Introduction to the charge density wave order . . . . .	71
4.2	Introduction to VSe <sub>2</sub> . . . . .	74
4.3	Methods . . . . .	77
4.4	Electronic structure of VSe <sub>2</sub> . . . . .	78
4.5	Bare electronic susceptibility and nesting function . . . . .	81
4.6	Dynamical properties of bulk VSe <sub>2</sub> in the undistorted phase . . . . .	84
4.7	Characterization of the CDW in bulk VSe <sub>2</sub> . . . . .	86
<b>III</b>	<b>Topology in condensed matter</b>	<b>93</b>
<b>5</b>	<b>Electronic properties of the strong topological insulator mercury telluride</b>	<b>94</b>
5.1	Introduction to topology and topological insulators . . . . .	95
5.1.1	The integer quantum Hall effect . . . . .	95
5.1.2	Berry phase and Chern-Gauss-Bonnet theorem . . . . .	95
5.1.3	$\mathbb{Z}_2$ topological insulators . . . . .	97
5.1.4	3D Topological Insulators . . . . .	103
5.2	Study of the electronic properties of mercury telluride . . . . .	104
5.2.1	Introduction . . . . .	104
5.2.2	Mercury telluride: a zero gap semiconductor . . . . .	105
5.2.3	Opening the gap in HgTe . . . . .	106
5.2.4	Presentation of the experimental setup . . . . .	107
5.2.5	DFT description of bulk HgTe . . . . .	108
5.2.6	Experimental results and discussion . . . . .	110
5.2.7	Computational details . . . . .	123

## Summary

Low dimensionality plays a central role both in condensed matter physics and technological advancement. Many of the outstanding physical properties of low-dimensional materials are the manifestation of their unique electronic structure, whose understanding represents a key challenge for the scientific community. My doctoral thesis consists in the study of certain classes of novel low dimensional systems, including graphene intercalation compounds, transition metal dichalcogenides and the interplay between topology and dimensionality in the topological insulator mercury telluride. I discuss the central ideas behind the observed physics, describing a wide class of electronic phenomena including superconductivity, topologically non trivial phases and charge-density wave phases by means of state of the art first principles techniques.

# Introduction

Many unconventional properties of the matter originate from quantum mechanical effects, which by their own nature become most evident in small sized systems. As such, the investigation and manipulation of matter at the nanoscale is at the center of modern science. We refer to this research field as nanotechnology. The discipline is focused on the study of systems having at least one spatial dimension in the range 1-100 nm, where the experimental evidences deviate substantially from the description of reality given by classical physics. The founding ideas of nanotechnology were first discussed by Nobel prize physicist Richard Feynman in the seminal lecture “There’s Plenty of Room at the Bottom” in 1959 at Caltech[1], where he considered the possibility to manipulate the matter with nanometric precision for the first time. The ideas discussed in the lecture have been of great inspiration for the physics community and tremendous progress has been made in all the aspects of this field in the last sixty years. The transistor, the fundamental constituent of the electronic devices ubiquitous in our daily life, is a notable example: the MOSFET (metal-oxide-semiconductor field-effect transistor) was invented by Mohamed Atalla and Dawon Kahng at Bell Labs in 1959. Following its invention, the mass production and progressive miniaturization of electronic components started, best summarized by the famous Moore’s law in 1965[2], *i.e.* the observation that the number of transistors in a dense integrated circuit doubles every two years. Many breakthroughs in the field of nanotechnology took place in the last 60 years, including Nobel prize worth inventions such as the laser, a dispositive based on the concept of stimulated emission for which the 1964 Nobel prize in physics was awarded to Townes, Prokhorov and Basov, the invention of scanning tunnel microscope (STM) in 1981 by Gerd Binnig and Heinrich Rohrer[3, 4], a microscope based on the concept of quantum tunneling, the discovery of fullerenes in 1985 by Harry Kroto, Richard Smalley and Robert Curl[5], the invention of the blue light-emitting diode (LED) by Akasaki, Amano and Nakamura, whom were awarded with the Nobel prize in 2014, and the groundbreaking isolation of

graphene, an individual layer of  $sp^2$  ibridized carbon atoms (graphite)[6] by Andrej Konstantinovič Gejm and Konstantin Sergeevič Novosëlov in 2004, which was awarded the Nobel prize in physics in 2010. Graphene isolation opened a whole new field of investigation in condensed matter physics, namely the study of low dimensional materials, which is the context where the present thesis is developed. Physicists have been trying to produce thin flakes from layered materials since the 1960's[7, 8], but failed to do so until the synthesis of graphene. The reason why atom-thick materials remained unknown for such a long time is that nature obstacles the growth of two dimensional (2D) crystals. The high temperature required to grow crystals is associated with big thermal fluctuations, detrimental to the stability of macroscopic 2D crystals[9]. There are two principal routes to overcome this limit: the first is to mechanically separate layered materials such as graphite using the so called scotch-tape technique[10],that is the same method originally used by Novosëlov and Gejm. The alternative route is to grow graphite epitaxially on top of another crystal, a process commonly known as heteroepitaxy. The epitaxial layers are bound to the substrate during the 3D growth. After the structure is cooled down, the substrate can be removed by chemical etching and the obtained thin film can be transferred to an arbitrary substrate for characterization[9, 11, 12, 13].

Graphene has attracted an enormous research interest due to a unique combination of physical properties[14, 15, 16]: to name a few, record breaking strength of  $\simeq 40$  N/m, thermal conductivity of 5000 W/mK, electron mobility at room temperature of 250000  $\text{cm}^2/(\text{V s})$ , large surface area of 2630  $\text{m}^2/\text{g}$ , high modulus of elasticity of  $\simeq 1$  TPa and good electrical conductivity, which make graphene a potential candidate for a vast number of applications, including high-end composite materials, field effect transistors, electromechanical systems, strain sensors, electronics, supercapacitors, hydrogen storage, solar cells and many more. Behind the properties of graphene lies an extremely rich fundamental physics which has attracted a lot of investigation itself. The most unique feature of graphene is the electronic spectrum. Eletrons propagate through graphene with zero effective mass, meaning that graphene electron gas is described in terms of a Dirac-like equation, as opposed to the Schrödinger equation. This makes graphene a condensed matter analogue of quantum electrodynamical massless fermionic systems except for the speed of particles, which is 300 times smaller than the speed of light in graphene[17]; as such, many electrodynamical phenomena have been predicted to take place in graphene[9]. For example, Dirac fermions behave very differently in presence of disorder because of their insensitivity to external electrostatic potentials. This enables electrons in graphene to

propagate for distances of the order of the micrometer[6]. Another striking differences between Dirac and Schrödinger electrons is their behavior under applied magnetic fields, which is made evident in the anomalous integer quantum Hall effect (IQHE). In this scenario, the system behaves as a collection of non-interacting harmonic oscillators. Each oscillator is characterized by the same frequency  $\omega_c$ , the cyclotron frequency, which depends on the inverse of the electron effective mass[18]. The system eigenvalues are thus  $\epsilon_m = \hbar\omega_c(m + 1/2)$ , and each eigenvalue is N times degenerate, where N is the number of the electrons in the system. Due to the null effective mass and the exceptional electron quality resulting from the very low scattering rate, graphene offers the unique possibility to observe quantum phenomena such as the anomalous IQHE even at room temperature[9, 17]. The anomalous IQHE measured in graphene[15, 19] is qualitatively different from the one measured in parabolic dispersing electrons in polar III-V semiconductors, where IQHE cannot be observed for temperatures higher than 30 K even for the ones with lower electron effective masses[20]. Moreover, graphene's electronic excitation close to the charge neutrality point have well defined chirality (not in relation to the spin of the electron, but to a pseudospin variable associated with the two components of the wave function[17]) and because of its flexibility, graphene, can be tailored chemically or structurally in many ways: deposition of metal atoms on top[21, 22], intercalation, as in graphite intercalated compounds[23, 24], and many others[17]. In particular, electron doping graphene by alkaline metal adatoms has been demonstrated to be a viable route to induce superconductivity in graphene first theoretically[25] and then experimentally.[26, 27]

Not surprisingly, research has not been limited to monolayer graphene. Multilayer graphene systems such as bilayer graphene ( two coupled graphene layers) and trilayer graphene ( three coupled graphene layers ) have also attracted a lot of interest. Bilayer graphene minimizes its energy in the so called Bernal (or AB) stacking[28, 29]. While retaining many of the properties of monolayer graphene[30], the electronic band structure of bilayer graphene is qualitatively different from the one of monolayer graphene, hosting massive chiral quasiparticles near charge neutrality and thus yet a different unconventional IQHE.[31] Recently bilayer graphene has known a tremendous interest after Cao and coworkers demonstrated the surprising physics originating from the application of a twist angle between the two layers[32, 33]. At a special magic angle of  $\simeq 1.1^\circ$  intrinsic unconventional superconductivity is observed together with a temperature-carrier density phase diagram in analogy with the one of cuprates and the strongest electron pairing ever measured. Another “hot” graphene based system is rhombohe-

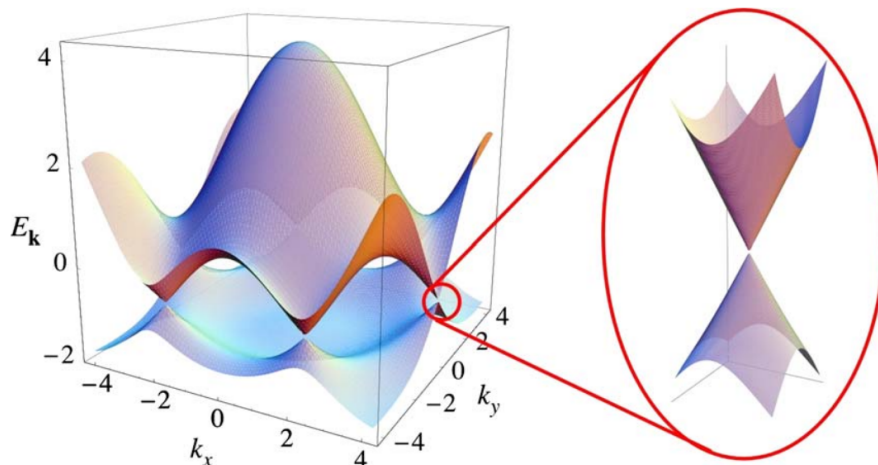


**Figure 1:** Electronic dispersion for a first neighbor model of graphene from Ref.[17]. The zoomed area is the energy region close to one of the Dirac points.

dally (ABC)-stacked trilayer graphene, which exhibits an antiferromagnetic ground state[34, 35, 36]. The formation of these highly correlated states in bilayer and trilayer graphene is strongly related to their electronic structure, namely to the formation of the called “flat band” dispersion, whose understanding is one of the main themes of this thesis.

The discovery and characterization of graphene has given unprecedented relevance to the investigation of 2D materials and to the role played by dimensionality in the physical properties of materials. There are many layered compounds besides graphite where strong in-plane hybridization and weak van der Waals out-of-plane interaction coexist and all of them are plausible candidates for the isolation of a monolayer: as a consequence, many monolayer materials have been synthesized and many more of them have been theoretically predicted to be stable[37]. An especially rich class of layered compounds is the family of *transition metal dichalcogenides* (TMDs). Dickinson and Pauling were the first to determine their structure almost a century ago[38] and more recently, in 1986, monolayer suspensions were reported for the first time[39]. They present the general formula  $\text{MX}_2$  where M, the transition metal atom, is sandwiched between two chalcogen layers ( $\text{X} = \text{S, Se, Te}$ )[40]. While one of graphene’s limitation in practical applica-

tions is the absence of a semiconducting gap, the structural and chemical versatility of TMDs allow a wide variability of electronic properties, including insulating, semiconducting, superconducting behavior and charge-density waves (CDWs), making them particularly desirable for applications in nanoelectronics as well as an important platform for fundamental physics. In this regard, many studies focused on the properties arising from their strong spin-orbit interactions and valley-dependent Berry curvature effects, manifesting in both single particle excitations[41, 42, 43] and collective quantum phenomena[44, 45]. Following the realization of the first MoS<sub>2</sub> transistor[46], the discovery of strong photoluminescence in MoS<sub>2</sub> monolayers[47, 48] (implying a drastical change of electronic properties with respect to bulk MoS<sub>2</sub>) and a general improving of sample preparation and manipulation techniques of 2D materials, the interest for TMDs has strongly increased in the last few years[49, 50]. Another limitation of graphene is that it is chemically inert and can only be made active by functionalization. In contrast monolayer TMDs' versatile chemistry offers opportunities for fundamental and technological research in a variety of fields including catalysis, energy storage and sensing[51]. Recently, a major research direction in 2D material science has been van der Waals heteroepitaxy[52], that is the growth of dissimilar 2D materials on top of each other. Graphene has turned out to be an excellent substrate for van der Waals heteroepitaxy and the growth of transition metal dichalcogenides such as MoS<sub>2</sub>, MoSe<sub>2</sub>, or TaS<sub>2</sub> has been achieved on epitaxial monolayer graphene[53, 54, 55].

From all of the above facts it follows that understanding and manipulating low dimensional materials is a fundamental aim of contemporary research in condensed matter physics. Yet, dimensionality has also been pivotal in another major research trend of modern condensed matter physics, i.e. the study of the *topological properties of matter*. The classification of distinctive phases of matter is traditionally dealt with the Landau's approach, where the states are characterized by the spontaneous symmetry breaking of some underlying symmetry. A different paradigm emerged after the discovery of the quantum Hall effect[57]. The system where quantum Hall effect manifests does not undergo any symmetry breaking, nevertheless topological phases can be defined in the sense that certain fundamental properties are insensitive to smooth changes in material parameters and cannot change unless the system passes through a quantum phase transition[58, 59, 60]. The interest in the topological properties has seen a rapid increase after Kane and Mele showed that spin-orbit interaction can lead to topological insulating electronic phases in 2D models[61, 62]; the results were then extended to 3D models[63]. Curiously, the effect was first demonstrated by extending the

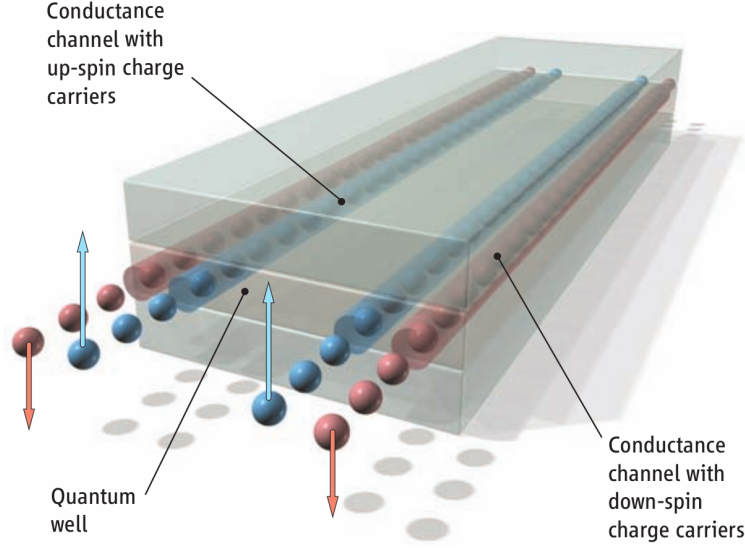


*Figure 2: Model of a 2D TI with spin-locked edge states from Ref.[56].*

work by the Nobel prize Duncan Haldane in a model of graphene, or “2D graphite” borrowing his words[64]. Topological insulators (TIs) behave like any insulator in that they present a bulk energy gap separating the highest occupied electronic band from the lowest empty band. What separates them from ordinary insulators is that the surfaces (or edges) of a TI are always conducting. The conducting states cannot be gapped as long as time-reversal symmetry is not broken. This and other properties, which will be further discussed in Chapter 5, make the surface states very robust against disorder, making them appealing for practical applications like spintronics and quantum computation[60]. Mathematically, 2D (3D) trivial and TIs can be distinguished by the value taken by an integer parameter (a set of integer parameters) which can take two distinct values, often referred to as the  $\mathbb{Z}_2$  invariant(s). The quantum spin Hall phase, another name for the TI phase, was observed for the first time in 2007 in mercury telluride-cadmium telluride (HgTe/CdTe) semiconductor quantum wells.[65, 56] After the discovery of TIs topological concepts have then been employed in the description of many different condensed matter systems, such as semimetals[66] and superconductors[67]. Moreover, a systematic topological description of physical systems, heavily involving dimensionality, has been given and relations between topological invariants and physical quantities have been identified[68].

## Brief description of the research work

The present original scientific investigation deals with the application of theoretical *ab-initio* and model techniques as tools for the quantitative analysis of novel physical phenomena in low dimensional materials. The central instrument of this thesis is density functional theory (DFT), a well established self-consistent computational technique allowing the theoretical investigation of many properties of solid materials. It is based on the formalism introduced by Hohenberg, Kohn and Sham in 1964-1965[69, 70]. The power of this method lies in the attribute *ab-initio*, i.e. once the constituents are specified no external ad-hoc parameters are needed to obtain the ground state electronic configuration of the system. Thus, in principle, one can reproduce the experimental results with virtually no informations besides the chemical composition of the system, recurring to the minimization of the appropriate thermodynamic potential. However in practice there are many delicate aspects which need to be considered when performing DFT calculations, both regarding the technical details and the approximations made. A large part of the research work contained in the dissertation has been realized in collaboration with other experimental and theoretical groups, which I acknowledge at the end of the thesis. Along with theoretical analyses, experimental results will be presented in the dissertation. While the theoretical aspects of the work will be discussed in depth, the reader will be redirected to the relevant literature for the technical details of the experimental results and for a complete description of the experimental techniques. The dissertation is organized in three parts, according to the three distinct classes of physical system treated in the course of the doctoral research.

- Part I deals with graphene based systems and the effect of alkali doping, exploring various levels of doping and new possibilities involving peculiar electronic and structural effects. The systems in question are investigated by means of various kinds of state of the art theoretical and experimental techniques.
- Part II is devoted to the TMDs, presenting the study of peculiar electronic effects and phase transitions, such as CDWs, topological phases and superconductivity, by means of theoretical *ab-initio* techniques.
- Part III is devoted to the TI mercury telluride (HgTe). I discuss how HgTe, a native semimetal, can become a TI and what is the best theoretical approach to describe its electronic properties, including the topological surface states characterization.

Part I

Graphene intercalation  
compounds

## Introduction to Part I

The ability to engineer layered compounds in order to induce new physical phenomena has been a major research trend of the last years. A key role has been played by graphene based compounds: for example, the deposition of metal atoms on top of graphene allows to tune its Fermi level, opening to new practical applications and fundamental investigations. A particularly appealing feature of graphene band structure is represented by saddle points located far from the Fermi level[71], causing a Van Hove singularity (VHS) in its density of states (DOS). By shifting the Fermi level of graphene in correspondence to the VHS it would be possible to observe many interesting phenomena since systems hosting a VHS are prone to various kind of instabilities. In this context, the intercalation of alkali metal atoms in graphene represents a way to realize *n*-type doped graphene[72] and at the same time to enhance its superconducting properties[73]. Part I of the thesis deals with the investigation of graphene systems in high doping conditions, realized by the deposition of large quantities of cesium (Cs) adatoms on top of graphene, with varying coverage. In the first Chapter we present a method to reach the VHS and to realize a “flat band system” in monolayer graphene by depositing a large quantity of Cs. The physics of the flat band is explained by a combination of experimental, model and *ab-initio* techniques. In the second Chapter we continue the study of low dimensional graphene based compounds, presenting the realization of a Cs/graphene heterostructure, resulting from excess Cs deposition of a very large quantity of Cs atoms over bilayer graphene. We observe the growth of thin Cs films on top of Cs intercalated bilayer graphene. State of the art theoretical techniques are combined with structural characterization by low energy electron diffraction (LEED) and spectroscopical characterization by angle-resolved photoemission spectroscopy (ARPES). The present research is part of a joint theoretical and experimental research project involving the experimental group led by Prof. Alexander Grüneis of University of Cologne and other researchers.

# Chapter 1

## Origin of the Flat Band in Heavily Cs-doped Graphene

### 1.1 Presentation of the scientific investigation

#### 1.1.1 What is a flat band?

Some lattice Hamiltonians possess a peculiar single particle energy spectrum, where one or more bands do not disperse in the  $\mathbf{k}$ -space, thus hosting energy eigenvalues  $E(\mathbf{k})$  not depending on the momentum  $\mathbf{k}$ . Such a dispersionless band is called a flat band. The wave transport is suppressed in a flat band as a consequence of the vanishing kinetic energy and electron velocity ( $\nabla E(\mathbf{k}) = 0$ )[74]. A perfect flat band, that is an energy dispersion independent of the momentum in all the Brillouin Zone (BZ) is unstable against any kind of perturbation: for this reason, a broader and more practical definition is often considered also including partially flat bands, i.e. systems presenting “flatness” only for a (relevant) portion of the BZ. Materials hosting flat bands of this kind are present in nature and are called “flat band materials”[34, 74] even though the dispersion is usually not perfectly flat. When the flat electronic dispersion is placed near  $E_F$ , the singularity in the electronic DOS due to the presence of the flat band causes the material to be unstable against the opening of an energy gap, possibly driving a phase transition of the system e.g. into a superconductor, a charge-density wave phase, or magnetic ordering.

### 1.1.2 Flat band in graphene

Flat bands have been reported to occur in various models: notable examples are the dice lattice[75], the Kagome lattice[76, 77, 78], the Lieb lattice[79] and the Tasaki lattice[80]. A flat band has been recently observed reproducing the Lieb lattice model in a chlorine monolayer on a Cu(100) surface[81, 82]. Graphene related systems provide ample opportunity for engineering flat bands. Theoretically, a carbon (C) Kagome lattice has been predicted[83], and recently, flat bands have been found in bilayer graphene[84] at  $\simeq 0.25$  eV below the  $E_F$  as well as in boron-doped graphene nanoribbons [85] at  $\simeq 1.5$  eV below the  $E_F$ . However, since these flat bands are not located at the  $E_F$ , application of a gate voltage or chemical doping is needed to make the flat band relevant for the emergent ground state. For this reason the possibility to induce the flat band near the  $E_F$  is still a hot research topic. In this regard, important results have been achieved in multilayer graphene systems by engineering the stacking order[35, 86] or the twist angle[32, 33]. Rhombohedrally-stacked trilayer graphene exhibits a flat band and, as a consequence, an antiferromagnetic ground state appears[35, 36], as mentioned in the Introduction. Bilayer graphene where the two layers are twisted with respect to each other by a magic angle of  $\simeq 1.1^\circ$  also exhibits a flat band close to the  $E_F$ [32, 33], where recently both Mott insulating and unconventional superconducting phases have been observed[33]. One drawback of both rhombohedrally-stacked and the twisted bilayer systems is that they are fabricated from exfoliated flakes and hence can not be prepared deterministically and in large areas. Furthermore, the crystal structure of the twisted bilayer graphene is unstable against a rotation of the two layers, that brings the system back to the Bernal (AB) stacking order, the global energy minimum configuration for the bilayer graphene system. It follows that the ability to fabricate and characterize large area systems having flat bands at  $E_F$  remains an important problem in condensed matter physics and materials science. In this regard, an alternative route to obtain a flat band is the extreme doping of monolayer graphene, which hosts a VHS with a quasi-flat band dispersion in a small region near the M point of the BZ. This feature can be observed in Fig.1.1, where we report the electronic dispersion of graphene resulting from the nearest-neighbor tight-binding (TB) model. A major problem is that the VHS is placed far from the charge neutrality point: a way to overcome this obstacle is the chemical doping of graphene, as demonstrated by McChesney *et al.* in Ref.[71], where they managed to obtain an highly doped graphene with a combination of calcium intercalation and calcium-potassium adsorption on top of the graphene. More recently, a sim-

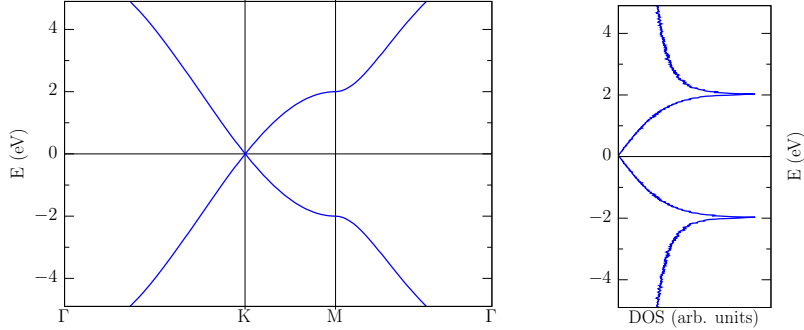


**Figure 1.1:** Band structure of graphene obtained in the TB model with the hopping parameter  $t = -2$  eV.

ilar result was reported in Ref.[87], employing a combination of ytterbium intercalation and potassium adsorption. In both cases, strong electronic structure renormalization effects have been considered at the origin of the observed flat band.

The idea of the present work is to study the possibility to reach the VHS in graphene by means of Cs deposition, according to the following rationale: Cs is an alkali metal, as such it will donate a considerable amount of charge when put in contact with graphene, consequently shifting the Fermi level far from the charge neutrality point. Being able to engineer such a system would be interesting for the possibility to induce an electron-phonon mediated superconducting transition in graphene. In fact, the large DOS at the  $E_F$  ( $N(0)$ ) due to the VHS (see the DOS panel in Fig.1.1) is positively correlated to a large EPC constant. Furthermore, it has been demonstrated that alkali-metal doped graphene can host conventional superconductivity thanks to the enhancement of the electron phonon coupling (EPC) due to the presence of the alkali metals[72, 88, 89]. In this regard, it is fundamental to have alkali metal bands located near the  $E_F$ . We believe that this could be the case in the present system: if a large amount of Cs is deposited, only part of the Cs charge would be transferred to the graphene, resulting in a partially occupied alkali metal band, going by the name of “interlayer” state[25, 90]. All previous works failed to engineer and characterize high-quality systems that allow for simultaneous observation of a flat band and the interlayer

state. For example, Ref.[71] reports a flat band but no interlayer state and Refs.[91] and [92] find the interlayer state in bilayer graphene but their doping level is considerably lower than what is needed to occupy the flat band. Incidentally, the high value of  $N(0)$  is also directly linked to the emergence of the ferromagnetic instability. For example, in the mean-field approximation of the Hubbard model the ferromagnetic phase sets in if the Stoner criterion  $N(0)U > 1$  is fulfilled,  $U$  being the on-site Coulomb repulsion (for graphene,  $U = 9.3$  eV has been proposed[93]). It is thus clear that a large value of  $N(0)$  is pivotal to the emergence of ferromagnetism, making flat band materials natural candidates for the observation of a ferromagnetic state.

### 1.1.3 Zone-folding effects as a route to the observation of the flat band

We will show in the following that the interaction between Cs and C atoms can considerably modify the graphene band structure, causing the emergence of a flat band in correspondence of the monolayer graphene's VHS. We believe that three distinct physical effects are fundamental in the formation of the flat band:

- 1) The aforementioned heavy electron doping by excess Cs / C stoichiometry.
- 2) Zone-folding.
- 3) Covalent C-Cs bonding happening as a consequence of the zone-folding.

Zone-folding consists in the folding of a system's eigenvalues into a smaller BZ occurring due to the presence of an external periodic potential whose spatial symmetry is lower than the one of the original system. When this happens, the electronic structure of the system is best described in the reduced BZ picture, corresponding to the lower periodicity induced by the external periodic potential, treating the effect of the potential itself in perturbation theory. The most common example of this approach is the case of simple metals, where the free-electron dispersion relation  $E(\mathbf{k}) = \hbar^2|\mathbf{k}|^2/2m$  is folded into the BZ of the crystal and the effect of the periodic potential is then treated in perturbation theory[23, 94]. In the present system, we expect graphene energy bands to fold due to the external potential induced by the Cs atoms. The zone-folding effects have already been widely treated in the context of graphite intercalation compounds[24], alkali-metal doped bilayer

graphene[92] and oxygen intercalation under graphene[95]. From previous literature, we know that Cs intercalation of graphene results in two possible Cs reconstructions depending on coverage, namely  $2 \times 2$  and  $(\sqrt{3} \times \sqrt{3})R30^\circ$  (we will refer to it as  $\sqrt{3} \times \sqrt{3}$ ). The external potential induced by the  $2 \times 2$  reconstruction is fundamental for the observation of the flat band: because of zone-folding, the bands of doped graphene close to the  $E_F$  fold back to the central region of the BZ (the  $\Gamma$ -point and the M-point of the BZ become equivalent in the  $2 \times 2$  folded BZ). Since the Cs band is also located around the BZ center for energies close to the  $E_F$ , hybridization between graphene and the Cs bands (i.e. a covalent coupling between C and Cs orbitals) is possible. Without zone-folding there would be no possibility of hybridization close to the  $E_F$  because the bands of graphene and Cs do not cross. Adding a coupling term between C and Cs atoms causes an anti-crossing of the energy bands, meaning that the two energy bands disperse away from the hypothetical crossing point of the non-coupled system originating two hybridized bands. Here we demonstrate that this precise fact plays a fundamental role in the formation of the flat band by recurring to a TB model.

#### 1.1.4 A tight binding model for $(2 \times 2)$ Cs/graphene

We illustrate the effects of zone-folding and hybridization between the Cs derived and graphene bands by means of orthogonal next-neighbor TB model. The TB model takes into account one Cs atom per  $2 \times 2$  graphene cell, which is a common reconstruction for alkali deposition on top of graphene. To simulate the Cs  $(2 \times 2)$  graphene structure a unit cell of 8 C atoms and 1 Cs atom is considered. The basis set is thus made up of 8  $p_z$  orbitals (one at each C site) and one s-orbital at the Cs site yielding a  $9 \times 9$  Hamiltonian matrix. Electronic spin is not included in the model. The Hamiltonian is:

$$H_{TB} = \begin{pmatrix} H_{Cs-Cs} & H_{Cs-C} \\ H_{Cs-C}^\dagger & H_{C-C} \end{pmatrix} \quad (1.1)$$

that can be decomposed into an  $8 \times 8$  Hamiltonian matrix  $H_{C-C}$  describing the C-C intralayer hopping in the  $(2 \times 2)$  unit cell, a  $1 \times 8$  matrix  $H_{C-Cs}$  describing the C-Cs interlayer interaction and a scalar function  $H_{Cs-Cs}$  describing the Cs-Cs intralayer hopping. Once defined the distance between C atoms as  $a_{C-C}$ , the distance between nearest neighbors in the Cs layer is given by  $d_{Cs-Cs} = 2\sqrt{3}a_{C-C}$ . The six nearest neighbor Cs atoms placed at  $\delta_j^{Cs}$  originating the following expression for the Cs-Cs hopping term:

$$H_{C_s-C_s} = \epsilon_{C_s} + t_{C_s-C_s} \sum_{j=1}^6 \exp(i\mathbf{k} \cdot \delta_j^{C_s}) \quad (1.2)$$

$$= \epsilon + t_{C_s-C_s} \cdot h_{C_s-C_s}(\mathbf{k}) \quad (1.3)$$

where  $t_{C_s-C_s}$  is the hopping integral,  $\epsilon_{C_s}$  the on-site potential of the Cs-lattice, and

$$h_{C_s-C_s} = (4 \cos(3k_x a_{C-C}) \cos(\sqrt{3}k_y a_{C-C}) + 2 \cos(2\sqrt{3}k_y a_{C-C})) \quad (1.4)$$

For the C-C and Cs-C hoppings, it is useful to define the hopping directions

$$\begin{aligned} \delta_1 &= a_{C-C}(1, 0)^T \\ \delta_2 &= a_{C-C}(-1/2, \sqrt{3}/2)^T \\ \delta_3 &= a_{C-C}(-1/2, -\sqrt{3}/2)^T \end{aligned} \quad (1.5)$$

and then the functions

$$f_j^\pm(\mathbf{k}) = \exp(\pm\mathbf{k} \cdot \delta_j) \quad (1.6)$$

The (2×2) Graphene Hamiltonian can then be written as

$$H_{C-C} = \begin{pmatrix} \epsilon_C & 0 & tf_1^+ & 0 & tf_3^+ & 0 & tf_2^+ & 0 \\ \epsilon_C & tf_3^+ & 0 & tf_1^+ & 0 & 0 & 0 & tf_2^+ \\ & \epsilon_C & tf_2^- & 0 & 0 & 0 & 0 & 0 \\ & & \epsilon_C & 0 & 0 & tf_1^+ & tf_3^+ & \\ & & & \epsilon_C & tf_2^- & 0 & 0 & \\ & & & & \epsilon_C & tf_3^+ & tf_1^+ & \\ & & & & & \epsilon_C & 0 & \\ & & & & & & \epsilon_C & 0 \end{pmatrix} \quad (1.7)$$

with  $t = t_{C-C}$  the hopping integral and  $\epsilon_C$  the on-site potential of the C lattice. The lower triangle can be constructed from the upper triangle by using the Hermitian condition. The C-Cs interlayer hopping is described by

$$H_{C-C_s} = \begin{pmatrix} 0 \\ t_{C-C_s}f_2^- \\ t_{C-C_s}f_1^+ \\ t_{C-C_s}f_3^- \\ t_{C-C_s}f_3^+ \\ t_{C-C_s}f_1^- \\ t_{C-C_s}f_2^+ \\ 0 \end{pmatrix} \quad (1.8)$$

where  $t_{C-C_s}$  is the hopping integral for nearest neighbor C-Cs hopping. The band structure can then be obtained by solving the secular equation

$$H(\mathbf{k})\mathbf{c}_n(\mathbf{k}) = \mathbf{c}_n(\mathbf{k})E_n(\mathbf{k}) \quad (1.9)$$

where  $\mathbf{c}_n(\mathbf{k})$  and  $E_n(\mathbf{k})$  are the  $n^{\text{th}}$  eigenvector and eigenvalue at the  $\mathbf{k}$  point of BZ, respectively. The parameters needed in the TB calculation are the two on-site energies for Cs and C orbitals (labeled  $\epsilon_{C_s}$  and  $\epsilon_C$ ) and the C-C, C-Cs and Cs-Cs hopping parameters indicated as  $t_{C-C}$ ,  $t_{C-C_s}$  and  $t_{C_s-C_s}$ , respectively. Starting from a non-interacting monolayer graphene plus a Cs atom, the  $2 \times 2$  potential is switched on first and then the Cs-C hybridization (i.e. the value of  $t_{C-C_s}$ ). The band structure of doped graphene monolayer is shown in Fig.1.2(a). We impose that the on-site C energy is such that the VHS is positioned exactly at the Fermi level. The geometry of the unit cell of the TB calculation and the hopping parameters  $t_{C-C}$  and  $t_{C-C_s}$  are shown in Figure 3b. The zone-folding of electron energy bands is “encoded” in the choice of the unit cell. Due to the zone-folding, the hybridization between the Cs bands and C band at the VHS becomes possible, resulting in the formation of a flat band. It makes thus sense to study the joint effect of zone-folding and the effect of Cs-C hybridization on the electronic structure. Fig.1.2(c) depicts the bands calculated in a  $2 \times 2$  supercell but without Cs-C hybridization (indicated by a matrix element  $t_{C_s-C} = 0$ ). Due to zone-folding, the Cs band and the graphene derived bands occupy the same region in the  $E(\mathbf{k})$  plot. Since  $t_{C_s-C}$  is set to 0 these bands do not interact with each other and they cross each other. The effect of non-zero  $t_{C_s-C}$  can be seen the regions in the BZ around  $\Gamma$  and M points. Figs.1.2 (d) and 1.2 (e) depict the calculated band structure of the  $2 \times 2$  system with values  $t_{C_s-C} = 0.04 t_{C-C}$  and  $t_{C_s-C} = 0.4 t_{C-C}$ . It

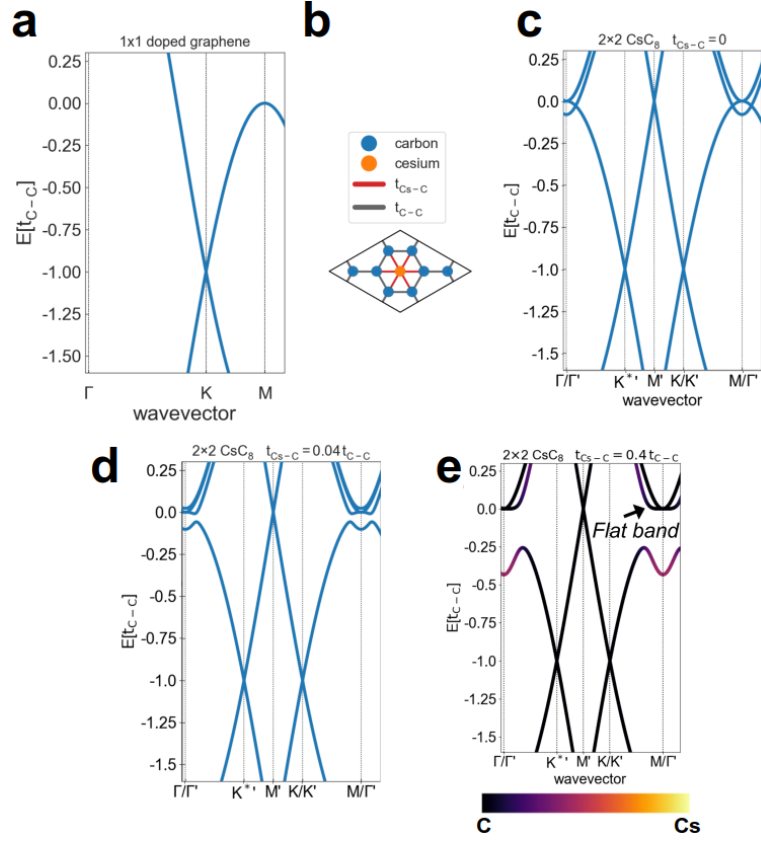


**Figure 1.2:** (a) TB calculation of the band structure of electrostatically doped graphene in the original  $1 \times 1$  cell without Cs. (b) Schematics of the  $2 \times 2$  TB unit cell. (c) TB calculation of the electronic structure of  $2 \times 2$  Cs on graphene without Cs-C hybridization, i.e.  $t_{Cs-C} = 0$ . (d,e) same as in (c) but with non-zero values of  $t_{Cs-C}$ . (e) The C (Cs) character of the band is indicated by black (purple) color.

can be seen that a hybridization gap opens in the electronic spectrum in the crossing region between graphene and Cs derived bands. As a consequence of the anti-crossing, two branches emerge from that region. The higher energy branch forms an extended flat band at the  $E_F$ . Importantly, the extent of the flat region is a function of  $t_{Cs-C}$  as can be seen by comparing Figs.1.2 (d) and (e). With increasing hybridization  $t_{Cs-C}$ , the flat band becomes more extended in the BZ. Fig.1.2(e) also shows the C and Cs character of the bands, obtained from the eigenvector of the TB Hamiltonian. This

calculation highlights that the flat band is derived from C states. Hence it is concluded that it is inherited from the saddle point in the band structure at the M point of the BZ of graphene.

### 1.1.5 A realistic model

The TB model demonstrates that Cs derived bands must lie near the Fermi level in order to trigger the formation of the flat band. We now want to understand how to reproduce this scenario in a realistic situation. To this aim, we consider epitaxial graphene grown on top of an iridium substrate. The iridium substrate adopts a face-centered cubic structure and is stacked along the (111) crystallographic direction; we refer to it as Ir(111). Graphene grown on top of Ir(111) is recognized for its structural quality, resulting in an electronic structure resembling that of free-standing graphene[96]. Previous investigations conducted on Cs deposited on graphene/Ir(111) showed that up to a certain coverage Cs tends to intercalate in between graphene and the Ir substrate, forming an ordered  $\sqrt{3} \times \sqrt{3}$  layer[96, 97], which however does not induce a zone folding, since its potential is screened by the Ir substrate. The Cs layer detaches the graphene from the substrate and dopes graphene[96], but not quite enough to reach the singularity. By further Cs deposition one enters an overdoped regime, where Cs deposits on top of the graphene layer. Up to a certain overdoping, no ordered Cs phase forms on top of graphene[97]. We hypothesize that if enough Cs is deposited another ordered Cs phase may form, effectively encapsulating the graphene layer in between two Cs layers[97]. A schematic model of this system is depicted in Fig.1.3: one Cs layer is intercalated in between the substrate and graphene, and acts as a charge reservoir by completely donating its charge to the substrate and the graphene. The other Cs layer is adsorbed on top of graphene and should be only partially ionized due to the charge that graphene already receives from the bottom layer. In any case, we expect very high doping levels to be reached and consequently the Fermi level to be positioned in close proximity to the saddle points of the conduction band, possibly causing the system to undergo a Lifshitz transition when  $E_F$  surpasses the conduction band at the M point[71, 97]. In particular, if the top Cs layer takes a  $2 \times 2$  order, we expect the low energy band structure to be similar to the one that we discussed for the TB model. In the following section, we present the realization of the proposed system. Before continuing, I briefly explain the concept of Lifshitz transition, introduced by Lifshitz in 1959[98]. The density of states of an electron system is characterized by some values of the energy,  $\epsilon = \epsilon_L$ , corresponding to a change of topology of the constant

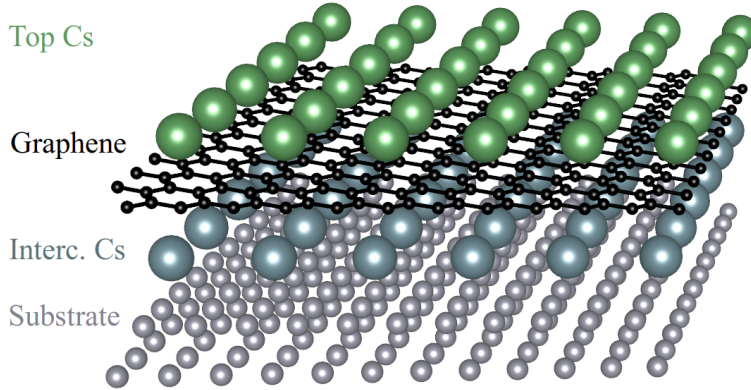


**Figure 1.3:** Model system for the realization of a flat band in monolayer graphene.

energy surfaces  $\epsilon_{\mathbf{k}} = \epsilon$ . Whenever there exists an external parameter, such as electron doping or external pressure, whose variation causes the quantity  $\mu - \epsilon_L$  to pass through zero ( $\mu$  is the chemical potential of the electrons), we observe the Lifshitz transition, which leads to thermodynamic anomalies and relevant changes for the Fermi surface of the system[98].

## 1.2 Discussion

### 1.2.1 System preparation and LEED

The experimental results presented in this Chapter have been obtained by the research group led by prof. Alexander Grüneis. The setup discussed in the previous section can be experimentally realized by first growing a monolayer graphene on an Ir(111) substrate by chemical vapor deposition, and subsequently depositing a large quantity of Cs on top of it. The details of the preparation can be found in Refs.[97, 99]. The spatial periodicity of the system is investigated using LEED[100, 101], which consists in the bombardment of the sample with a collimated beam of low energy electrons. The analysis of the LEED diffraction pattern and the spot positions allows the identification of spatial symmetries of the surface structure. In this case, LEED is important both for the observation of the hexagonal pattern due to the graphene and the possible reconstructions of the deposited Cs atoms, which have been observed multiple times in the case of alkali-intercalated graphene compounds[96, 97]. The observed LEED pattern is reported in Fig.1.4 and is indeed composed of three subpatterns: the hexagonal pattern

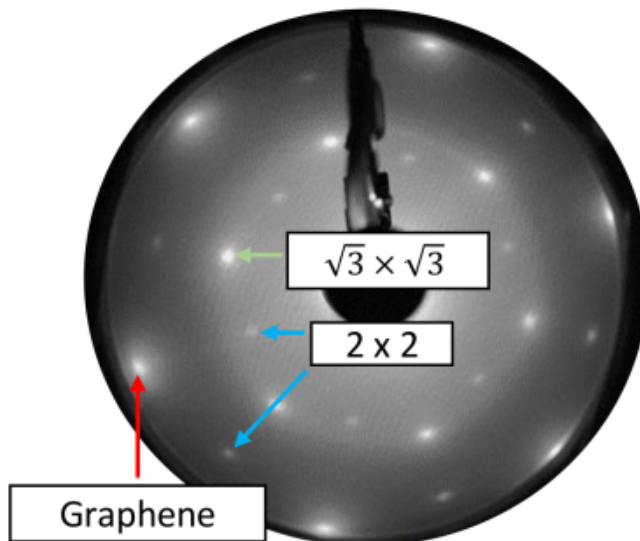


**Figure 1.4:** Characterization of  $Cs (2 \times 2)/graphene/Cs (\sqrt{3} \times \sqrt{3})/Ir(111)$ : LEED pattern taken at an energy  $E=73$  eV and a temperature  $T = 13$  K.

due to monolayer graphene, a  $Cs \sqrt{3} \times \sqrt{3}$  pattern and a  $Cs 2 \times 2$  pattern. Since LEED is a very surface sensitive technique, the sharp diffraction spots of graphene and Cs in the LEED pattern demonstrate that only negligible extra Cs atoms stick to the surface of the trilayer structure. From previous literature it is known that the  $Cs \sqrt{3} \times \sqrt{3}$  phase occurs for the Cs in between graphene and the metal substrate while we expect the  $2 \times 2$  phase grows above the graphene since it has been observed that Cs starts to be adsorbed on top of graphene after the intercalated  $\sqrt{3} \times \sqrt{3}$  phase occurs. Thus, the LEED observations strongly point towards the fact that the graphene layer is encapsulated by one  $Cs \sqrt{3} \times \sqrt{3}$  layer and one  $Cs 2 \times 2$  layer.

### 1.2.2 Density functional theory description of the system

We employ density functional theory (DFT) in order to obtain a first principles quantitative description of the electronic structure of the experimental system. As a first step, we make an attempt to describe its relevant physical properties by proceeding in the same way we did for the TB calculation, i.e. by considering only 1 Cs atom and a  $(2 \times 2)$  graphene cell. We consider monolayer graphene in a  $2 \times 2$  cell with a single Cs atom on top. We em-

ploy a fixed-cell relaxation procedure in order to determine the position of the atoms in the unit cell. We find that the most energetically favorable position for the Cs atom is the hollow site of graphene.

In Fig.1.5 we report the DFT electronic band structure obtained employing the same unit cell used in the TB calculation (panel (a)), and compare it to the TB band structure (panel (b)). There are two main differences with respect to the TB model: first, the doping is considerably lower than the one we imposed in the TB model. Second, we do not observe the formation of a proper flat band within this setup; the obtained electronic band structure is more resembling of the one in panel (d) of Fig.1.2, indicating that the hybridization between Cs and C is not sufficiently high for the formation of a flat band. We argue that both the intercalated Cs layer and the Ir substrate need to be included in the calculation for a proper description of the experimental system. In the following, we demonstrate that this is indeed the case. To this end, we first need to address several aspects of the DFT calculation:

- 1) How to simulate the Ir(111) substrate.
- 2) How to deal with the incommensurate Ir and C lattice parameters.
- 3) How to simulate the two incommensurate  $2 \times 2$  and  $\sqrt{3} \times \sqrt{3}$  Cs superstructures.

Regarding the first point, some aspects regarding DFT simulations of graphene on Ir(111) systems have already been discussed in past works, demonstrating that four layers of Ir are sufficient to simulate the bulk conditions [102, 103]. We thus include the Ir substrate considering four Ir layers in the *fcc* (111) stacking. Regarding point 2): the lattice parameter for *fcc* Ir is  $a = 3.84 \text{ \AA}$ , resulting in a Ir-Ir distance of  $3.84/\sqrt{2} \text{ \AA} = 2.715 \text{ \AA}$ , while the C-C distance is  $b = 2.47 \text{ \AA}$ , with a lattice mismatch of  $\simeq 10\%$ . The mismatch can be approximately accounted for within the supercell approach, i.e. a Gr( $10 \times 10$ )/Ir( $9 \times 9$ ) supercell[104]. This framework would provide a good description of the C-Ir interaction and of the modulated C-Ir interlayer distance[104], reducing the spurious effect due to the incommensurability. There are two problems with this approach: the first is that this simulation is demanding in terms of computational cost. The second is that the electronic dispersion would be folded in the corresponding primitive BZ and the ARPES measurements could not be directly compared to the results because of folding effects[102]. An alternative approach is to apply a compression ( $\approx$

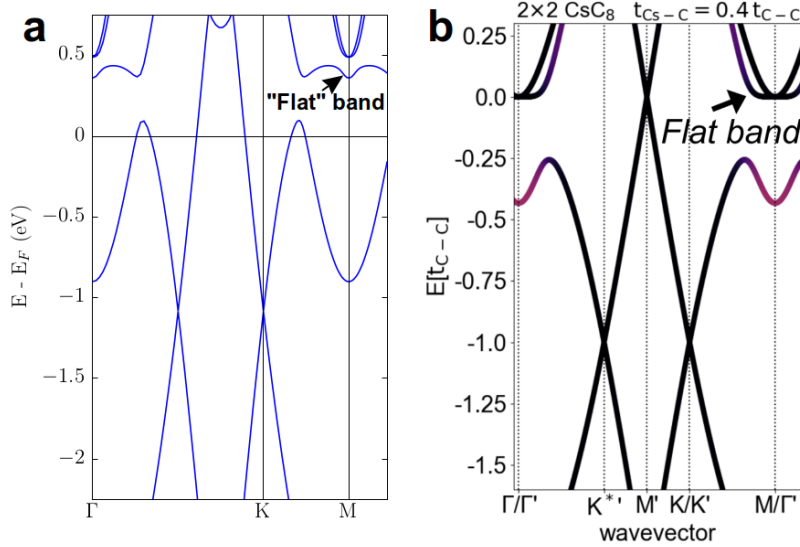


**Figure 1.5:** DFT simulation (panel (a)) and TB model (panel (b)) performed in the geometry of Fig.1.2(b).

9%) to the Ir substrate, reducing its *fcc* lattice parameter to 3.5 Å, so that Ir-Ir distance matches the C-C one (or vice-versa, enlarging the C-C lattice constant). In this way, we get a less accurate description of the C-Ir distance but on the other hand the DFT simulation is less computationally intensive. We believe that it makes sense to perform the less demanding simulation first, and then decide if there is the necessity to resort to the better description given by the supercell approach, depending on the obtained results. We thus start with the compressed Ir approach. We compress the in-plane components of the Ir *fcc* structure, while we leave the out-of-plane Ir-Ir interlayer distance fixed to the bulk value of 3.84 Å in order to avoid spurious effects stemming from out-of-plane compression.

Regarding point 3), we observe that the  $2 \times 2$  and  $\sqrt{3} \times \sqrt{3}$  are never commensurate, no matter how large the employed supercell is. However, we believe that the essential physical properties of the system can be reproduced in a simpler model, by substituting the intercalated  $\sqrt{3} \times \sqrt{3}$  Cs layer by a  $2 \times 2$  Cs layer, obtaining a commensurate Cs ( $2 \times 2$ )/graphene/Cs( $2 \times 2$ )/Ir(111) configuration. We believe that this approximation is justified as long as the intercalated Cs layer does not induce a band folding. Nevertheless, we note that the substitution of the  $\sqrt{3} \times \sqrt{3}$  Cs layer by the  $2 \times 2$  Cs layer will cause a different charge transfer to the graphene (less Cs is intercalated). We

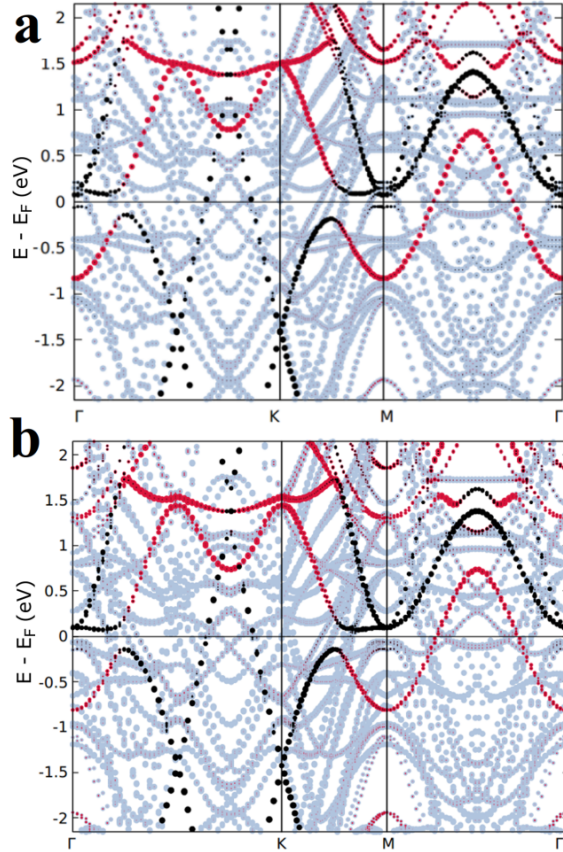


**Figure 1.6:** Comparison of DFT calculation (a) without spin-orbit interaction and (b) with spin-orbit interaction. The color and the size of the dots indicate the atomic character of the corresponding projected eigenfunction of the Kohn-Sham eigenvalues (red for Cs, black for C and grey for Ir-derived bands).

believe that this effect can be described to a first approximation by a Fermi level shift, provided that the intercalated Cs layer is completely ionized and thus only acts as a charge reservoir, not influencing the electronic structure near the Fermi level. This assumption seems reasonable since we expect the intercalated Cs layer to transfer all its charge to the substrate and the graphene, however it has to be experimentally verified.

We now discuss the electronic structure obtained within these approximations. In Fig.1.6, we report the Kohn-Sham eigenvalues with and without

the inclusion of spin-orbit coupling (SOC) (panel (a) and (b), respectively). Looking at panel (a), we observe that the obtained C and Cs band structure is qualitatively similar to the one in Fig.1.5. However, there are important differences: first of all, the graphene is much more doped, and the Fermi level lies in close proximity to the VHS, at  $\simeq -0.07$  eV. We note that the formation of an extended flat band is hindered by the hybridization of the graphene states with the Ir states lying near the Fermi level. The strong hybridization between Cs and C derived states already observed in the TB model is observed also here. In Fig.1.6 b) we consider the effect of SOC on the band structure. Both the position and the dispersion of the flat band are affected by SOC induced by the Ir substrate, as can be seen in Fig.1.6. Although SOC in graphene is negligible, the presence of the Ir substrate induces a relevant reconstruction of the band structure around the  $\Gamma$ -point. The strong hybridization observed between the Ir-derived hole-pocket at the  $\Gamma$ -point and the graphene  $\pi$  bands is not present when SOC is included. Indeed, we get a significant change for the Ir states when we switch on the spin-orbit interaction in the calculation. In particular, at the M point, SOC induces a gap-opening: the Ir bands become lower in energy by strongly reducing the hybridization with graphene bands. Thus the Ir band becomes fully occupied with a band maximum at 175 meV below the  $E_F$ . The Ir band just below the Fermi level shows a Rashba-type splitting of  $2\Delta k_{\parallel} = 0.079 \text{ \AA}^{-1}$  which is calculated following the indications of Ref.[105] and results in good agreement with the value reported in Ref.[106].

### Computational details

The DFT calculations were performed using the pseudopotentials approximation for the electron-ion interaction and a plane-wave expansion of the Kohn-Sham wavefunctions as implemented in the VASP package[107, 108, 109]. Generalized gradient approximation (GGA) in the Perdew, Burke and Ernzerhof (PBE) formulation has been adopted for the exchange-correlation potential. A 400 eV cutoff for the plane waves basis set and  $14^2$   $\Gamma$ -centered k-point grid with a gaussian smearing of 0.1 eV have been employed. We included long range van der Waals interactions in the calculation for a better description of the graphene-substrate interactions, by the Grimme's semiempirical correction (DFT-D2) to the functional[110]. Due to the presence of Ir, we also studied the effect of the spin-orbit coupling (SOC) term, by self-consistently taking it into account. Since the DFT Hamiltonian is diagonalized in periodic boundary conditions, 25  $\text{\AA}$  of vacuum have been used in order to avoid interactions between the system and its periodic image along

the growth axis, further adding dipole correction to account for the long range interactions stemming from the inequivalent top and bottom surfaces of the slab.

In the final calculation, the substrate has been simulated with four Ir layers. We treated Cs doping adding one Cs atom per unit cell below the graphene layer as intercalant to detach graphene from the substrate and additional Cs atoms on-top of the graphene layer, relaxing their position in the unit cell. The positions of the C and Cs atoms have been relaxed until the forces on the atoms are less than  $0.01 \text{ eV}/\text{\AA}^{-1}$ , while the Ir atoms were fixed to their bulk sites. We find that the lowest energy configuration for the adsorbed Cs atoms (above and below graphene) is the one with Cs atoms occupying the center of the two inequivalent hexagons of the  $2 \times 2$  unit cell. We further find that the preferential position of the intercalated Cs relative to the Ir substrate is the hollow site. The two Cs layers are relatively shifted within in-plane direction by  $\mathbf{a}_1 + \mathbf{a}_2$ , where  $\mathbf{a}_1$  and  $\mathbf{a}_2$  are the unit cell vectors of graphene. After Cs intercalation and subsequent adsorption we find that the graphene-Ir(111) perpendicular distance is  $6.17 \text{ \AA}$ , indicating a complete detaching of graphene from the substrate. The deposited Cs atoms are at distances of  $2.97 \text{ \AA}$  (for top Cs) and  $3.01 \text{ \AA}$  (for the bottom Cs) from the graphene layer.

### 1.2.3 Angle-resolved photoemission spectroscopy

One of the main tools for the experimental investigation of electronic structure is angle-resolved photoemission spectroscopy (ARPES), which has been employed to investigate the band structure of the trilayer. ARPES consists in studying the photoemission of electron from a sample after illumination with soft X-rays, allowing to observe the electronic excitations resolved in the reciprocal space. Further experimental details and in depth description of the physical principles behind this technique can be found in Refs.[111] and [112]. Fig.1.7(a) depicts the energy band structure of this sample as is measured by ARPES along the high symmetry lines of the two-dimensional BZ. The observed zone-folding of the electronic bands for the  $2 \times 2$  superstructure is a clear indication of both a highly ordered Cs lattice and a sufficiently strong scattering potential. It is important to note that the Cs  $\sqrt{3} \times \sqrt{3}$  order below the graphene does not induce zone-folding, justifying the DFT approximations and confirming the interpretation given to the LEED results, i.e. that the Cs  $\sqrt{3} \times \sqrt{3}$  is in between the graphene and the substrate. On the other hand, for the Cs atoms on top of graphene, the potential is sufficiently large to form the superstructure. The  $2 \times 2$  superlattice causes the folded BZ to be

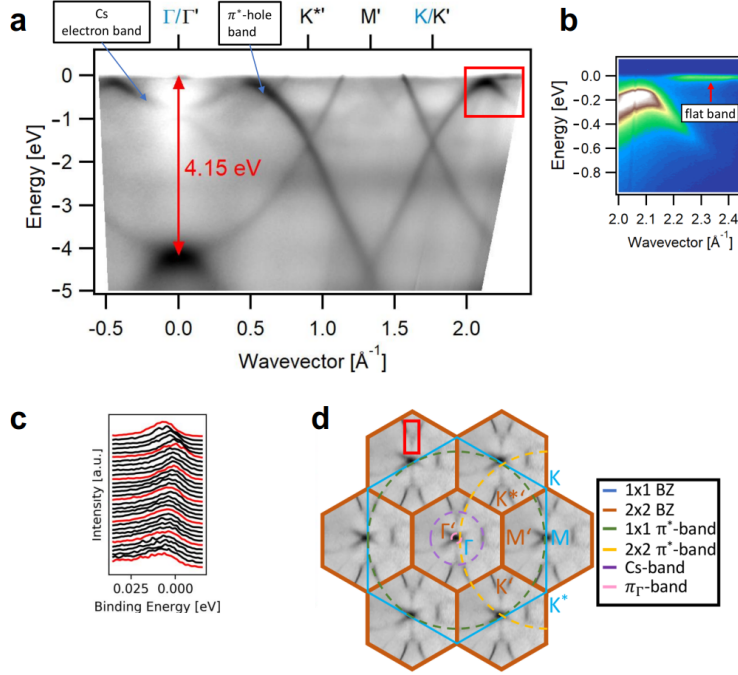
one quarter of the original one. The high symmetry points of the original BZ which are relevant for the ARPES are  $\Gamma, K, K^*$ , and M points. The relevant high symmetry points of the folded BZ are indicated by primed symbols as  $\Gamma', K', K'^*$  and  $M'$  (see Fig.1.7(a) and Fig.1.7(d)). Due to the zone-folding, the  $K'^*$  and  $K'$  points of the zone-folded BZ appear at the centers of  $\Gamma$ -K and  $\Gamma$ - $K^*$  of the original BZ. From the ARPES, two Dirac cones are visible: one at K which corresponds to a wave vector  $k \simeq 1.7 \text{ \AA}^{-1}$  and the other one at  $K'^*$  at  $k \simeq 0.8 \text{ \AA}^{-1}$ . The  $\pi$  conduction bands are located above each of the two Dirac points in the ARPES spectra. In the present case, the conduction bands are partially occupied because of the heavy Cs doping. Each of the two  $\pi$  conduction bands consists of two branches that disperse in opposite direction to each other with positive and negative curvatures, which will be referred as  $\pi^*$  electron and hole band, respectively. Around the  $\Gamma$  point, there lies an electron band whose minimum is located at 0.7 eV below the  $E_F$ . This electron band appears only after the Cs doping is performed. As demonstrated later by calculations, the electron band mainly consists of Cs ( $6s$ ) states. For this reason, it will be referred to as Cs electron band in the following. The Cs electron band hybridizes with the  $\pi^*$  hole band whose maximum is at  $\simeq 0.5 \text{ \AA}^{-1}$  as a result of the interaction between C atoms and Cs atoms of the upper layer. Zone-folding of the graphene bands is fundamental for the observed hybridization since the graphene bands cross the  $E_F$  in the original  $1 \times 1$  BZ at wave vectors  $\simeq 1.5 \text{ \AA}^{-1}$  and  $\simeq 2.2 \text{ \AA}^{-1}$ , while the Cs electron band close to the  $E_F$  lies in proximity of the  $\Gamma$  point. An hybridization between graphene and Cs electrons becomes possible when the zone-folded Dirac cone is considered, it can be seen immediately that the Cs electron band and the zone-folded  $\pi^*$  hole band hybridize close to the  $E_F$  near  $\simeq 0.5 \text{ \AA}^{-1}$ . The hybridization results in an anti-crossing of two branches. An extended flat band emerges as the higher energy branch of the anti-crossing located around  $\Gamma/\Gamma'$  and M points in the BZ. The fact that part of the conduction band is below the  $E_F$ , allows us to determine the transition energy at  $\Gamma/\Gamma'$  to be  $\approx 4.15$  eV from ARPES (see Fig.1.7(a)). Due to zone-folding  $\Gamma$  and M points of the  $1 \times 1$  BZ become equivalent and thus the transition also appears at the M point.

Fig.1.7(b) depicts high resolution ARPES data in the region close to the  $E_F$  where the  $\pi^*$  hole band and the Cs electron band display the anti-crossing behavior. The region appears at  $k = 2.2 \text{ \AA}^{-1}$  as discussed before but due to zone-folding it is equivalent to the region around  $k = 0.5 \text{ \AA}^{-1}$ . From Fig.1.7(b), evidence for a hybridization gap between the two branches near the  $E_F$  can be found. The ARPES scan in Fig.1.7(b) shows the flat band in a range from  $k = 2.2 \text{ \AA}^{-1}$  to a  $k = 2.4 \text{ \AA}^{-1}$ . However, considering the full 2D

BZ, the flat band covers a much larger area as it will be demonstrated later. Fig.1.7(c) shows the energy distribution curves of the flat band with a band width less than 10 meV. Notably, this band width is even smaller than the one observed for rhombohedrally stacked graphene where a band width of  $\simeq 25$  meV has been reported[86]. In Fig.1.7(d), the 2D map of the ARPES intensity at the  $E_F$  is plotted with highlighting the  $2 \times 2$  zone-folding and the C and Cs derived energy bands. Due to zone-folding, there are  $\pi^*$  bands from the original  $1 \times 1$  BZ and the folded  $2 \times 2$  BZ that are indicated by green and yellow color, respectively. The  $\pi^*$  derived Fermi surface contours and the Cs derived Fermi surface contours can be approximated well by circles (see the dashed circles in Fig.1.7(d)).

The fact that there are only segments with a strong ARPES intensity along the Fermi surface contours is attributed to ARPES matrix element effects, i.e. due the anisotropic light-matter interaction, depending both on the light polarization and the electronic states under investigation. Because of zone-folding, the  $\Gamma'$   $K'$  and the K-M directions are equivalent. This allows the observation of the flat band segment shown in Fig.1.7(a) and 1.7(b) multiple times along the  $\Gamma'$   $K'$  directions of the zone-folded BZs. One such segment is highlighted by a red rectangle in Fig.1.7(d). We characterize the observed Fermi surface (and the flat band) by analyzing the charge carriers that occupy Cs and C derived bands. Using circles as approximations of the Fermi surface contours, a total carrier concentration of  $n = 5.0 \times 10^{14} \text{ cm}^{-2}$  is obtained. This value of  $n$  can be compared to the theoretical carrier concentration obtained in the nearest- neighbor TB of graphene at  $5/8$  filling[113], corresponding to an extra electron per  $(2 \times 2)$  cell (per spin) with respect to the charge-neutrality point. For this case, a large carrier concentration of  $n = 9.0 \times 10^{14} \text{ cm}^{-2}$  is evaluated. However, due to the trigonal warping effect a much lower experimental value of  $n = 5.0 \times 10^{14} \text{ cm}^{-2}$  is found[114] (the equi-energy contour in the  $1 \times 1$  BZ does not connect adjacent M points by straight lines as in the nearest-neighbor model but rather by trigonally warped curves, causing a reduction of  $n$ ). Dividing the total carrier concentration into Cs and C states contributions, 0.54 Cs electrons remain in the Cs band, corresponding to a carrier concentration in the Cs band alone of  $n = 2.56 \times 10^{14} \text{ cm}^{-2}$ . per  $2 \times 2$  unit cell (note: for a full charge transfer, zero electrons would remain in the Cs band and thus the Cs band would appear above the  $E_F$  ).

*ARPES was performed at the BaDElPh beamline[115] of the Elettra synchrotron in Trieste (Italy) The reader is invited to look at Ref.[116] for details on ARPES measurements.*



**Figure 1.7:** ARPES measurements of Cs ( $2 \times 2$ )/graphene/Cs ( $\sqrt{3} \times \sqrt{3}$ )/Ir(111). (a) ARPES scan ( $\hbar\nu = 31$  eV and  $T = 17$  K) along the  $\Gamma$ - $K$ - $M$  directions. The region with the flat band is indicated by a red rectangle. The transition energy at the van Hove singularity of 4.15 eV is indicated. The high symmetry points of the original  $1 \times 1$  and the zone-folded ( $2 \times 2$ ) BZ are denoted in blue and black color, respectively. (b) Zoom-in to the region indicated by a red rectangle in (a) showing the flat band at the  $E_F$ . (c) Energy distribution curves (EDCs) for the flat band (stepsize  $0.01 \text{ \AA}^{-1}$ ) taken between  $2.2 \text{ \AA}^{-1}$  (lower EDC) and  $2.5 \text{ \AA}^{-1}$  (upper EDC). EDCs at every  $0.05 \text{ \AA}^{-1}$  are colored red. (d) Map at the  $E_F$  with the  $1 \times 1$  and ( $2 \times 2$ ) BZs. The map has been generated from a symmetrized azimuthal map taken in the first BZ. The  $\pi^*$  bands of the original  $1 \times 1$  and the ( $2 \times 2$ ) superstructure, the Cs band and the  $\pi^*$  band from close to the  $\Gamma$  point ( $\pi_{\Gamma}$ ) are indicated. The red rectangle indicates a region along  $\Gamma$ - $K'$  containing the flat band.

### Analysis of the electron-phonon coupling

As mentioned in the introduction, the investigation of this system is closely related to superconductivity. The tendency to undergo a superconducting transition is measured by the EPC constant  $\lambda$ . Informations on EPC can

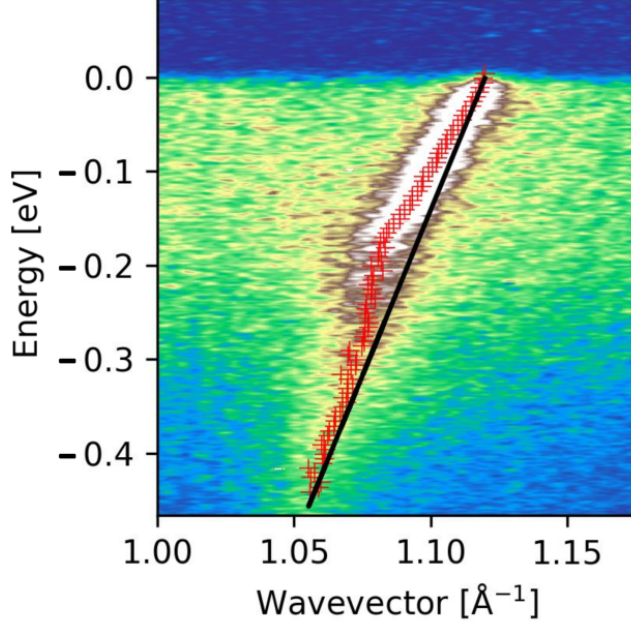


**Figure 1.8:** Analysis of the high resolution ARPES data in the region close to the Fermi level along  $K^* M'$  direction. ARPES was taken at  $\hbar\nu = 31$  eV and at  $T = 10$  K. ARPES scan in the vicinity of the Fermi wave vector and Fermi energy. The red crosses denote the ARPES maxima and the black line the bare band.

be found in the ARPES data since EPC causes a renormalized electronic dispersion that manifests as a kink in the measured spectral function close to the Fermi wave vectors along  $\Gamma$ -K. The self-energy analysis of the kink is performed according to a previously established technique[117, 72, 88, 118], by extracting the self-energy from the momentum dispersion curves according to the expressions

$$Re\Sigma(\omega) = (k_m - k)\nu_0(\omega), \quad Im\Sigma(\omega) = \frac{\Delta k}{2}\nu_0(\omega)$$

where  $\Delta k$  and  $k_m$  are the peak positions and widths at each  $\omega$ . The Eliashberg function  $\alpha^2(F)(\omega)$  is then obtained inverting the equation

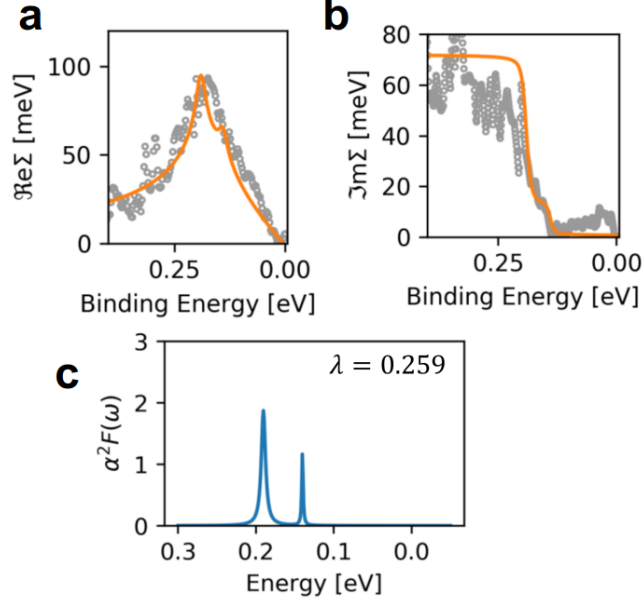


**Figure 1.9:** Real (a) and imaginary (b) part of the self-energy, respectively. (c) The extracted Eliashberg function used for the calculation of the self-energy real and imaginary part calculations shown in (a) and (b) as solid lines, respectively.

$$\text{Im}\Sigma(\epsilon, \mathbf{k}, T) = \pi \int \alpha^2 F(\omega, \epsilon, \mathbf{k}) (1 - f(\epsilon - \omega) + f(\epsilon + \omega) + 2n(\omega)) d\omega$$

where  $T$  is the temperature and  $f$  is the Fermi-Dirac distribution. The Eliashberg function is directly related to the value of the EPC constant  $\lambda$  through the relation

$$\lambda = 2 \int \frac{\alpha^2(F)(\omega)}{\omega}$$

In Fig.1.8, high resolution ARPES data taken in the vicinity of the EPC induced “kink” feature are shown. Figs.1.9 (a) and 1.9 (b) depict the real and imaginary part of the self energy, respectively. The corresponding Eliashberg function extracted from the experimental data is shown in Fig.1.9(c) and has peaks at  $\simeq 200$  meV and  $\simeq 150$  meV for intravalley and intervalley EPC, respectively. The value of  $\lambda$  in the  $\Gamma$ -K direction of the present sample

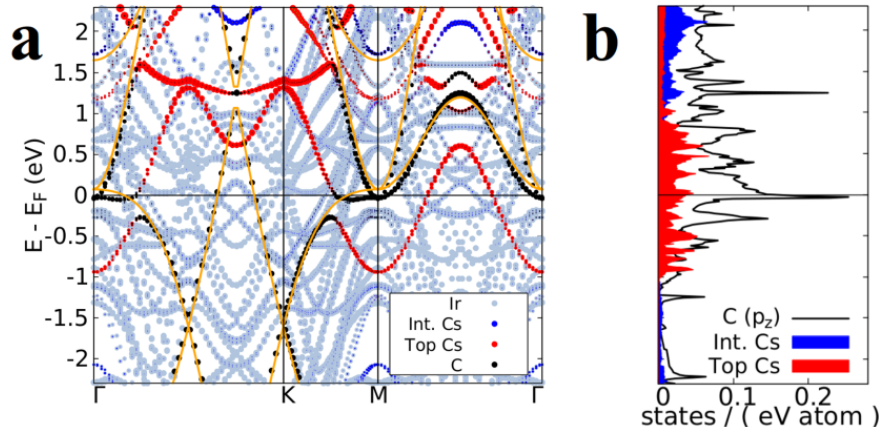


**Figure 1.10:** (a) DFT calculations of the band structure projected on Ir (grey), C (black), intercalated Cs (blue) and Cs adatoms (red). The orange lines are calculations of electrostatically doped (i.e. without Cs) free-standing graphene in a  $2 \times 2$  supercell. (b) Corresponding partial density of states of C, intercalated Cs and top Cs.

with a flat band can be compared to alkali metal doped samples with a smaller carrier concentration. In the present sample with the flat band,  $\lambda = 0.26$  along  $\Gamma$ -K is measured. Previous works of doped graphene have significantly lower  $\lambda$  in the same direction, e.g.  $\lambda = 0.17$  (Ref.[72]) and  $\lambda = 0.16$  (Ref.[119]). The larger electron phonon coupling constant observed here is therefore related to the presence of the flat band. This result makes the present system promising for electron-phonon coupling induced phase transitions such as superconductivity and charge-density wave order.

#### 1.2.4 Comparison between theory and experiment

We now compare the DFT results with the ARPES measurements. Looking at the ARPES data, we notice that only the  $2 \times 2$  periodic Cs layer, which we established to be the top adsorbate layer, plays a role in the band folding of graphene. We conclude that in a first approximation the structure can be simulated with  $2 \times 2$  Cs adsorbate layers on either side and taking into account the different charge transfer between the real  $\sqrt{3} \times \sqrt{3}$  Cs layer and the simulated  $2 \times 2$  Cs layer by means of a rigid Fermi level shift, thus justifying the way we proceeded in Sec.1.2.2. The calculated band structure of the Cs ( $2 \times 2$ )/graphene/Cs( $2 \times 2$ )/Ir(111) system is plotted again in Fig.1.10(a), in

the unfolded  $1 \times 1$  graphene BZ (with SOC). In the same plot we also include the band structure of electrostatically doped graphene in the zone-folded BZ (orange lines), in order to clarify the effect of the interaction with Cs atoms and the Ir substrate on the graphene band structure. The electrostatic doping was chosen so that the the energy of the Dirac cones matches the energy of the Dirac cones of the Cs doped system. The band structure of electrostatically doped graphene shows no such gap opening. We observe that the anti-crossing results in an electron-like branch with Cs character centered at the M point. The other branch of the band with avoided crossing disperses along the  $E_F$  with a very narrow band width. We obtain a flat band that extends for one half of the K-M distance and quantitatively explains the origin of the flat band observed in the ARPES spectra. The flat dispersion gives rise to a van Hove singularity in the DOS; the corresponding peak is seen in Fig.1.10(b). We now analyze the DOS by projecting it over the atomic orbitals. The intercalated Cs layer underneath graphene is almost completely ionized and acts as a charge transfer layer while the adsorbed Cs layer above graphene is only partially ionized and forms part of the Fermi surface. The DOS calculation corroborates full and partial ionization of the Cs layers below and above graphene, respectively. This can be seen in Fig.1.10(b) where the partial DOS of the upper Cs layer's  $6s$  orbital crosses the  $E_F$  (red color area of the DOS of Fig.1.10(b)) whereas the partial DOS of the lower layer is localized mostly above the  $E_F$ . Fig.1.11(a) depicts a plot of the DFT calculations overlaid to the ARPES data. The calculated bands have been shifted down by 0.13 eV in order to match the experimental Fermi level. Looking at the comparison between the theory and the experiment, we infer that the DFT model satisfyingly describes the experimental system, provided that the higher charge transfer associated with the presence of the  $\sqrt{3} \times \sqrt{3}$  layer is accounted for with a Fermi level shift. This is a reasonable result if the intercalated Cs layer is assumed to act as a charge reservoir, thus donating more electrons in the  $\sqrt{3} \times \sqrt{3}$  with respect to the  $2 \times 2$  reconstruction. The comparison of the calculated results with the experimental ARPES spectrum reveals an impressive agreement between the theoretical and experimental bands. The effect of Cs on the band structure is crucial: apart from the obvious doping effect, the Cs ( $6s$ ) orbital couples to the C ( $2p_z$ ) orbitals. Along the K-M direction, we observe a clear anti-crossing and the opening of a local hybridization gap of  $\simeq 200$  meV. In the region of the gap opening, the orbital character of the band changes from C to Cs (see Figs.1.10(a) and 1.11(a)). This change in band character is in good agreement to the TB-calculated change in band character shown in the previous section. Density functional theory, contrary to the nearest-neighbor TB model (see Fig.3(f)

of[116]), gives also a quantitatively adequate description of the Fermi surface. Fig.1.11(b) and (c) depict the Fermi surface as calculated by DFT overlaid to the experimental Fermi surface that was measured by ARPES (see Fig.1(e)). The Fermi surface is composed by three sheets. Two of them have conduction character: the first consists in a small circle around the  $\Gamma$  ( $M$ ) point of the BZ, where one of the two branches of the saddle point of graphene's band structure crosses the Fermi level. The second is composed by three elongated structures around the  $\Gamma$ -point representing the points of the BZ where the flat band crosses the Fermi level. The third disjoint sheet has mixed Cs and C character and is composed by electron pockets encircling the  $M'$  point of the  $2 \times 2$  BZ. The DFT Fermi surface is in good agreement with the experimentally observed Fermi surface.

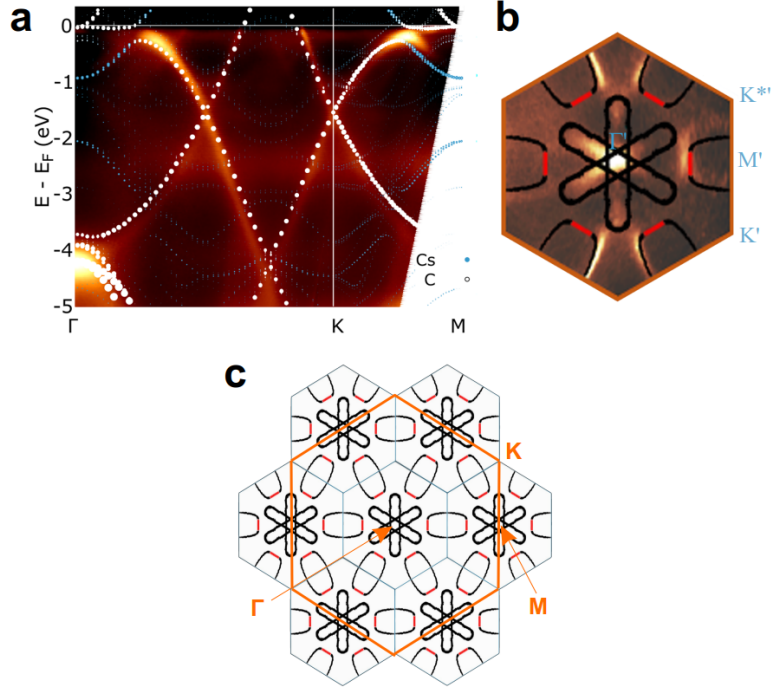


**Figure 1.11:** (a) DFT calculations (a shift of -130 meV was applied to match the experimental Fermi level) of  $(2 \times 2)$ Cs/graphene/ $(2 \times 2)$  Cs along the  $\Gamma$ -K-M directions (high symmetry points of the original  $1 \times 1$  BZ) overlaid on the experimental ARPES intensity. The color and the size of the dots indicate the atomic character of the corresponding projected eigenfunction of the Kohn-Sham eigenvalues (white for C and cyan for Cs-derived bands). (b) DFT calculated Fermi surface corresponding to the calculation shown in (a) overlaid to the experimental Fermi surface measured by ARPES. Red and black segments denote the Cs and C character, respectively. (c) Calculated Fermi surface extended to the whole  $1 \times 1$  graphene BZ.

## Chapter 2

# Coexistence of massive and massless charge carriers in an epitaxially strained alkali metal quantum well on bilayer graphene

In the previous Chapter we demonstrated that the deposition of Cs over graphene is a reliable method to reach high levels of doping and to access unexplored zones of the graphene's band structure. We observed the formation of a few layer compound constituted by two ordered Cs layers encapsulating the graphene monolayer. Motivated by these interesting results, we believe that it is worth to further investigate Cs/graphene based systems, aiming at the observation of other intriguing physical phenomena.

The work presented in this Chapter can be framed in a very active research trend for current 2D materials science, *i.e* the epitaxial growth of dissimilar 2D materials on top of each other. A prominent example is van der Waals heteroepitaxy[52], that is the specialization of the previous concept to layered van der Waals materials such as graphene and transition metal dichalcogenides. This technique allows both the realization of innovative devices with unprecedented mechanical and electronic properties[120] and the observation of clean physical effects on 2D materials. For example, superconductivity has been recently observed in a newly fabricated van der Waals heterostructure, where NbS<sub>2</sub> monolayers are separated by Ba<sub>3</sub>NbS<sub>5</sub> spacers, which also protect the NbS<sub>2</sub> layers from external perturbations, thus

reaching a clean superconducting regime[121].

Graphene has turned out to be an excellent substrate for van der Waals heteroepitaxy and the growth of transition metal dichalcogenides such as MoS<sub>2</sub>, MoSe<sub>2</sub> or TaS<sub>2</sub> has been achieved on epitaxial monolayer graphene[53, 122, 54]. However, the epitaxial growth of thin films of conventional materials such as simple metals on van der Waals substrates is complicated by the notoriously low wettability of van der Waals materials[123, 124, 125]. Improving the wettability of graphene for adsorbed water has been achieved by doping graphene[126] and changing the layer under graphene[123]. Yet, the growth techniques and the characterization of hybrid structures consisting of van der Waals materials and metals remain unexplored.

In this Chapter we present the fabrication of a thin multilayer compound obtained by Cs deposition on top of graphene. In particular, we consider bilayer graphene, which is characterized by a variety of electronic properties depending on the stacking order and offers ample opportunities for intercalation. The fabricated system shows close resemblance to the so called misfit layer compounds, *i.e.* layered compounds constituted by two types of slabs, which alternate according to a AB or ABB sequence, having a strong intra-slab bonding and a weaker interaction between them. One of them is typically a layered transition metal dichalcogenide and the other a monochalcogenide[127]. Similarly to the case of misfit layer compounds, we realize a layered structure with alternating graphene and Cs layers. At variance with the previously discussed examples, the interactions between graphene and Cs are not negligible. The study of Cs deposition on top of epitaxial bilayer graphene has revealed that, at low Cs coverages, the energetically favorable position of Cs is below the bilayer[128]. However, the structure and the electronic properties of the large Cs coverages on bilayer graphene are completely unexplored. Its development can have a large impact on electronic structure engineering of 2D matter and extend growth techniques that use van der Waals materials as substrates. Here an epitaxial growth method for the synthesis of crystalline and strained alkali-metal films on top of bilayer graphene is introduced. We study the interaction of epitaxial bilayer graphene with high Cs coverages by performing longer Cs evaporation onto the graphene bilayer than the previous reports[96, 128, 97]. In these conditions, Cs intercalates under and in between the graphene bilayer and even grows on top of bilayer as a crystalline, thin Cs film. Intercalation between the graphene layers has been reported in the literature[91, 24, 129, 130].

The Chapter is organized as follows: first we present the experimental characterization of the system, in Sec.2.1. Then, in Sec.2.2, we perform a

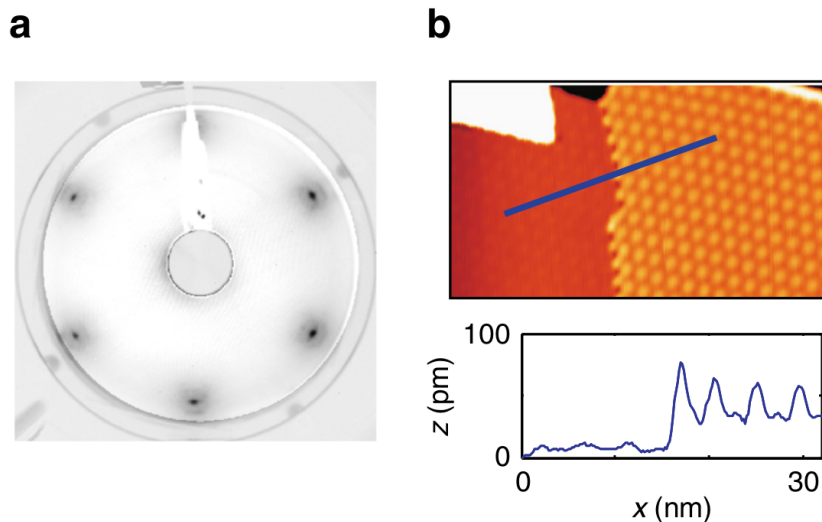


**Figure 2.1:** Characterization of bilayer graphene/Ir(111). (a) LEED pattern ( $E = 98$  eV and  $T = 20$  K) and (b) upper panel: STM topograph taken at 300 K over monolayer (left) and bilayer (right) graphene on Ir(111). Lower panel: height profile along blue line in STM topograph.

theoretical analysis in order to determine the structure of the the experimentally observed Cs-graphene multilayer. Finally, in Sec.2.2.4 we discuss the electronic band structure by introducing a minimal TB model.

## 2.1 Experimental characterization

### 2.1.1 Characterization of epitaxial bilayer graphene

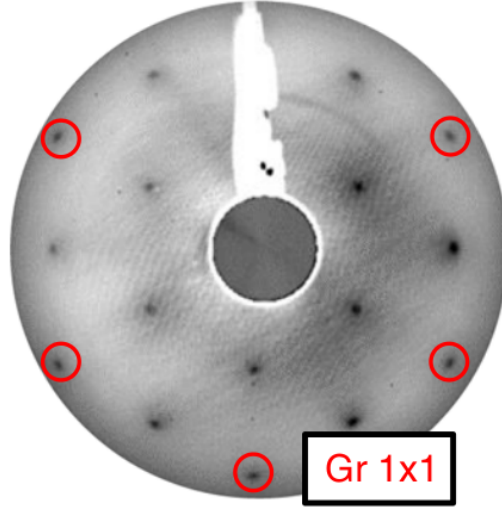
The experimental results presented in this Chapter have been obtained by the research group led by prof. Alexander Grüneis. We start by presenting the experimental characterization of the graphene before Cs deposition. We refer to the “Methods” section of Ref.[131] for the synthesis process. The low energy electron diffraction (LEED) pattern of epitaxial bilayer graphene on Ir(111) is shown in Fig.2.1(a). Six diffraction spots can be identified with a very weak moiré pattern. The six diffraction spots that correspond to bilayer graphene are sharp and hence indicate negligible azimuthal disorder. The weak moiré pattern in LEED is an interesting feature, at variance with monolayer graphene/Ir(111), where a pronounced moiré pattern in LEED

is present[99]. In the upper panel of Fig.2.1 (b), a scanning tunneling microscopy (STM) topograph of a region with monolayer and bilayer domains visible is reported. The lower panel of Fig.2.1(b), depicts a line profile of the height ( $z$ ) variation of a scan across the domain boundary. The scan of the  $z$  profile in the bilayer domain reveals that the corrugation in the bilayer domain is at least a factor 3 larger compared with the monolayer domain which is the reason for the weak moiré pattern observed in LEED. Note that for ARPES, the synthesized sample had a complete bilayer coverage while for the STM measurements shown in Fig.2.1(b), the bilayer coverage was chosen about 50%. See Ref.[131] for further details on the experimental characterization.

### 2.1.2 Cesium-derived quantum well states

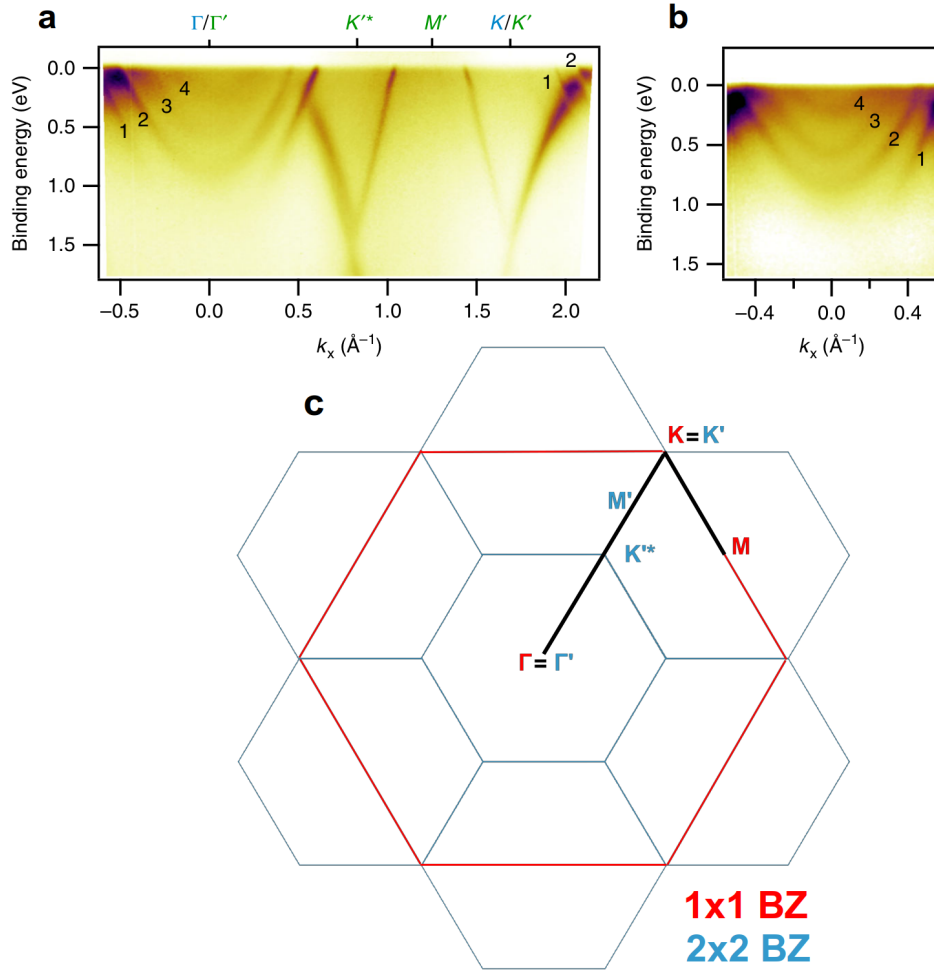
Fig.2.2 depicts the LEED pattern of bilayer graphene/Ir(111) after evaporation of Cs. It can be seen that new spots appear in addition to the diffraction spots of bilayer graphene after the Cs deposition (cf. Fig.2.1(a)); we attribute them to the formation of an ordered Cs layer. Cs grows in a  $2 \times 2$  superstructure with respect to the graphene lattice. The corrugation of bilayer graphene discussed in Fig.2.1(a),(b) is significantly reduced by Cs intercalation. This is evident from previous works which measured Fourier transform scanning tunneling spectroscopy on Cs-intercalated bilayer graphene[128].

Fig.2.3(a) depicts an ARPES scan along the  $\Gamma$ -K-M direction of the original Brillouin zone (BZ). The interesting features that can be observed from the ARPES scan are (1) a large downshift of the Dirac points corresponding to an electron doping, (2) a single  $\pi$  band at the K point which is broadened in the  $\Gamma'$ -K\*(K-M) direction, (3) a  $2 \times 2$  zone-folding of the band structure yielding a new Dirac cone at the K'\* point, and (4) a series of Cs-derived quantum well states located at the BZ center that cross the Fermi level ( $E_F$ ). The observations (1)-(4) will now be discussed in more detail. First, the Cs doping causes a partial charge transfer of the Cs(6s) electron to graphene and thus a downshift in energy of the full graphene band structure. Second, an important difference to the ARPES spectrum before Cs doping is that in the present case a single  $\pi$  band is observed while before doping two  $\pi$  bands (see Fig.2.1(b)) are present. The disappearance of one  $\pi$  band means that the out-of-plane coupling between the two graphene layers ceases. This can be explained by Cs intercalation in between the bilayer which is consistent with the observed Cs  $2 \times 2$  order which is also observed in graphite intercalation compounds[24]. Third, the zone-folding of the band structure is caused by the Coulomb potential of the Cs  $2 \times 2$  superstructure. The zone-folding



**Figure 2.2:** LEED pattern ( $E = 98$  eV and  $T = 20$  K) of bilayer graphene/Ir(111) after evaporation of Cs.

of the electronic structure of graphene is similar to what discussed in the previous Chapter for intercalated monolayer graphene and in Ref.[116] for Cs-functionalized monolayer graphene/Ir(111) and what has been reported for oxygen intercalated graphene[95]. Zone-folding causes the appearance of a new BZ with new high-symmetry points that are labeled by  $\Gamma'$ ,  $K'$ ,  $K'^*$  and  $M'$  that are indicated in Fig.2.3(a) (see Fig.1.7(d) for a sketch of the zone-folded BZ). The broadening of the  $\pi$  conduction band of graphene along the  $\Gamma'$ - $K'^*$  ( $K$ - $M$ ) direction is a result of covalent bonding of C to Cs and also present in the calculations shown in the rest of the Chapter. Fourth, a series of four quantum well states with parabolic dispersion can be observed around the  $\Gamma$  point. Regarding the linearity of graphene related bands in Fig.2.3(a), the dispersion of one  $\pi$  branch is nonlinear in the regions of  $k = 1.7 - 2.0 \text{ \AA}^{-1}$  and  $k = 0.5 - 0.86 \text{ \AA}^{-1}$ . However, a linear dispersion is observed in the other branch, that is for the regions of  $k = 1.5 - 1.7 \text{ \AA}^{-1}$  and  $k = 0.86 - 1.0 \text{ \AA}^{-1}$ . Irrespective of the existence of one nonlinear branch, Dirac Fermion behavior is retained for important physical properties such as the optical properties. These are determined by the electronic states far



**Figure 2.3:** Panel (a): ARPES scan ( $\hbar\nu = 31$  eV and  $T = 17$  K) of bilayer graphene/Ir(111) with Cs evaporated onto it. The quantum well states are labeled by 1-4. Panel (b): zoom-in into the region around  $\Gamma$  that shows four parabolic Cs quantum well states (1-4). (c) Schematic depiction of  $2 \times 2$  (light blue) and  $1 \times 1$  (red) BZs. The black line indicates the path considered for the ARPES scan in panel (a).

away from the K point, i.e., by states far from the nonlinear bands. In the visible spectral range, graphene absorbs about 2.3% of light, independent of the photon energy up to  $\simeq 3$  eV [132]. From Fig. 2.3(a), it is clear that the Dirac crossing point appears at roughly 1.5 eV binding energy. This means

that an optical transition induced by light of 3 eV energy involves states in the nonlinear segment of the band structure and yet results in an optical absorption governed by Dirac fermions. Fig.2.3(b) shows the cut through  $\Gamma$  at improved contrast and with the quantum well states labeled by 1-4. We perform a parabolic fit of the quantum well state dispersion measured by ARPES in order to extract the electron effective mass. From the fits it is found that, starting from high binding energy, the masses of the sub bands 1-4 are equal to  $m_1 = 1.0m_0$  ,  $m_2 = 1.0m_0$  ,  $m_3 = 0.8m_0$  , and  $m_4 = 0.6m_0$  . Here  $m_0$  is the free electron mass. Since the bottom of the parabolic band of the quantum well state 1 has a very low ARPES intensity, a parabolic fit of this band is too unreliable to draw conclusions regarding Fermi gas behavior from it. Instead, the self-energy of this band can be evaluated to confirm a Fermi gas behavior. We present this analysis in Ref.[131]. The origin of the deviations from the free electron mass of quantum well states 3 and 4 could be related to zone-folding of the bulk Cs band structure or the fact the Cs orbitals that make up quantum well states 3 and 4 are adjacent to graphene. Quantum well state 3 comes from Cs orbitals that belong to the first layer of Cs atoms grown on top of the bilayer and quantum well state 4 is from Cs orbitals of intercalated Cs atoms. The proximity of C and Cs orbitals can cause hybridization between them[133] which is clearly visible from Fig.2.3(a). The hybridization of the C-derived  $\pi$  bands and the Cs quantum well states is clearly visible along the  $\Gamma'$ - $K'^*$  direction of the  $\pi$  band. Importantly, structures with more Cs bands than observed in Fig.2.3(b) could not be synthesized.

*ARPES measurements were carried out at the ANTARES beamline[134] of the SOLEIL synchrotron in St. Aubin (France) and at the BaDELPH beamline[115] of the Elettra synchrotron in Trieste (Italy).*

## 2.2 Structural characterization

### 2.2.1 General considerations

We now want to determine the experimentally observed structure by recurring to DFT calculations in the light of the informations obtained from the LEED and ARPES measurements. The experimental results strongly suggest that Cs deposition induces a  $2 \times 2$  order on the graphene band structure, similarly to what we discussed in the previous Chapter for the monolayer graphene. We have deposited about five atomic layers of Cs onto bilayer graphene. The appearance of four Cs bands in the ARPES after Cs deposition leads us to the conclusion that all (or almost all) the deposited Cs

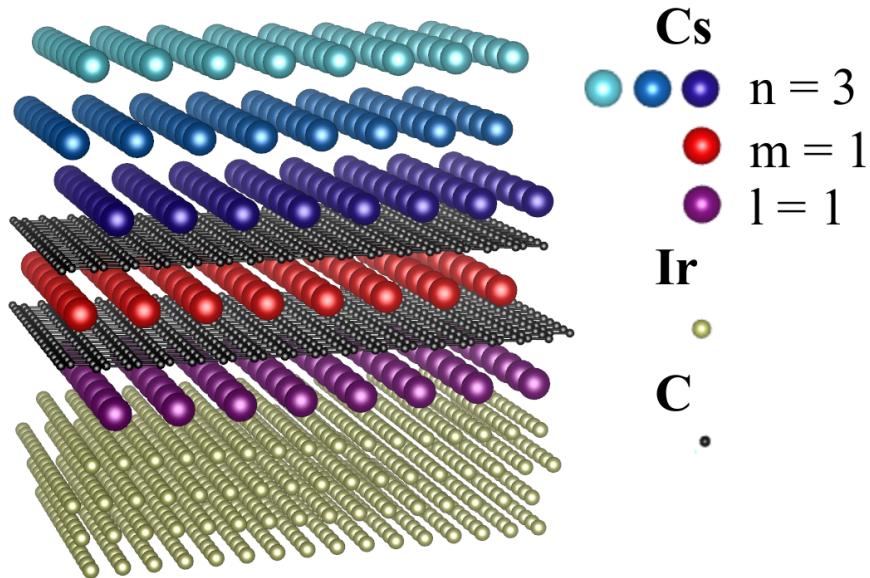


**Figure 2.4:** Schematic depiction of one of the plausible structures,  $lmn = 113$ .

assumes an ordered atomic disposition. However, there are many possible configurations for the deposited Cs. In the following, we try to determine the most likely structure based on the experimental informations at our disposal and DFT calculations. In Fig.2.4, we present one of the considered structures: one Cs layer (purple) is intercalated in between the bilayer graphene and the substrate, one in between the two graphene sheets and the other three form a thin Cs film on top of the intercalated graphene bilayer.

Before performing the DFT calculations for the determination of the ground state, we make some additional considerations. The observed  $2 \times 2$  reconstruction fixes the Cs-Cs in-plane distance to  $4.94 \text{ \AA}$  (two times the assumed graphene unit cell parameter of  $2.47 \text{ \AA}$ ). We now consider the out-of-plane stacking of consecutive Cs layers. The  $2 \times 2$  Cs imposes an hexagonal in-plane symmetry for the Cs layer, which is compatible with three possible out-of-plane stacking configurations: *fcc* (111) stacking, hexagonal close-packed (*hcp*) stacking or body centered cubic (*bcc*) (111) stacking. We can confidently exclude the possibility of a *bcc* (111) stacking: indeed, the in-plane Cs-Cs distance of  $4.94 \text{ \AA}$  is not compatible with the *bcc* (111) in-plane distance of  $a' = \sqrt{2}a_{bcc} \simeq 8.71 \text{ \AA}$  obtained for bulk *bcc* Cs in DFT (see Computational details), unless an unrealistic in-plane compression of  $\simeq 45\%$

of its value is assumed. Instead, both *fcc* and *hcp* stacking are compatible with the experimental distance of 4.94 Å by assuming a  $\simeq 11\%$  in-plane compressive strained Cs, which is a high but not unrealistic value. Since *fcc* and *hcp* stackings show very similar electronic structure, we will consider the *fcc* stacking in the following.

Thus, we conclude that the Cs film adopts a highly in-plane compressed ( $\simeq 11\%$ ) *fcc* (or *hcp*) structure, corresponding to an effective in-plane stress of 11 kbar, while the Cs-Cs out-of-plane distance is compatible with the equilibrium bulk fcc phase in the out-of-plane direction. This observation is reminiscent of the phase transition of many alkali metals to an *fcc* structure under pressure[135, 136, 137, 138, 139] which has been observed for lithium[140], potassium[141] and rubidium[142]. Bulk Cs has been reported to maintain the *bcc* structure (this phase is termed Cs-I) down to 4 K[143, 144], and a *bcc* to *fcc* (Cs-II) structural transition has been observed at a pressure of 23.7 kbar[138]. The additional Cs phases termed Cs-III, Cs-IV, and Cs-V appear upon further compression[145, 146, 147]. However *ab-initio* methods predict that the Cs-I and Cs-II structures are degenerate within few meV and there is no consensus which is the structure of the ground state[148, 149, 150]. It has been pointed out that electronic and dynamical effects are also important for the *bcc* to *fcc* structural transition[150, 151]. In the present case the *fcc* (*hcp*) stacking is favored by the presence of the graphene.

### 2.2.2 Ground state identification

With these premises, we now employ DFT to identify the structure of the Cs/bilayer graphene system. The experimentally observed structure needs to fulfill two criteria. First, its energy must be reasonably close to the calculated global energy minimum so that its stabilization in the experiment is plausible (the energy scale is given by  $\simeq k_B T$ , where  $k_B$  is the Boltzmann constant and  $T = 300$  K). Second, the obtained band structure must be in reasonable agreement with the experimental ARPES spectra. Some constraints can be established regarding the candidate structures, considering the amount of deposited Cs and the Cs structure observed. Since we deposit about 5 Cs layers on top of the graphene, we will consider structures with four, five and six Cs layers to take into account eventual Cs loss during the intercalation or inaccuracies of the quartz microbalance. We observed a  $2 \times 2$  Cs order with respect to graphene which enforces an in-plane Cs-Cs distance of 4.94 Å. Since we observed four Cs-derived bands, it is clear that we have at least four Cs layers. More layers are possible if their Cs atoms are fully ionized and hence their bands are above  $E_F$ . Indeed, we observed

this occurrence in the previous Chapter and in Ref.[116], where Cs layer intercalated in between graphene and the Ir(111) substrate is fully ionized and the electronic band formed by these Cs orbitals is located above  $E_F$  and hence cannot be measured using ARPES. However, intercalation of a second Cs layer under graphene has not been reported and for Cs-intercalated monolayer graphene, excess Cs forms a layer on top of graphene rather than a second intercalant layer. For the discussion of possible structures, it is convenient to adopt the following notation for the structure that consists of bilayer graphene and Cs layers which can be intercalated or adsorbed. In our notation, an  $lmn$  system represents  $l$  Cs layers intercalated in between Ir(111) and the bottom graphene layer,  $m$  Cs layers intercalated in between the two graphene layers, and  $n$  Cs layers grown on top of bilayer graphene. All Cs layers have a  $2 \times 2$  Cs order with respect to graphene. We have analyzed, using DFT, all possible  $lmn$  structures that fulfill the above mentioned constraints. In particular, we cast the above mentioned constraints as  $l + m + n = 4, \dots, 6$ ,  $l = 0, 1$ ,  $m = 0, \dots, 3$ , and  $n = 0, \dots, 6$ . Applying these constraints results in the following 24 possible  $lmn$  structures:  $lmn = 004, 005, 006, 013, 014, 015, 022, 023, 024, 031, 032, 033, 103, 104, 105, 112, 113, 114, 121, 122, 123, 130, 131$ , and  $132$ . We observe that after the Cs intercalation, graphene preferential stacking changes from AB (Bernal) to AA stacking for all the investigated structures. This is consistent with previous findings on Li-intercalated graphene[152]. The formation energy difference between any given  $lmn$  phase and the reference 113 configuration is defined as

$$\Delta E_X(\mu_{Cs}) = E_X - E_{113} - (N_X^{Cs} - N_{113}^{Cs})\mu_{Cs}, \quad (2.1)$$

where  $\mu_{Cs}$  is the chemical potential of the Cs atom. The number of Cs atoms in the X-phase is given by  $N_X^{Cs}$  and in the ground state by  $N_{GS}^{Cs}$ . We have systematically investigated the stability and the electronic properties of these  $lmn$  structures, finding that most of them can be excluded from being candidates that can describe the experimental results on the basis of having a too high total energy or a misfit of the electronic structure with the experiment. Varying  $\mu_{Cs}$  between  $E_{Cs-Bulk}$  and  $E_{Cs-atom}$  (energy of an isolated Cs atom) in order to mimic Cs-rich and Cs-poor experimental conditions, we find that the 113 phase is favored for  $(\mu_{Cs} - E_{Cs-Bulk}) < 6$  meV, in the vicinity of the Cs-rich experimental conditions, while 114 phase becomes favored for  $(\mu_{Cs} - E_{Cs-Bulk}) > 6$  meV (see Fig.2.5). Figs.2.6(a),(b) depict sketches of the 113 structure. In Figs.2.6(c),(d), we show a comparison of the experimental ARPES spectra to calculations of the 113 electronic

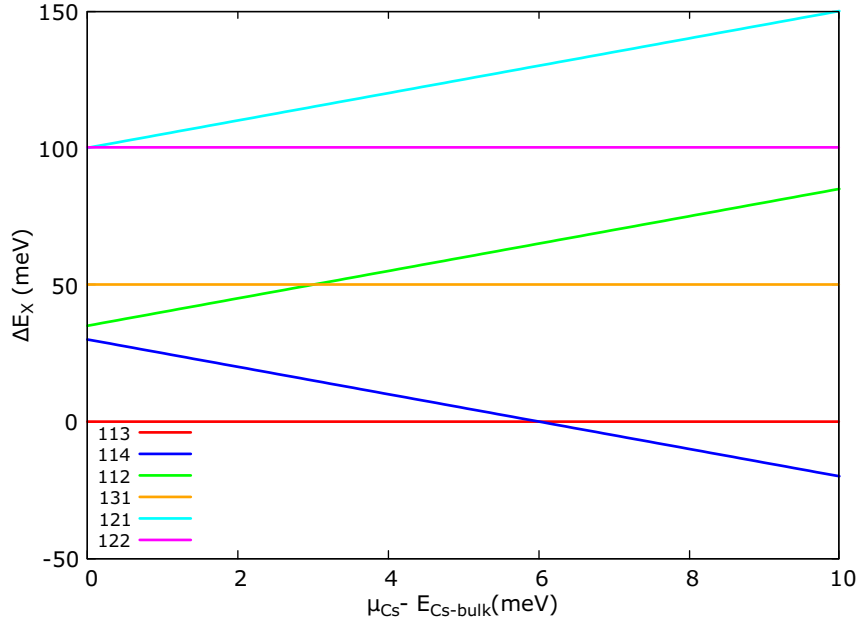


**Figure 2.5:** Phase diagram for the Cs-graphene system as a function of the chemical potential.

structure which reveals reasonable agreement to the ARPES measurements. Interestingly, the 114 band structure is in better agreement with the ARPES experiment (Figs.2.6(e)-(h) depict the structure and electronic structure of the 114 phase, respectively). Fig.2.7 contains comparisons between the DFT calculations and ARPES of several  $lmn$  structures. The improved agreement to the experiment is particularly true for the Cs-derived quantum well states. Since the 114 phase has five incompletely ionized Cs layers, we obtain five calculated Cs bands. This seems to be inconsistent to the experiment at first sight since the ARPES band structure shows only four Cs quantum well states. Nevertheless, a close look to the comparison of ARPES with the calculated band structures in Fig.2.6(g),(h) reveals that only four Cs bands cross  $E_F$  and that two Cs band merge with each other below  $E_F$ . Since the photoemission intensity of the lowest energy Cs state is practically equal to zero around the  $\Gamma$  point, we cannot exclude the presence of a fifth Cs band in its proximity. Given the better agreement of the 114 band structure with the ARPES and the unknown experimental  $\mu_{Cs}$  value, we conclude that the experimental structure is likely the 114 phase.

Thus, the layer-by-layer intercalation of bilayer graphene with Cs can be summarized as follows. With increasing Cs amount, the Cs will first intercalate between the bilayer graphene and the metal followed by intercalation in between the bilayer. Finally, adsorption on top of bilayer graphene will occur. From an energetic perspective, such a hierarchy of intercalation events is reasonable because intercalated Cs has a higher binding energy than adsorbed Cs. Energetically preferred intercalation of Cs was reported also for graphene monolayer/Ir[96] and the long-standing literature of intercalated few-layer graphene[91, 129] and graphite intercalation compounds[24] have made a case that the intercalation of Cs in between the bilayer is not surprising. What is rather surprising in the present work is the fact that high-quality Cs quantum wells can be grown on top of such intercalated samples.

### 2.2.3 Physics of the Cs growth on graphene

We now discuss the reason why Cs metal grows in 2D films on bilayer graphene and does not form clusters like most other metals do. Because of their low cohesive energy, alkali metals generally possess a relatively high ratio between adhesive energy on graphene and cohesive energy ( $E_a / E_c$ )[153, 154]. This ratio is generally very low for non-alkali metals (the only notable exceptions are Nd and Sm). The low value of  $E_a / E_c$  is ultimately the reason why most of the transition metals, noble metals, and rare earth metals favor a 3D growth mode when deposited on graphene as highlighted in refs.[153, 154]. For Cs however, this ratio is relatively higher than for other metals and also higher than for other alkali metals. In particular, the  $E_a$  of Cs on graphene is comparably high with respect to other alkali metals[155] and its surface energy is among the lowest in the periodic table[156] (nonalkali metals can have up to 10-50 times higher surface energy). For example, the bcc (110) Cs surface energy has been experimentally measured[157] to be  $\simeq 0.095 \text{ J m}^{-2}$ . Following the technique illustrated in ref.[158], we calculated the surface energy of the (111) surface of fcc Cs  $\Gamma_{fcc}(111) = 0.06 \text{ J m}^{-2}$ . This is the same value reported for the hexagonal (0001) surface in Ref.[158], which is not surprising given the similarity between the two stackings.

In conclusion of the structural analysis, we want to investigate thickness-dependent stability of the Cs film grown on intercalated bilayer graphene. We schematize the energetics of the film formation as follows: two energies contribute to the total energy of the Cs film. One is the adsorption energy which is negative and the other one is the compression energy which is positive. We first consider the binding energy for one Cs atom on the Cs-intercalated graphene in the  $2 \times 2$  unit cell, defined as  $\Delta E_1 = E_{Cs-adsorbed} - E_{Cs-bulk}$ .

Here,  $E_{Cs-adsorbed}$  is the total energy of the Cs atom on the graphene and  $E_{Cs-bulk}$  is the total energy per atom of Cs in its equilibrium bulk form. The result  $\Delta E_1 = -0.092$  eV means that the adsorption of Cs onto the bilayer is energetically favored. The same quantity can also be calculated increasing the number of adsorbed Cs layers. In particular, for the trilayer, the formation energy is equal to  $\Delta E_3 = (E_{trilayer} - 3E_{Cs-bulk})/3 = -0.04$  eV. This demonstrates that the trilayer is still favored with respect to the formation of the unstrained bulk Cs. The same calculation for the case of four Cs layers (following the same fcc stacking) on top of the intercalated graphene bilayer results in a small positive value of  $\Delta E_4 = 0.005$  eV. This would suggest that  $n = 3$  is the limit for the Cs film thickness. Nevertheless, the analysis from the DFT section suggests that the 114 phase with  $n = 4$  is a possibility. The value of  $\Delta E_4$  is small compared with the energy corresponding to room temperature and the experimental  $\mu_{Cs}$  value may be higher than  $E_{Cs-bulk}$ . Moreover, the calculation does not include external effects such as the film morphology which might alter the value of the computed energies. It is therefore likely that systems up to  $n = 4$  Cs layers can be stabilized.

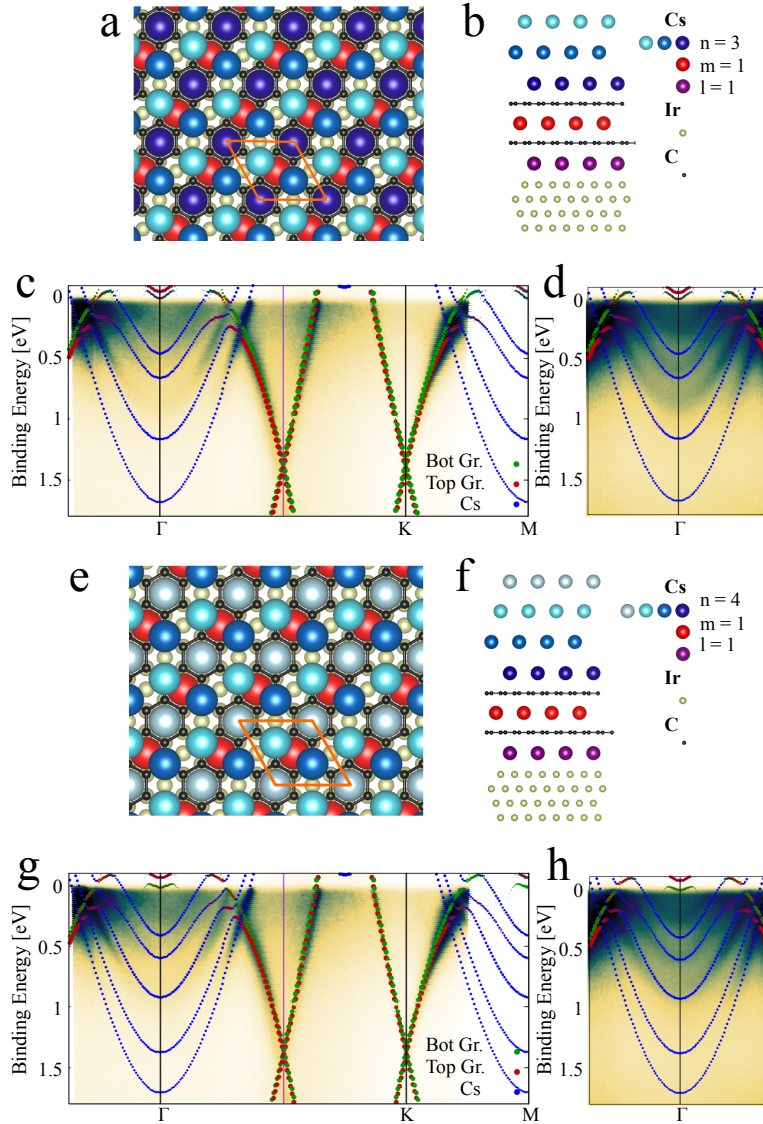


**Figure 2.6:** Comparison of band structure calculations to ARPES experiment. Panels (a),(b):  $lmn = 113$  structural model viewed from top and from the side. The unit cell is indicated by an orange rhombus in (a). Panel (c): ARPES data overlaid by the DFT calculations of the 113 structure shown in (a),(b). Panel (d): region of the quantum well states overlaid with the calculation with a modified color scale to (c). Panels (e),(f):  $lmn = 114$  structural model viewed from top and from the side. Panels: (g),(h): same as (c),(d) but for  $lmn = 114$ .

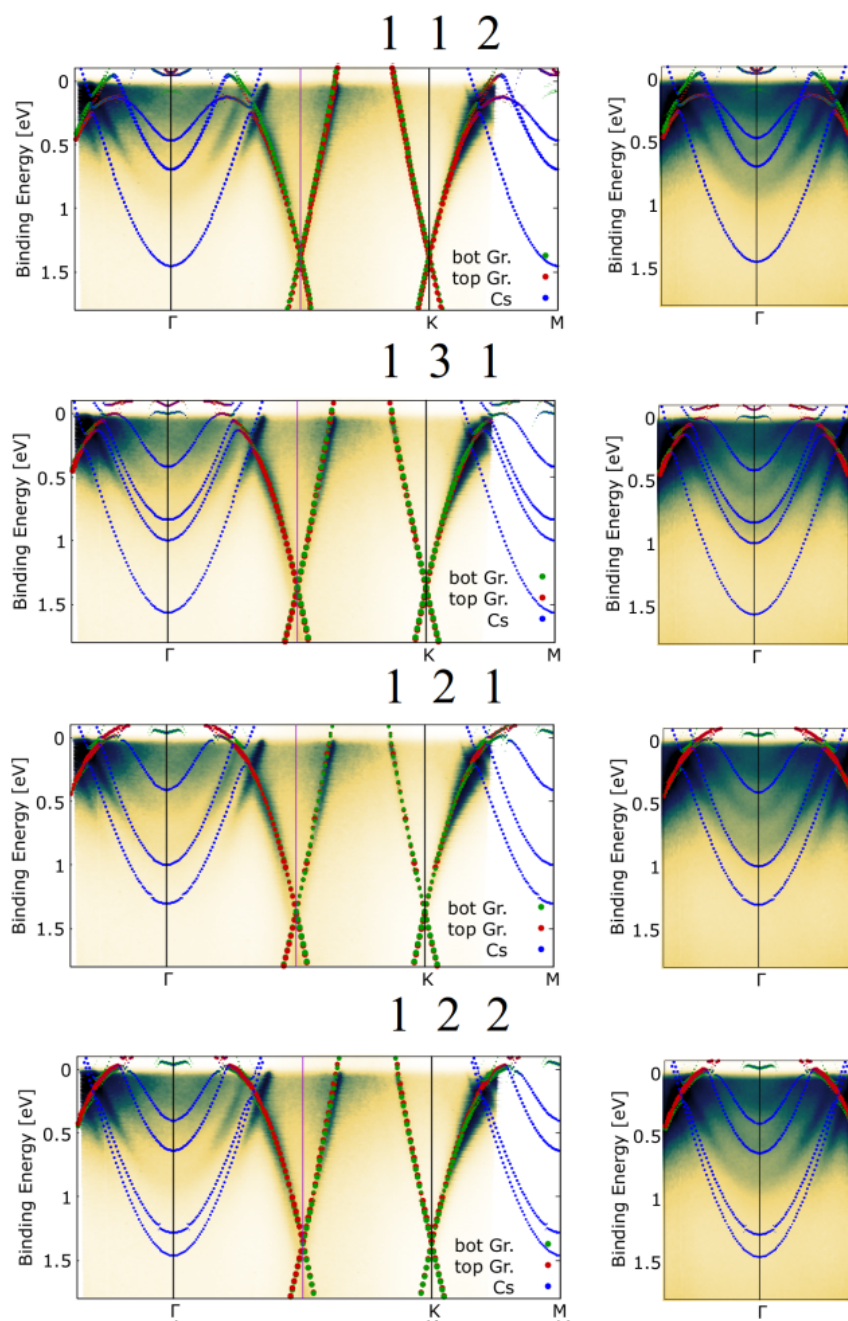


**Figure 2.7:** Comparison between ARPES spectra of Cs quantum wells grown on intercalated graphene and theoretical calculations of various other  $lmn$  structures.

### 2.2.4 A tight binding model for the Cs/bilayer graphene system

The relevant physical parameters determining the energy separation between Cs quantum wells can be captured by an effective orthogonal TB model, analogous to the one presented for Cs/monolayer graphene system. This TB model is built to describe the 113 ground state structure but can be easily modified to describe each one of the other relevant structures. The cesium trilayer and the intercalated graphene bilayer are taken into account, discarding the Ir substrate and the cesium layer adjacent to the Ir substrate, whose energy levels are far from the Fermi level as highlighted by first-principles calculations. Thus, the unit cell consists of 16 C atoms (forming a  $2 \times 2$  bilayer graphene supercell) and 4 Cs atoms. The basis set is made up of 16  $p_z$ -orbitals (one at each C site) and one s-orbital at each Cs site, yielding a  $20 \times 20$  Hamilton matrix of the form:

$$H_{TB} = \begin{pmatrix} H_{Cs-Cs} & H_{Cs-C} \\ H_{Cs-C}^\dagger & H_{C-C} \end{pmatrix} \quad (2.2)$$

where  $H_{Cs-Cs}$  is a  $4 \times 4$  matrix,  $H_{C-C}$  is a  $16 \times 16$  matrix, and  $H_{Cs-C}$  is a  $16 \times 4$  matrix, with  $H_{Cs-C}^\dagger$  being its  $4 \times 16$  Hermitian conjugate. Both in-plane and out-of-plane Cs-Cs interactions in the trilayer are included in  $H_{Cs-Cs}$ , while only the in-plane interactions in the intercalated Cs layer are included, thus omitting interactions between the trilayer and the intercalated Cs layer. In order to include all the relevant interactions, we need to consider terms up to the next-nearest-neighbors in  $H_{Cs-Cs}$  (due to the strain induced by the lattice mismatch, in-plane and out-of-plane Cs distances have different values). On the other hand, the  $H_{Cs-C}$  and  $H_{C-C}$  interactions are sufficiently well described by the nearest-neighbor terms.

In Tab.2.1, we report the relevant parameters, which produce a good qualitative description of the experimental band structure;  $t_{in}^{Cs_i-Cs_i}$  is the in-plane Cs-Cs hopping in the  $i^{th}$  layer and  $t_{out}^{Cs-Cs}$  the out-of-plane Cs-Cs hopping. The TB band structure obtained with parameters in Tab.2.1 is reported in Fig.2.8. We label the four quantum well bands using the same convention of Fig.2.3(a). According to the TB model, band 4 is derived by the Cs layer intercalated in between the graphene bilayer (Cs<sub>4</sub>), in agreement with the DFT calculation (the atomic character of the Kohn-Sham eigenvalues of band 4 is mainly Cs<sub>4</sub>-derived, not shown). As a consequence, its energy is the highest,

on-site energies (eV)	hoppings (eV)
$E_4^{Cs} = 2$	$t^{C-C} = -2$
$E_3^{Cs} = 1.2$	$t^{Cs-C} = -0.2$
$E_2^{Cs} = 0.2$	$t_{out}^{Cs-Cs} = -0.25$
$E_1^{Cs} = 0.2$	$t_{in}^{Cs_4-Cs_4} = -0.35$
$E_{up}^C = -1.6$	$t_{in}^{Cs_3-Cs_3} = -0.3$
$E_{down}^C = -1.6$	$t_{in}^{Cs_2-Cs_2} = -0.25$
	$t_{in}^{Cs_1-Cs_1} = -0.25$

**Table 2.1:** On-site energies (left) and hoppings (right) used in the TB model.

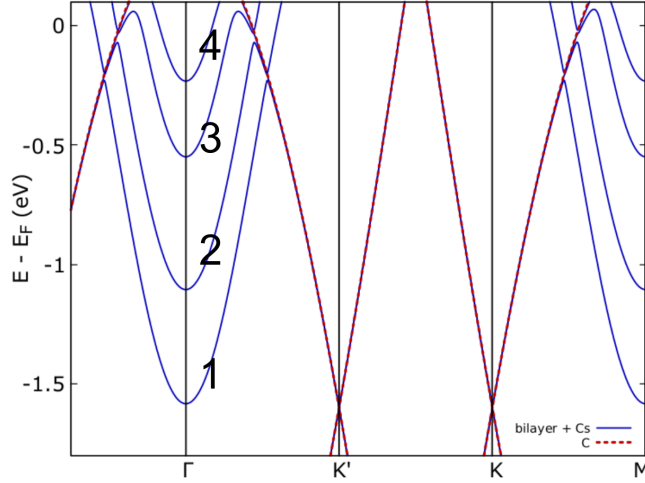


**Figure 2.8:** TB band structure obtained with parameters in Tab.2.1. Red dashed line highlights the graphene-derived bands.

due to the higher charge transfer because of its position in between the two graphene layers. The other three quantum well states are derived by the Cesium trilayer on top of the graphene. The experimentally measured effective

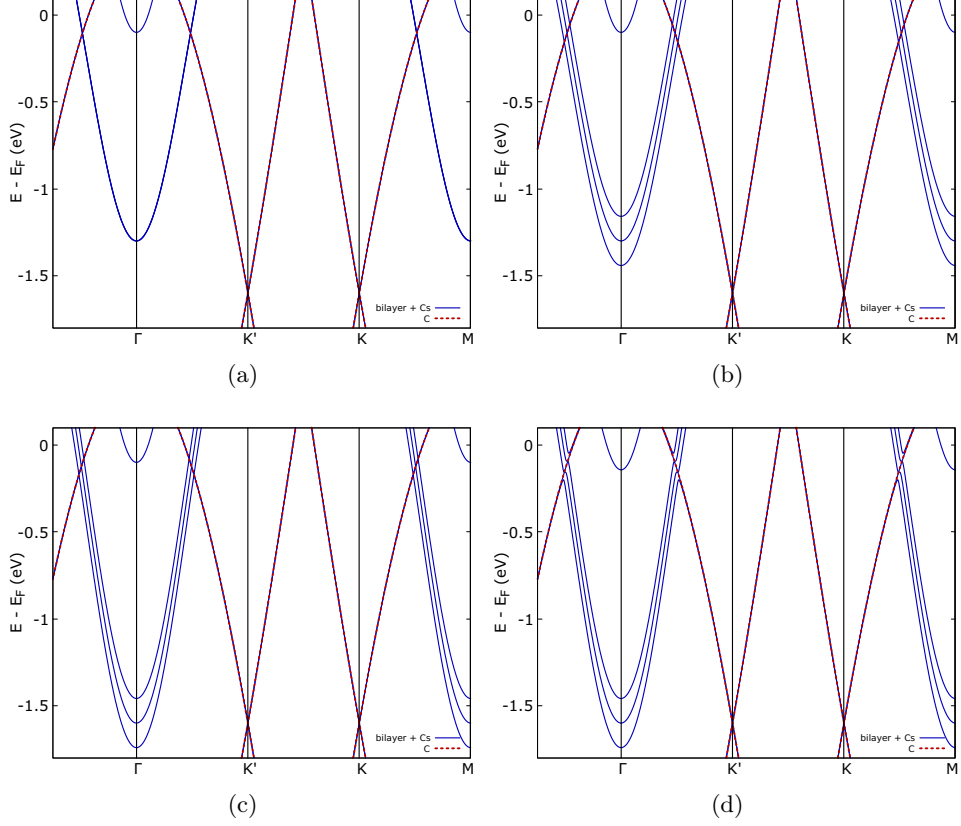


**Figure 2.9:** TB band structure obtained with  $t_{out}^{Cs-Cs} = t^{Cs-C} = 0$  eV and  $t_{in}^{Cs1-Cs1} = t_{in}^{Cs2-Cs2} = t_{in}^{Cs3-Cs3} = -0.25$  eV (Panel (a)), with the out-of-plane interaction  $t_{out}^{Cs-Cs} = -0.1$  eV (Panel (b)), multiplying all the in-plane hoppings  $t_{in}^{Cs-Cs}$  by 1.2 (Panel (c)) and finally turning on the Cs-C interaction  $t^{Cs-C} = -0.1$  eV (Panel (d)).

masses ( $m_1 = 1.0 m_0$ ,  $m_2 = 1.0 m_0$ ,  $m_3 = 0.8 m_0$  and  $m_4 = 0.6 m_0$ ) are ultimately determined by the reduced screening of the Cs atomic potential in layers 3 and 4, caused by the charge transfer to the graphene, which determines an higher value of  $t_{in3}^{Cs-Cs}$  and  $t_{in4}^{Cs-Cs}$  with respect to  $t_{in1,2}^{Cs-Cs}$ . On the other hand, the energy separation between the trilayer derived energy bands is mainly determined by the combination of three factors:

(i) the difference in the on-site parameter for Cs in each of the three layers,  $E_i^{Cs}$ ,  $i = 1, 3$ .

(ii) the strength of the out-of-plane interaction between successive Cs layers,  $t_{out}^{Cs-Cs}$ , and

(iii) the different bandwidth of the wells, related to the in-plane Cs-Cs hopping integral,  $t_{in_i}^{Cs-Cs}$ ,  $i = 1, 3$ .

For example, to highlight the role played by the out-of-plane Cs-Cs we can consider the expression of the eigenvalues at the  $\Gamma$ -point considering a constant on-site parameters ( $E_i^{Cs} = E_0$ ,  $i = 1, 3$ ) and same in-plane hopping ( $t_{in_1}^{Cs-Cs} = t_{in_2}^{Cs-Cs} = t_{in_3}^{Cs-Cs}$ ) for the different Cs layers

$$E_{\Gamma}^1 = E_0, E_{\Gamma}^{+,-} = E_0 \pm \sqrt{2} \cdot t_{out}^{Cs-Cs}$$

Within this approximation, the energy splitting is linear in  $t_{out}^{Cs-Cs}$  parameter. The overall effect in the band structure is clearly shown comparing Fig.2.9(a) ( $t_{out}^{Cs-Cs} = 0$ ) and Fig.2.9(b) ( $t_{out}^{Cs-Cs} = -0.1$  eV). The bandwidth of the four wells is determined by the in-plane Cs-Cs hopping integral,  $t_{in}^{Cs-Cs}$ , as evident comparing Fig.2.9(b) with Fig.2.9(c) in which we increased them by 20%. Finally, the role played by the C-Cs hopping term,  $t_{Cs-C}$ , is to hybridize the bands in correspondence of the crossing between C( $p_z$ )-like and Cs( $s$ )-like bands (Fig.2.9(d)).

### 2.2.5 Methods

We perform DFT calculations with the projector augmented-wave pseudopotential method[159], adopting PBE (GGA) exchange and correlation functional[160]. In the present system, the Cs-graphene interaction is strong enough to neglect the van der Waals contributions. Nevertheless we verified that the inclusion of the van der Waals contributions (using the Grimme's semiempirical correction (DFT-D2) to the functional[110]) does not make a relevant difference in the description of Cs-C interaction (the predicted Cs-C bonding distances differ by less than 5% with GGA calculation). An energy cutoff of 400 eV for the plane wave basis and  $14 \times 14 \times 1$  Monkhorst-Pack grid[161] for BZ sampling were used in order to ensure a total energy convergence of 1 meV. In our calculations of the Cs layer, we obtain a bulk bcc equilibrium lattice constant of  $a_{bcc} = 6.16$  Å,  $\sim 2\%$  larger than the experimental one[143]. Our results are in line with those in ref.[150], predicting that Cs-II (fcc) is the ground state (only 1 meV difference with respect to Cs-I). As pointed out in ref.[151], also the hcp structure, which is very similar

to the fcc structure, should emerge as a competing phase at low temperature. Indeed, we find that *hcp* and *fcc* phases are energetically degenerate up to less than 1 meV.

## Part I: Conclusions and outlook

I come to the conclusions of the first part of this thesis, which was devoted to the study of two graphene-based systems. The presented systems are the realization of various physical concepts and call for a wide range of future experimental and theoretical investigations. In Chapter 1, we discussed the realization of a flat band in a Cs/graphene/Cs trilayer and its observation by means of ARPES measurements. A combination of TB and DFT calculations have revealed the mechanism at play in the flat band formation. Two effects were found to be crucial: 1) zone-folding of the graphene bands in a  $2 \times 2$  supercell and 2) hybridization of the zone-folded graphene bands with the Cs metal  $6s$  bands at the  $E_F$ . Condition 2) also implies a partially occupied Cs band, i.e. an incomplete charge transfer of the upper Cs layer. The relevance to superconductivity is clear from the large electron-phonon coupling that has been measured as “kink” feature in ARPES (and as a phonon frequency renormalization in Raman spectroscopy, see Ref.[116]). The presented system is relevant to both chiral and conventional superconductivity because it hosts both, a flat band and a partially filled Cs band and has strong electron-phonon interaction. Concerning chiral superconductivity, it could be interesting to determine if the chiral superconducting phase is still favored if the three inequivalent M -points of the original BZ are made equivalent due to zone-folding like in the present system. It is at this point not clear, if the system thus enters into a superconducting or a ferromagnetic phase in its ground state. The determination of the more energetically favorable is beyond the scope of this work but it is undoubtedly an interesting topic for future theoretical and experimental works. An interesting future experiment on this system would be to measure the magnetic properties of graphene doped to the flat band phase using e.g. magnetic scanning tunneling spectroscopy or tip-on-SQUID measurements. Our TB calculations also reveal that the “flatness”, i.e. the extension of the flat band in the 2D BZ can directly be controlled by the wavefunction overlap of the alkali metal  $s$  orbital and the C ( $2p_z$ ) orbital. The wavefunction overlap is given by the parameter  $t_{Cs-C}$  in the TB calculations. This parameter is expected to change its value according to the type of alkali or earth alkali metal deposited and thus offers a wide tunability. Cs is expected to have a

comparably large hybridization amongst the alkali metals because its outer electron occupies the  $6s$  orbital with large spatial extent. It therefore has a large overlap with the adjacent C ( $2p_z$ ) wavefunctions. The flat band is thus predicted to be less extended in the 2D BZ for other  $MC_8$  structures (M being lithium, sodium, potassium or rubidium). From the variation of the parameter  $t_{Cs-C}$  (Figure 2) it can be seen that the flatness increases for increasing  $|t_{Cs-C}|$ . In principle, the presented strategy to induce flat bands could be applied to any 2D material where the alkali metal order implies zone-folding of the electronic structure of the host. It would be interesting to induce flat bands in the transition metal dichalcogenides (TMDs) family. TMDs are known to also host ordered alkali metal intercalant and adsorbate phases. For example, Cs evaporated onto  $TiS_2$  forms a Cs  $2 \times 2$  superstructure at certain Cs densities[162]. Another TMD where the presented approach might work is the semiconductor  $MoS_2$ . The conduction band of  $MoS_2$  has several flat segments at Q and K points and in the segment between  $\Gamma$  and M in the 2D BZ. These points give rise to maxima in the tunneling current in scanning tunneling experiments[163]. Moreover, alkali metal evaporation onto the surface of  $MoS_2$  results in a charge transfer to  $MoS_2$  and the shift of the  $E_F$  into the conduction band[164]. A sufficiently large charge transfer and an ordered alkali metal adsorbate layer could cause hybridization of the  $MoS_2$  conduction band with the alkali metal band and hence bring the flat segments of the conduction band down to the  $E_F$ .

In Chapter 2, Cs-intercalated epitaxial bilayer graphene has been prepared and used it as a substrate for the growth of epitaxially strained Cs quantum wells. This material system is a realization of a vertical heterostructure between a layered material and a metal quantum well. The well-ordered growth of Cs is understood from the improved flatness of bilayer graphene after Cs intercalation and the energy balance of the Cs surface free energy and the adhesion energy to intercalated bilayer graphene. A Cs layer forms on the intercalated bilayer graphene if the surface free energy of Cs metal is smaller than the adhesion energy to the intercalated bilayer substrate. In this case, the Cs metal can wet the intercalated bilayer graphene and an ordered thin film can grow. The surface energy of the fcc Cs(111) surface is found to have a very low value compared with other metals. Furthermore, alkali metals are very soft materials, and in particular Cs has a very low bulk modulus[148, 150, 165] ( $B' \simeq 2$  GPa). This allows Cs to match the graphene lattice parameter with an 11% in-plane compressive strain. While it is explained by these arguments why alkali metals can wet the substrate, one would expect that a Cs layer forms equally well on monolayer graphene. Nevertheless, an ordered Cs thin film on monolayer graphene could not be

grown under the same conditions. We thus speculate this could be related to the adhesion energy which might be lower for the monolayer. This could be due to the fact that Cs intercalates in a  $\sqrt{3} \times \sqrt{3}$  pattern under graphene which does not form a commensurate superstructure with the observed Cs  $2 \times 2$  film that grows on top of graphene. Performing ARPES, we investigated the electronic structure and found quantum well states with a parabolic electron energy dispersion coming from the Cs ( $6s$ ) electrons as well as a Dirac like dispersion of the  $\pi$  electrons of graphene. The electronic structure of this heterostructure thus hosts both, Schrödinger and Dirac like charge carriers.

By analyzing the ARPES data the linewidth of the Cs bands is found to be extremely narrow and  $I\Sigma(E)$  is constant as a function of binding energy  $E$  until the value of  $E$  which corresponds to the crossing point of the quantum well state and the Dirac cone. At the crossing point, the lifetime of the carriers decreases (revealed by an increase of  $I\Sigma$ ) because of hybridization between the Cs and C bands. The sharpness of the quantum well state bands is a result of the low electron density and the constant value of  $I\Sigma(E)$  points towards a small contribution of the electron-electron scattering suggesting that this system is a realization of a 2D Fermi gas.

Regarding further photoemission experiments, this system should be suitable for laser ARPES measurements employing the commonly used  $h\nu = 6.05$  eV. The Cs quantum well state 4 (see Fig.2.3(c)) has a Fermi wave vector  $\simeq 0.2 \text{ \AA}^{-1}$ , similarly to the Cu(111) surface state that was probed using this laser source. Thus, part of the observed ARPES spectra could also be measured by laser ARPES. Such a laser ARPES experiment would benefit from better spatial, energy and momentum resolution as compared with the synchrotron light source used here. This experiment could therefore be useful for the investigation of fine details in the quantum well states such as electron-phonon coupling and spin-orbit interactions. The Cs/bilayer graphene heterostructure synthesized here could serve as a substrate to grow quantum wells made of conventional metals and semiconductors on top. The role of Cs would be crucial in such an experiment since it could provide the large adhesion energy needed so that the conventional metal or semiconductor wets the surface. The large adhesion energy could come from deposited metals that form alloys with Cs. For example, Cs forms a well-studied alloy with Au[166] and an interesting future experiment could therefore be to grow Au on top of the Cs/bilayer graphene heterostructure. Another interesting future experiment is the study of the plasmon dispersion relation of the thin Cs film/bilayer graphene heterostructure. The plasmon dispersion can be studied using high-resolution electron energy loss spectroscopy and could

reveal the presence of two distinct plasmon dispersion relations that correspond to 2D massive and massless particles. A knowledge of the plasmon dispersion relations would also allow to assess the usefulness of this material for nanoplasmonics. Finally, it would be interesting to vary the alkali-metal type and hence the electron density in the hybrid structure.

The results presented in the first part have been published in Refs.[116] and [131].

## Part II

# Transition metal dichalcogenides

In the second part of the thesis we present our research on transition metal dichalcogenides (TMDs). TMDs are a class of layered compounds presenting the general formula  $\text{MX}_2$  where M, the transition metal atom, is sandwiched in between two chalcogen layers ( $\text{X} = \text{S, Se, Te}$ )[40] and held together by van der Waals interactions. As already discussed in the Introduction, the versatility of TMDs make them of special interest for applications in nanoelectronics (i.e., they show insulating, semiconducting, superconducting behavior, magnetism and CDWs), as well as a considerable interest for fundamental phenomena, especially regarding topological phases and the relation between CDWs and superconductivity, which can be both observed as a function of the external pressure in some TMDs. The electronic and dynamical properties of TMDs crucially depend on the number of layers of the sample under analysis: metal-insulator transitions[167] or the insurgence of a superconducting transition[168] can be observed as the number of layers is decreased, and even more complicated scenarios exist where there is no consensus on the ground state in the monolayer limit[169, 170]. A fundamental step in order to understand the complicated scenarios observed in the monolayer limit is to have a clear understanding of their bulk properties. Here, we specifically focus on the bulk limit of two compounds belonging to the TMDs family, namely  $\text{NiTe}_2$  and  $\text{VSe}_2$ . Our purpose is to give a first principles perspective on the intricate experimental scenario. In particular we consider the superconducting transition under pressure in bulk  $\text{NiTe}_2$  and the exotic 3D CDW transition in  $\text{VSe}_2$ . In the course of part II, we will explore the rich physical properties characterizing these compounds with a variety of different techniques. In particular, in the third Chapter we present our investigation on the electronic properties of  $\text{NiTe}_2$ , considering the possibility to induce superconductivity under pressure in its type-II Dirac semimetal phase. In the second part we focus on the exotic CDW in  $\text{VSe}_2$ , presenting a detailed investigation on the origin of the CDW instability by means of accurate first principles calculations.

## Chapter 3

# Study of NiTe<sub>2</sub> electronic and superconducting under pressure

### 3.1 Introduction

In the recent past, several experimental and theoretical investigations have been conducted in regard to the topological properties of TMDs, leading to the identification of type-II Weyl semimetals in WTe<sub>2</sub>[171] and MoTe<sub>2</sub>[172] and type-II Dirac semimetals in PdTe<sub>2</sub>[173], PtTe<sub>2</sub>[174] and PtSe<sub>2</sub>[175]. The linear dispersing tilted Dirac (or Weyl) cones characterizing type-II Dirac (Weyl) semimetals, arising due to the violation of Lorentz symmetry, typically result in an ultrahigh carrier mobility and large magnetoresistance, making these materials highly appealing for new applications both in electronics and spintronics[176, 177].

Recently, a new topologically non trivial TMD has been identified in NiTe<sub>2</sub>. Various evidences of type-II Dirac semimetal behavior in NiTe<sub>2</sub> have been collected, first through quantum oscillation measurements[178] and then by spin- and angle-resolved photoemission spectroscopy[179]. A unique feature of NiTe<sub>2</sub> is that its Dirac points are located in proximity of the Fermi level ( $\simeq 0.02$  eV above), much more closely than the other compounds belonging to the same topological family (PdTe<sub>2</sub> at 0.5 eV, PtTe<sub>2</sub> at 0.8 eV and PtSe<sub>2</sub> at 1.2 eV above the Fermi level). Furthermore, according to *ab-initio* calculations, monolayer NiTe<sub>2</sub> is superconducting with a critical temperature of 5.7 K[168], making this compound a potential candidate for topological superconductivity. Contrarily, there have been no reports of superconductivity

for pristine bulk NiTe<sub>2</sub> at ambient pressure up to now. Nevertheless, superconductivity with a critical temperature of  $\simeq 4$  K in bulk NiTe<sub>2</sub> has been induced by the intercalation of Ti atoms[180]. The picture becomes even more intricate when the application of external pressure is considered: on one hand, superconductivity has been reported to emerge in polycrystalline NiTe<sub>2</sub> with a critical pressure of 12 GPa and critical temperature of 3.5 K, reaching 7.5 K at 52.8 GPa[181]. On the other hand, no evidences for superconductivity has been documented in single crystal NiTe<sub>2</sub> down to 1.8 K, and up to an applied pressure of 71.2 GPa[182]. In the same work, a Lifshitz transition has been reported to occur at a pressure of  $\simeq 16$  GPa through the observation of pressure coefficient and Raman mode E<sub>g</sub> anomalies, and further confirmed by the sign change of the Hall coefficient[182].

Another controversial point is the pressure phase diagram of NiTe<sub>2</sub>. There is no consensus regarding the structural evolution of NiTe<sub>2</sub> under pressure. NiTe<sub>2</sub> in its bulk form crystallizes in the layered CdI<sub>2</sub>-type structure (space group P $\bar{3}$ m1, No. 164) at ambient pressure. In Ref.[183], NiTe<sub>2</sub> in the pyrite-type phase (space group Pa $\bar{3}$ , No. 205) has been synthesized at 6.5 GPa from reaction of Ni and Te in the Ni/2Te atom ratio at 1000-1200° C followed by a slow cool down to 400° C and a subsequent quench. In Ref.[182], NiTe<sub>2</sub> maintained the layered CdI<sub>2</sub>-type structure up to 71.2 GPa where pressure was gradually increased at room temperature. To the best of our knowledge, an *ab-initio* perspective on the behavior of NiTe<sub>2</sub> under pressure lacks in literature. In this Chapter we present an investigation of the electronic and structural properties of NiTe<sub>2</sub>, with the aim of clarifying the following points:

- i) Define the DFT enthalpy-pressure (H(P)) phase diagram of NiTe<sub>2</sub>.
- ii) Confirm the presence of a Lifshitz transition in NiTe<sub>2</sub> under applied pressure.
- iii) The origin of the observed superconductivity in polycrystalline NiTe<sub>2</sub>.

## 3.2 Methods

First-principles calculations have been performed within the DFT. We used ultrasoft pseudopotentials to describe the electron-ion interaction and plane-wave expansion of the Kohn-Sham wavefunctions as implemented in the *Quantum Espresso* package [184, 185]. The generalized gradient approxi-

mation (GGA) in the Perdew, Burke and Ernzerhof (PBE) formulation has been adopted for the exchange-correlation potential[186]. The kinetic energy cutoff for plane-wave expansion has been set to 60 Ry (400 Ry for the charge density). Different Monkhorst-Pack[187] wave vector grids were adopted, depending on the crystalline phase, ensuring a total energy convergence of 1 meV/atom for the considered phases. The Monkhorst-Pack mesh was set to  $12 \times 12 \times 9$  for the  $\text{CdI}_2$ -type phase and  $8 \times 8 \times 8$  for the pyrite-type phase.

Phonon frequencies and electron-phonon coupling matrix elements were determined within the Density Functional Perturbation Theory (DFPT)[188]. A  $4 \times 4 \times 3$  phonon wave vector grid was used for  $\text{CdI}_2$ -type phase. The Eliashberg function,  $\alpha^2 F(\omega)$ , and the electron-phonon coupling (EPC) parameter,  $\lambda$ , were evaluated as:

$$\alpha^2 F(\omega) = \frac{1}{N(E_F)} \sum_{\mathbf{q}\nu} \sum_{mn} \delta(\omega - \omega_{\mathbf{q}\nu}) \sum_{\mathbf{k}} |g_{\mathbf{k}+\mathbf{q},\mathbf{k}}^{\mathbf{q}\nu,mn}|^2 \times \delta(\epsilon_{\mathbf{k}+\mathbf{q}}^m - E_F) \delta(\epsilon_{\mathbf{k}}^n - E_F) \quad (3.1)$$

and

$$\lambda = 2 \int \frac{\alpha^2 F(\omega)}{\omega} d\omega \quad (3.2)$$

through integration of the squared electron-phonon matrix element  $|g_{\mathbf{k}+\mathbf{q},\mathbf{k}}^{\mathbf{q}\nu,mn}|^2$  over a  $12 \times 12 \times 9$  electronic  $\mathbf{k}$ -grid. The EPC parameter  $\lambda$  was first evaluated in the ‘‘double delta function’’ approximation of the phonon self energy, assuming a gaussian approximation of the delta function with a smearing of  $\sigma = 0.015$  Ry, and then in the formalism of the open-source software EPW[189], by interpolating the electron-phonon matrix elements on denser  $\mathbf{q}$   $12 \times 12 \times 9$  and  $\mathbf{k}$   $36 \times 36 \times 27$  grids by means of a Wannier representation based technique.

We estimated the SC critical temperature with the Allen-Dynes modified McMillan formula

$$T_c = \frac{f_1 f_2 \omega_{ln}}{1.20} \exp\left(\frac{-1.04(1 + \lambda)}{\lambda - \mu^*(1 + 0.62\lambda)}\right) \quad (3.3)$$

where  $\mu^*$  is the renormalized Coulomb pseudopotential (see below),  $\omega_{ln}$  the logarithmic average phonon frequency and  $f_1, f_2$  are correction factors introduced in Ref.[190]. We assumed  $\mu^* = 0.12$ .

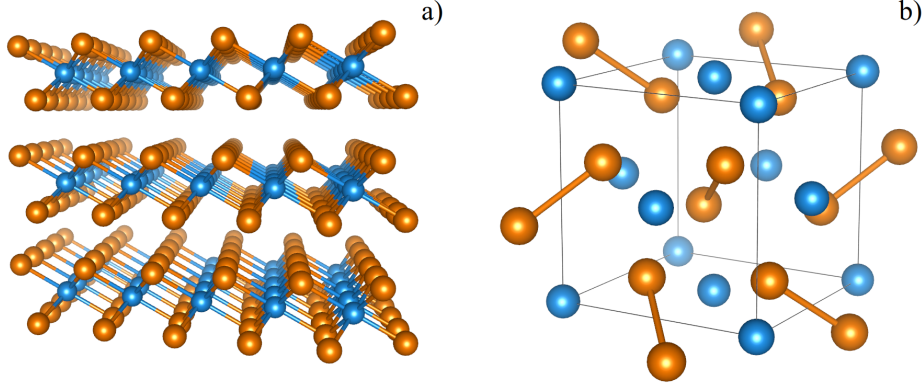


**Figure 3.1:** Sketch of the  $\text{CdI}_2$ -type (panel (a)) and pyrite-type (panel (b)) crystal structures of  $\text{NiTe}_2$ .

### 3.3 Enthalpy-pressure phase diagram of $\text{NiTe}_2$

The structural phase diagram was constructed calculating the enthalpy  $H(P) = E[V(P)] + PV(P)$  as a function of the pressure, by performing a variable-cell relaxation procedure (relaxing both the structural parameters and the internal degrees of freedom of the unit cell) for selected values of the external pressure ( $P = 0, 5, 10, 20, 50$  GPa). SOC has not been taken into account in the structural phase diagram. According to the experimental observations, two competing crystal structures were considered: i) hexagonal  $\text{CdI}_2$ -type structure, and ii) cubic pyrite-type phase. The two considered structures are sketched in Fig.3.1.

In Fig.3.2, we report the  $H(P)$  phase diagram of  $\text{NiTe}_2$ , as obtained within the DFT-GGA. The predicted equilibrium structural parameters are in remarkable agreement with the experimental measurements, with a slight overestimation of the volume for both phases ( $\simeq 2\%$ ,  $6.422 \text{ \AA}$  (DFT) vs  $6.37 \text{ \AA}$  (exp., Ref.[183]) for the cubic lattice parameter of the pyrite-type phase,  $3.899 \text{ \AA}$  (DFT) vs  $3.877 \text{ \AA}$  (exp., Ref.[182]) and  $5.328 \text{ \AA}$  (DFT) vs  $5.265$  (exp., Ref.[182]) for the in-plane and out-of-plane parameters of the hexagonal  $\text{CdI}_2$ -type structure respectively). We attribute the slight volume overestimation to the known tendency of the PBE functional to underbind solids[191]. DFT predicts that the hexagonal  $\text{CdI}_2$ -type phase is the ground state structure at 0 GPa by a wide energy margin. However, when pressure is increased, the enthalpy difference between the cubic pyrite-type structure and the  $\text{CdI}_2$  type structures reduces (see Fig.3.2), and the pyrite-type struc-

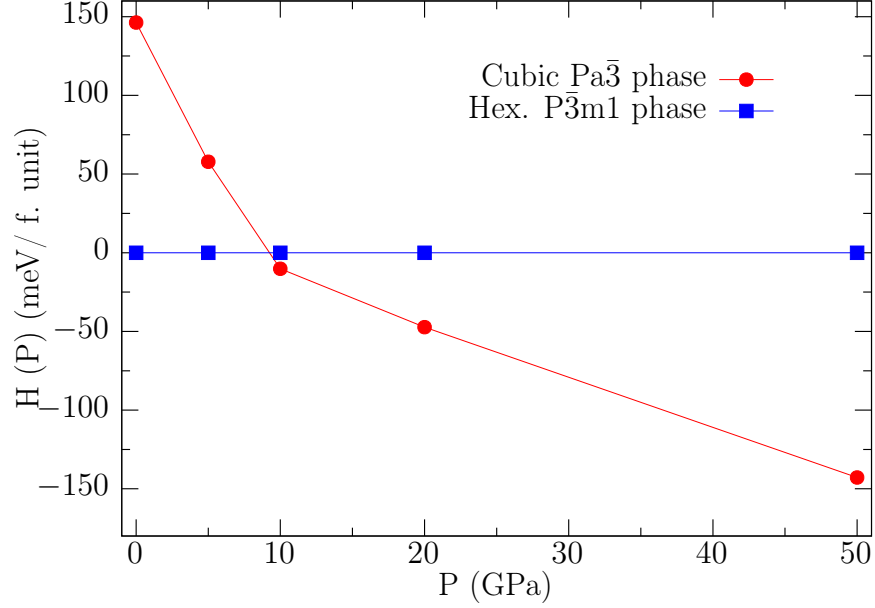


**Figure 3.2:** *Enthalpy-pressure phase diagram for the type-II Weyl semimetal  $NiTe_2$*

ture becomes the ground state just before the external pressure reaches 10 GPa. This result justifies the formation of a pyrite-type  $NiTe_2$  at 6.5 GPa observed in Ref.[183], especially considering that the GGA functional tends to overestimate the volume of the unit cell with respect to the experiment. At the same time, it is not clear why no structural phase transition has been detected in the XRD measurements of Ref.[182]. A plausible explanation could be that the hexagonal  $CdI_2$ -type phase remains metastable in all the pressure range, and the room temperature is not sufficient for the system to escape the local minimum by surpassing the energy barrier separating the metastable  $CdI_2$  phase and the global minimum represented by the cubic pyrite-type phase.

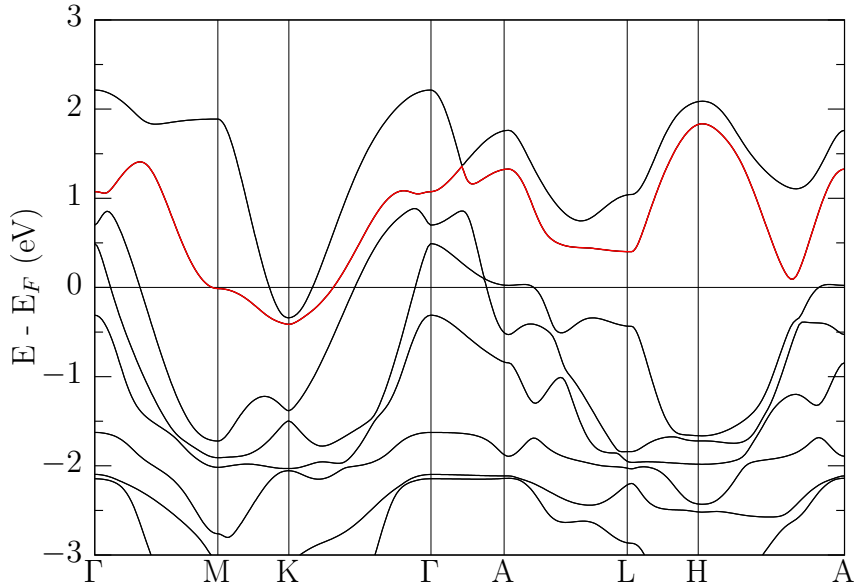


**Figure 3.3:** *Electronic band structure of NiTe<sub>2</sub> at 0 GPa. In red, the band responsible for the Lifshitz transition under applied external pressure.*

### 3.4 Lifshitz transition in NiTe<sub>2</sub> under high pressure

We now consider the electronic properties of NiTe<sub>2</sub> in the CdI<sub>2</sub>-type phase, as a first step to understand the discussed experimental observations. In particular, we are interested in the pressure evolution of the band structure. SOC has been taken into account in the calculation of the band structure. The calculated Kohn-Sham eigenvalues at 0 GPa along the high symmetry directions of the hexagonal Brillouin Zone (BZ) are reported in Fig.3.3. The results show a nice agreement with previous band structure calculations for NiTe<sub>2</sub> in literature[179, 178]. In particular, we note the presence of the type-II Dirac point in the  $\Gamma$ -A direction, which GGA predicts to be 0.1 eV above the Fermi level, in reasonable agreement with the experimental evidences.

In Fig.3.4, we report the DFT electronic band structure at 20 GPa. The

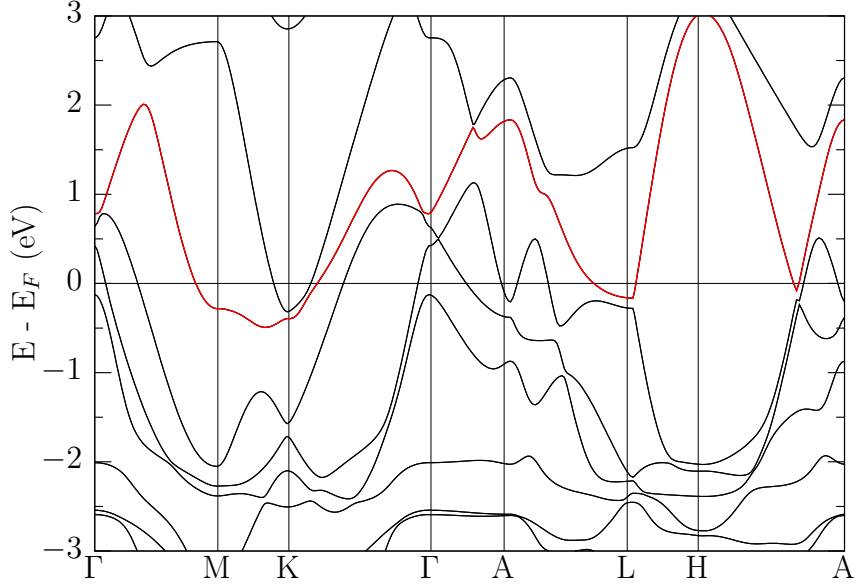


**Figure 3.4:** *Electronic band structure of NiTe<sub>2</sub> at 20 GPa. In red, the band responsible for the Lifshitz transition under applied external pressure.*

effect of the pressure is to enhance the bandwidth both for the conduction and valence bands. In particular, differently for what we observe at 0 GPa, the conduction band crosses the Fermi level in the A-L direction of the reciprocal space, giving origin to a new portion of the Fermi Surface. These results confirm that band structure changes are at the origin of the observed transport anomalies at 16 GPa[182]. In particular, we speculate that the new Fermi surface portion originating from the crossing of the Fermi level by the conduction band is likely to be responsible for the observed change in the Hall coefficient sign. We further comment on the evolution of the Dirac point under applied pressure. The Dirac point shifts towards the  $\Gamma$  point and is shifted up in energy (0.5 eV). Furthermore, the tilting of the Dirac point is much reduced with respect to what is observed at 0 GPa, transforming

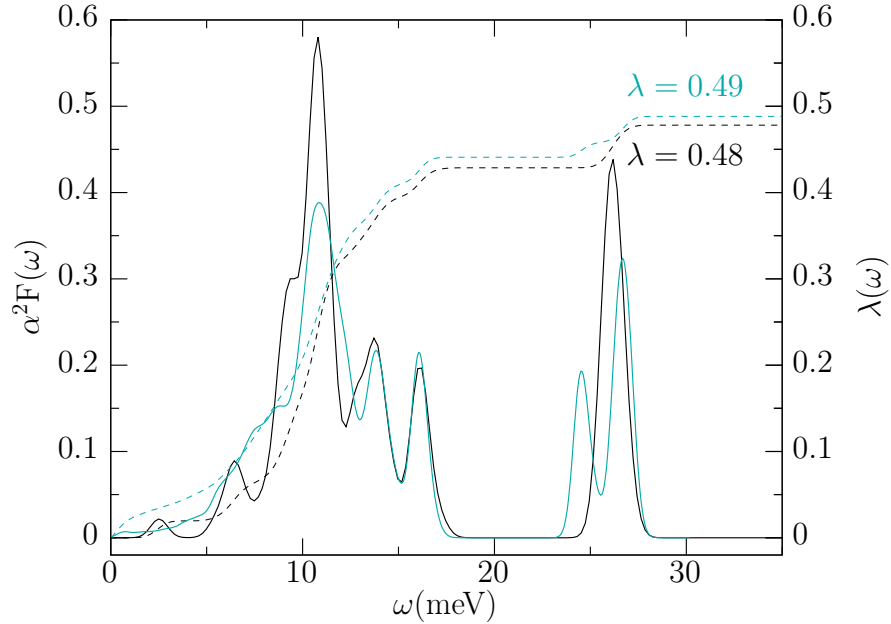


**Figure 3.5:** Eliashberg function of  $\text{NiTe}_2$  in the  $\text{CdI}_2$ -type phase at 0 GPa.

from a type-II Dirac point to a quasi type-I Dirac point.

### 3.5 Superconductivity in bulk $\text{NiTe}_2$

The possibility of superconducting transition in  $\text{NiTe}_2$  is a hotly debated matter, and is especially important considering the topological properties of this compound and thus the possibility to observe topological superconductivity. As already mentioned, a recent first principles study demonstrated how low dimensionality and Li intercalation can in principle enhance the superconducting critical temperature in  $\text{NiTe}_2$ [168]. Moreover, superconductivity was observed in polycrystalline  $\text{NiTe}_2$  after 12 GPa, while no superconducting transition was observed in single crystal  $\text{NiTe}_2$  up to 71.2 GPa. In order to clarify the origin of these observations, we investigated electron-

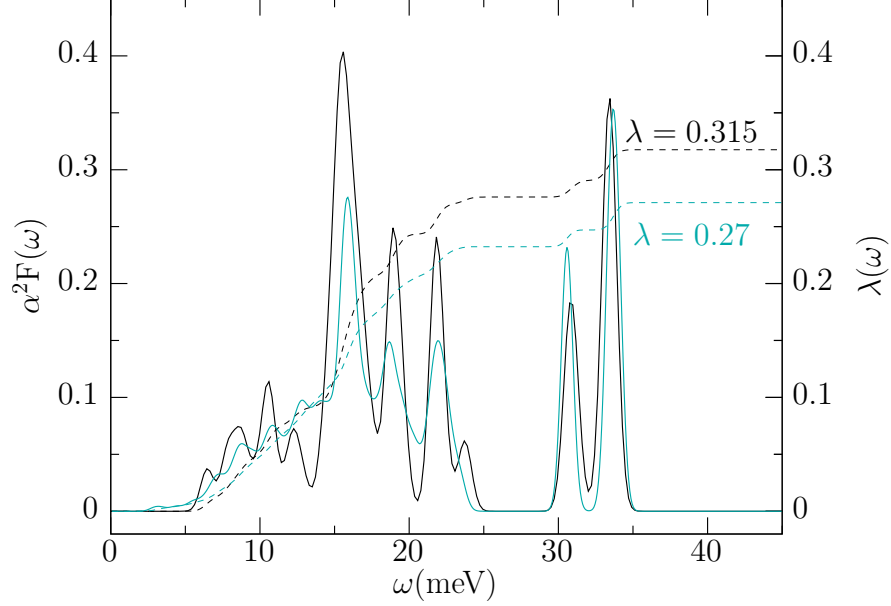


**Figure 3.6:** Eliashberg function of  $\text{NiTe}_2$  in the  $\text{CdI}_2$ -type phase at 20 GPa.

phonon coupling mediated superconductivity in bulk  $\text{NiTe}_2$  at 0 and 20 GPa.

The results are reported in Figs.3.5 and 3.6. We observe a qualitative good agreement between the Eliashberg function obtained in the “double delta function” approximation of the phonon self energy (black lines) and the interpolated Eliashberg function obtained with the EPW code (light blue lines). The Eliashberg function  $\alpha^2 F(\omega)$  is characterized by two main areas, separated by an energy gap of  $\simeq 10$  meV at 0 GPa, which reduces to  $\simeq 5$  meV at 20 GPa. The results we obtain for the Eliashberg function at ambient pressure are in very good agreement with the ones already published in the Supplemental Information of Ref.[168].

We observe a distinct detrimental effect of the pressure over the Eliashberg function and the EPC parameter. We obtain  $T_c \simeq 0.8$  K at 0 GPa and  $T_c \leq 0.1$  K at 20 GPa. These results exclude the possibility to have a pressure

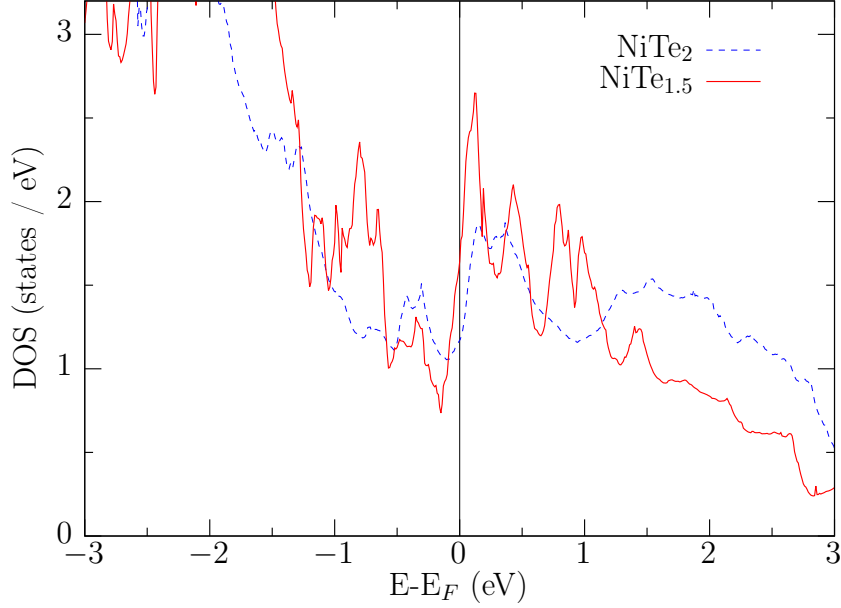


**Figure 3.7:** Comparison between the DOS of  $\text{NiTe}_2$  and  $\text{NiTe}_{1.5}$  at 20GPa.

enhanced superconducting transition in layered  $\text{NiTe}_2$ . Provided that an unconventional pairing mechanism may be responsible of the observed superconducting transition, we consider two scenarios in order to explain the experimental observation of superconductivity in bulk  $\text{NiTe}_2$  in the framework of conventional superconductivity:

1) The role of Te-defects. It is pointed out in Ref.[181], that the analyzed sample is highly Te-defective, with a measured molar ratio Ni/Te of 38/62. Thus, it is interesting to study the defective compound  $\text{NiTe}_{1.5}$  and possible changes in the electronic structure which may be at the origin of substantial differences in the superconducting transition.  $\text{NiTe}_{1.5}$  in the  $\text{CdI}_2$ -type phase has been already studied at 0GPa in Ref.[180], reporting an anomalous resistivity behavior around 56 K. A possible origin for this anomaly is the

transition towards a magnetic phase or a CDW/spin-density wave phase. We investigate a possible magnetic ground state by means of first principles magnetic calculations. We do not report the emergence of a magnetic ground state neither starting from a ferromagnetic nor from antiferromagnetic configuration, neither in the collinear approach nor in the non-collinear approach.

We then address the changes in the electronic structure provoked by the Te defect. In order to do this, we compare the density of states of  $\text{NiTe}_2$  and  $\text{NiTe}_{1.5}$  at 0 GPa. The results are shown in Fig.3.7. The defective compound presents a peak in the electronic DOS near the Fermi level, which can in principle be responsible for the observed superconducting transition. We do not speculate on the (conventional or unconventional) origin of the transition, which will be studied in a future work.

2) The superconducting transition is observed in the  $\text{Pa}\bar{3}$  phase and not in the layered  $\text{CdI}_2$ -type phase. This hypothesis is plausible since no XRD measurements under applied external pressure have been performed together with the resistivity measurements in Ref.[181] and thus a structural phase transition from the  $\text{CdI}_2$ -type to the pyrite-type phase cannot be excluded in principle. However, in order to study this possibility, one needs to estimate the electron-phonon coupling in the pyrite-type phase, requiring rather involved calculations which are beyond the scope of this work. Thus, this scenario will be considered in a future work.

## Chapter 4

# Characterization of the charge density wave in 1T-VSe<sub>2</sub>

### 4.1 Introduction to the charge density wave order

In 1930's, Peierls discovered that a one-dimensional equally spaced chain with one electron per ion is unstable. The instability arises from the coupling between the metal and its sublattice and manifests itself as a dimerization of the atom chain, i.e. the equally spaced atoms undergo a lattice distortion, causing the transition from an equally spaced crystal to a different one where the spacing between atoms alternates, resulting in the formation of atom pairs. Such a coupled electron-phonon system presents a gap in the single-particle excitation spectrum and hosts a collective mode formed by electron-hole pairs at finite wave vector  $q = 2k_F$ ,  $k_F$  being the Fermi wave vector. The rearrangement of the atoms due to the Peierls distortion produces a modulation of the electron charge density  $\rho(r)$  due to the collective mode of the electrons, which is described by

$$\rho(r) = \rho_0 + \rho_1 \cos(2k_F \cdot r + \phi)$$

where  $\rho_0$  is the unperturbed electron density of the metal.

The condensate is commonly referred as charge-density wave (CDW)[192]. The CDW phase resembles the superconducting phase in the fact that its order parameter is complex and that time and spatial derivatives of the order parameter's phase determine the electric current and the condensate density[192]. The notion of Peierls distortion remained out of the spotlight until highly anisotropic crystals became experimentally accessible. In 1964 it was proposed that some organic compounds composed by polymer chains

could exhibit superconductivity with high critical temperature, based on the idea that a mechanism involving the conducting electrons in one chain and nonconducting electrons in side chains could be at play, with light side-chain electrons playing the role played by the heavy ions in the standard BCS theory, leading to much higher energy scales and an enhanced  $T_c$ . Organic materials of this kind, such as TTF-TCNQ, were experimentally measured and theoretically studied (see Refs.[193, 194]). It was found that they would undergo a metal-insulator transition which prevented the observation of superconductivity. It is now well accepted that this was the first experimental observation of the Peierls transition.

Nowadays, CDWs ground states have been observed in a wide variety of low-dimensional (layered) compounds, including cuprate superconductors (e.g. YBCO[195]), TMDs[196] and other transition metal compounds[197]. CDWs in TMDs in particular have been investigated many times in the last forty years, ever since the anomalous properties of TaS<sub>2</sub> were attributed to CDW order in 1974[198]. McMillan developed a phenomenological theory based on the Landau free-energy expansion in order to describe the CDW phase transition in TMDs. Thanks to McMillan theory and its extensions, many aspects of the CDW transition in TMDs have been successfully understood[197]. Nevertheless, there are still many open questions, especially regarding the relationship between CDW and other low temperature phases such as superconductivity and magnetic orders (see e.g. Ref.[199] for the relation between the CDW phase and the pseudogap and superconducting phases in cuprates, Ref.[200] for the coexistence of CDW and ferromagnetism in Ni<sub>2</sub>MnGa).

A detailed explanation of the Peierls transition and CDWs can be found elsewhere in literature. In the following, we will present the fundamental concepts for the description of the CDW phase, along the lines of Ref.[192]. Peierls transition can be described by the mean-field treatment of the 1D electron-phonon Hamiltonian

$$H_{e-ph} = \sum_{k,\sigma} \epsilon(k) c_{k\sigma}^+ c_{k\sigma} + \sum_{k,\sigma} \hbar\omega_q b_q^+ b_q + \sum_{k,q,\sigma} g(k) c_k^+ c_{k,\sigma} (b_q + b_{-q}^+)$$

where  $c_k^+$  and  $b_q^+$  are the electron and phonon creation operators with momenta  $k$  and  $q$  respectively,  $\sigma$  is the spin index,  $\epsilon_k$  and  $\omega_q$  are the electron and phonon energies and  $g(k)$  is the EPC constant. The CDW complex order

parameter is defined as

$$\Delta e^{i\phi} = g(2k_F)\langle b_{2k_F} + b_{-2k_F}^+ \rangle,$$

The electronic part of the electron-phonon Hamiltonian can be diagonalized in mean field theory by replacing  $b_{2k_F}$  with  $\langle b_{2k_F} \rangle$  and using a linear dispersion relation to describe the electron band near the Fermi level:

$$\epsilon(k) = v_F(|k| - k_F),$$

where  $v_F$  is the Fermi velocity. Similarly to what happens for the superconducting phase, the gap can then be expressed in terms of the electron-phonon coupling constant, which is defined as  $\lambda' = g^2(2k_F)(\omega_{2k_F}\epsilon_F)^{-1}$ , as:

$$\Delta(T = 0) = 2D \exp(-1/\lambda'),$$

where  $D$  is the one-dimensional bandwidth. The temperature dependence of  $\Delta$  is also BCS-like and vanishes at the critical temperature  $T_P = \Delta(T = 0)/1.76k_B$ . The presence of a gap in the single particle spectrum and of collective modes described by a complex order parameter are features of both the superconducting system and the CDW system. However, the collective mode of a CDW state involves electron-hole pairs located at the opposite side of the Fermi surface and connected by a wave vector equal to  $2k_F$ . The fact that a non-interacting 1D system's ground state with one electron per lattice site is always the CDW, no matter how small the EPC is, is related to the logarithmically divergent bare density response function

$$\chi_0(q, \omega) = \sum_k \frac{f(k) - f(k+q)}{\epsilon(k) - \epsilon(k+q) - \omega} \simeq -\frac{1}{\pi v_F} \frac{2k_F}{q} \ln \frac{|1 + q/2k_F|}{|1 - q/2k_F|} \quad (4.1)$$

with  $f$  the Fermi-Dirac distribution, corresponding to an electronic energy gain depending on amplitude of the lattice distortion  $u$  as  $u^2 \log u$ , which is always bigger than the quadratic elastic energy increase of the lattice. Such an ideal picture deviates from real systems, where, according to DFT, the change in energy due to a lattice distortion can be expressed in terms of the change in the potential of the nuclei,  $\delta V_{ext}$ , as

$$\delta E_{tot} = -(1/2)\delta V_{ext}\chi\delta V_{ext} \quad (4.2)$$

in implicit matrix notation[201]. Here, the density response function is dressed by the electron interactions according to

$$\chi = \chi_0/\epsilon = \chi_0/(1 - v_i\chi_0) \quad (4.3)$$

where  $\epsilon$  is the dielectric function of the metal and  $v_i$  is the total DFT interaction. The total electronic susceptibility  $\chi$  is screened by the DFT interaction and does not diverge. This means that in interacting systems (*i.e.* real materials) the Peierls picture is not exact anymore, *i.e.* a divergent non-interacting susceptibility is not enough to provoke an instability. Adding to that, other effects are at play in real systems: a small deviation from a perfect nesting of the Fermi surface (which is always present) can critically reduce the electronic susceptibility divergence observed in the Peierls model: furthermore, if a relaxation rate due to some mechanism is assumed, the enhancement of the electronic susceptibility at  $k_F$  is further reduced.[201] Indeed, this can be immediately understood in the linear response picture: an half-filled electronic system is stable against an infinitesimal perturbation; a distortion can only become stable if it is finite and if EPC is larger than a critical values[201]. All these considerations imply that the description of CDWs in real materials needs to go beyond the Peierls model in order to give quantitative predictions. To this aim, Chan *et al.* developed a formalism where periodic lattice distortions and spin density waves (a related low energy phenomenon) are treated simultaneously[202], giving the following condition for the insurgence of a CDW accompanied by a lattice instability:

$$\frac{4|g(q)|^2}{\hbar\omega(q)} - (2\bar{U}_q - \bar{V}_q) \geq \frac{1}{\chi_0(q)} \quad (4.4)$$

where  $|g(q)|$  is the electron-phonon coupling constant,  $\omega_q$  is the phonon frequency of the unstable lattice mode,  $\bar{U}_q$  and  $\bar{V}_q$  are the direct and exchange Coulomb interactions. From Eq.4.4 it is clear that a finite EPC is needed for the formation of an instability, since  $\chi_0$  is always positive and  $2\bar{U}_q > \bar{V}_q$ .

Having introduced the physical quantities at play in the formation of the CDW state, we now discuss the application of these concepts for the characterization of the CDW in a real material, namely VSe<sub>2</sub>.

## 4.2 Introduction to VSe<sub>2</sub>

Layered TMDs constitute one of the most actively researched family of materials in regard to structural phase transitions associated with a CDW. The occurrence of such phenomena in TMDs is favored by their anisotropic layered structure prone to FS nesting and the relatively high values for the electron-phonon coupling[203]. One of the most studied compounds in this regard

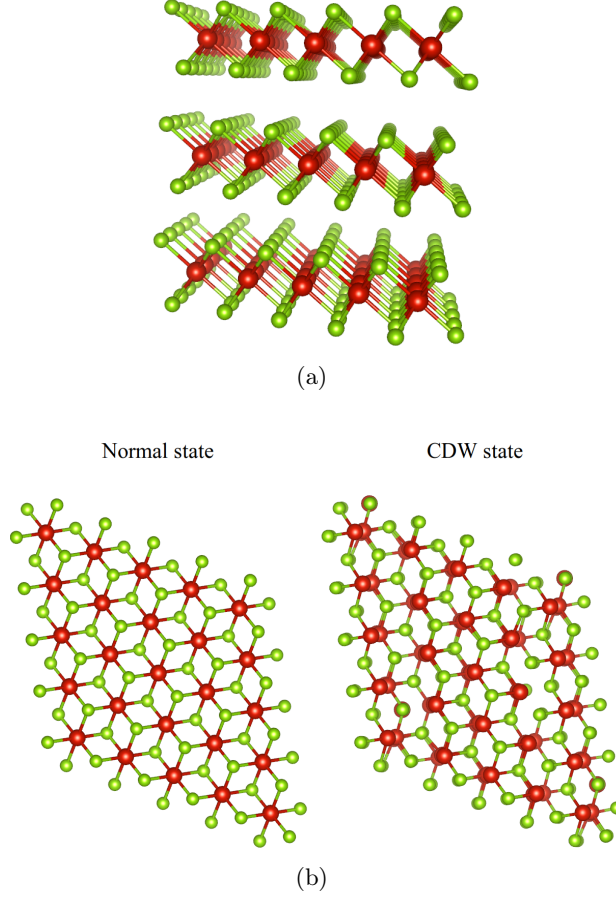


**Figure 4.1:** Side view of 1T-VSe<sub>2</sub> crystal structure (panel (a)) in the normal state. Top view of 1T-VSe<sub>2</sub> crystal structure in the normal state and after the CDW distortion (panel(b)).

is VSe<sub>2</sub>. Bulk VSe<sub>2</sub> crystallizes in the distorted octahedral 1T-polytype (P $\bar{3}$ m1 Space Group, No. 164). This compound is known to undergo two CDW phase transitions at  $T \simeq 110\text{K}$  and  $T \simeq 80\text{K}$ [204, 205]. The CDW phases present uncommon characteristics: they possess three dimensional character, with a commensurate in-plane CDW wave vector  $\mathbf{q}_{CDW}^{in} = 0.250 \mathbf{a}^*$  (primitive translation of the reciprocal lattice) and an incommensurate out-of-plane component  $\mathbf{q}_{CDW}^{out} \simeq 0.3 \mathbf{c}^*$ [205, 197]. The second CDW transition has not been found by X-ray measurements nor by magnetic susceptibility measurements below 100 K[206] by Di Salvo and Waszczak, while

it has been observed by X-ray diffraction by Tsutsumi[204] and by electron diffraction by Eaglesham *et. al.*[207]. From the observation of the satellite reflections, Tsutsumi determined the out-of-plane component of the CDW to be  $0.314 \pm 0.003 \text{ c}^*$  above 85 K and  $0.307 \pm 0.003 \text{ c}^*$  below 85 K ( $\text{c}^*$  being the out-of-plane reciprocal lattice vector). Early experiments reported other inconsistencies, such as the existence of one or multiple commensurate phases below 70K[197]. It has been observed that such inconsistencies may be the consequence of the nonstoichiometry of some of the investigated samples[206]: indeed, nominal  $\text{VSe}_2$  samples are prone to host some excess Vanadium, taking the form  $\text{V}_{1+\delta}\text{Se}_2$ . Interestingly, the application of external pressure enhances the CDW transition temperature  $T_P$  up to  $\simeq 290$  K at 15 GPa, where the CDW phase abruptly disappears in favor of a superconducting ground state[208]. More recently, CDW transition in  $\text{VSe}_2$  has been investigated via ARPES by Terashima *et.al.*[209] and soft x-ray ARPES by Strocov *et. al.*[210], focusing on the exotic 3D character of the CDW. The 3D character of the CDW is surprising in the sense that CDWs are typically regarded as a low dimensional phenomenon, whose formation is related to the favorable nesting conditions reached in layered materials due to their marked anisotropy. However, FS nesting is not the only factor in the formation of a CDW state in real materials, as discussed in the previous section. In particular, the role of EPC is equally important in TMDs, as observed by Castro Neto[203].

Interestingly, there is no consensus regarding the ground state of monolayer  $\text{VSe}_2$ : in the work by Chen *et al.* the free-standing single layer  $\text{VSe}_2$  has been reported to host a completely different  $\sqrt{7} \times \sqrt{3}$  CDW order with  $T_P = 220\text{K}$  and no ferromagnetic exchange splitting[211]. Two other groups concluded that ferromagnetism is not present due to the insurgence of the CDW[169, 212]. On the other hand, Wong *et al.*[213] and Chua *et al.* attribute the ferromagnetic phase to extrinsic factors, e.g. defects, while Bonilla *et al.*[170] and other groups[214, 215] showed experimental evidences for intrinsic magnetism in monolayer  $\text{VSe}_2$ . First principles calculations predict an enhancement of the ferromagnetic instability in the 2D limit[216, 217]. Very recently, the possibility to obtain a flat band in  $\text{VSe}_2/\text{Bi}_2\text{Se}_3$  heterostructures has been reported[218].

DFT is an important tool in the study of the CDW phase, allowing to address both the electronic structure and the dynamical and coupling properties of materials. A recent *ab-initio* study showed that both FS nesting and electron-phonon are relevant in the description of the CDW order in bulk  $\text{VSe}_2$ [219]. In the rest of the Chapter, we present our theoretical investigation of the CDW phase transition in  $\text{VSe}_2$  by means of *ab-initio* techniques.

First, we will present the electronic structure of  $VSe_2$  in the undistorted phase. Then, we will investigate the formation of the CDW by analyzing the dynamical properties of the material and the bare electronic susceptibility of  $VSe_2$ . The effect of the CDW on the electronic band structure is finally simulated using the band unfolding technique[220].

### 4.3 Methods

First-principles calculations have been performed within the DFT. We used ultrasoft pseudopotentials to describe the electron-ion interaction and plane-wave expansion of the Kohn-Sham wavefunctions as implemented in the *Quantum Espresso* package [184, 185]. The generalized gradient approximation (GGA) in the Perdew, Burke and Ernzerhof (PBE) formulation has been adopted for the exchange-correlation potential[186]. The kinetic energy cutoff for plane-wave expansion has been set to 70 Ry (700 Ry for the charge density). Different Monkhorst-Pack[187] wave vector grids were adopted, depending on the crystalline phase, ensuring a total energy convergence of 1 meV/atom for the considered phases. The simulation is performed using the experimental structural parameters for the octahedral 1T-polytype phase of

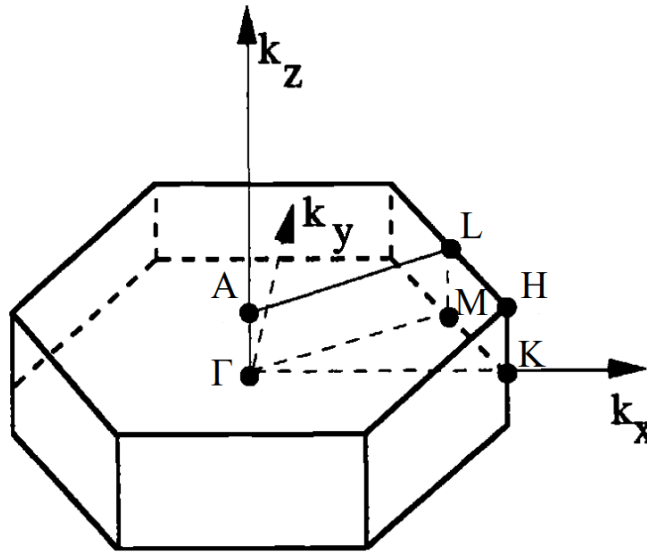


**Figure 4.2:** Depiction of the hexagonal BZ. High symmetry points are indicated. Adapted from Ref.[221].

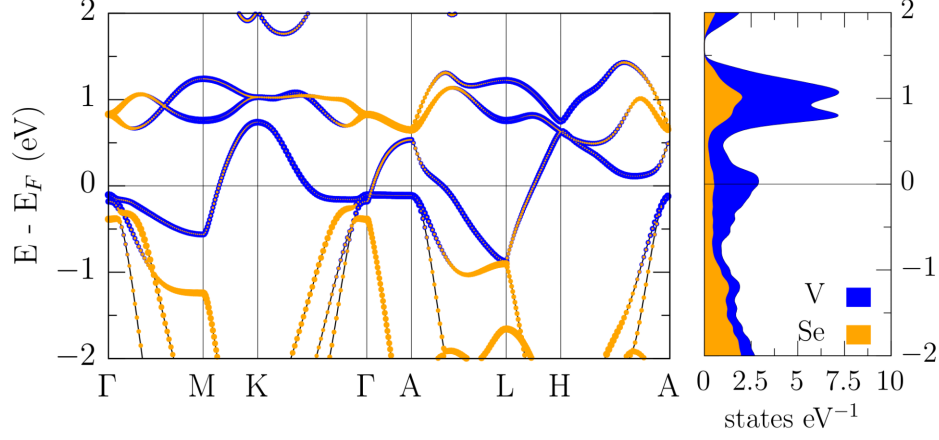


**Figure 4.3:** DFT band structure of 1T-polytype  $VSe_2$  along the BZ high symmetry paths  $\Gamma$ -M-K- $\Gamma$  and A-L-H-A and DOS projected onto V( $d$ ) orbitals (blue surface) and Se( $p$ ) orbitals (orange surface).

$a = 3.355 \text{ \AA}$  (in-plane parameter) and  $c = 6.16 \text{ \AA}$  (out-of-plane parameter). The Monkhorst-Pack mesh was set to  $16 \times 16 \times 10$  for the 1T-polytype  $VSe_2$ . Phonon frequencies were determined within the Density Functional Perturbation Theory (DFPT)[188]. A  $4 \times 4 \times 3$  phonon wave vector grid was used in the phonon calculation.

#### 4.4 Electronic structure of $VSe_2$

We start the analysis of the electronic properties of  $VSe_2$  by presenting the normal state electronic band structure of the 1T-polytype  $VSe_2$ . In Fig.4.3, the calculated Kohn-Sham eigenvalues in the normal state along high symmetry directions of the hexagonal lattice  $\Gamma$ -M-K- $\Gamma$ -A-L-H-A are reported (see the BZ in Fig.4.2). The obtained band structure can be compared to the DFT predictions and ARPES spectra already present in literature. In particular, we report a good agreement with the DFT band structure reported in Ref.[210]. As already discussed in Ref.[210], the main features of the ARPES spectrum are well described by the DFT calculation, except for the observed Se ( $4p_z$ ) - Se ( $4p_{xy}$ ) hybridization gap near the  $\Gamma$ -point, which is severely underestimated by DFT.

The electronic band structure around the Fermi level is mainly constituted by V( $d$ ) derived eigenstates and some S( $p$ ) derived eigenstates. A Fermi level crossing can be observed along the M-K direction in the  $k_z = 0$  plane

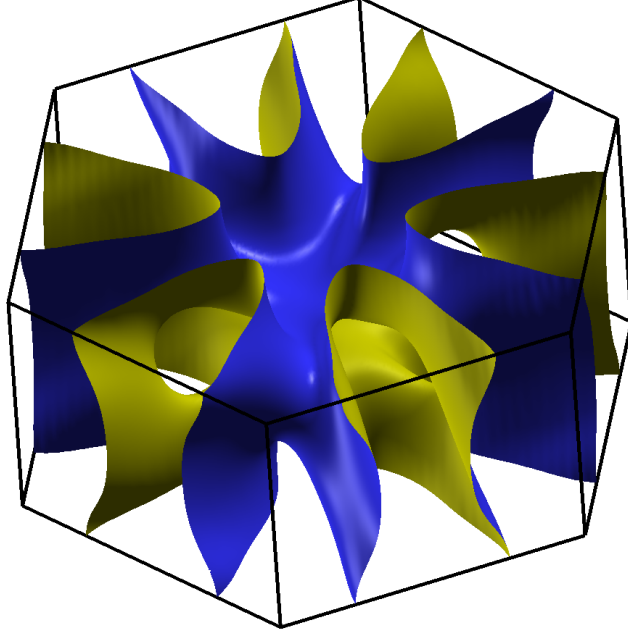


*Figure 4.4: Fermi surface for 1T-polytype VSe<sub>2</sub>.*

of the BZ, while two Fermi level crossings are present in the high symmetry directions of the  $k_z = 0.5$  plane, one along the A-L direction and a second one along the L-H direction of the BZ. Indeed, despite being a layered material, VSe<sub>2</sub> shows an important anisotropy along the  $k_z$  direction of the BZ, which crucially affects the CDW formation. A further Fermi level crossing can be also observed in the  $\Gamma$ -A direction.

The FS calculated in DFT is reported in Fig.4.4. Many properties of the VSe<sub>2</sub> FS were already pointed out in earlier works, employing the layer method[222], the APW method[223] and the self-consistent LCAO method[224]. The FS of VSe<sub>2</sub> is derived from Se(4*p*) states and is constituted by six structures with elliptical section encircling the M-L segments of the BZ. These structures tightly encircle the M-L axes in the plane perpendicular to M-L and larger when moving away from *M* towards L in the out-of-plane direction. Despite being a layered material, VSe<sub>2</sub> manifests an important

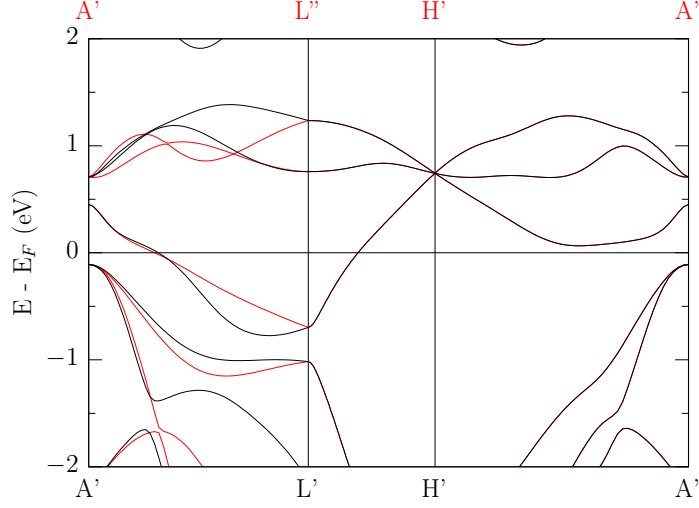


**Figure 4.5:** Inequivalent band structure along the high symmetry  $A'-L'-H'-A'$  and  $A'-L''-H'-A'$  paths of the BZ.

out-of-plane anisotropy in the Fermi surface, mainly due to a portion of the FS encircling the  $\Gamma$  point and then connecting to the previously analyzed structures.

As already pointed out[197], an interesting feature of  $VSe_2$  electronic structure is the absence of mirror symmetry with respect to the plane passing through the  $\Gamma$ -point and perpendicular to the out-of-plane  $\Gamma$ -A direction. As a consequence, a generic plane perpendicular to  $\mathbf{c}^*$  hosts two inequivalent  $A'-L'/A'-L''$  directions ( $A' = (0,0,c_1)$ ,  $L' = (0.5,0,c_1)$ ,  $L'' = (0,0.5,c_1)$  in terms of reciprocal lattice vectors,  $c_1 \neq 0, 0.5$ ) as it is demonstrated in Fig.4.5, where a comparison between Kohn-Sham eigenvalues along  $A'-L'$  and  $A'-L''$  directions for  $c_1 = 0.3$  is reported.

## 4.5 Bare electronic susceptibility and nesting function

As mentioned earlier, the electronic susceptibility is of fundamental importance in order to shed light on the physical mechanism of the CDW transition. In DFT the  $\mathbf{k}$ -resolved noninteracting electronic susceptibility can be obtained from the knowledge of the Kohn-Sham eigenvalues in the normal phase:

$$\chi_0(\mathbf{q}, \omega) = \sum_{\mathbf{k}, m, n} \frac{f(\epsilon(\mathbf{k}, n)) - f(\epsilon(\mathbf{k} + \mathbf{q}, m))}{\epsilon(\mathbf{k}, n) - \epsilon(\mathbf{k} + \mathbf{q}, m) - \omega - i\delta} \times |\langle m, \mathbf{k} | e^{i\mathbf{q}\mathbf{r}} | n, \mathbf{k} + \mathbf{q} \rangle|^2 \quad (4.5)$$

where  $\delta$  is a vanishing quantity. Assuming that the matrix elements  $|\langle m, \mathbf{k} | e^{i\mathbf{q}\mathbf{r}} | n, \mathbf{k} + \mathbf{q} \rangle|^2$  do not have particularly structured features, we can set them to unity[225]. In this case, the real part of the noninteracting electronic susceptibility reads :

$$\chi'_0(\mathbf{q}, \omega) = \sum_{\mathbf{k}, m, n} \frac{f(\epsilon(\mathbf{k}, n)) - f(\epsilon(\mathbf{k} + \mathbf{q}, m))}{\epsilon(\mathbf{k}, n) - \epsilon(\mathbf{k} + \mathbf{q}, m) - \omega} \quad (4.6)$$

The divergence of this quantity is related to the insurgence of an instability in the electron gas and the transition to a CDW phase[201]. Moreover, we can extract information on the topology of the FS from the imaginary part of  $\chi_0$ , by calculating the so called nesting function[201]:

$$\lim_{\omega \rightarrow 0} \chi''_0(\mathbf{q}, \omega)/\omega = \sum_k \delta(\epsilon_k - \epsilon_F) \delta(\epsilon_{k+q} - \epsilon_F) \quad (4.7)$$

This function measures the geometric correlation of the FS for a generic coupling wave vector  $\mathbf{q}$ , thus its peaks indicate the FS nesting  $\mathbf{q}$ -vectors. Despite it was shown in Ref.[201] that nesting does not necessarily cause to an instability in real systems since a certain value of electron-phonon coupling is needed, they are definitely correlated. For the calculation of both the real and the imaginary part of the electronic susceptibility, we do not consider the effects of the temperature, *i.e.* we put  $T = 0$  K and thus  $f(\epsilon) = \theta(\epsilon)$ , where  $\theta$  is the Heaviside function.

In order to investigate the role played by the out-of-plane anisotropy of

the electronic structure, we report in Fig.4.6 the real part of the electronic susceptibility and the nesting function for three values of  $\mathbf{q}_z$ :  $\mathbf{q}_z = 0 \mathbf{R}_3$  (first row),  $\mathbf{q}_z \simeq \mathbf{R}_3/3$  (second row) and  $\mathbf{q}_z = 0.5 \mathbf{R}_3$  (third row), where  $\mathbf{R}_3$  is the out-of-plane reciprocal lattice vector. Due to the lack of inversion symmetry, the hexagonal symmetry is lost for  $\mathbf{q}_z \simeq \mathbf{R}_3/3$ . We recover it in by averaging  $\mathbf{q}_z \pm \mathbf{R}_3/3$  values. For all the considered  $\mathbf{q}_z$  values, both the real part of the electronic susceptibility and the nesting function show peaks in correspondence to the parallel component of  $\mathbf{q}_{CDW}$ , indicating that the electronic system is prone to a CDW instability characterized by the in plane vector  $\mathbf{q}_{\parallel}^{CDW} = (0.25, 0)$  and the symmetry related wave-vectors related to it. The nesting function has an evident dependence on  $\mathbf{q}_z$ , and its main peaks are present at  $\mathbf{q}_z = \mathbf{R}_3/3$ , indicating that the FS is especially nested in the BZ sector near  $\mathbf{q}_{CDW}$ . The  $\mathbf{q}_z$  dependence of the electronic susceptibility is especially evident in the nesting function. Apart from the trivial peak at the  $\Gamma$  point, strong nesting peak are observed for  $\mathbf{R}_3/3$ . These peaks are much less pronounced for other values of  $\mathbf{q}_z$ , as it is visible in Fig.4.6, indicating that the CDW develops in correspondence to a  $\mathbf{q}_{CDW}$  corresponding to a strong FS nesting.

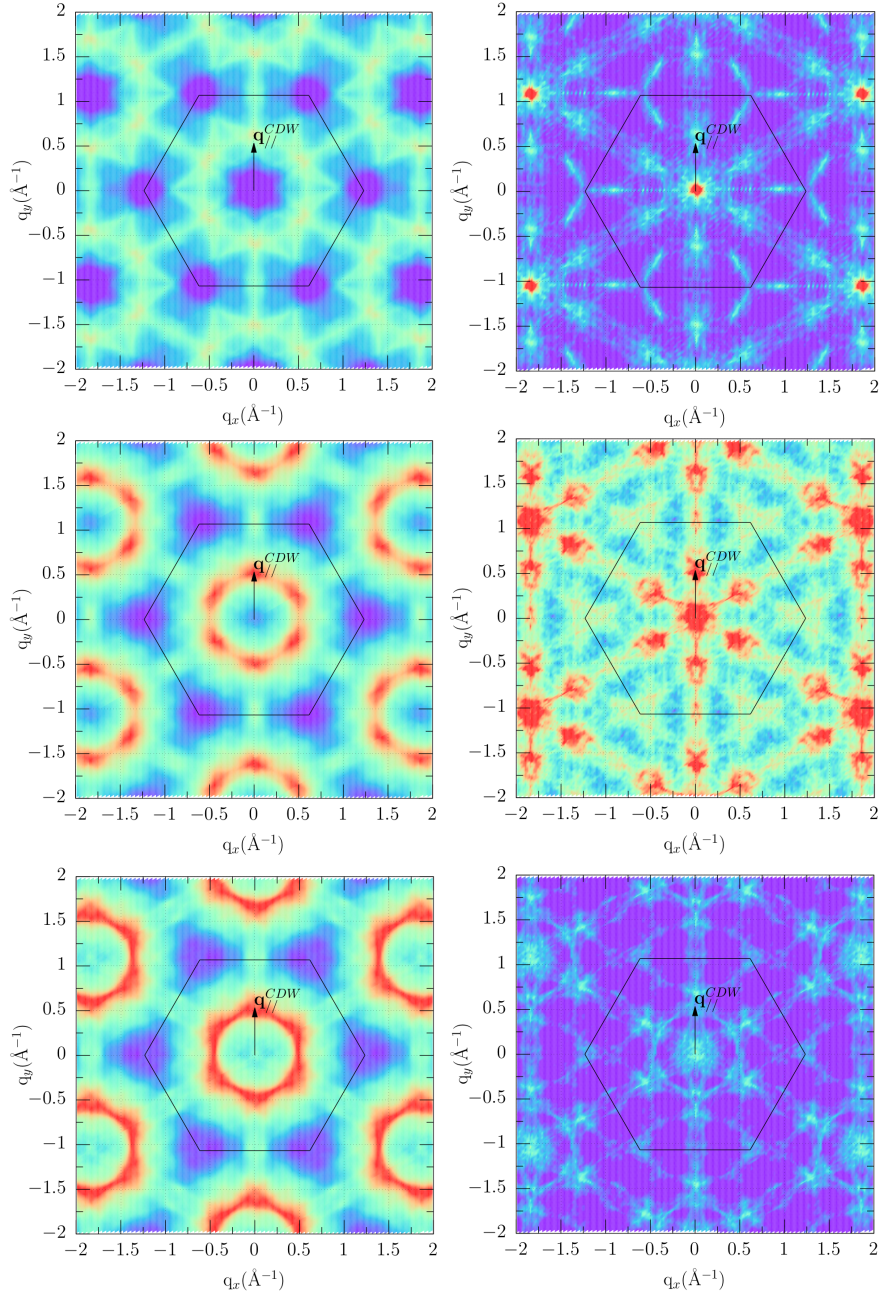


**Figure 4.6:** Real part of the electronic susceptibility and nesting function for  $q_z = 0 R_3$  (first row),  $q_z \simeq R_3/3$  (second row) and  $q_z = 0.5 R_3$  (third row).

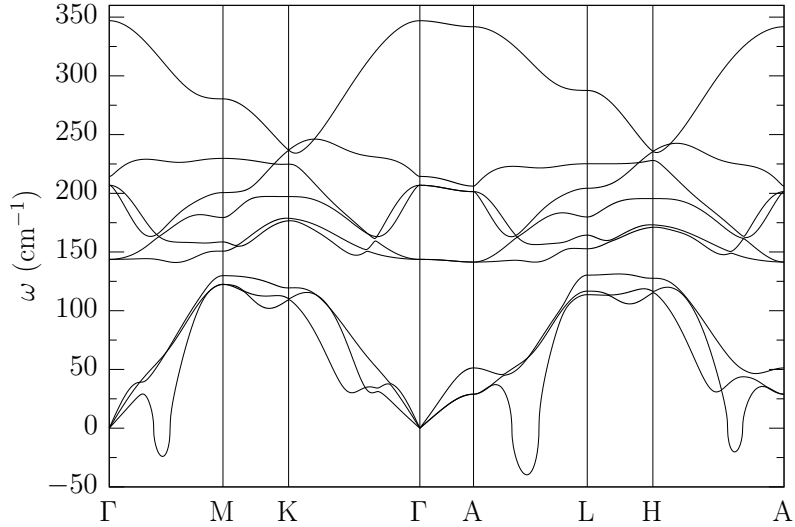


**Figure 4.7:** Phonon frequencies along high symmetry directions. Softening can be observed in the  $\Gamma$ -M, A-L and H-A directions of the BZ.

## 4.6 Dynamical properties of bulk VSe<sub>2</sub> in the undistorted phase

After analyzing the electronic structure of VSe<sub>2</sub>, we now consider the dynamical properties of the undistorted phase, as a first important step to demonstrate the dynamical instability and to justify the possible formation of a CDW. The phonon band structure along the high symmetry directions of the hexagonal lattice is reported in Fig.4.7, as calculated in DFPT. Many softenings can be observed in the phonon dispersions, in agreement with previous results[226, 219]. In Fig.4.8, we report the lowest phonon frequency behavior along the L-M-L and L'-M'-L' BZ paths. A broad softening range is present. Here, we observe once more the discussed lack of mirror symmetry, which is reflected in the phonon spectrum properties. Two softening minima are present, corresponding to the phonon wave vectors (0.25,0,0.287) and (0,0.25,-0.287), and they are close to the experimental CDW wave vec-

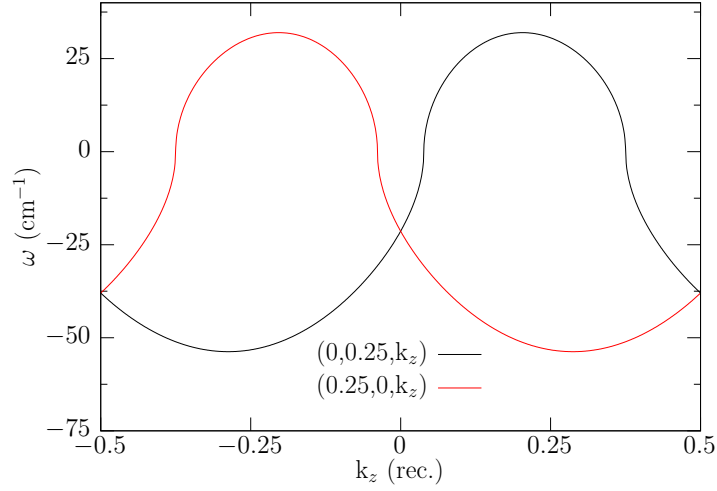


**Figure 4.8:** Phonon frequencies along  $L$ - $M$ - $L$  and  $L'$ - $M'$ - $L'$  directions.

tor of  $\mathbf{q}_{CDW}=(0.25,0,0.307)$  at low temperature. The broad plateau observed around the minimum frequency value is compatible with the multiple CDW transitions observed experimentally[204]. Other smaller instabilities are present in the phonon spectrum, e.g. in the A-H direction of the reciprocal lattice, which can potentially give rise to other kinds of CDW orders, e.g. the  $4a \times \sqrt{3} a$  order observed in Ref.[226] after the application of tensile strain.

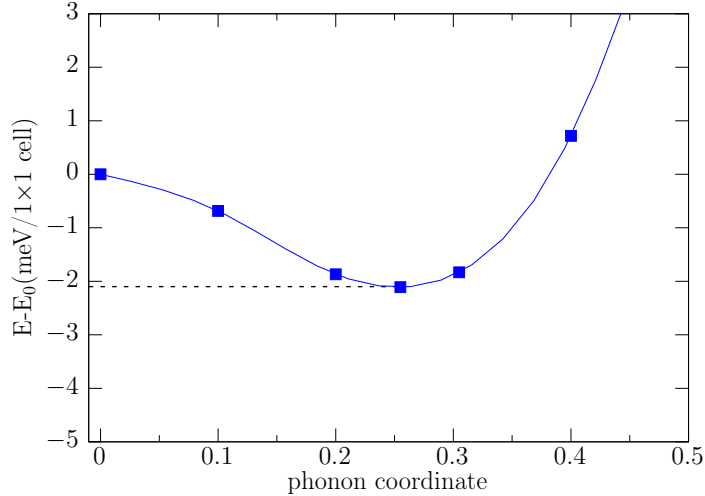


**Figure 4.9:** Energy profile along the normalized soft phonon mode at  $\mathbf{q}_{CDW'} = (1/4, 0, 1/3)$ .

## 4.7 Characterization of the CDW in bulk VSe<sub>2</sub>

### Energetics of CDW phase in bulk VSe<sub>2</sub>

Up to now, we described the electronic and dynamical properties of VSe<sub>2</sub> in the normal state. We concluded that hints of a CDW instability can be found in both the electronic band structure and phonon spectrum. Motivated by this finding, we further investigate the CDW formation by directly reproducing the lattice distortion in DFT, performing a supercell calculation. We now briefly explain how we can simulate commensurate CDW distortions within this approach. A generic phonon mode having frequency  $\omega_{\lambda, \mathbf{k}}$  causes the following atomic displacement for the atom  $\tau$ :

$$\mathbf{u}_{\tau, \mathbf{R}}(t) = \frac{1}{\sqrt{Nm_{\tau}}} \mathbf{e}_{\tau}^{\lambda}(\mathbf{k}) e^{i\mathbf{k} \cdot \mathbf{R}} A_{\lambda}(\mathbf{k}) \cos(\omega_{\lambda, \mathbf{k}} t + \phi_{\lambda, \mathbf{k}}) \quad (4.8)$$

where  $\mathbf{R}$  is the equilibrium position of the atom  $\tau$ ,  $m_{\tau}$  its mass,  $\mathbf{e}_{\tau}^{\lambda}$  represents the dynamical matrix eigenvector associated to the eigenvalue  $\omega_{\lambda, \mathbf{k}}$ ,  $A_{\lambda}(\mathbf{k})$  and  $\phi_{\lambda, \mathbf{k}}$  are determined by the initial conditions,  $N$  is the number

of atoms in the unit cell. A generic phonon distortion can be simulated in a supercell where the  $\mathbf{k}$ -point characterizing the distortion folds back to the  $\Gamma$ -point. In the case under examination, we consider a distortion of the VSe<sub>2</sub> periodic structure along the wave vector  $\mathbf{q}_{CDW'}=(1/4,0,1/3)$ , which is close to the observed  $\mathbf{q}_{CDW}=(0.25,0,0.307)$  and can be simulated in a relatively small  $4\times 1\times 3$  supercell. We follow the soft crystal distortion along  $\mathbf{q}_{CDW'}=(1/4,0,1/3)$ , finding a new energy minimum. The energy profile along the soft phonon mode is reported in Fig.4.9. It results that the CDW is energetically favored with respect to the normal state by 2.1 meV/formula unit.

### Electronic reconstruction and band unfolding

We demonstrated that a structural distortion towards the CDW phase in the  $4\times 1\times 3$  supercell is energetically favorable, so it is reasonable to also study the modification occurring in the electronic band structure. To this aim, we want to compare the band structure of the undistorted phase to the one of the CDW phase. In order to recover the primitive cell picture for the distorted CDW structure, we apply the band unfolding technique[227, 228, 229] using the BandUP software[220], which we briefly introduce in the following paragraph. The idea is to obtain an effective primitive cell picture of the electronic band structure starting from the band structure in a supercell, thanks to the mathematical relations between the eigenstates and eigenvalues of the Hamiltonian in the supercell and primitive cell representations. This approach can be applied to the study of a lattice distortion, since no volume change takes place and the distorted system lives in a supercell commensurate to the original unit cell. Folding relations are determined by the geometrical relations existing between the supercell and the primitive cell, and thus between the corresponding BZs. A wave vector of the primitive cell BZ  $\mathbf{k}$  is said to fold into a wave vector  $\mathbf{K}$  in the supercell BZ if a reciprocal lattice vector of the primitive cell  $\mathbf{G}$  such that

$$\mathbf{K} = \mathbf{k} - \mathbf{G} \quad (4.9)$$

exists. Conversely, a wave vector  $\mathbf{K}$  of the supercell BZ is said to unfold into  $\mathbf{k}_i$  belonging to the primitive cell BZ if is verified the relation

$$\mathbf{k}_i = \mathbf{K} + \mathbf{G}_i \quad (4.10)$$

The index  $i$  in Eq. 4.10 denotes the fact that a given wave vector  $\mathbf{K}$  can be obtained from a given number of different  $(\mathbf{k}_i, \mathbf{G}_i)$  pairs[229].

The folding and unfolding geometric relations lead to the property that any supercell eigenvector  $|\mathbf{K}, \mathbf{m}\rangle$  can be formally expressed in terms of primitive cell eigenvectors  $|k_i, n\rangle$

$$|\mathbf{K}, m\rangle = \sum_i \sum_n F(\mathbf{k}_i, n; \mathbf{K}, m) |k_i, n\rangle \quad (4.11)$$

It follows that, once the eigenvalues and eigenvectors on the appropriate  $\mathbf{K}$ -points have been calculated within the supercell calculation, an unfolding procedure can be built to obtain the projection of the supercell eigenstates onto the primitive cell eigenstates,  $\langle \mathbf{K}, m | \mathbf{k}_i, n \rangle$ , making it possible to calculate the spectral weight

$$P_{\mathbf{K}m}(\mathbf{k}_i) = \sum_n |\langle \mathbf{K}, m | \mathbf{k}_i, n \rangle|^2 = \sum_{\mathbf{G}} |C_{\mathbf{K},m}(\mathbf{G} + \mathbf{k} - \mathbf{K})|^2 \quad (4.12)$$

where the  $\mathbf{G}$  sum is extended to the primitive cell reciprocal lattice and the coefficients  $C_{m,\mathbf{K}}$  represent the coefficients of the plane waves spanning the supercell eigenstate  $|\mathbf{K}, m\rangle$ . From the second equality, it can be explicitly seen that the spectral weight  $P$  can be obtained entirely from the knowledge of the coefficients  $C_{m,\mathbf{K}}$ , without the need to know the primitive cell eigenstates[220]. From  $P$ , it is possible to derive the spectral function of  $E$ :

$$A(\mathbf{k}_i, E) = \sum_m P_{\mathbf{K}m}(\mathbf{k}_i) \delta(E_m - E) \quad (4.13)$$

which can be interpreted as an effective primitive cell representation of the original and often complicated  $E(\mathbf{K})$ .

In the specific case of  $VSe_2$ , our idea is to study the effects that CDW has on the band structure, with a special focus on the states near the Fermi level, by comparing the obtained spectral function  $A(\mathbf{k}_i, E)$  with the undistorted band structure in selected segments of the A-L-H-A plane of the BZ (see Fig.4.10). The obtained results are shown in Fig.4.11. We analyze various scenarios, namely: the undistorted band structure (first row), the spectral function corresponding to the lattice distortion along the wave vector  $\mathbf{q}_{CDW'} = (1/4, 0, 1/3)$  and the spectral function corresponding to the lattice distortion along the wave vector  $\mathbf{q}_{dist} = (1/4, 0, 0)$ , where the  $k_z$  component has been put to 0 in order to understand what is the role played by the out-of-plane CDW component. In both the distorted cases we observe the formation of gaps in the electronic band structure, as one would expect to happen in the nested parts of the Fermi surface. We observe that when

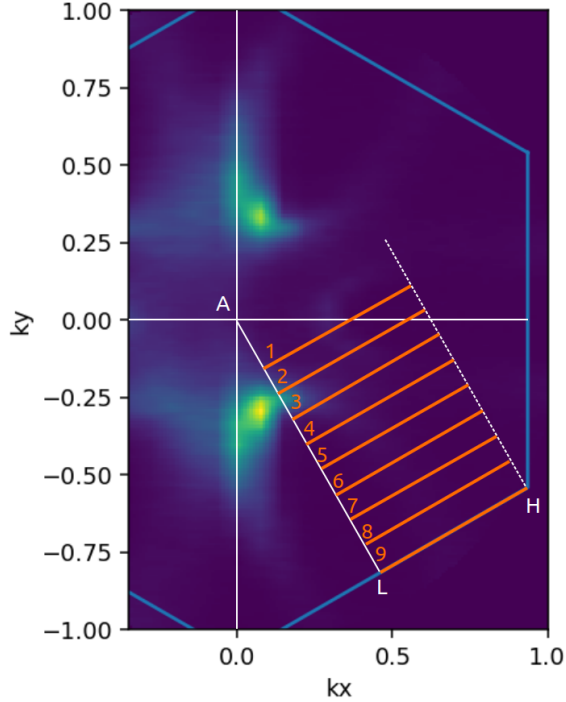


**Figure 4.10:** ARPES spectrum of the A-L-H-A of the BZ (unpublished experimental data by the group of Prof. Alexander Grüneis). Unfolded band structure has been calculated along the red cuts.

the out-of-plane component of the distortion is not included, a very different reconstruction is observed: in particular, most of the gap openings are not found in correspondence of the Fermi level. On the contrary, when the  $k_z$  component is included, we observe partial gap openings along various cuts in correspondence of the Fermi level, with a maximum gap of  $2\Delta \simeq 45$  meV in correspondence to the 6<sup>th</sup> cut. This value is in line with values found in the experiments, which however show a wide variability: Terashima *et al.* reported a partial gap opening on the M(L) centered Fermi surface of  $2\Delta = 80$ -100 meV[209]; Sato *et al.* report a gap of  $2\Delta = 40$ -60 meV[230], Strocov *et al.* don't report a gap opening[210], Wang *et al.* reported a gap of  $2\Delta = 80$  meV at 4.2 K[231], Ekvall *et al.* found  $2\Delta = 160$  meV at 60 K[232], Jolie *et al.* reported a pseudogap opening of 24 meV[205] while Páztor *et al.* did not find any gap related features at 78 K[233]. Experimentally, STM measurements demonstrate the formation of a  $4 \times 4$  in-plane superstructure[205]. We believe that the observed experimental  $4 \times 4 \times 3$  super-periodicity is due to

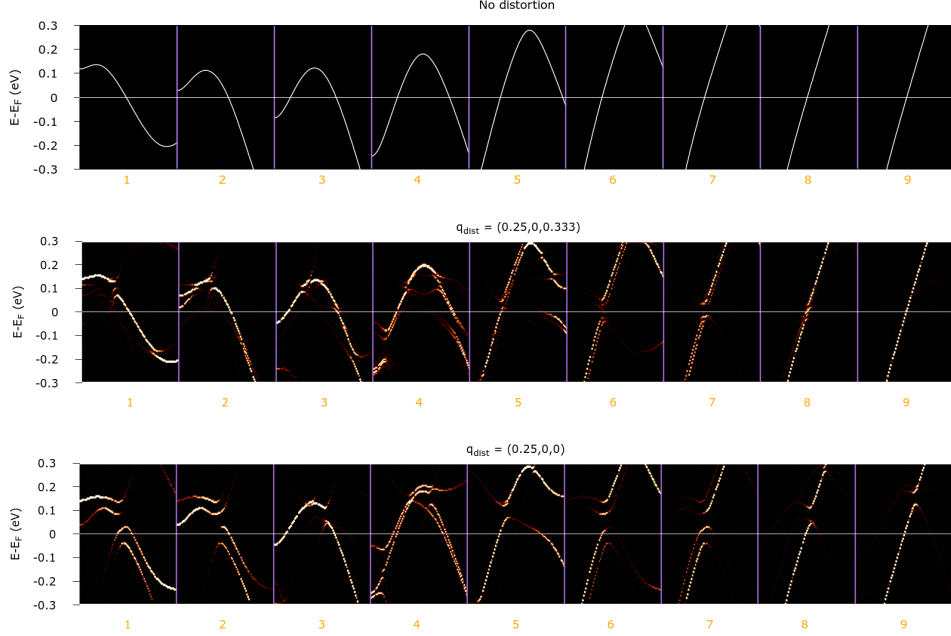


**Figure 4.11:** Unfolded electronic band structure of  $VSe_2$  along the red cuts shown in Fig.4.10. First row: undistorted band structure. Second row: unfolded band structure along the soft phonon mode at  $\mathbf{q}_{CDW'} = (1/4, 0, 1/3)$ . Third row: unfolded band structure along the soft phonon mode at  $\mathbf{q}_{dist} = (1/4, 0, 0)$ .

the combined effect of the two soft phonon modes at  $\mathbf{q}_{CDW} = (1/4, 0, 0.307)$  and at its symmetry related partner  $\mathbf{q}_{CDW} = (0, 1/4, -0.307)$ . For this reason, while a  $4 \times 1 \times 3$  super-periodicity is sufficient to simulate the distortion caused by the experimental  $\mathbf{q}_{CDW} = (1/4, 0, 0.307)$ , the full distortion and its effects on the band structure can only be observed in the  $4 \times 4 \times 3$  supercell, which we will address in a future investigation.

The CDW can be also identified by comparing the DOS in the normal state with the one in the CDW state. The comparison between the normal state DOS and the one in the case of  $\mathbf{q}_{CDW'} = (1/4, 0, 1/3)$  is reported in Fig.4.12. In the normal state (blue line), two DOS peaks can be identified near the Fermi level, one is found at  $\simeq 0.15$  eV below and one at  $\simeq 0.1$  eV above the Fermi level. When the CDW sets in (red line), the electronic structure of the system is reorganized due to the structural distortion. As a consequence, a clear loss of states around the Fermi level can be observed.

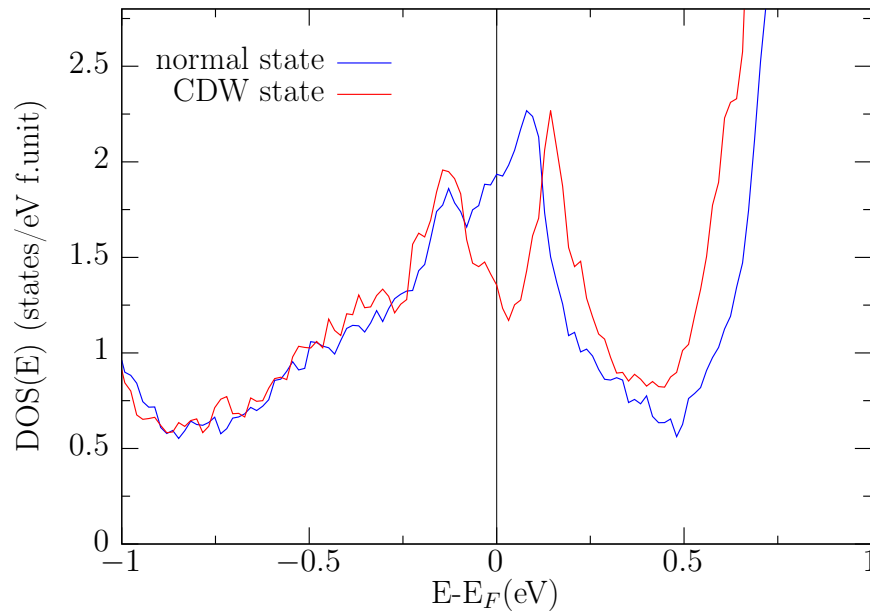


**Figure 4.12:** Comparison between the DOS in the normal state (blue line) and in the CDW state with  $\mathbf{q}_{CDW} = (1/4, 0, 1/3)$  (red line).

## Part II: Conclusions and outlook

In the second part of this thesis we presented our work on two compounds belonging to the TMDs family. In the third Chapter, we discussed our results on NiTe<sub>2</sub>. We have studied the effects of pressure over the electronic and superconducting properties of the compound NiTe<sub>2</sub> by means of first principles techniques. First of all, we determined the 0 K H(P) phase diagram of NiTe<sub>2</sub>. We find that the layered CdI<sub>2</sub>-type topological phase is stable up to  $\simeq 10$  GPa, where a phase transition of the first order towards the pyrite-type phase is predicted to occur. The applied pressure causes important changes in the electronic band structure, especially for what concerns the conduction bands, which cross the Fermi energy in the A-L direction of the reciprocal space, causing a qualitative change in the transport properties of the compound.

Furthermore, we establish that pressure has a detrimental effect over the value of the electron-phonon coupling in the CdI<sub>2</sub>-type NiTe<sub>2</sub>. For this reason, we exclude that the observed superconductivity in polycrystalline NiTe<sub>2</sub> can be simply attributed to electron-phonon pairing mechanism in CdI<sub>2</sub>-type NiTe<sub>2</sub>. We propose three possible scenarios to explain the observed superconducting transition: the first is that the superconducting properties of NiTe<sub>2</sub> under pressure are crucially affected by the Te defects. In this regard, we showed that the DOS of the defective compound is characterized by a peak near the Fermi level, which could in principle be at the origin of the observed superconducting transition. A second scenario is that the superconducting transition takes place in the pyrite-type phase, which we here show to be the 0 K ground state after 10 GPa. The third scenario is that of an unconventional pairing mechanism. Further experiments and theoretical analyses are due to confirm or deny each of the proposed hypotheses. In the fourth Chapter we presented our theoretical analysis of the CDW in 1T-VSe<sub>2</sub>. First principles calculations demonstrate the presence of a structural instability in the 4×4×3 supercell, in agreement with the experimental findings. Signals of the instability can be already found in the normal state, both in the electronic susceptibility, which presents maxima in close correspondence to the experimental CDW wave vector,  $\mathbf{q}_{CDW}$ , and in the phonon spectrum, which presents multiple soft phonons, signaling an unstable structure. The study of the CDW phase in the 4×1×3 supercell revealed that a stable distortion exists. We investigate this instability by distorting the crystal structure along the soft phonon mode close to the experimental CDW wave vector, obtaining an energy gain of 2 meV/formula unit with respect to the normal state. We studied the effects of the distortion on the electronic band structure, finding a maximum gap opening of  $\simeq 45$  meV in the A-L-H-A plane of the BZ. While many effects, such as gap openings in specific regions of the the A-L-H-A plane, are observed in the 4×1×3 supercell simulation, a quantitative description of the CDW effects on the electronic structure needs to take into account the full 4×4×3 structural distortion, which we will investigate in a subsequent work. In this regard, a joint theoretical-experimental work on the CDW in VSe<sub>2</sub> realized in collaboration with the research group led by prof. Alexander Grüneis is in preparation. Further theoretical investigations regarding VSe<sub>2</sub> will be performed, with special attention on the behavior under pressure, trying to explain the disappearance of the CDW and the appearance of superconductivity after 15 GPa[208]. In conclusion, we believe that the present results will be helpful in order to unravel the complicated experimental scenarios for both monolayer and bulk NiTe<sub>2</sub> and VSe<sub>2</sub>.

## Part III

# Topology in condensed matter

## Chapter 5

# Electronic properties of the strong topological insulator mercury telluride

In part III of the thesis we investigate a different kind of low dimensional electron system existing at the edge of a bulk material, namely the topologically protected states localized at the edge of the topological insulator mercury telluride (HgTe). HgTe holds a very special place in the field of topological condensed matter, being the material where the topological insulator (TI) phase has been observed for the first time in 2007[65, 56]. It is thus of great importance to be able to describe its electronic and topological properties by means of *ab-initio* methods. However there are several difficulties to face in order to obtain adequate results, as we will show in the course of this Part. In Sec.5.1 we give a general overview of the fundamental concepts of topology, in particular to the ones related to the TI state. Then, in Sec.5.2, we present our results on the electronic properties of HgTe, including experimental measurements with unprecedented resolution and state-of-the-art theoretical calculations. We determine the best framework to describe the electronic properties of HgTe from first principles by analyzing the results of various DFT functionals, illustrating how to obtain a correct description of the electronic and topological properties of HgTe by means of *ab-initio* methods. The present research is part of a joint theoretical and experimental research project with the experimental group led by Prof. Laurens W. Molenkamp of University of Würzburg and Giorgio San-giovanni and Domenico Di Sante from the theoretical group of University of Würzburg.

## 5.1 Introduction to topology and topological insulators

### 5.1.1 The integer quantum Hall effect

The notion of *topological order* has introduced a new paradigm in the classification of distinctive phases of matter[58]: indeed, some phases of the matter cannot be classified according to the symmetry breaking mechanism. Instead, these "topological" phases can be characterized by a quantized value of some inherent property. Historically, the topological classification was first introduced after the discovery of integer quantum Hall effect (IQHE) in 1980[57]. The effect occurs when electrons confined to two spatial dimensions are placed in a strong magnetic field. In this scenario, the system behaves as a collection of non-interacting harmonic oscillators. Each oscillator is characterized by the same frequency  $\omega_c$ , the cyclotron frequency. The system eigenvalues are thus  $\epsilon_m = \hbar\omega_c(m + 1/2)$ , and each eigenvalue is  $N$  times degenerate, where  $N$  is the number of the electrons in the system[18]. If  $N$  Landau levels are completely filled while the rest are empty, the system is an electric insulator, since an energy gap separates the last filled electronic level from the first empty level[60]. However, this system is inherently different from an ordinary insulator: indeed, the introduction of an electric field causes a drift of the cyclotron orbits, leading to a finite transverse Hall conductivity according to the equation

$$\sigma_{xy} = Ne^2/h, \quad (5.1)$$

whose quantized value is proportional to the number of filled Landau levels ( $h$  is the Planck constant,  $e$  the electron charge).

### 5.1.2 Berry phase and Chern-Gauss-Bonnet theorem

The previous argument gives an intuitive idea of the difference between an ordinary insulator and the quantum Hall state. From a formal point of view, the two phases belong to topologically different classes. 2D Bloch Hamiltonians can be classified by introducing equivalence classes, containing Hamiltonians smoothly deformable into one another, *i.e.* without closing the energy gap. Each class is distinguished by an integer invariant  $n \in \mathbb{Z}$  called Chern number[58]. The fundamental mathematical object behind this construction is the Berry phase[234]. Consider a system whose Hamiltonian  $H$  depends parametrically on a vector  $\mathbf{R}$  (as in the case of the Bloch Hamiltonian) and imagine that  $\mathbf{R}$  depends on time  $t$ . Provided that the eigenvalue  $\epsilon_m(\mathbf{R})$

remains non-degenerate along the evolution path of  $\mathbf{R}$  and the evolution is adiabatic, a system initially in the eigenstate  $|m(\mathbf{R}(0))\rangle$  will instantaneously find itself in the eigenstate  $|m(\mathbf{R}(t))\rangle$ , up to a phase, according to the relation:

$$|\Psi_m(t)\rangle = e^{i\gamma_m(t)} e^{-\frac{i}{\hbar} \int_0^t dt' \epsilon_m(\mathbf{R}(t'))} |m(\mathbf{R}(t))\rangle, \quad (5.2)$$

where  $|\Psi_m(t)\rangle$  is the state of the system at time  $t$ . The second exponential is this the dynamical phase factor coming from the usual Schrödinger time evolution. The first exponential is a geometric term coming from the time dependence of the parameter. By imposing that  $|\Psi_m(t)\rangle$  satisfies the Schrödinger equation, we define the Berry phase  $\gamma_m$  as

$$\gamma_m(t) = i \int_{\mathbf{R}_i}^{\mathbf{R}_f} d\mathbf{R} \langle m(\mathbf{R}) | \nabla_{\mathbf{R}} | m(\mathbf{R}) \rangle. \quad (5.3)$$

A case of particular interest is when the space of parameters  $\mathbf{R}$  coincides with the reciprocal space  $\mathbf{k}$  and the generic eigenstate is the Bloch wave function  $|u_m(\mathbf{k})\rangle$ . By considering a closed path in the reciprocal space  $\mathcal{C}$  where no accidental eigenvalue degeneracy happens, the wave function acquires a well defined Berry phase given by the line integral of the Berry connection  $\mathcal{A}_m$ :

$$\gamma_m = \oint_{\mathcal{C}} \mathcal{A}_m \cdot d\mathbf{l}, \quad \mathcal{A}_m = i \langle u_m | \nabla_{\mathbf{k}} | u_m \rangle \quad (5.4)$$

The line integral can be re-written using the Stokes theorem as the flux of the Berry curvature  $\mathcal{F}_m = \nabla \times \mathcal{A}_m$  extended to the area subtended by the considered path. The Chern invariant (or TKNN invariant, from the authors of Ref.[58]) is then defined as the integral:

$$n_m = \frac{1}{2\pi} \int_{BZ} d^2\mathbf{k} \mathcal{F}_m \in \mathbb{Z} \quad (5.5)$$

The quantization value of this integral is demonstrated by the Chern-Gauss-Bonnet theorem[235]. This fundamental theorem connects topology and Riemannian geometry according to the following relation:

$$\chi_E(M) = \int_M e(\Omega) \quad (5.6)$$

We define the quantities involved in Eq.5.6:

- i) M is a compact orientable 2n-dimensional Riemann manifold without

boundary.

ii)  $\Omega$  is the associated curvature form of any metric connection on a vector bundle over  $M$  (a vector bundle is a family of vector spaces parametrized by another space, in this case  $M$ ).

iii)  $\chi_E$  is an integer number called the Euler characteristic of a surface,  $\chi_E = V - E + F \in \mathbb{Z}$ , where  $V, E, F$  are the vertices, edges, faces of the surface. The Euler characteristic of a general surface can be calculated by finding a polygonalization of the surface itself.

iv) The Euler class is defined as  $e(\Omega) = \frac{-1^k}{(2\pi)^k} \text{Pf}(\Omega)$ , where  $\text{Pf}(\Omega)$  is the Pfaffian and  $k$  the dimension of the manifold  $M$ .

In the case of the TKNN invariant,  $n_m$  corresponds to the Euler characteristic, while the manifold  $M$  is the 2D BZ and  $\Omega$  is the Berry curvature associated to the Berry connection on the Bloch eigenspace vector bundle,  $\mathcal{F}$ .

Summing over all the occupied bands  $n = \sum_{m=1}^N n_m$  one obtains the total Chern number, whose value is not influenced by the presence of eigenvalue degeneracies in the occupied bands. TKNN showed that the number of full Landau levels  $N$  (Eq.5.1) is equal to the total Chern number  $n$  [60, 58]. The fact that the topological index is directly related to the Hall conductivity (Eq.5.1) explains why its value is independent from (weak) disorder and interactions, *i.e.* as long as the topological classification stands.

### 5.1.3 $\mathbb{Z}_2$ topological insulators

The quantized conductivity observed in the IQHE explicitly breaks time-reversal symmetry ( $\mathcal{T}$ ). Hence, a nontrivial state, in the sense of the TKNN invariant can only exist when  $\mathcal{T}$  is broken; conversely,  $\mathcal{T}$  invariant systems will always be topologically trivial from a TKNN point of view. A different topological classification for  $\mathcal{T}$  invariant 2D systems can be found. It is characterized by an integer number  $m \in \mathbb{Z}_2$ , which can take only two distinct values and was first studied by Kane and Mele in 2005[62]. Some premises are due in order to understand the Kane-Mele model and the topological classification of  $\mathcal{T}$  invariant systems.

### Premise 1: Kramers' theorem

In the case of  $\mathcal{T}$  invariant systems with half-integer total spin, the Kramers' theorem ensures that every eigenstate is at least doubly degenerate. Furthermore, the two states are related by  $|\Psi_T\rangle = \mathcal{T}|\Psi\rangle$  and are orthogonal. A demonstration can be found in Ref.[236].

### Premise 2: Haldane Model

As we discussed in Sec.5.1.1, IQHE is typically associated with the presence of an external magnetic field. Haldane showed that this condition can be in principle lifted, provided that time-reversal symmetry is broken by the system. Haldane showed that a magnetic ordered 2D system without a net magnetic flux through the unit cell can present a IQHE.

In the IQHE, the energy gap is provoked by the external magnetic field. Haldane considered a different scenario involving graphene, i.e. a 2D semimetal whose contact points between conduction and valence bands are protected by the presence of both inversion symmetry and time-reversal invariance[64]. In this case, a gap opening resulting from an inversion-symmetry ( $\mathcal{I}$ ) breaking results in a normal semiconductor, while a gap opening due to a  $\mathcal{T}$  breaking causes the system to enter a  $n = \pm 1$  quantum Hall state.

Haldane started from the spinless nearest-neighbor graphene model investigated by Semenoff [237], having a real hopping matrix element  $t_1$  and a  $\mathcal{I}$  breaking on-site energy  $\pm M$  on the A/B sublattices. Then, he added a  $t_2$  hopping term between next-nearest neighbor sites (nearest-neighbor of the same sublattice), eliminating the particle-hole symmetry of the model. Finally, in order to break the  $\mathcal{T}$  symmetry, he added a local normal magnetic field  $\mathbf{B}(\mathbf{r})$ , which can be taken into account by the Peierls substitution, adding the phase factor  $e^{i(e/\hbar)\int \mathbf{A}\cdot d\mathbf{r}}$  along the hopping path, where  $\mathbf{A}(\mathbf{R})$  is the periodic vector potential due to the magnetic field. The first-neighbor hopping matrix elements  $t_1$  are unaffected by the phase factors, since closed paths enclose complete unit cells and hence no net flux. The  $t_2$  matrix elements acquire a geometric phase  $\phi$  depending on the magnetic field. Defining  $\mathbf{a}_i$  as the set of three nearest neighbors displacements and  $\mathbf{b}_i$  as the set of six next-nearest neighbor sites, the Hamiltonian of the Haldane model is[64]

$$H(\mathbf{k}) = 2t_2 \cos \phi \left( \sum_i \cos(\mathbf{k} \cdot \mathbf{b}_i) \right) \mathbb{1} + t_1 \left( \sum_i [\cos(\mathbf{k} \cdot \mathbf{a}_i)\sigma_x + \sin(\mathbf{k} \cdot \mathbf{a}_i)\sigma_y] \right)$$

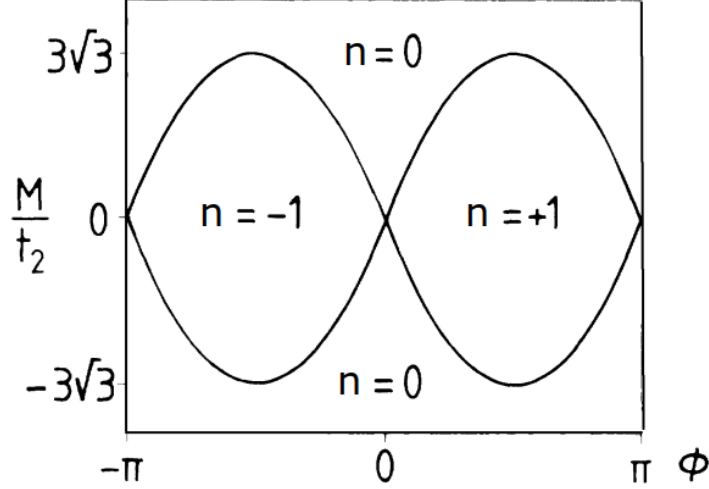


**Figure 5.1:** Phase diagram of the spinless electron model with  $|t_2/t_1| < 1/3$  (adapted from the original Haldane paper, Ref.[64]).

$$+ \left[ M - 2t_2 \sin \phi \left[ \sum_i \sin(\mathbf{k} \cdot \mathbf{b}_i) \right] \right] \sigma_z, \quad (5.7)$$

where  $\sigma$  matrices are Pauli matrices acting on the two sublattices. As long as  $|t_2/t_1| < 1/3$ , the energy bands of this model can only touch in correspondence of the  $K, K'$  points of the hexagonal BZ, if the condition  $M = 3\sqrt{3}\alpha t_2 \sin \phi$  ( $\alpha = \pm 1$  for  $K, K'$ ) is satisfied. From the evaluation of transverse conductivity  $\sigma^{xy} = \partial \sigma / \partial B_0|_{\mu, T}$  at  $B_0=0$  in linear response, one gets the phase diagram in Fig.5.1, with two trivial domains  $n = 0$  and two nontrivial domains with  $n = \pm 1$ , separated by critical lines having a low energy massless spectrum.

### Kane-Mele model

In the Haldane model, the spin degree of freedom is not taken into account. The spinful case can be as two noninteracting copies of the Haldane model as long as the perpendicular component of the spin  $S_z$  is conserved. Correspondingly, two TKNN invariants can be defined,  $n_\uparrow$  and  $n_\downarrow$ . Imposing  $\mathcal{T}$  symmetry, one has the condition that  $n_\uparrow + n_\downarrow = 0$  and thus no net conductivity, however the difference  $n_\uparrow - n_\downarrow$  can be nonzero and give rise to a quantized spin Hall conductivity[61]. The Kane-Mele model is the general-

ization of such a model with the inclusion of spin and  $\mathcal{T}$ -invariant spin-orbit interactions. It is described in second quantization by the Hamiltonian

$$H = t \sum_{\langle ij \rangle} c_i^\dagger c_j + i\lambda_{SO} \sum_{\langle\langle ij \rangle\rangle} \nu_{ij} c_i^\dagger s^z c_j + i\lambda_R \sum_{\langle ij \rangle} c_i^\dagger (\mathbf{s} \times \hat{\mathbf{d}}_{ij})_z c_j + \lambda_\nu \sum_i \zeta_i c_i^\dagger c_i \quad (5.8)$$

Here, the first term is the nearest neighbor hopping term on the honeycomb lattice, the second term is the spin-orbit interaction, involving spin dependent second neighbor hopping, with  $\nu_{ij} = (2/\sqrt{3})(\hat{\mathbf{d}}_1 \times \hat{\mathbf{d}}_2)_z = \pm 1$ , where  $\hat{\mathbf{d}}_1$  and  $\hat{\mathbf{d}}_2$  are unit vectors along the two hopping going from  $j$  to  $i$ . The third term is the Rashba term, arising due to a perpendicular electric field or due the interaction with the substrate; it explicitly violates the  $S_z$  conservation. The fourth term is a staggered sublattice potential ( $\zeta_i = \pm 1$ ). The phase diagram of the model is reported in Fig.5.2. As long as a finite  $\lambda_{SO}$  is present, there exists a region of parameters which is topologically distinct from the trivial insulator. In particular, a finite  $\lambda_R < 2\sqrt{3}\lambda_{SO}$  breaks  $S_z$  conservation but does not induce a topological phase transition since the band gap does not close.

Similarly to what happens in the case of the TKNN classification, the  $\mathbb{Z}_2$  classification of  $\mathcal{T}$ -invariant systems emerges naturally from the study of the Bloch wave functions, which form vector bundles behaving in well-defined ways under the application of the time-reversal operator. The  $\mathbb{Z}_2$  invariant is constructed by evaluating the zeros of the quantity

$$P(\mathbf{k}) = \text{Pf}[\langle u_i(\mathbf{k}) | \mathcal{T} | u_j(\mathbf{k}) \rangle], \quad (5.9)$$

The presence of a pair of zeros for  $P(\mathbf{k})$ , whose existence is guaranteed by the  $\mathcal{T}$  symmetry, distinguishes the non trivial phase, also called the quantum spin-Hall (QSH) phase, from the trivial phase. The number of pairs of zeros is the  $\mathbb{Z}_2$  topological invariant, whose detailed construction can be found in Ref.[62]. The two topological classes can be equivalently understood by recurring to the *bulk-boundary* correspondence. The idea is that whenever an interface between two topologically distinct states exists, the energy gap has to vanish somewhere at the interface because otherwise the topological invariant could not change. As a consequence, one always expects some kind of conducting states to live at the interface between a topological phase and a trivial insulator. In the case of the QSH state, there is a pair of eigenstates for every value of energy in the bulk gap at each edge. The corresponding eigenstates form a Kramers pair of counter propagating helical modes having

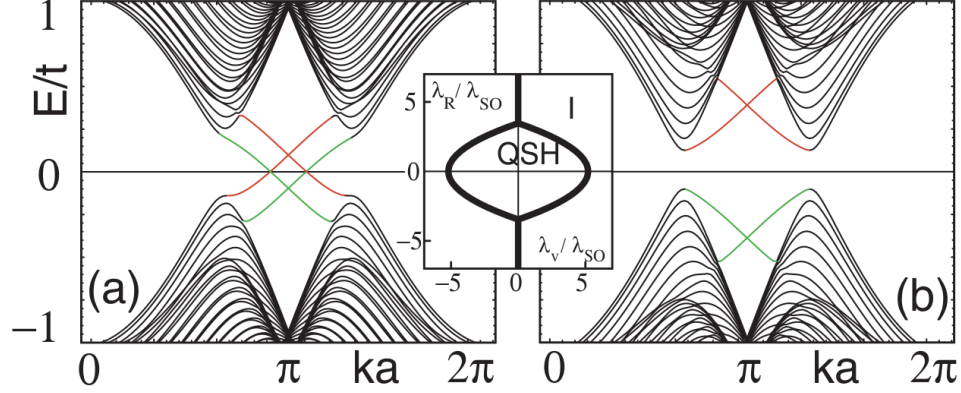


**Figure 5.2:** Band structure for the QSH phase (a) and for the trivial insulating phase (b), solved in a "zigzag" strip geometry. The inset shows the phase diagram of the Kane-Mele model. Figure taken from Ref.[62].

opposite spin. They cannot mix due to  $\mathcal{T}$  symmetry, in fact the relation  $\langle \Psi | \Psi_T \rangle = 0$  holds for any Kramers' doublet, implying that no backscattering between the two states exist as long as  $\mathcal{T}$ -symmetry is maintained. Thus the edge states are robust against small perturbations[62]. Generally speaking, when an even number of pairs of helical states is present at each edge (*e.g.* 2), scattering channels in between the edge states can open a gap: the system is in the trivial insulator phase. When an odd number of pairs is present however, at least one Kramers' pair is bound to remain ungapped and the system is in the QSH phase. No such protection exists without Kramers theorem, *e.g.* in the case of integer spin models.

### HgTe/CdTe quantum wells and the Bernevig-Hughes-Zhang model

The Kane-Mele model captures all the essential features of the QSH state. However, the QSH state has never been observed in graphene due to the very low SOC value, with a gap-opening of the order of  $10^{-3}$  meV[238], which is too small to be experimentally accessible. A decisive advance in the experimental observation of the QSH effect was due to the Bernevig-Hughes-Zhang (BHZ), who first proposed that QSH state could be realized in type-III semiconductor quantum wells[65]. The idea is to exploit the inverted band progression of some semiconductors, such as HgTe (see *e.g.* [239]), in order to tailor a system where the QSH state can be observed. The normal band progression sees the two-dimensional  $\Gamma_6$  band(using the double group notation[239]), originating from Hg *s-type* orbitals, above the

four-dimensional Te *p-type*  $\Gamma_8$ . Conversely, in HgTe the  $\Gamma_6$  band lies below the  $\Gamma_8$  band. BHZ investigated the properties of a CdTe/HgTe/CdTe heterostructure as a function of the thickness  $d_{QW}$  of HgTe. They predicted the system to be a trivial insulator for  $d_{QW} < d_c$  and a transition towards the QSH state for  $d_{QW} > d_c$ , where  $d_c$  is a critical HgTe thickness. Their six-band model takes into account the already mentioned six bands, which in the experimental geometry combine as a result of the spatial symmetry breaking to form six quantum well subbands:  $E1_{\uparrow,\downarrow}, H1_{\uparrow,\downarrow}, L1_{\uparrow,\downarrow}$ . Neglecting the  $L1$  subband, which is energetically separated from the other two, an effective four-band model is obtained, which is described by the following Hamiltonian in the basis of  $E1/H1$  states:

$$H_{\text{eff}}(k_x, k_y) = \begin{pmatrix} H(k) & 0 \\ 0 & H^*(-k) \end{pmatrix}, H(k) = \epsilon(k) + d_i(k)\sigma_i \quad (5.10)$$

where  $\sigma_i$  are the Pauli matrices and the form of  $d_i(k)$  functions are constrained by symmetry arguments as follows:

$$d_1 + id_2 = A(k_x + ik_y), d_3 = M - B(k_x^2 + k_y^2), \epsilon(k) = C - D(k_x^2 + k_y^2)$$

$A, B, C, D$  depend on the heterostructure and  $M$  is the gap parameter, *i.e.* the energy difference between  $E1$  and  $H1$ .  $E1$  and  $H1$  bands cross as a function of  $d_{QW}$ , giving rise to a sign change in the mass  $M$ , which in turn causes a well-defined change in the Hall conductance  $\Delta\sigma_{\uparrow,\downarrow}^{xy} = \pm 1$  in the two blocks of the effective Hamiltonian, such that the charge-Hall conductance does not vary  $\Delta\sigma_{\uparrow}^{xy} + \Delta\sigma_{\downarrow}^{xy} = 0$ , while the spin-Hall conductance  $\Delta\sigma_{\uparrow}^{xy} - \Delta\sigma_{\downarrow}^{xy} = 2$  in units of  $e^2/h$ , signaling that the pairs of edge states between the two phases differ by 1 and thus a topological phase transition is taking place[65]. The first experimental observation of the QSH state came from Molenkamp group at Würzburg university, in the HgTe/CdTe system proposed by BHZ[56]. They observed that the insulating regime of the material showed a residual conductance close to  $2e^2/h$  for a thick HgTe well ( $d_{QW} > d_c = 6.3nm$ ), independent of the sample width, and thus unequivocally due to some edge state. The topological nature of the edge states was further confirmed by applying a small magnetic field perpendicularly to the well, breaking the  $\mathcal{T}$  symmetry and consequently gapping the edge states, destroying the conducting channels.

### 5.1.4 3D Topological Insulators

Up to now, we only considered 2D systems, following the historical development of the field. However, one may extend the topological classification to higher dimensional systems. Hamiltonians in a  $d$ -dimensional space can be topologically classified according to how they behave under the application of the two fundamental antiunitary symmetries of time-reversal  $\mathcal{T}$  and charge-conjugation  $\mathcal{C}$  and their product  $\mathcal{S} = \mathcal{T} \cdot \mathcal{C}$ . The classification is due to Zirnbauer and Atland[240, 241], who first recognized the one-to-one correspondence between single particle Hamiltonians and the set of symmetric spaces classified by the mathematician Cartan in 1926. Ten symmetry classes per dimension exist and for this reason is often referred as the "Tenfold Way". Furthermore, hierarchical relations exist between topological phases in different dimensions[242, 243].

Here we focus on  $\mathbb{Z}_2$  TIs and their extension to the 3D case. A convenient way to evaluate the  $\mathbb{Z}_2$  invariant in 2D TIs can be given in terms of the already mentioned overlap matrix  $w_{ij} = \langle u_i(\mathbf{k}) | \mathcal{T} | u_j(\mathbf{k}) \rangle$ , by considering the four  $\mathcal{T}$ -invariant time reversal momenta (TRIM). By defining

$$\delta_i = \sqrt{\text{Det}[w(\Gamma_i)]} / \text{Pf}[w(\Gamma_i)] = \pm 1, i = 1, 4 \quad (5.11)$$

the  $\mathbb{Z}_2$  invariant is defined by the relation

$$(-1)_{2D}^{\nu} = \prod_{i=1,4} \delta_i \quad (5.12)$$

In 3D systems, there are 8 distinct TRIM, defined by  $\Gamma_{i=(n_1, n_2, n_3)} = (n_1 \mathbf{b}_1 + n_2 \mathbf{b}_2 + n_3 \mathbf{b}_3) / 2$  with  $n_j = 0, 1$ . There are 16 distinct gauge invariant configurations of the  $\delta_i$ , which can be indexed by 4  $\mathbb{Z}_2$  invariants  $\nu_0; (\nu_1, \nu_2, \nu_3)$ , defined by[63]

$$(-1)^{\nu_0} = \prod_{n_j=0,1} \delta_{n_1 n_2 n_3}, (-1)^{\nu_{i=1,2,3}} = \prod_{n_j \neq i=0,1; n_i=1} \delta_{n_1 n_2 n_3} \quad (5.13)$$

When  $\nu_0 = 0$ , each face has either 0 or 2 Dirac points enclosed by the Fermi arc. This face can host topological surface states, however they are sensitive to changes in the lattice (*e.g.*, cell doubling) and disorder, and will generically be localized in the Anderson sense. For this reason, the  $\nu_0 = 0$  topological phases are often called *weak* TI. When  $\nu_0 = 1$ , the surface Fermi arc encloses 1 or 3 Dirac points on all faces. While the weak topological phase can be thought as a stack of 2D TIs, the strong TI is intrinsically different,

since the fermion doubling theorem would not allow the presence of a single Dirac cone in 2D as long as  $\mathcal{T}$  is preserved. In a (2+1)D system, however, this is possible because Dirac point partners can live on opposite surfaces. In this sense, if the Fermi energy is placed exactly at the Dirac point, the strong TI is the realization the 2+1 dimensional parity anomaly[63].

## 5.2 Study of the electronic properties of mercury telluride

### 5.2.1 Introduction

The discovery of the QSH phase in CdTe/HgTe quantum wells sparked further research on the inverted band structure of HgTe and its potential as a topological material. It is now understood that HgTe hosts many topological non trivial phenomena, like 3D strong TI phase[244], Weyl physics, Kane fermions as well as the possibility of introducing magnetism into the system[56, 245, 246, 247, 248]. As of today, HgTe remains one of the most studied topological compounds and a textbook example of TI. As such, the correct theoretical description of its electronic band structure is of considerable importance. In the past, good results have been obtained with semi-empirical methods like  $\mathbf{k} \cdot \mathbf{p}$ ; however, this method is not accurate in all the BZ and relies on experimental inputs. On the other hand, a satisfying first principles description of HgTe electronic properties is notably difficult to achieve: some critical points are the correct band ordering, the energy position of the Hg(*d*)-orbitals and a realistic dependence on the wave vector  $\mathbf{k}$  of the bands near the Fermi level. Despite a lot of work has been performed in this sense (see Refs.[249, 250, 251, 252], to name a few) it is still not completely clear what is the best framework for the description of the HgTe electronic structure in DFT due to various reasons: the presence of a gap[253], the important role played by relativistic effects[254], the presence of sizable exchange and correlation effects and, in part, also the lack of clear experimental data. In this work, we give a comprehensive overview of the electronic properties of HgTe by combining theoretical calculations and experimental techniques, with the aim of establishing once and for all the best framework for the description of HgTe electronic structure. The work is organized as follows: we start by discussing the electronic properties of HgTe in its bulk form and the physical mechanism responsible for the band inversion. Then, in Sec.5.2.3, we illustrate why the application of an in-plane tensile strain is needed in order to observe the TI phase. In Sec.5.2.5, we present

and discuss the DFT calculations, explaining how we determined the best method to describe HgTe electronic structure in DFT. Then, in Sec.5.2.6 we present the experimental measurements, discuss them in the light of the theoretical results. Finally, we will draw our conclusions.

### 5.2.2 Mercury telluride: a zero gap semiconductor

Mercury telluride is a binary compound, formed by group II metal Hg and group VI chalcogen Te. Like many other II-VI and III-V compounds, bulk HgTe crystallizes in the cubic zincblende crystal structure ( $F\bar{4}3m$ , space group No. 216), consisting in two interpenetrating  $fcc$  lattices displaced along the (111) direction by 1/4 of the diagonal of the cube. In this structural configuration, each Hg(Te) atom has four Te(Hg) nearest neighbors, and four  $sp^3$  states are formed, resulting from the two Hg(6s) valence electrons and the six Te(2 5s + 4 5p) valence electrons. The electronic band structure of HgTe was first studied with the application of the Groves-Paul model, originally constructed for  $\alpha$ -Tin[255] and then applied to mercury chalcogenides[256], which allowed to establish some general features of HgTe band structure. More recently,  $\mathbf{k} \cdot \mathbf{p}$  method has been often used to describe the HgTe band structure because it allows an accurate description of the electronic eigenstates in the vicinity of the  $\Gamma$ -point, which is where the band inversion takes place in HgTe (see *e.g.* the  $16 \times 16$  relativistic model by Cardona *et al.* in Ref.[257]). The main drawback of  $\mathbf{k} \cdot \mathbf{p}$  method is the limited range of reliability in the BZ (see Ref.[239] for a general perspective on the method). A realistic description of HgTe band structure cannot neglect neither the spin degree of freedom nor the relativistic correction to the Hamiltonian. The former is a fundamental aspect of a TI; the latter because the relativistic term is the physical origin of the band inversion. The relativistic part of the Hamiltonian can be written:

$$H_{rel} = H_D + H_{kin} + H_{SOC} \quad (5.14)$$

where  $H_D$  is the Darwin correction, representing the extra energy coming from the interaction of  $s$  electrons with the nucleus,  $H_{kin}$  is the correction to the kinetic operator due to increase of the relativistic effective mass with velocity and  $H_{SOC}$  is the spin-orbit interaction. The first two terms can only shift energy levels in energy while SOC can also split them, due to the angular momentum dependence. In the case of II-VI compounds, the  $\Gamma_6$ -type states are derived from the  $p$  electrons of the chalcogen while the  $\Gamma_8$ -type from the  $s$ -type states of the metal. Both the Darwin and the kinetic

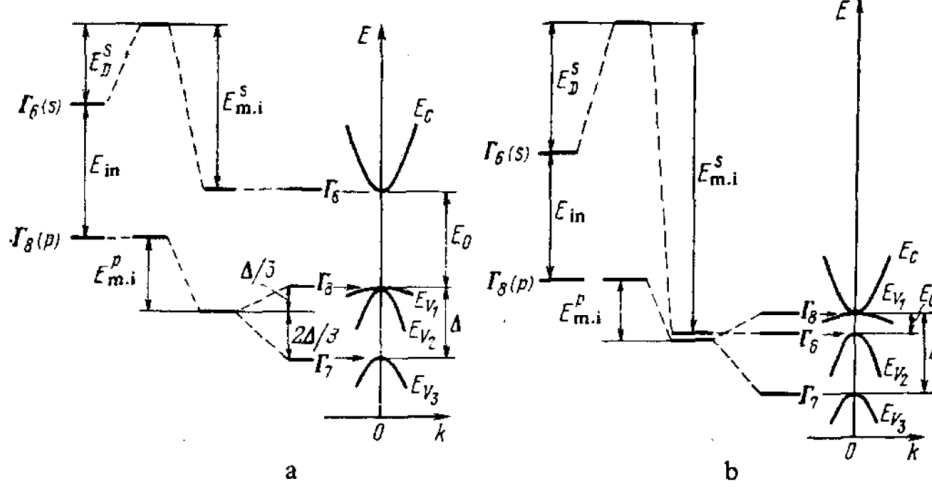


**Figure 5.3:** Schematics of the band formation in CdTe (panel (a)) and HgTe (panel (b)) around the  $\Gamma$  point. Here,  $E_D$  represents the Darwin correction,  $E_m^{s,p}.i.$  the kinetic correction due to  $H_{kin}$  and  $\Delta$  the spin-orbit splitting. Figure taken from Ref.[254]

correction mostly influence  $s$  states. Their value depends on the atomic number of the atom (kinetic corrections scale with the fourth power of the atomic number[258]). As such, Hg( $s$ ) orbitals are particularly affected by the correction due to  $H_D + H_{kin}$ , as exemplified in Fig.5.3 where the band formation is compared between CdTe (panel (a)) and HgTe (panel (b)) in the reciprocal space region near the  $\Gamma$ -point. The two compounds present a very similar crystal structure, and their lattice parameters differ of  $\simeq 0.3\%$ . However, since Hg is heavier, the  $\Gamma_6$  band position is more affected by  $H_{kin}$  and  $H_D$ , resulting in a sensible energy downshift. This, combined with the effect of  $H_{kin}$  and  $H_{SOC}$  over the  $\Gamma_8$  band, causes the band inversion. Conversely, the kinetic correction in CdTe is too small to alter the band ordering.

### 5.2.3 Opening the gap in HgTe

One of the consequences of the band inversion is that the Fermi level is pinned in the middle of the  $\Gamma_8$  fourfold degenerate band (see Fig.5.3). Thus, HgTe is not an insulator nor a gapped semiconductor; rather it has semimetallic properties, with the Fermi level lying in a zone with vanishing DOS. The four  $\Gamma_8$  bands are degenerate at the  $\Gamma$  point. Moving away from the  $\Gamma$

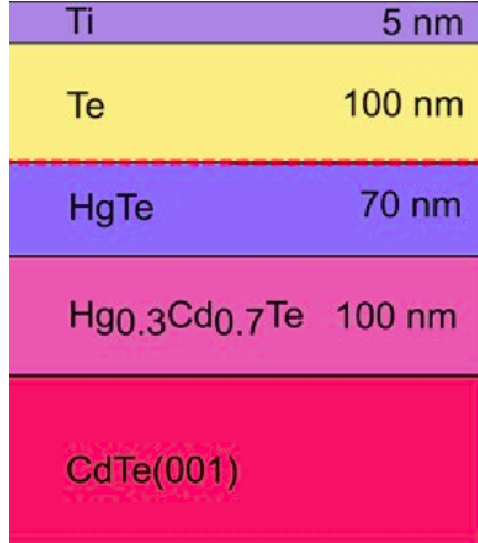


**Figure 5.4:** Schematization of the experimental setup.

point, valence and conduction slightly overlap, with a maximum value (of the order of the meV) along the (111) reciprocal direction[254]. From the above discussion it results that HgTe, as it is, is not a topological insulator, in fact it is not an insulator in the first place. It follows that we need to induce a gap in the band structure to observe the TI phase in HgTe. In this regard, it is known since a long time that one way to do this is by lowering the symmetry of the crystal, *e.g.* by applying an anisotropic strain, such as a tensile strain along the (0,0,1) crystal direction[259] or in-plane tensile strain[245]: a well established procedure is to epitaxially grow HgTe on CdTe substrates. CdTe has a lattice constant that is 0.3% larger than that of HgTe; consequently, slabs under a critical thickness of 200 nm grow with the same in-plane lattice constant of the CdTe substrate, inducing an in-plane tensile strain. The resulting system was studied with an  $8 \times 8 \mathbf{k} \cdot \mathbf{p}$  model, where an energy gap of  $\simeq 22$  meV has been calculated for a 0.3% lattice mismatch model, *i.e.* the experimental lattice mismatch[245]. In this setup, the quantum Hall effect due to the topological surface states of HgTe has been measured, proving that strained HgTe is a 3D TI[245].

#### 5.2.4 Presentation of the experimental setup

We investigate the electronic and topological properties of strained HgTe in collaboration with the experimental group of the University of Würzburg,

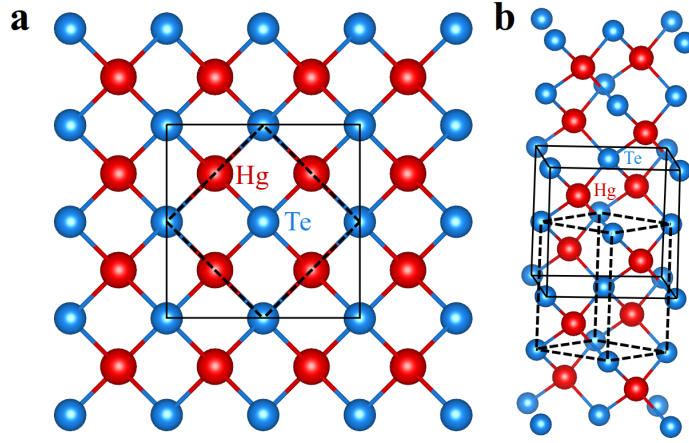


**Figure 5.5:** Top view (panel (a)) and side view (panel (b)) of HgTe crystal structure. Solid black lines mark the fcc unit cell, dashed lines the tetragonal unit cell.

led by prof. Laurens Molenkamp. The experimental results presented here are still unpublished and belong to the experimental research group of the University of Würzburg. The full list of collaborators can be found at the end of the thesis. The samples are grown by means of molecular beam epitaxy on top of a CdTe substrate, in the setup schematically shown in Fig.5.4. By depositing a 80 nm Te layer subsequent to the growth, we ensure a contaminant free surface. The capping layer was removed under ultra-high vacuum conditions in the ARPES chamber enabling investigation with pristine surface quality, similar to the procedure used for Bi<sub>2</sub>Te<sub>3</sub>-derived materials[260]. We apply vacuum ultraviolet angle resolved photoemission to investigate the bulk and surface electronic structure. The experiments were conducted at the  $\mu$  ARPES end station of the beamline of the ALS (USA). Further measurements were realized with the He I $_{\alpha}$ -line (21.2 eV) of a monochromatized He-discharge source which enables, due to higher surface sensitivity, a more detailed look at the topological surface state (TSS).

### 5.2.5 DFT description of bulk HgTe

As we already mentioned, electronic structure calculations for HgTe are particularly delicate in DFT. For this reason, we compare the performances of different DFT exchange and correlation (XC) functionals in order to determine the most suited for the description of the HgTe electronic structure

by comparing the results to the ARPES spectrum. Further details of the DFT calculation can be found in the computational details at the end of the section. In Fig.5.6, we compare the band structure obtained with different XC functionals in the vicinity of the  $\Gamma$ -point, along the two in-plane high symmetry directions.

We first discuss the results obtained with the bare local density approximation (LDA)[261] (grey lines in Fig.5.6). The LDA functional predicts the following band ordering at the  $\Gamma$ -point:  $\Gamma_8 > \Gamma_7 > \Gamma_6$ . This is at variance with the accepted  $\Gamma_8 > \Gamma_6 > \Gamma_7$  band ordering, as already observed in previous literature (see *e.g.* Ref.[262]). This fact makes LDA not suited for a good description of HgTe electronic properties. We thus explore various “beyond” LDA methods to obtain a better description of the band structure. As a first attempt, we consider on-site correlation effects by introducing the Hubbard  $U$  on-site energy, in the rotationally invariant LDA+ $U$  formalism described by *Dudarev et al.* in Ref.[263]. This approach has been already used in the past literature with good results, and reproduces the experimentally observed band ordering at the  $\Gamma$  point of the BZ[249]. However it relies on a tunable parameter (the value of the on-site energy  $U$ ), which makes the description not fully *ab-initio*. The resulting band structure is shown in Fig.5.6 (dashed green lines). We consider a value  $U - J = 10$  eV in order to obtain direct band gaps at the  $\Gamma$ -point in agreement with the experimental measurements. Alternatively to the LDA+ $U$ , we considered the Modified Becke-Johnson (MBJ) potential correction to the LDA XC functional[264, 265]. The MBJ correction is a local approximation to an atomic exact-exchange potential and significantly improves the results of the bare LDA exchange functional for the prediction of the band-gap of most semiconductors, while leaving the calculation relatively cheap (dashed red lines in Fig.5.6). The best agreement with the experimental data was obtained using the hybrid HSE06 functional[266], which explicitly includes the atomic exact-exchange term in the functional. While the LDA results are qualitatively different, all the other three functionals give qualitatively similar results regarding the band structure near the Fermi level.

The obtained direct band gaps at  $\Gamma$  are reported in Tab.5.1. Although the LDA+ $U$  and the LDA-MBJ predict the correct band ordering at  $\Gamma$ , the resulting band structure is still not adequate when compared to the experimental results: both methods fail to reproduce the Fermi velocity of the bands of interest and also the energy position of the deep Hg( $5d$ ) states is quite off with respect to the experimentally measured position (see Fig.5.7). This is because these two features are related, since the interaction with the  $d$  states contributes to determine the energy-momentum dispersion of

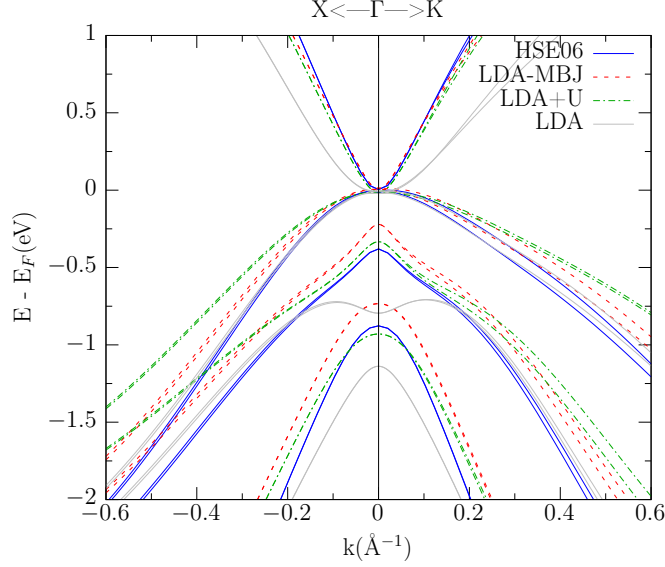


**Figure 5.6:** Comparison among the electronic band structures obtained employing different XC functionals.

the valence bands[257]. In Fig.5.7 we see that the LDA-MBJ functional puts the two Hg(5d) peaks at a substantially lower binding energy with respect to the experiments, while they are found at higher binding energies in the LDA+U approach. Since the shift of the Hg(5d) states towards higher binding energies is caused by the value of the  $U$ , it could be argued that a lower value of  $U - J$  may fix this occurrence; anyway, by doing so (e.g. by reducing the value of  $U - J$  to 7.5 eV), we obtain  $\Gamma_6, \Gamma_7$  and  $\Gamma_8$  bands in poor agreement with the ARPES measurements. On the contrary, both these feature are well captured by the HSE06 functional. which shows a far better agreement with the experimental energy position of the Hg(5d) states. Furthermore, the low energy band structure is in remarkable agreement with the ARPES data, as we will show in the following.

### 5.2.6 Experimental results and discussion

As already mentioned, HgTe crystallizes in the zincblende cubic structure ( $F\bar{4}3m$ ), space group No. 216, Fig.5.5). The corresponding Brillouin zone, schematically shown in Fig.5.8(a), takes the shape of a truncated octahedron.

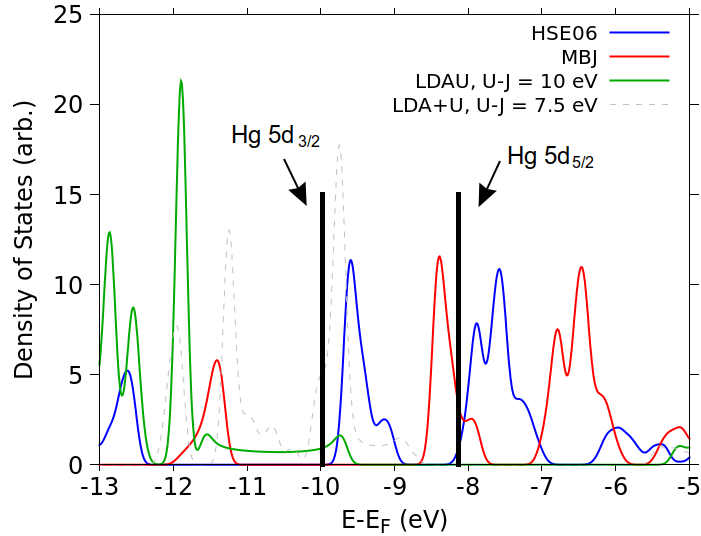


**Figure 5.7:** Density of states plot in the region of the Hg(5d) levels. Black thick lines mark the position of the experimental peaks.

XC Functional	$\Delta E(\Gamma_8 - \Gamma_6)$ (eV)	$\Delta E(\Gamma_8 - \Gamma_7)$ (eV)
LDA	1.12	0.77
LDA+U	0.3	0.91
LDA-MBJ	0.23	0.74
HSE06	0.37	0.87
Exp.	0.29	0.91

**Table 5.1:** Direct band gaps at  $\Gamma$  for the different considered functionals compared to the experimental values[267].

We are especially interested in the electronic properties in the region of the BZ near the  $\Gamma$ -point, where the band inversion takes place.

In Fig.5.8(b) we report the ARPES intensity in proximity of the  $\Gamma$  point along the  $\Gamma$ -K direction, compared to the bulk DFT-HSE06 eigenstates obtained with the HSE06 method. The agreement between theory and experiment is impressive: it is possible to unequivocally assign the spectral features to the corresponding DFT  $\Gamma_8$ -,  $\Gamma_6$ - and  $\Gamma_7$ -bands. We observe the inverted  $\Gamma_8 > \Gamma_6 > \Gamma_7$  band ordering both in theory and in the experiment. An additional feature is present in the ARPES spectrum, which is not reproduced by

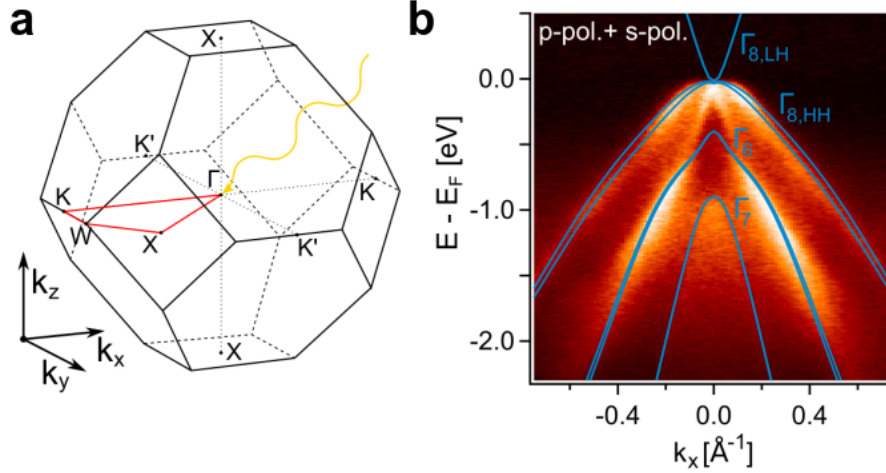


**Figure 5.8:** Panel (a): bulk Brillouin zone showing the relevant high symmetry points as well as the path in  $\mathbf{k}$ -space of the electronic structure. Panel (b): ARPES spectrum along the  $\Gamma$ -K point overlaid by calculated bulk band dispersion. The theoretical band structure shows various bulk bands as well as the TSS as the feature not reproduced by the calculation.

the bulk DFT calculation, *i.e.* a band with a linear dispersion connecting the top of the  $\Gamma_8$  band at  $E_F$  with the second valence band at finite  $k_x$ . This additional Dirac-type state has been already observed in previous less resolved ARPES measurements and its Dirac-like behavior was confirmed by means of magnetotransport experiments[245]. In the following we demonstrate that this state is the topologically protected surface state characterizing the TI phase of HgTe, emerging as a consequence of the inverted band ordering.

As a first step, we address this problem by means of a *ab-initio* calculation of the surface band structure. Surface calculations have been performed using the tetragonal cell (Fig.5.5, black dashed lines), breaking the periodicity of the bulk system along the (001) direction with a Te-terminated supercell, while leaving the other two directions periodic, and considering an HgTe slab with a thickness  $d \simeq 15.5$  nm. A vacuum of 25 Å was included in the calculation in order to avoid spurious interactions between the periodic images of the system. Due to the large system in consideration, the calculation has been performed using the  $LDA + U$  approach instead of the heavier HSE06 hybrid functional. Although the  $LDA + U$  approach does not guarantee the same quantitative precision of the HSE06 functional, we believe that all the

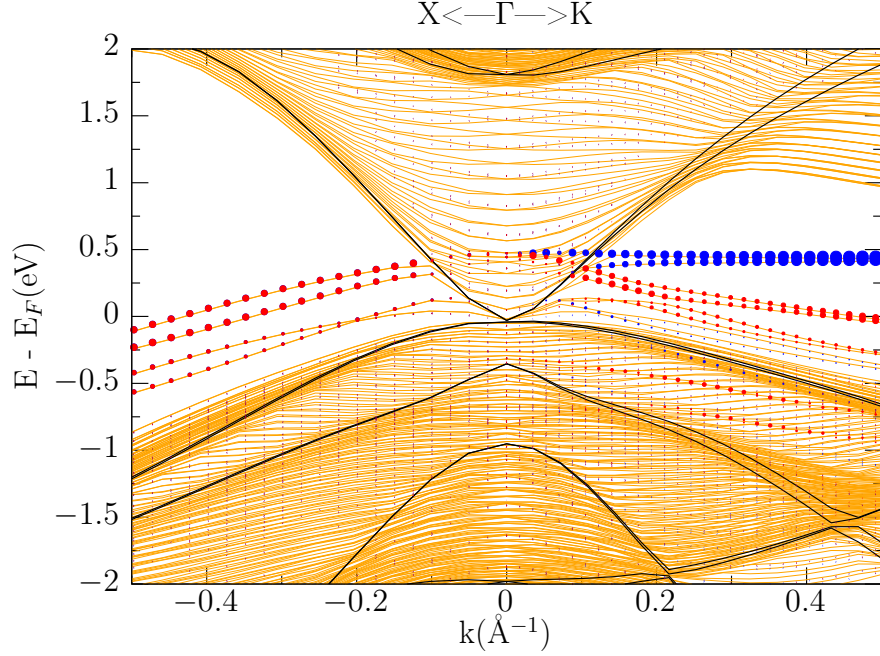


**Figure 5.9:** Surface band structure calculation for a 15.5 nm thick Te-terminated HgTe slab. Red and blue dots are proportional to the surface character of the corresponding eigenstate.

qualitative aspects can be captured by the LDA+U calculation which, as we discussed, is able to reproduce the right experimental band ordering. The eigenvalues obtained in the surface calculation are reported in Fig.5.9.

We observe the formation of surface states on both the inequivalent Te-terminated surfaces. However, they disperse far away from  $\Gamma$  and do not show a behavior compatible with the one observed in the ARPES spectrum of Fig.5.8(b). Thus, the surface states resulting from this calculation do not correspond to the topologically protected surface states. The difference observed between the ARPES spectrum and the calculation is surprising and not easy to explain. However, this discrepancy has already been pointed out in previous literature: in Ref.[268] an Hg-terminated slab *ab-initio* calcula-

tion was performed, including the effect of the  $c(2\times 2)$  surface reconstruction experimentally observed[269] and no linear dispersing surface state was observed near  $\Gamma$ . Furthermore, in Ref.[251], *Wu et al.* report that both slab calculations with Te or Hg terminations yield several trivial dangling bond states without Dirac-type states. They attributed the discrepancy with the experimental observations to the roughness of the cleaved surface in ARPES, arguing that the ordered surface configuration of the *ab-initio* calculation cannot reproduce adequately the surface bands of this system. They further suggested that the optimal method to simulate this system is employing a Wannier basis function. They analyzed the case of a large 3% strain, demonstrating the formation of a Dirac cone at the  $\Gamma$ -point, localized at the Te-terminated surface. Thus, we believe that the failure of the *ab-initio* calculation regarding the Dirac state could be attributed to the presence of a disordered surface. However, other reasons could lie behind this discrepancy, *e.g.* the presence of an uncompensated charge or some degree of polarity. Here, we extended the results by *Wu et al.* passing to the localized Wannier basis through the interpolation of the HSE06 bands.

I briefly present the main ideas behind the maximally localized Wannier function theory, which we employ for the description of our Hamiltonian in the real space. While it is often convenient to describe a spatially periodic electron system in the crystal momentum space, where the Hamiltonian is diagonal, it is still possible to represent the Bloch Hamiltonian in an arbitrary space operating a basis change in the Hilbert space. A very useful alternative description is represented by the Wannier functions (WFs) basis, having the property to be localized in real space.[270] In the following, we consider the case of an isolated band, for the sake of maintaining a simple theoretical formalism. The WF corresponding to the band  $n$  localized in the cell described by the lattice vector  $\mathbf{R}$  in real space can be written as

$$w_n(\mathbf{R}) = \frac{V}{(2\pi)^3} \int_{BZ} d\mathbf{k} e^{-i \mathbf{k} \cdot \mathbf{R}} |\psi_{n,\mathbf{k}}\rangle \quad (5.15)$$

From Eq.5.15, it can be seen that WFs are related to the Bloch functions by a Fourier transform. Since this transformation is unitary, both the Bloch and the Wannier descriptions represent two equivalent ways to describe the electron system under investigation. Some complications stem from the strong non-unicity of the WFs, due to the presence of a gauge freedom in the choice of the Bloch eigenfunctions:

$$\psi_{n\mathbf{k}} \rightarrow e^{i\phi_n(\mathbf{k})} \psi_{n\mathbf{k}}$$

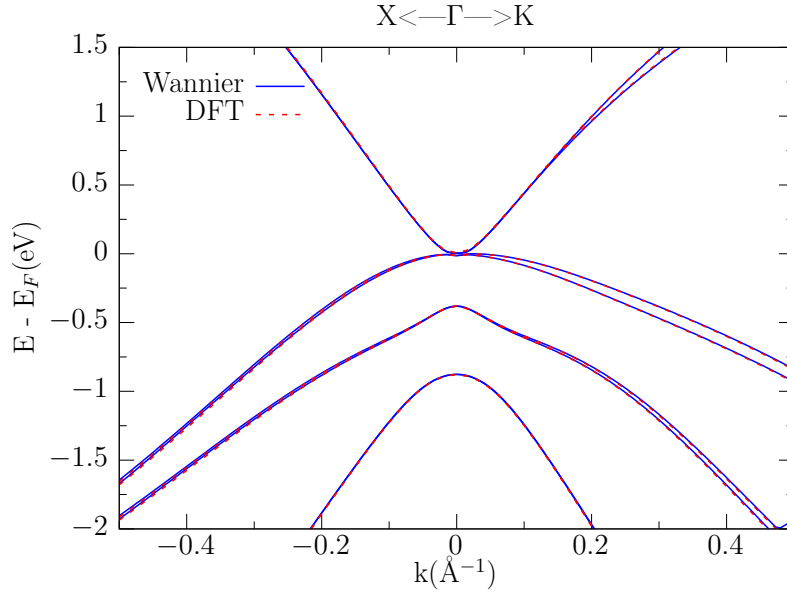


**Figure 5.10:** Comparison between the Kohn-Sham electron bands obtained with the HSE06 functional and the band structure obtained with the Wannier Hamiltonian.

One way to overcome this difficulty due to Marzari and Vanderbilt[271] consists in imposing an additional condition, *i.e.* the maximal possible localization of the WF, by the minimization of a functional representing the WF spread  $\langle r^2 \rangle_n - \langle \mathbf{r} \rangle_n^2$ . Once that the technical difficulties of the Wannierization procedure are addressed, the resulting Hamiltonian in the Wannier basis is very useful for calculations involving many atoms, due to its local character, as we demonstrate in the following. We extracted the maximally localized Wannier functions from the *ab-initio* calculation using the wannier90 package [272]. We project the DFT Hamiltonian over the basis of the spin-orbited atomic Hg(6s) and Te(5p) states, obtaining a  $16 \times 16$  real space Hamiltonian in the tetragonal cell description. In Fig.5.10, we compare the band structure resulting from the Wannier Hamiltonian to the DFT calculation. The excellent agreement between the two confirms the completeness of the basis functions.

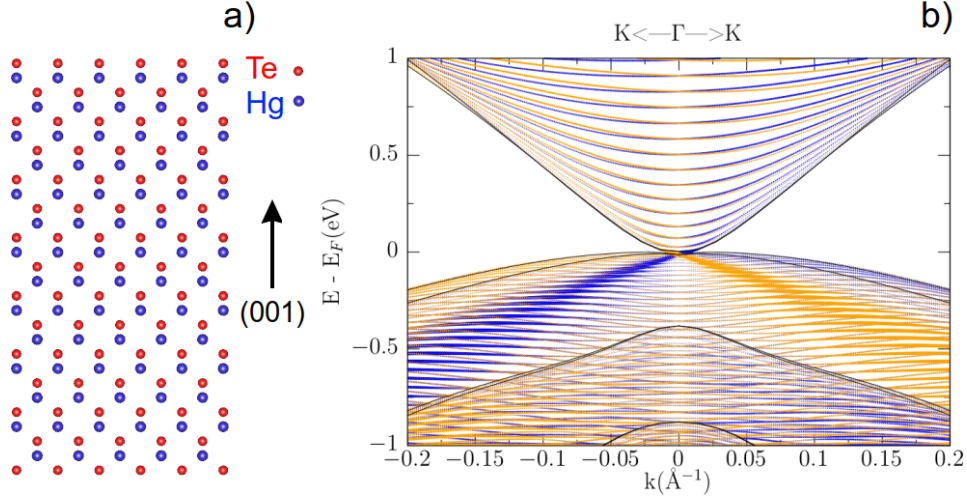


**Figure 5.11:** Panel (a): schematic representation of a  $5 \times 5 \times 7$  Te-terminated HgTe slab. In the calculation, the periodicity is only broken in the (001) direction. Panel (b): Wannier surface band structure calculation for a 24 nm thick Te-terminated HgTe slab, projected over the two spin components (orange and blue dots). Black lines represent the bulk band structure.

The short ranged Wannier Hamiltonian allows us to perform large slab calculations with an affordable computational cost. However, contrary to the full *ab-initio* calculation, in the Wannier calculation the surface charge is not allowed to self consistently screen the discontinuity induced by the surface and the surface only affects the coordination number of the surface atoms. From the Wannier Hamiltonian, we build a Te-terminated 24 nm thick slab in order to describe the surface states of HgTe. A schematic representation of the slab is depicted in Fig.5.11(a). The resulting band structure is reported in Fig.5.11(b), where the eigenstates are projected over the two spin component of the four outermost layers of one Te-terminated surface (blue and orange, respectively). Here, the formation of a linear electronic dispersion near  $\Gamma$  is evident. We observe that the spin character of the linear surface state depends on the considered  $\mathbf{k}$ -direction, confirming the topological nature of the surface state with the spin-momentum locking, a characteristic feature of TI's surface states[60].

In order to properly compare the calculated bands with the experimental ARPES spectrum, we consider a semi-infinite slab whose spectrum whose spectrum can be obtained applying the iterative Green's function method

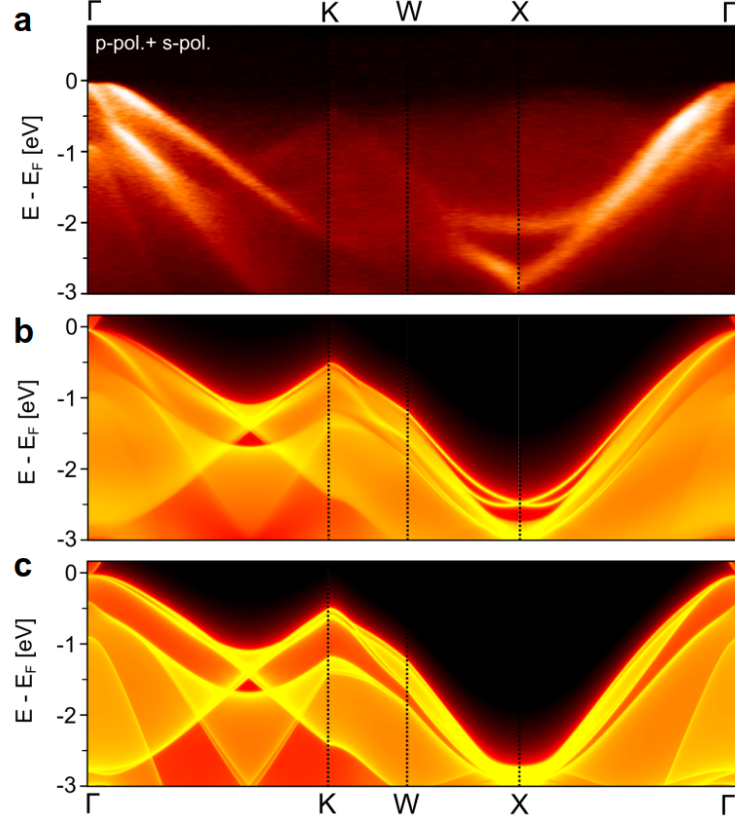


**Figure 5.12:** Panel (a): sum of ARPES intensities for *p*- and *s*-polarized light. Panel (b): semi-infinite surface spectrum considering a *Te*-termination. Panel (c): surface projected bulk bands.

in the Wannier basis in the scheme developed in Ref.[273], using the same Wannier Hamiltonian as before. In Fig.5.12(a) the ARPES spectrum along an high-symmetry closed loop in the BZ, indicated by the red lines in Fig.5.8(a) and Figs.5.12(b),(c) show the corresponding electronic theoretical band structure resulting from the semi-infinite approach obtained taking into consideration the surface projected bulk bands (b) and *Te*-surface related features (c). Comparing the ARPES spectrum with the calculated one, we find a surface state located around the *X*-point of the BZ. The agreement between theory and experiment is impressive; both energy on-sets as well as band

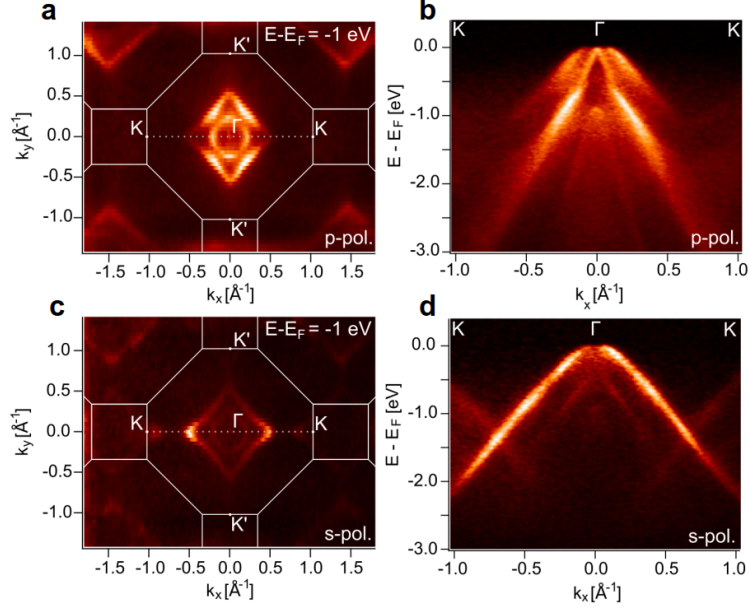


**Figure 5.13:** Panel (a): experimental constant energy contour maps overlaid by the boundaries of the bulk BZ. Panel (b): electronic structure along the  $K$ - $\Gamma$ - $K$  direction. Both measurements were taken with  $p$ -polarized light. Panels (c) and (d): experimental constant energy contour and band structure along the  $K$ - $\Gamma$ - $K$  direction measured with  $s$ -polarized light. All spectra were taken with  $h\nu = 123$  eV.

dispersion get reproduced over a broad energy and momentum range, for the bulk and the surface states, including the TSS at  $\Gamma$ .

Additionally, we want to investigate the orbital contributions to the electronic structure. This can be done by utilizing the transition matrix element in the form of dipole selection rules. The transition probability and thus the photo emission-current in a photo-excitation process is dependent on the product of the irreducible representations of the initial state, the final state and the perturbation operator. However, this complex problem can be greatly simplified in the dipole approximation, omitting non-relevant processes like two photon excitations. This results in a proportionality of the photo-current to one-electron dipole matrix element  $J \propto |\langle \phi_f | \mathbf{A} \cdot \mathbf{p} | \phi_i \rangle|^2$  of the electromagnetic vector potential  $\mathbf{A}$ , the momentum operator  $\mathbf{p}$  as well as the one-electron initial and final states  $\phi_i$  and  $\phi_f$ , respectively[274].

The experimental geometry is schematically shown in Fig.5.13(d). Refer-

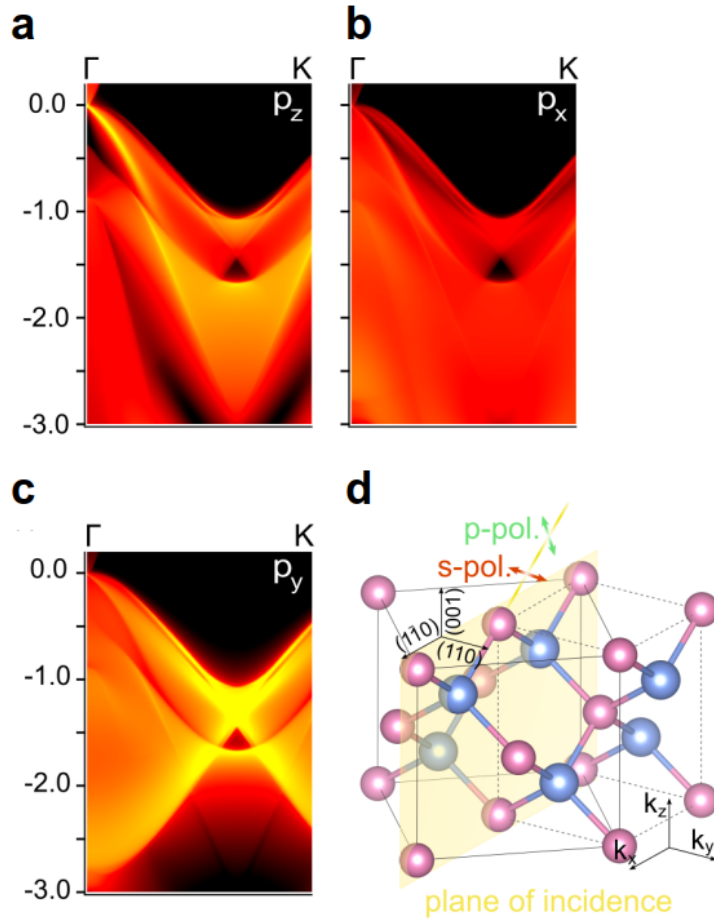


**Figure 5.14:** Panel (a) and (b): calculated surface spectrum from the  $\Gamma$ - to the K-point projected onto Te  $p_z$ - and  $p_x$ -orbitals, shown in the left and right panel, respectively. Panel (c): calculated surface spectrum projected onto Te  $p_y$ -orbitals. Panel (d): schematic of the experimental geometry showing the crystal structure, the plane of incidence as well as the orientation of p- and s-polarization (pol.). All spectra were taken with  $h\nu = 123$  eV.

ring to the laboratory frame of reference, the plane of incidence (POI, the plane where both the incident light and the emitted photoelectron lie) as well as the detector slit lie within the plane  $P_{xz}$  defined by  $k_x$  and  $k_z$ . The crystal is oriented in such a way that  $P_{xz}$  coincides with one of its 110-planes. These

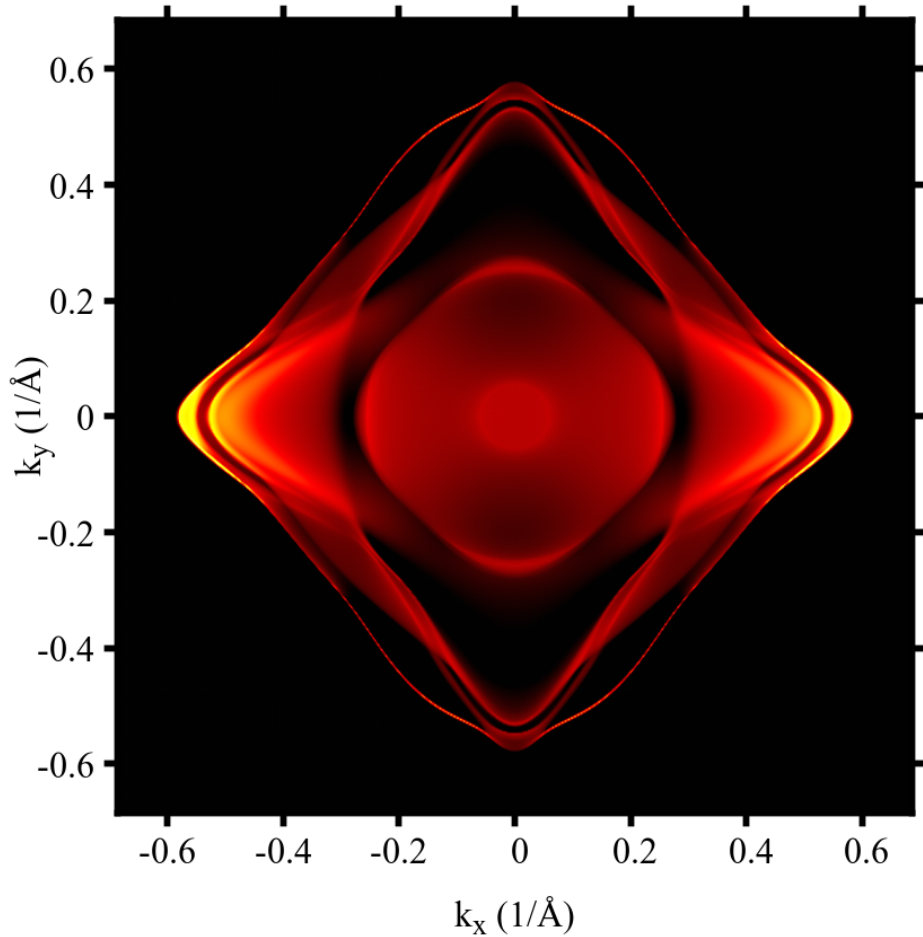


*Figure 5.15: Calculated energy cut at  $-1.0$  eV, projected over  $p_y$  orbitals.*

define the mirror planes of the system and correspond to the  $\Gamma K$ -direction. When both the POI as well as the detector slit are oriented along a mirror plane of the crystal system, there are only two irreducible representations possible, even or odd with respect to the mirror plane. The complete product has to be of even parity in order for the overlap integral to give a non-zero contribution. Furthermore, the final state can only be even since having a node in the mirror plane would make it undetectable by the analyzer. These conditions leave two possible combinations for a finite transition probability:  $A$  and  $\phi_i$  have to be either both even or odd. The present geometry allows

for excitations since it satisfies the transitions rules that we discussed above, from the mirror-even (odd) states  $p_x$  and  $p_z$  ( $p_y$ ) by  $p$ -pol. ( $s$ -pol.) light.

Fig.5.13(a) shows a constant energy cut (CEC) taken with  $p$ -pol. light at  $E - E_F = 1$  eV. The borders of the BZ are indicated by white lines. The dotted line marks the K- $\Gamma$ -K-direction, whose corresponding cut is shown in Fig.5.13(b). Taken with in-plane polarized light, this measurement enables excitation from  $p_x$ - and  $p_z$ -derived states within the POI. We compare the  $p$ -pol. ARPES spectrum to the orbital separated surface calculations in the semi-infinite approach, reported in Figs.5.14(a) and (b) for the  $\Gamma$ -K direction. We can identify the  $p_z$ -orbitals as the main contributor to the electronic structure. The TSS as well as the outer parts of the  $\Gamma_6$ - and inner part of the  $\Gamma_8$ -bands are derived from  $p_z$ -orbitals, whereas the overall  $p_x$ -character is comparatively faint. An equivalent evaluation can be made for experiments performed with  $s$ -pol and the odd  $p_y$ -states which are depicted in Figs.5.13(c),(d) and Fig.5.14(c), respectively. Virtually all measured intensity in the  $s$ -pol. spectrum stems from the  $\Gamma_8$ -band with only minor contributions from parts of the  $\Gamma_6$ -band at small but finite  $k_x$ . The orbital projection of  $p_y$ -states in Fig.5.14(c) mirrors this spectral weight distribution. We further reproduce the CEC in Fig.5.13(c) realizing a constant energy calculation at -1 eV and projecting it over the  $p_y$  orbital. The result, shown in Fig.5.15, shows a precise correspondence between the experimental observation and the calculated spectral weight, confirming that the primary contribution to the spectral weight originates from the outer band along  $\Gamma$ -K, having mainly  $p_y$  character. The relative intensity of different bands is slightly different in the experiment with respect to the theoretical calculation: we attribute this effect to the already discussed photo-current matrix element.

In addition to the low energy valence band regime the DFT calculation accurately reproduces higher energy states like the outermost Hg 5(d) core levels, as can be seen in Fig.5.7. The spin-orbit coupling induced splitting of the  $\Gamma_8$ -band can be written as  $E_D = (1 \pm \sqrt{3}/4 C)k_x$  for the [110] direction[275]. The splitting parameter  $C$  can be traced back to the interaction between the valence band state  $\Gamma_8$  and the cation  $d$ -levels and according to *Cardona et al.* can be expressed by  $C = -A \frac{\Delta_{d,c}}{E(\Gamma_8) - E_{d,c}}$  where  $E(\Gamma_8)$  is the band position of the  $\Gamma_8$ -state,  $\Delta_{d,c}$  is the spin-orbit splitting and  $E_{d,c}$  the energy of the outermost cation  $d$ -levels[276, 257]. The positive constant  $A$  can be estimated to be 350 meV  $\text{\AA}$  for II-VI compounds[276]. Using these parameters obtained from our experimental and theoretical approach we find  $C_k = -80.4$  meV  $\text{\AA}$  and  $C_k = -87.5$  meV  $\text{\AA}$ , which are in agreement with

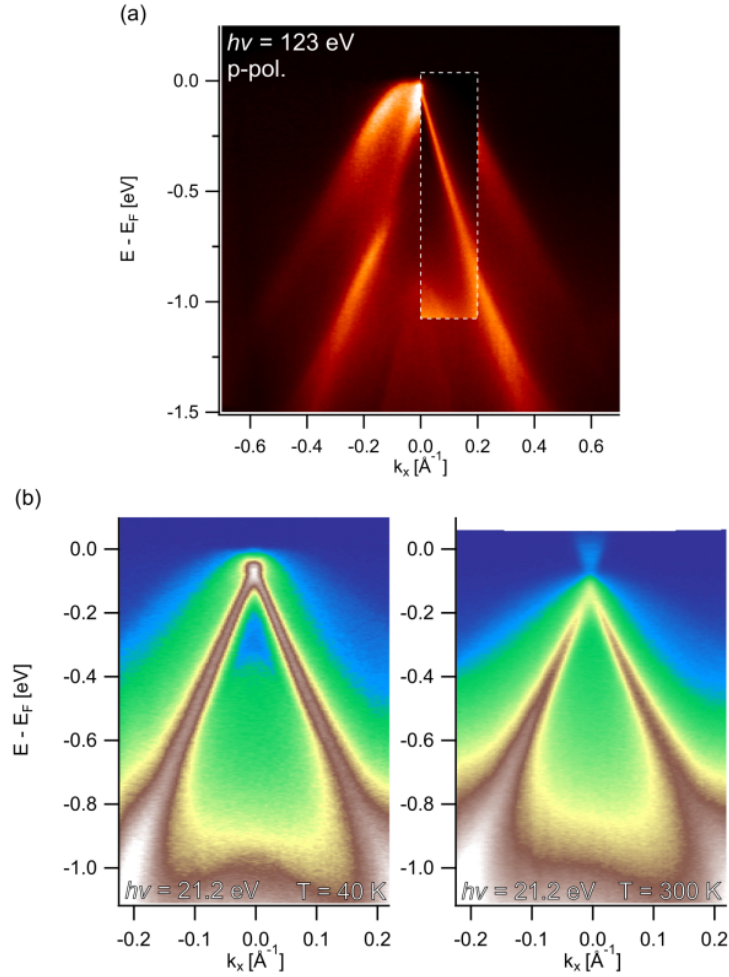


**Figure 5.16:** ARPES intensity near the  $\Gamma$ -point. (a) Photoemission intensity taken with  $h\nu = 123$  eV and p-polarized light. The inset depicts the electronic structure measured with He I  $\alpha$ -line, demonstrating the high sensitivity for the topological surface state at this photon energy. (b) Surface electronic structure measured with  $h\nu = 21.2$  eV at  $T = 40$  K and 300 K.

previous estimations[276, 257]. Further insights on the surface bands can be obtained from ARPES spectrum obtained with surface sensitive photons from He-I discharge lamps ( $h\nu = 21.2$  eV) as a function of the temperature. Fig.5.16(a) shows an ARPES spectrum taken at  $h\nu = 123$  eV overlaid by the surface electronic structure measured at 21.2 eV. The lower photon energy

yields a higher cross section for the TSS. The merging of  $\Gamma_6$ -band and TSS appears more continuously compared to measurement at  $h\nu=123$  eV. Overall, the TSS exhibits a virtually ideal linear dispersion. Fig.5.16(b),(c) show ARPES spectra taken at  $T=40$ K and  $300$ K, respectively. A pronounced shift in energy can be seen with a more electron doped behavior for the room temperature measurement. We gave a theoretical interpretation of this puzzling experimental result considering two effects: thermal expansion and Fermi distribution broadening. From  $50$ K to  $300$ K the lattice constant expands by  $\simeq 0.1\%$ [277]. We calculated the bands with the lattice constant at  $300$  K and included the Fermi broadening in the calculation of the chemical potential. The value of the chemical potential  $\mu$  can be obtained imposing the conservation of the total number of electrons  $n_{e^-}$  in the integral equation

$$n_{e^-} = \int_{-\infty}^{\mu} N(\epsilon) f(\epsilon - \mu) d\epsilon \quad (5.16)$$

, which we iteratively solved for  $\mu$ . Here,  $f$  is the Fermi-Dirac distribution and  $N(\epsilon)$  is the density of states. While the lattice expansion does not change the electronic structure in a meaningful way, we find that the effect of the temperature on the chemical potential is large: the effect of the broadening and the consequent repopulation of electronic states are due to the very asymmetric density of states of HgTe, causing a large shift of  $\Delta E=55$  meV, which is in excellent agreement with the value measured in the experiment.

### 5.2.7 Computational details

We perform DFT calculations with the projector augmented-wave pseudopotential method[159, 109] as implemented in the Vienna Ab-initio Simulation Package (VASP)[278, 279, 108, 107]. An energy cutoff of  $350$  eV for the plane wave basis and  $8 \times 8 \times 8$  Monkhorst-Pack grid for Brillouin zone (BZ) sampling were used, ensuring a convergence of  $1$  meV on the electronic eigenvalues. Spin-orbit coupling was included in the calculation. The conventional zincblende unit cell is shown in Fig.5.5 (black solid lines). We considered the experimental HgTe lattice parameter  $a = 6.46$  Å and applied a  $0.3\%$  in-plane strain to the HgTe lattice parameter in order to match the CdTe experimental lattice parameter ( $0.3\%$  tensile biaxial strain,  $a' = 6.481$  Å). The corresponding out of plane lattice parameter can be calculated from the stiffness coefficients of HgTe[280, 281], obtaining  $c = 6.435$  Å. The surface calculations have been performed with the open-source software Wannier Tools[282].

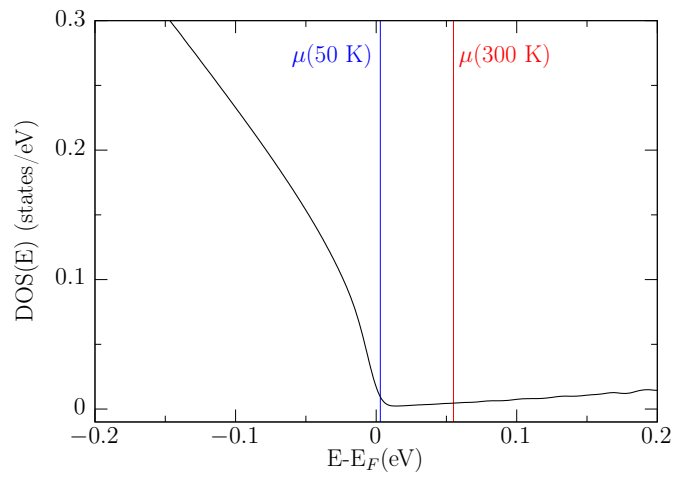


**Figure 5.17:** DOS plotted in the vicinity of the Fermi level. The blue and red line indicate the chemical potential at 50K and 300K, respectively.

### Part III: Conclusions and outlook

The focus of the third part of the thesis has been the description of the properties of bulk HgTe. Its electronic properties were characterized by a combination of experimental and theoretical techniques. From the experimental point of view, we present ARPES measurements with unprecedented accuracy, with clear evidence both of the band inversion and the surface states. From the theoretical point of view, we determined that the inclusion of the non local exchange term via the HSE06 functional is of fundamental importance in order to obtain a coherent description, both for the low energy band structure and the deep Hg( $5d$ ) states. Subsequently, we first attempted the description of the surface structure by means of a full *ab-initio* calculation, however the results are not compatible with the ARPES spectrum. We believe that the roughness of the experimental surface, as well as other effects such as the presence of an uncompensated charge or some degree of polarity may be at the origin of the discrepancy. This aspect, however, deserves further investigation. Successively, we calculated the surface electronic structure using a wannierization procedure, observing the appearance of the spin-resolved TSS state. In order to obtain the best possible comparison with the ARPES spectrum, the electronic structure has been also calculated by means of the Green's function method, finding an impressive agreement with the experimental ARPES data and allowing the identification of all the experimentally observed features in a wide energy and momentum range, signaling that the relevant physical aspects have been captured by the DFT calculation. We further explained the significant Fermi level shift with increasing temperature ( $\simeq 55$  meV) by the peculiar form of the DOS. With this work we provide a solid framework for the first principles description of HgTe properties, offering a reliable comparison for further experimental and *ab-initio* investigations on the material. Having demonstrated that the electronic properties of HgTe can be described by first-principles theory, we can extend the calculations in the Wannier basis to interesting systems based on HgTe and its superlattices CdTe/HgTe to investigate new topological phases, including the possible formation of corner states and hinge states[283, 284].

# List of the collaborators

## Chapter 1

**Niels Ehlen** *II. Physikalisches Institut, Universität zu Köln, Zülpicher Strasse 77, 50937 Cologne, Germany*

**Martin Hell** *II. Physikalisches Institut, Universität zu Köln, Zülpicher Strasse 77, 50937 Cologne, Germany*

**Yannic Falke** *II. Physikalisches Institut, Universität zu Köln, Zülpicher Strasse 77, 50937 Cologne, Germany*

**Riichiro Saito** *Department of Physics, Tohoku University, Sendai 980-8578, Japan*

**Eddwi Hesky Hasdeo** *Research Center for Physics, Indonesian Institute of Sciences, Kawasan Puspiptek Serpong, Tangerang Selatan, 15314, Indonesia*

**Mark Oliver Goerbig** *Laboratoire de Physique des Solides, CNRS UMR 8502, Université Paris-Sud, 91405 Orsay Cedex, France*

**Giovanni Di Santo** *Elettra Sincrotrone Trieste, Strada Statale 14 km 163.5, 34149 Trieste, Italy*

**Luca Petaccia** *Elettra Sincrotrone Trieste, Strada Statale 14 km 163.5, 34149 Trieste, Italy*

**Alexander Grüneis** *II. Physikalisches Institut, Universität zu Köln, Zülpicher Strasse 77, 50937 Cologne, Germany*

## Chapter 2

**Martin Hell II.** *Physikalisches Institut, Universität zu Köln, Zülpicher Strasse 77, 50937 Cologne, Germany*

**Niels Ehlen II.** *Physikalisches Institut, Universität zu Köln, Zülpicher Strasse 77, 50937 Cologne, Germany*

**Boris V. Senkovskiy II.** *Physikalisches Institut, Universität zu Köln, Zülpicher Strasse 77, 50937 Cologne, Germany*

**Charlotte Herbig II.** *Physikalisches Institut, Universität zu Köln, Zülpicher Strasse 77, 50937 Cologne, Germany*

**Christian Teichert II.** *Physikalisches Institut, Universität zu Köln, Zülpicher Strasse 77, 50937 Cologne, Germany and Institute of Physics, Montanuniversität Leoben, Franz Josef Str. 18, 8700 Leoben, Austria*

**Wouter Jolie II.** *Physikalisches Institut, Universität zu Köln, Zülpicher Strasse 77, 50937 Cologne, Germany and Institute for Molecules and Materials, Radboud University, AJ Nijmegen, Netherlands*

**Thomas Michely II.** *Physikalisches Institut, Universität zu Köln, Zülpicher Strasse 77, 50937 Cologne, Germany*

**Jose Avila** *ANTARES Beamline, Synchrotron SOLEIL and Universite Paris-Saclay, L'Orme des Merisiers, Saint Aubin-BP 48, 91192 Gif sur Yvette Cedex, France*

**Giovanni Di Santo** *Elettra Sincrotrone Trieste, Strada Statale 14 km 163.5, 34149 Trieste, Italy*

**Diego M. de la Torre II.** *Physikalisches Institut, Universität zu Köln, Zülpicher Strasse 77, 50937 Cologne, Germany*

**Luca Petaccia** *Elettra Sincrotrone Trieste, Strada Statale 14 km 163.5, 34149 Trieste, Italy*

**Alexander Grüneis II.** *Physikalisches Institut, Universität zu Köln, Zülpicher Strasse 77, 50937 Cologne, Germany*

## Chapter 5

**Raphael Crespo Vidal** *Experimental physics VII, Universität Würzburg, Am Hubland, D-97074 Würzburg, Germany*

**Lukas Lunczer** *Experimental physics III, Universität Würzburg, Am Hubland, D-97074 Würzburg, Germany*

**Simon K. Moser** *Experimental physics IV, Universität Würzburg, Am Hubland, D-97074 Würzburg, Germany*

**Lena Füst** *Experimental physics III, Universität Würzburg, Am Hubland, D-97074 Würzburg, Germany*

**Hartmut Buhmann** *Experimental physics III, Universität Würzburg, Am Hubland, D-97074 Würzburg, Germany*

**Giorgio Sangiovanni** *Theoretical physics I, University of Würzburg, Am Hubland, D-97074 Würzburg, Germany*

**Domenico Di Sante** *Theoretical physics I, University of Würzburg, Am Hubland, D-97074 Würzburg, Germany*

**Laurens W. Molenkamp** *Experimental physics III, Universität Würzburg, Am Hubland, D-97074 Würzburg, Germany*

**Hendrik Bentmann** *Experimental physics VII, Universität Würzburg, Am Hubland, D-97074 Würzburg, Germany*

**Friedrich Reinert** *Experimental physics VII, Universität Würzburg, Am Hubland, D-97074 Würzburg, Germany*

# Bibliography

- [1] R. P. Feynman, *There's Plenty of Room at the Bottom*, Perseus Books, USA, 1999, p. 63–76.
- [2] G. E. Moore, Cramming more components onto integrated circuits, reprinted from *electronics*, volume 38, number 8, april 19, 1965, pp.114 ff., *IEEE Solid-State Circuits Society Newsletter* 11 (3) (2006) 33–35. doi:10.1109/n-ssc.2006.4785860.  
URL <https://doi.org/10.1109/n-ssc.2006.4785860>
- [3] G. Binnig, H. Rohrer, C. Gerber, E. Weibel, Tunneling through a controllable vacuum gap, *Applied Physics Letters* 40 (2) (1982) 178–180. arXiv:<https://doi.org/10.1063/1.92999>, doi:10.1063/1.92999.  
URL <https://doi.org/10.1063/1.92999>
- [4] G. Binnig, H. Rohrer, C. Gerber, E. Weibel, Surface studies by scanning tunneling microscopy, *Phys. Rev. Lett.* 49 (1982) 57–61. doi:10.1103/PhysRevLett.49.57.  
URL <https://link.aps.org/doi/10.1103/PhysRevLett.49.57>
- [5] H. W. Kroto, J. R. Heath, S. C. O'Brien, R. F. Curl, R. E. Smalley, C60: Buckminsterfullerene, *Nature* 318 (6042) (1985) 162–163. doi:10.1038/318162a0.  
URL <https://doi.org/10.1038/318162a0>
- [6] K. S. Novoselov, A. K. Geim, S. V. Morozov, D. Jiang, Y. Zhang, S. V. Dubonos, I. V. Grigorieva, A. A. Firsov, Electric field effect in atomically thin carbon films, *Science* 306 (5696) (2004) 666–669. arXiv:<https://science.sciencemag.org/content/306/5696/666.full.pdf>, doi:10.1126/science.1102896.  
URL <https://science.sciencemag.org/content/306/5696/666>
- [7] H. P. Boehm., A. Clauss, G. O. Fischer, U. Hofmann, Dünnschichtenkohlenstoff-folien, *Zeitschrift für Naturforschung B* 17 (3) (1962)

150–153. doi:10.1515/znb-1962-0302.  
URL <https://doi.org/10.1515/znb-1962-0302>

- [8] R. F. Frindt, A. D. Yoffe, F. P. Bowden, Physical properties of layer structures : optical properties and photoconductivity of thin crystals of molybdenum disulphide, Proceedings of the Royal Society of London. Series A. Mathematical and Physical Sciences 273 (1352) (1963) 69–83. arXiv:<https://royalsocietypublishing.org/doi/pdf/10.1098/rspa.1963.0075>, doi:10.1098/rspa.1963.0075.  
URL <https://royalsocietypublishing.org/doi/abs/10.1098/rspa.1963.0075>
- [9] A. K. Geim, Graphene: Status and prospects, Science 324 (5934) (2009) 1530–1534. arXiv:<https://science.sciencemag.org/content/324/5934/1530.full.pdf>, doi:10.1126/science.1158877.  
URL <https://science.sciencemag.org/content/324/5934/1530>
- [10] M. Yi, Z. Shen, A review on mechanical exfoliation for the scalable production of graphene, Journal of Materials Chemistry A 3 (22) (2015) 11700–11715. doi:10.1039/c5ta00252d.  
URL <https://doi.org/10.1039/c5ta00252d>
- [11] A. Reina, X. Jia, J. Ho, D. Nezich, H. Son, V. Bulovic, M. S. Dresselhaus, J. Kong, Large area, few-layer graphene films on arbitrary substrates by chemical vapor deposition, Nano Letters 9 (1) (2009) 30–35. doi:10.1021/nl801827v.  
URL <https://doi.org/10.1021/nl801827v>
- [12] K. S. Kim, Y. Zhao, H. Jang, S. Y. Lee, J. M. Kim, K. S. Kim, J.-H. Ahn, P. Kim, J.-Y. Choi, B. H. Hong, Large-scale pattern growth of graphene films for stretchable transparent electrodes, Nature 457 (7230) (2009) 706–710. doi:10.1038/nature07719.  
URL <https://doi.org/10.1038/nature07719>
- [13] J. Hass, W. A. de Heer, E. H. Conrad, The growth and morphology of epitaxial multilayer graphene, Journal of Physics: Condensed Matter 20 (32) (2008) 323202. doi:10.1088/0953-8984/20/32/323202.  
URL <https://doi.org/10.1088/0953-8984/20/32/323202>
- [14] D. G. Papageorgiou, I. A. Kinloch, R. J. Young, Mechanical properties of graphene and graphene-based nanocomposites, Progress

in *Materials Science* 90 (2017) 75 – 127.  
doi:<https://doi.org/10.1016/j.pmatsci.2017.07.004>.  
URL  
<http://www.sciencedirect.com/science/article/pii/S0079642517300968>

- [15] K. S. Novoselov, A. K. Geim, S. V. Morozov, D. Jiang, M. I. Katsnelson, I. V. Grigorieva, S. V. Dubonos, A. A. Firsov, Two-dimensional gas of massless dirac fermions in graphene, *Nature* 438 (7065) (2005) 197–200. doi:10.1038/nature04233.  
URL <https://doi.org/10.1038/nature04233>
- [16] A. K. Geim, K. S. Novoselov, The rise of graphene, *Nature Materials* 6 (3) (2007) 183–191. doi:10.1038/nmat1849.  
URL <https://doi.org/10.1038/nmat1849>
- [17] A. H. Castro Neto, F. Guinea, N. M. R. Peres, K. S. Novoselov, A. K. Geim, The electronic properties of graphene, *Rev. Mod. Phys.* 81 (2009) 109–162. doi:10.1103/RevModPhys.81.109.  
URL <https://link.aps.org/doi/10.1103/RevModPhys.81.109>
- [18] L. Landau, Diamagnetismus der metalle, *Zeitschrift für Physik* 64 (9-10) (1930) 629–637. doi:10.1007/bf01397213.  
URL <https://doi.org/10.1007/bf01397213>
- [19] Y. Zhang, Y.-W. Tan, H. L. Stormer, P. Kim, Experimental observation of the quantum hall effect and berry’s phase in graphene, *Nature* 438 (7065) (2005) 201–204. doi:10.1038/nature04235.  
URL <https://doi.org/10.1038/nature04235>
- [20] S. Murphy, J. Hicks, W. Liu, S. Chung, K. Goldammer, M. Santos, Studies of the quantum hall to quantum hall insulator transition in insb-based 2dss, *Physica E: Low-dimensional Systems and Nanostructures* 6 (1) (2000) 293 – 296.  
doi:[https://doi.org/10.1016/S1386-9477\(99\)00157-5](https://doi.org/10.1016/S1386-9477(99)00157-5).  
URL  
<http://www.sciencedirect.com/science/article/pii/S1386947799001575>
- [21] M. Calandra, F. Mauri, Electron-phonon coupling and electron self-energy in electron-doped graphene: Calculation of angular-resolved photoemission spectra, *Phys. Rev. B* 76 (2007) 205411. doi:10.1103/PhysRevB.76.205411.  
URL <https://link.aps.org/doi/10.1103/PhysRevB.76.205411>

- [22] B. Uchoa, C.-Y. Lin, A. H. Castro Neto, Tailoring graphene with metals on top, *Phys. Rev. B* 77 (2008) 035420.  
doi:10.1103/PhysRevB.77.035420.  
URL <https://link.aps.org/doi/10.1103/PhysRevB.77.035420>
- [23] M. Dresselhaus, G. Dresselhaus, Intercalation compounds of graphite, *Advances in Physics* 30 (2) (1981) 139–326.  
arXiv:<https://doi.org/10.1080/00018738100101367>,  
doi:10.1080/00018738100101367.  
URL <https://doi.org/10.1080/00018738100101367>
- [24] M. S. Dresselhaus, G. Dresselhaus, Intercalation compounds of graphite, *Advances in Physics* 51 (1) (2002) 1–186.  
arXiv:<https://doi.org/10.1080/00018730110113644>,  
doi:10.1080/00018730110113644.  
URL <https://doi.org/10.1080/00018730110113644>
- [25] G. Profeta, M. Calandra, F. Mauri, Phonon-mediated superconductivity in graphene by lithium deposition, *Nature Physics* 8 (2) (2012) 131–134. doi:10.1038/nphys2181.  
URL <https://doi.org/10.1038/nphys2181>
- [26] J. Chapman, Y. Su, C. A. Howard, D. Kundys, A. N. Grigorenko, F. Guinea, A. K. Geim, I. V. Grigorieva, R. R. Nair, Superconductivity in ca-doped graphene laminates, *Scientific Reports* 6 (1) (Mar. 2016). doi:10.1038/srep23254.  
URL <https://doi.org/10.1038/srep23254>
- [27] S. Ichinokura, K. Sugawara, A. Takayama, T. Takahashi, S. Hasegawa, Superconducting calcium-intercalated bilayer graphene, *ACS Nano* 10 (2) (2016) 2761–2765, pMID: 26815333.  
arXiv:<https://doi.org/10.1021/acsnano.5b07848>,  
doi:10.1021/acsnano.5b07848.  
URL <https://doi.org/10.1021/acsnano.5b07848>
- [28] S. B. Trickey, F. Müller-Plathe, G. H. F. Diercksen, J. C. Boettger, Interplanar binding and lattice relaxation in a graphite dilayer, *Phys. Rev. B* 45 (1992) 4460–4468. doi:10.1103/PhysRevB.45.4460.  
URL <https://link.aps.org/doi/10.1103/PhysRevB.45.4460>
- [29] K. Yan, H. Peng, Y. Zhou, H. Li, Z. Liu, Formation of bilayer bernal graphene: Layer-by-layer epitaxy via chemical vapor deposition,

Nano Letters 11 (3) (2011) 1106–1110, pMID: 21322597.  
arXiv:<https://doi.org/10.1021/nl104000b>, doi:10.1021/nl104000b.  
URL <https://doi.org/10.1021/nl104000b>

- [30] E. McCann, M. Koshino, The electronic properties of bilayer graphene, Reports on Progress in Physics 76 (5) (2013) 056503.  
doi:10.1088/0034-4885/76/5/056503.  
URL <https://doi.org/10.1088/2F0034-4885/2F76/2F5/2F056503>
- [31] K. S. Novoselov, E. McCann, S. V. Morozov, V. I. Fal’ko, M. I. Katsnelson, U. Zeitler, D. Jiang, F. Schedin, A. K. Geim, Unconventional quantum hall effect and berry’s phase of  $2\pi$  in bilayer graphene, Nature Physics 2 (3) (2006) 177–180.  
doi:10.1038/nphys245.  
URL <https://doi.org/10.1038/nphys245>
- [32] R. Bistritzer, A. H. MacDonald, Moiré bands in twisted double-layer graphene, Proceedings of the National Academy of Sciences 108 (30) (2011) 12233–12237.  
arXiv:<https://www.pnas.org/content/108/30/12233.full.pdf>,  
doi:10.1073/pnas.1108174108.  
URL <https://www.pnas.org/content/108/30/12233>
- [33] Y. Cao, V. Fatemi, S. Fang, K. Watanabe, T. Taniguchi, E. Kaxiras, P. Jarillo-Herrero, Unconventional superconductivity in magic-angle graphene superlattices, Nature 556 (7699) (2018) 43–50.  
doi:10.1038/nature26160.  
URL <https://doi.org/10.1038/nature26160>
- [34] N. B. Kopnin, T. T. Heikkilä, G. E. Volovik, High-temperature surface superconductivity in topological flat-band systems, Phys. Rev. B 83 (2011) 220503. doi:10.1103/PhysRevB.83.220503.  
URL <https://link.aps.org/doi/10.1103/PhysRevB.83.220503>
- [35] Y. Henni, H. P. Ojeda Collado, K. Nogajewski, M. R. Molas, G. Usaj, C. A. Balseiro, M. Orlita, M. Potemski, C. Faugeras, Rhombohedral multilayer graphene: A magneto-raman scattering study, Nano Letters 16 (6) (2016) 3710–3716, pMID: 27164265.  
arXiv:<https://doi.org/10.1021/acs.nanolett.6b01041>,  
doi:10.1021/acs.nanolett.6b01041.  
URL <https://doi.org/10.1021/acs.nanolett.6b01041>

- [36] D. Pierucci, H. Sediri, M. Hajlaoui, J.-C. Girard, T. Brumme, M. Calandra, E. Velez-Fort, G. Patriarche, M. G. Silly, G. Ferro, V. Soulière, M. Marangolo, F. Sirotti, F. Mauri, A. Ouerghi, Evidence for flat bands near the fermi level in epitaxial rhombohedral multilayer graphene, *ACS Nano* 9 (5) (2015) 5432–5439, pMID: 25893537. doi:10.1021/acs.nano.5b01239.  
URL <https://doi.org/10.1021/acs.nano.5b01239>
- [37] M. Ashton, J. Paul, S. B. Sinnott, R. G. Hennig, Topology-scaling identification of layered solids and stable exfoliated 2d materials, *Phys. Rev. Lett.* 118 (2017) 106101.  
doi:10.1103/PhysRevLett.118.106101.  
URL <https://link.aps.org/doi/10.1103/PhysRevLett.118.106101>
- [38] R. G. Dickinson, L. Pauling, The crystal structure of molybdenite, *Journal of the American Chemical Society* 45 (6) (1923) 1466–1471.  
arXiv:<https://doi.org/10.1021/ja01659a020>, doi:10.1021/ja01659a020.  
URL <https://doi.org/10.1021/ja01659a020>
- [39] P. Joensen, R. Frindt, S. Morrison, Single-layer mos<sub>2</sub>, *Materials Research Bulletin* 21 (4) (1986) 457 – 461.  
doi:[https://doi.org/10.1016/0025-5408\(86\)90011-5](https://doi.org/10.1016/0025-5408(86)90011-5).  
URL <http://www.sciencedirect.com/science/article/pii/0025540886900115>
- [40] S. Das, J. A. Robinson, M. Dubey, H. Terrones, M. Terrones, Beyond graphene: Progress in novel two-dimensional materials and van der waals solids, *Annual Review of Materials Research* 45 (1) (2015) 1–27. arXiv:<https://doi.org/10.1146/annurev-matsci-070214-021034>, doi:10.1146/annurev-matsci-070214-021034.  
URL <https://doi.org/10.1146/annurev-matsci-070214-021034>
- [41] X. Xu, W. Yao, D. Xiao, T. F. Heinz, Spin and pseudospins in layered transition metal dichalcogenides, *Nature Physics* 10 (5) (2014) 343–350. doi:10.1038/nphys2942.  
URL <https://doi.org/10.1038/nphys2942>
- [42] D. Xiao, G.-B. Liu, W. Feng, X. Xu, W. Yao, Coupled spin and valley physics in monolayers of mos<sub>2</sub> and other group-vi dichalcogenides, *Phys. Rev. Lett.* 108 (2012) 196802.  
doi:10.1103/PhysRevLett.108.196802.

URL

<https://link.aps.org/doi/10.1103/PhysRevLett.108.196802>

- [43] K. F. Mak, K. He, J. Shan, T. F. Heinz, Control of valley polarization in monolayer MoS<sub>2</sub> by optical helicity, *Nature Nanotechnology* 7 (8) (2012) 494–498. doi:10.1038/nnano.2012.96. URL <https://doi.org/10.1038/nnano.2012.96>
- [44] X. Xi, Z. Wang, W. Zhao, J.-H. Park, K. T. Law, H. Berger, L. Forró, J. Shan, K. F. Mak, Ising pairing in superconducting NbSe<sub>2</sub> atomic layers, *Nature Physics* 12 (2) (2015) 139–143. doi:10.1038/nphys3538. URL <https://doi.org/10.1038/nphys3538>
- [45] J. M. Lu, O. Zheliuk, I. Leermakers, N. F. Q. Yuan, U. Zeitler, K. T. Law, J. T. Ye, Evidence for two-dimensional ising superconductivity in gated mos<sub>2</sub>, *Science* 350 (6266) (2015) 1353–1357. arXiv:<https://science.sciencemag.org/content/350/6266/1353.full.pdf>, doi:10.1126/science.aab2277. URL <https://science.sciencemag.org/content/350/6266/1353>
- [46] B. Radisavljevic, A. Radenovic, J. Brivio, V. Giacometti, A. Kis, Single-layer MoS<sub>2</sub> transistors, *Nature Nanotechnology* 6 (3) (2011) 147–150. doi:10.1038/nnano.2010.279. URL <https://doi.org/10.1038/nnano.2010.279>
- [47] K. F. Mak, C. Lee, J. Hone, J. Shan, T. F. Heinz, Atomically thin mos<sub>2</sub>: A new direct-gap semiconductor, *Phys. Rev. Lett.* 105 (2010) 136805. doi:10.1103/PhysRevLett.105.136805. URL <https://link.aps.org/doi/10.1103/PhysRevLett.105.136805>
- [48] A. Splendiani, L. Sun, Y. Zhang, T. Li, J. Kim, C.-Y. Chim, G. Galli, F. Wang, Emerging photoluminescence in monolayer mos<sub>2</sub>, *Nano Letters* 10 (4) (2010) 1271–1275, pMID: 20229981. arXiv:<https://doi.org/10.1021/nl903868w>, doi:10.1021/nl903868w. URL <https://doi.org/10.1021/nl903868w>
- [49] S. Manzeli, D. Ovchinnikov, D. Pasquier, O. V. Yazyev, A. Kis, 2d transition metal dichalcogenides, *Nature Reviews Materials* 2 (8) (Jun. 2017). doi:10.1038/natrevmats.2017.33. URL <https://doi.org/10.1038/natrevmats.2017.33>

- [50] Q. H. Wang, K. Kalantar-Zadeh, A. Kis, J. N. Coleman, M. S. Strano, Electronics and optoelectronics of two-dimensional transition metal dichalcogenides, *Nature Nanotechnology* 7 (11) (2012) 699–712. doi:10.1038/nnano.2012.193. URL <https://doi.org/10.1038/nnano.2012.193>
- [51] M. Chhowalla, H. S. Shin, G. Eda, L.-J. Li, K. P. Loh, H. Zhang, The chemistry of two-dimensional layered transition metal dichalcogenide nanosheets, *Nature Chemistry* 5 (4) (2013) 263–275. doi:10.1038/nchem.1589. URL <https://doi.org/10.1038/nchem.1589>
- [52] A. Koma, Van der waals epitaxy—a new epitaxial growth method for a highly lattice-mismatched system, *Thin Solid Films* 216 (1) (1992) 72 – 76, papers presented at the International Workshop on Science and Technology of Thin Films for the 21st Century, Evanston,IL, USA, July 28-August 2, 1991. doi:[https://doi.org/10.1016/0040-6090\(92\)90872-9](https://doi.org/10.1016/0040-6090(92)90872-9). URL <http://www.sciencedirect.com/science/article/pii/0040609092908729>
- [53] Y. Zhang, T.-R. Chang, B. Zhou, Y.-T. Cui, H. Yan, Z. Liu, F. Schmitt, J. Lee, R. Moore, Y. Chen, H. Lin, H.-T. Jeng, S.-K. Mo, Z. Hussain, A. Bansil, Z.-X. Shen, Direct observation of the transition from indirect to direct bandgap in atomically thin epitaxial MoSe<sub>2</sub>, *Nature Nanotechnology* 9 (2) (2013) 111–115. doi:10.1038/nnano.2013.277. URL <https://doi.org/10.1038/nnano.2013.277>
- [54] J. Hall, B. Pilić, C. Murray, W. Jolie, T. Wekking, C. Busse, M. Kralj, T. Michely, Molecular beam epitaxy of quasi-freestanding transition metal disulphide monolayers on van der waals substrates: a growth study, *2D Materials* 5 (2) (2018) 025005. doi:10.1088/2053-1583/aaa1c5. URL <https://doi.org/10.1088/2053-1583/aaa1c5>
- [55] N. Ehlen, J. Hall, B. V. Senkovskiy, M. Hell, J. Li, A. Herman, D. Smirnov, A. Fedorov, V. Y. Voroshnin, G. D. Santo, L. Petaccia, T. Michely, A. Grüneis, Narrow photoluminescence and raman peaks of epitaxial MoS<sub>2</sub> on graphene/ir(1 1 1), *2D Materials* 6 (1) (2018) 011006. doi:10.1088/2053-1583/aaebd3. URL <https://doi.org/10.1088/2053-1583/aaebd3>

- [56] M. König, S. Wiedmann, C. Brüne, A. Roth, H. Buhmann, L. W. Molenkamp, X.-L. Qi, S.-C. Zhang, Quantum spin hall insulator state in hgte quantum wells, *Science* 318 (5851) (2007) 766–770.  
arXiv:<https://science.sciencemag.org/content/318/5851/766.full.pdf>,  
doi:10.1126/science.1148047.  
URL <https://science.sciencemag.org/content/318/5851/766>
- [57] K. v. Klitzing, G. Dorda, M. Pepper, New method for high-accuracy determination of the fine-structure constant based on quantized hall resistance, *Phys. Rev. Lett.* 45 (1980) 494–497.  
doi:10.1103/PhysRevLett.45.494.  
URL <https://link.aps.org/doi/10.1103/PhysRevLett.45.494>
- [58] D. J. Thouless, M. Kohmoto, M. P. Nightingale, M. den Nijs, Quantized hall conductance in a two-dimensional periodic potential, *Phys. Rev. Lett.* 49 (1982) 405–408. doi:10.1103/PhysRevLett.49.405.  
URL <https://link.aps.org/doi/10.1103/PhysRevLett.49.405>
- [59] X.-G. Wen, Topological orders and edge excitations in fractional quantum hall states, *Advances in Physics* 44 (5) (1995) 405–473.  
arXiv:<https://doi.org/10.1080/00018739500101566>,  
doi:10.1080/00018739500101566.  
URL <https://doi.org/10.1080/00018739500101566>
- [60] M. Z. Hasan, C. L. Kane, Colloquium: Topological insulators, *Rev. Mod. Phys.* 82 (2010) 3045–3067. doi:10.1103/RevModPhys.82.3045.  
URL <https://link.aps.org/doi/10.1103/RevModPhys.82.3045>
- [61] C. L. Kane, E. J. Mele, Quantum spin hall effect in graphene, *Phys. Rev. Lett.* 95 (2005) 226801. doi:10.1103/PhysRevLett.95.226801.  
URL <https://link.aps.org/doi/10.1103/PhysRevLett.95.226801>
- [62] C. L. Kane, E. J. Mele,  $Z_2$  topological order and the quantum spin hall effect, *Phys. Rev. Lett.* 95 (2005) 146802.  
doi:10.1103/PhysRevLett.95.146802.  
URL <https://link.aps.org/doi/10.1103/PhysRevLett.95.146802>
- [63] L. Fu, C. L. Kane, E. J. Mele, Topological insulators in three dimensions, *Phys. Rev. Lett.* 98 (2007) 106803.  
doi:10.1103/PhysRevLett.98.106803.  
URL <https://link.aps.org/doi/10.1103/PhysRevLett.98.106803>

- [64] F. D. M. Haldane, Model for a quantum hall effect without landau levels: Condensed-matter realization of the "parity anomaly", *Phys. Rev. Lett.* 61 (1988) 2015–2018. doi:10.1103/PhysRevLett.61.2015. URL <https://link.aps.org/doi/10.1103/PhysRevLett.61.2015>
- [65] B. A. Bernevig, T. L. Hughes, S.-C. Zhang, Quantum spin hall effect and topological phase transition in hgte quantum wells, *Science* 314 (5806) (2006) 1757–1761. arXiv:<https://science.sciencemag.org/content/314/5806/1757.full.pdf>, doi:10.1126/science.1133734. URL <https://science.sciencemag.org/content/314/5806/1757>
- [66] B. Yan, C. Felser, Topological materials: Weyl semimetals, *Annual Review of Condensed Matter Physics* 8 (1) (2017) 337–354. arXiv:<https://doi.org/10.1146/annurev-conmatphys-031016-025458>, doi:10.1146/annurev-conmatphys-031016-025458. URL <https://doi.org/10.1146/annurev-conmatphys-031016-025458>
- [67] X.-L. Qi, S.-C. Zhang, Topological insulators and superconductors, *Rev. Mod. Phys.* 83 (2011) 1057–1110. doi:10.1103/RevModPhys.83.1057. URL <https://link.aps.org/doi/10.1103/RevModPhys.83.1057>
- [68] S. Ryu, A. P. Schnyder, A. Furusaki, A. W. W. Ludwig, Topological insulators and superconductors: tenfold way and dimensional hierarchy, *New Journal of Physics* 12 (6) (2010) 065010. doi:10.1088/1367-2630/12/6/065010. URL <https://doi.org/10.1088/2F1367-2630/2F12/2F6/2F065010>
- [69] P. Hohenberg, W. Kohn, Inhomogeneous electron gas, *Phys. Rev.* 136 (1964) B864–B871. doi:10.1103/PhysRev.136.B864. URL <https://link.aps.org/doi/10.1103/PhysRev.136.B864>
- [70] W. Kohn, L. J. Sham, Self-consistent equations including exchange and correlation effects, *Phys. Rev.* 140 (1965) A1133–A1138. doi:10.1103/PhysRev.140.A1133. URL <https://link.aps.org/doi/10.1103/PhysRev.140.A1133>
- [71] J. L. McChesney, A. Bostwick, T. Ohta, T. Seyller, K. Horn, J. González, E. Rotenberg, Extended van hove singularity and superconducting instability in doped graphene, *Phys. Rev. Lett.* 104

(2010) 136803. doi:10.1103/PhysRevLett.104.136803.

URL

<https://link.aps.org/doi/10.1103/PhysRevLett.104.136803>

- [72] A. V. Fedorov, N. I. Verbitskiy, D. Haberer, C. Struzzi, L. Petaccia, D. Usachov, O. Y. Vilkov, D. V. Vyalikh, J. Fink, M. Knupfer, B. Büchner, A. Grüneis, Observation of a universal donor-dependent vibrational mode in graphene, *Nature Communications* 5 (1) (Feb. 2014). doi:10.1038/ncomms4257.  
URL <https://doi.org/10.1038/ncomms4257>
- [73] R. P. Smith, T. E. Weller, C. A. Howard, M. P. Dean, K. C. Rahnejat, S. S. Saxena, M. Ellerby, Superconductivity in graphite intercalation compounds, *Physica C: Superconductivity and its Applications* 514 (2015) 50 – 58, *superconducting Materials: Conventional, Unconventional and Undetermined*.  
doi:<https://doi.org/10.1016/j.physc.2015.02.029>.  
URL <http://www.sciencedirect.com/science/article/pii/S0921453415000568>
- [74] D. Leykam, A. Andreanov, S. Flach, Artificial flat band systems: from lattice models to experiments, *Advances in Physics: X* 3 (1) (2018) 1473052. doi:10.1080/23746149.2018.1473052.  
URL <https://doi.org/10.1080/23746149.2018.1473052>
- [75] B. Sutherland, Localization of electronic wave functions due to local topology, *Phys. Rev. B* 34 (1986) 5208–5211.  
doi:10.1103/PhysRevB.34.5208.  
URL <https://link.aps.org/doi/10.1103/PhysRevB.34.5208>
- [76] I. Syôzi, Statistics of Kagomé Lattice, *Progress of Theoretical Physics* 6 (3) (1951) 306–308. arXiv:<https://academic.oup.com/ptp/article-pdf/6/3/306/5239621/6-3-306.pdf>, doi:10.1143/ptp/6.3.306.  
URL <https://doi.org/10.1143/ptp/6.3.306>
- [77] A. Mielke, Ferromagnetism in the hubbard model on line graphs and further considerations, *Journal of Physics A: Mathematical and General* 24 (14) (1991) 3311–3321. doi:10.1088/0305-4470/24/14/018.  
URL <https://doi.org/10.1088/0305-4470/24/14/018>
- [78] T. Bilitewski, R. Moessner, Disordered flat bands on the kagome lattice, *Phys. Rev. B* 98 (2018) 235109.

doi:10.1103/PhysRevB.98.235109.

URL <https://link.aps.org/doi/10.1103/PhysRevB.98.235109>

- [79] E. H. Lieb, Two theorems on the hubbard model, *Phys. Rev. Lett.* 62 (1989) 1201–1204. doi:10.1103/PhysRevLett.62.1201.  
URL <https://link.aps.org/doi/10.1103/PhysRevLett.62.1201>
- [80] H. Tasaki, Ferromagnetism in the hubbard models with degenerate single-electron ground states, *Phys. Rev. Lett.* 69 (1992) 1608–1611. doi:10.1103/PhysRevLett.69.1608.  
URL <https://link.aps.org/doi/10.1103/PhysRevLett.69.1608>
- [81] R. Drost, T. Ojanen, A. Harju, P. Liljeroth, Topological states in engineered atomic lattices, *Nature Physics* 13 (7) (2017) 668–671. doi:10.1038/nphys4080.  
URL <https://doi.org/10.1038/nphys4080>
- [82] M. R. Slot, T. S. Gardenier, P. H. Jacobse, G. C. P. van Miert, S. N. Kempkes, S. J. M. Zevenhuizen, C. M. Smith, D. Vanmaekelbergh, I. Swart, Experimental realization and characterization of an electronic lieb lattice, *Nature Physics* 13 (7) (2017) 672–676. doi:10.1038/nphys4105.  
URL <https://doi.org/10.1038/nphys4105>
- [83] C. Zhong, Y. Xie, Y. Chen, S. Zhang, Coexistence of flat bands and dirac bands in a carbon-kagome-lattice family, *Carbon* 99 (2016) 65 – 70. doi:<https://doi.org/10.1016/j.carbon.2015.11.073>.  
URL <http://www.sciencedirect.com/science/article/pii/S0008622315304814>
- [84] D. Marchenko, D. V. Evtushinsky, E. Golias, A. Varykhalov, T. Seyller, O. Rader, Extremely flat band in bilayer graphene, *Science Advances* 4 (11) (2018).  
arXiv:<https://advances.sciencemag.org/content/4/11/eaau0059.full.pdf>, doi:10.1126/sciadv.aau0059.  
URL <https://advances.sciencemag.org/content/4/11/eaau0059>
- [85] B. V. Senkovskiy, D. Y. Usachov, A. V. Fedorov, T. Marangoni, D. Haberer, C. Tresca, G. Profeta, V. Caciuc, S. Tsukamoto, N. Atodiresei, N. Ehlen, C. Chen, J. Avila, M. C. Asensio, A. Y. Varykhalov, A. Nefedov, C. Wöll, T. K. Kim, M. Hoesch, F. R. Fischer, A. Grüneis, Boron-doped graphene nanoribbons: Electronic

structure and raman fingerprint, ACS Nano 12 (8) (2018) 7571–7582, PMID: 30004663. arXiv:<https://doi.org/10.1021/acsnano.8b04125>, doi:10.1021/acsnano.8b04125. URL <https://doi.org/10.1021/acsnano.8b04125>

- [86] H. Henck, J. Avila, Z. Ben Aziza, D. Pierucci, J. Baima, B. Pamuk, J. Chaste, D. Utt, M. Bartos, K. Nogajewski, B. A. Piot, M. Orlita, M. Potemski, M. Calandra, M. C. Asensio, F. Mauri, C. Faugeras, A. Ouerghi, Flat electronic bands in long sequences of rhombohedral-stacked graphene, Phys. Rev. B 97 (2018) 245421. doi:10.1103/PhysRevB.97.245421. URL <https://link.aps.org/doi/10.1103/PhysRevB.97.245421>
- [87] P. Rosenzweig, H. Karakachian, D. Marchenko, K. Küster, U. Starke, Overdoping graphene beyond the van hove singularity, Phys. Rev. Lett. 125 (2020) 176403. doi:10.1103/PhysRevLett.125.176403. URL <https://link.aps.org/doi/10.1103/PhysRevLett.125.176403>
- [88] N. I. Verbitskiy, A. V. Fedorov, C. Tresca, G. Profeta, L. Petaccia, B. V. Senkovskiy, D. Y. Usachov, D. V. Vyalikh, L. V. Yashina, A. A. Eliseev, T. Pichler, A. Grüneis, Environmental control of electron–phonon coupling in barium doped graphene, 2D Materials 3 (4) (2016) 045003. doi:10.1088/2053-1583/3/4/045003. URL <https://doi.org/10.1088/2053-1583/3/4/045003>
- [89] D. Y. Usachov, A. V. Fedorov, O. Y. Vilkov, I. I. Ogorodnikov, M. V. Kuznetsov, A. Grüneis, C. Laubschat, D. V. Vyalikh, Electron-phonon coupling in graphene placed between magnetic li and si layers on cobalt, Phys. Rev. B 97 (2018) 085132. doi:10.1103/PhysRevB.97.085132. URL <https://link.aps.org/doi/10.1103/PhysRevB.97.085132>
- [90] G. Csányi, P. B. Littlewood, A. H. Nevidomskyy, C. J. Pickard, B. D. Simons, The role of the interlayer state in the electronic structure of superconducting graphite intercalated compounds, Nature Physics 1 (1) (2005) 42–45. doi:10.1038/nphys119. URL <https://doi.org/10.1038/nphys119>
- [91] K. Kanetani, K. Sugawara, T. Sato, R. Shimizu, K. Iwaya, T. Hitosugi, T. Takahashi, Ca intercalated bilayer graphene as a thinnest limit of superconducting c6ca, Proceedings of the National

Academy of Sciences 109 (48) (2012) 19610–19613.  
arXiv:<https://www.pnas.org/content/109/48/19610.full.pdf>,  
doi:10.1073/pnas.1208889109.  
URL <https://www.pnas.org/content/109/48/19610>

- [92] J. Kleeman, K. Sugawara, T. Sato, T. Takahashi, Enhancement of electron–phonon coupling in cs-overlayered intercalated bilayer graphene, *Journal of Physics: Condensed Matter* 28 (20) (2016) 204001. doi:10.1088/0953-8984/28/20/204001.  
URL <https://doi.org/10.1088/0953-8984/28/20/204001>
- [93] T. O. Wehling, E. Şaşıoğlu, C. Friedrich, A. I. Lichtenstein, M. I. Katsnelson, S. Blügel, Strength of effective coulomb interactions in graphene and graphite, *Phys. Rev. Lett.* 106 (2011) 236805.  
doi:10.1103/PhysRevLett.106.236805.  
URL <https://link.aps.org/doi/10.1103/PhysRevLett.106.236805>
- [94] N. Ashcroft, N. Mermin, *Solid State Physics*, Saunders College, Philadelphia, 1976.
- [95] Y. Lin, G. Chen, J. T. Sadowski, Y. Li, S. A. Tenney, J. I. Dadap, M. S. Hybertsen, R. M. Osgood, Observation of intercalation-driven zone folding in quasi-free-standing graphene energy bands, *Phys. Rev. B* 99 (2019) 035428. doi:10.1103/PhysRevB.99.035428.  
URL <https://link.aps.org/doi/10.1103/PhysRevB.99.035428>
- [96] M. Petrović, I. Š. Rakić, S. Runte, C. Busse, J. T. Sadowski, P. Lazić, I. Pletikosić, Z.-H. Pan, M. Milun, P. Pervan, N. Atodiresei, R. Brako, D. Šokčević, T. Valla, T. Michely, M. Kralj, The mechanism of caesium intercalation of graphene, *Nature Communications* 4 (1) (Nov. 2013). doi:10.1038/ncomms3772.  
URL <https://doi.org/10.1038/ncomms3772>
- [97] M. G. Hell, N. Ehlen, B. V. Senkovskiy, E. H. Hasdeo, A. Fedorov, D. Dombrowski, C. Busse, T. Michely, G. di Santo, L. Petaccia, R. Saito, A. Grüneis, Resonance raman spectrum of doped epitaxial graphene at the lifshitz transition, *Nano Letters* 18 (9) (2018) 6045–6056, pMID: 30157652.  
arXiv:<https://doi.org/10.1021/acs.nanolett.8b02979>,  
doi:10.1021/acs.nanolett.8b02979.  
URL <https://doi.org/10.1021/acs.nanolett.8b02979>

- [98] I. M. Lifshitz, Anomalies of electron characteristics in the high pressure region, *Zhur. Eksptl'. i Teoret. Fiz.*  
URL <https://www.osti.gov/biblio/4173345>
- [99] J. Coraux, A. T. N'Diaye, C. Busse, T. Michely, Structural coherency of graphene on ir(111), *Nano Letters* 8 (2) (2008) 565–570, pMID: 18189442. arXiv:<https://doi.org/10.1021/nl0728874>, doi:10.1021/nl0728874.  
URL <https://doi.org/10.1021/nl0728874>
- [100] E. J. Scheibner, L. H. Germer, C. D. Hartman, Apparatus for direct observation of low-energy electron diffraction patterns, *Review of Scientific Instruments* 31 (2) (1960) 112–114.  
arXiv:<https://doi.org/10.1063/1.1716903>, doi:10.1063/1.1716903.  
URL <https://doi.org/10.1063/1.1716903>
- [101] L. H. Germer, C. D. Hartman, Improved low energy electron diffraction apparatus, *Review of Scientific Instruments* 31 (7) (1960) 784–784. arXiv:<https://doi.org/10.1063/1.1717051>, doi:10.1063/1.1717051.  
URL <https://doi.org/10.1063/1.1717051>
- [102] C. Struzzi, C. S. Praveen, M. Scardamaglia, N. I. Verbitskiy, A. V. Fedorov, M. Weigl, M. Schreck, A. Grüneis, S. Piccinin, S. Fabris, L. Petaccia, Controlled thermodynamics for tunable electron doping of graphene on ir(111), *Phys. Rev. B* 94 (2016) 085427.  
doi:10.1103/PhysRevB.94.085427.  
URL <https://link.aps.org/doi/10.1103/PhysRevB.94.085427>
- [103] S. Schumacher, T. O. Wehling, P. Lazić, S. Runte, D. F. Förster, C. Busse, M. Petrović, M. Kralj, S. Blügel, N. Atodiresei, V. Caciuc, T. Michely, The backside of graphene: Manipulating adsorption by intercalation, *Nano Letters* 13 (11) (2013) 5013–5019.  
arXiv:<https://doi.org/10.1021/nl402797j>, doi:10.1021/nl402797j.  
URL <https://doi.org/10.1021/nl402797j>
- [104] C. Busse, P. Lazić, R. Djemour, J. Coraux, T. Gerber, N. Atodiresei, V. Caciuc, R. Brako, A. T. N'Diaye, S. Blügel, J. Zegenhagen, T. Michely, Graphene on ir(111): Physisorption with chemical modulation, *Phys. Rev. Lett.* 107 (2011) 036101.  
doi:10.1103/PhysRevLett.107.036101.

URL

<https://link.aps.org/doi/10.1103/PhysRevLett.107.036101>

- [105] G. Nicolay, F. Reinert, S. Hüfner, P. Blaha, Spin-orbit splitting of the l-gap surface state on au(111) and ag(111), *Phys. Rev. B* 65 (2001) 033407. doi:10.1103/PhysRevB.65.033407.  
URL <https://link.aps.org/doi/10.1103/PhysRevB.65.033407>
- [106] A. Varykhalov, D. Marchenko, M. R. Scholz, E. D. L. Rienks, T. K. Kim, G. Bihlmayer, J. Sánchez-Barriga, O. Rader, Ir(111) surface state with giant rashba splitting persists under graphene in air, *Phys. Rev. Lett.* 108 (2012) 066804. doi:10.1103/PhysRevLett.108.066804.  
URL <https://link.aps.org/doi/10.1103/PhysRevLett.108.066804>
- [107] G. Kresse, J. Furthmüller, Efficient iterative schemes for ab initio total-energy calculations using a plane-wave basis set, *Phys. Rev. B* 54 (1996) 11169–11186. doi:10.1103/PhysRevB.54.11169.  
URL <https://link.aps.org/doi/10.1103/PhysRevB.54.11169>
- [108] G. Kresse, J. Furthmüller, Efficiency of ab-initio total energy calculations for metals and semiconductors using a plane-wave basis set, *Computational Materials Science* 6 (1) (1996) 15 – 50.  
doi:[https://doi.org/10.1016/0927-0256\(96\)00008-0](https://doi.org/10.1016/0927-0256(96)00008-0).  
URL <http://www.sciencedirect.com/science/article/pii/0927025696000080>
- [109] G. Kresse, D. Joubert, From ultrasoft pseudopotentials to the projector augmented-wave method, *Phys. Rev. B* 59 (1999) 1758–1775. doi:10.1103/PhysRevB.59.1758.  
URL <https://link.aps.org/doi/10.1103/PhysRevB.59.1758>
- [110] S. Grimme, Semiempirical gga-type density functional constructed with a long-range dispersion correction, *Journal of Computational Chemistry* 27 (15) (2006) 1787–1799.  
arXiv:<https://onlinelibrary.wiley.com/doi/pdf/10.1002/jcc.20495>,  
doi:10.1002/jcc.20495.  
URL <https://onlinelibrary.wiley.com/doi/abs/10.1002/jcc.20495>
- [111] A. Damascelli, Z. Hussain, Z.-X. Shen, Angle-resolved photoemission studies of the cuprate superconductors, *Rev. Mod. Phys.* 75 (2003)

473–541. doi:10.1103/RevModPhys.75.473.  
URL <https://link.aps.org/doi/10.1103/RevModPhys.75.473>

- [112] S. Moser, An experimentalist's guide to the matrix element in angle resolved photoemission, *Journal of Electron Spectroscopy and Related Phenomena* 214 (2017) 29 – 52.  
doi:<https://doi.org/10.1016/j.elspec.2016.11.007>.  
URL  
<http://www.sciencedirect.com/science/article/pii/S0368204816301724>
- [113] R. Nandkishore, L. S. Levitov, A. V. Chubukov, Chiral superconductivity from repulsive interactions in doped graphene, *Nature Physics* 8 (2) (2012) 158–163. doi:10.1038/nphys2208.  
URL <https://doi.org/10.1038/nphys2208>
- [114] R. Saito, G. Dresselhaus, M. S. Dresselhaus, *Physical Properties of Carbon Nanotubes*, PUBLISHED BY IMPERIAL COLLEGE PRESS AND DISTRIBUTED BY WORLD SCIENTIFIC PUBLISHING CO., 1998. doi:10.1142/p080.  
URL <https://doi.org/10.1142/p080>
- [115] L. Petaccia, P. Vilmercati, S. Gorovikov, M. Barnaba, A. Bianco, D. Cocco, C. Masciovecchio, A. Goldoni, Bad elph: A 4m normal-incidence monochromator beamline at elettra, *Nuclear Instruments and Methods in Physics Research Section A: Accelerators, Spectrometers, Detectors and Associated Equipment* 606 (2009) 780–784. doi:10.1016/j.nima.2009.05.001.
- [116] N. Ehlen, M. Hell, G. Marini, E. H. Hasdeo, R. Saito, Y. Falke, M. O. Goerbig, G. Di Santo, L. Petaccia, G. Profeta, A. Grüneis, Origin of the flat band in heavily cs-doped graphene, *ACS Nano* 14 (1) (2020) 1055–1069, pMID: 31825586.  
arXiv:<https://doi.org/10.1021/acsnano.9b08622>,  
doi:10.1021/acsnano.9b08622.  
URL <https://doi.org/10.1021/acsnano.9b08622>
- [117] D. Haberer, L. Petaccia, A. V. Fedorov, C. S. Praveen, S. Fabris, S. Piccinin, O. Vilkov, D. V. Vyalikh, A. Preobrajenski, N. I. Verbitskiy, H. Shiozawa, J. Fink, M. Knupfer, B. Büchner, A. Grüneis, Anisotropic eliashberg function and electron-phonon coupling in doped graphene, *Phys. Rev. B* 88 (2013) 081401.

doi:10.1103/PhysRevB.88.081401.

URL <https://link.aps.org/doi/10.1103/PhysRevB.88.081401>

- [118] T. Valla, J. Camacho, Z.-H. Pan, A. V. Fedorov, A. C. Walters, C. A. Howard, M. Ellerby, Anisotropic electron-phonon coupling and dynamical nesting on the graphene sheets in superconducting  $\text{CaC}_6$  using angle-resolved photoemission spectroscopy, *Phys. Rev. Lett.* 102 (2009) 107007. doi:10.1103/PhysRevLett.102.107007.  
URL <https://link.aps.org/doi/10.1103/PhysRevLett.102.107007>
- [119] J. Kleeman, K. Sugawara, T. Sato, T. Takahashi, Anisotropic electron-phonon coupling in rb-intercalated bilayer graphene, *Journal of the Physical Society of Japan* 83 (12) (2014) 124715.  
arXiv:<https://doi.org/10.7566/JPSJ.83.124715>,  
doi:10.7566/JPSJ.83.124715.  
URL <https://doi.org/10.7566/JPSJ.83.124715>
- [120] J. Jiang, Y. Bitla, C.-W. Huang, T. H. Do, H.-J. Liu, Y.-H. Hsieh, C.-H. Ma, C.-Y. Jang, Y.-H. Lai, P.-W. Chiu, W.-W. Wu, Y.-C. Chen, Y.-C. Zhou, Y.-H. Chu, Flexible ferroelectric element based on van der waals heteroepitaxy, *Science Advances* 3 (6) (2017) e1700121.  
doi:10.1126/sciadv.1700121.  
URL <https://doi.org/10.1126/sciadv.1700121>
- [121] A. Devarakonda, H. Inoue, S. Fang, C. Ozsoy-Keskinbora, T. Suzuki, M. Kriener, L. Fu, E. Kaxiras, D. C. Bell, J. G. Checkelsky, Clean 2d superconductivity in a bulk van der waals superlattice, *Science* 370 (6513) (2020) 231–236. doi:10.1126/science.aaz6643.  
URL <https://doi.org/10.1126/science.aaz6643>
- [122] J. A. Miwa, M. Dendzik, S. S. Grønberg, M. Bianchi, J. V. Lauritsen, P. Hofmann, S. Ulstrup, Van der waals epitaxy of two-dimensional  $\text{mos}_2$ -graphene heterostructures in ultrahigh vacuum, *ACS Nano* 9 (6) (2015) 6502–6510, pMID: 26039108.  
arXiv:<https://doi.org/10.1021/acsnano.5b02345>,  
doi:10.1021/acsnano.5b02345.  
URL <https://doi.org/10.1021/acsnano.5b02345>
- [123] M. Annamalai, K. Gopinadhan, S. A. Han, S. Saha, H. J. Park, E. B. Cho, B. Kumar, A. Patra, S.-W. Kim, T. Venkatesan, Surface energy and wettability of van der waals structures, *Nanoscale* 8 (2016)

5764–5770. doi:10.1039/C5NR06705G.  
URL <http://dx.doi.org/10.1039/C5NR06705G>

- [124] Y. J. Shin, Y. Wang, H. Huang, G. Kalon, A. T. S. Wee, Z. Shen, C. S. Bhatia, H. Yang, Surface-energy engineering of graphene, *Langmuir* 26 (6) (2010) 3798–3802, pMID: 20158275.  
arXiv:<https://doi.org/10.1021/la100231u>, doi:10.1021/la100231u.  
URL <https://doi.org/10.1021/la100231u>
- [125] R. Raj, S. C. Maroo, E. N. Wang, Wettability of graphene, *Nano Letters* 13 (4) (2013) 1509–1515, pMID: 23458704.  
arXiv:<https://doi.org/10.1021/nl304647t>, doi:10.1021/nl304647t.  
URL <https://doi.org/10.1021/nl304647t>
- [126] G. Hong, Y. Han, T. M. Schutzius, Y. Wang, Y. Pan, M. Hu, J. Jie, C. S. Sharma, U. Müller, D. Poulikakos, On the mechanism of hydrophilicity of graphene, *Nano Letters* 16 (7) (2016) 4447–4453, pMID: 27248183.  
arXiv:<https://doi.org/10.1021/acs.nanolett.6b01594>,  
doi:10.1021/acs.nanolett.6b01594.  
URL <https://doi.org/10.1021/acs.nanolett.6b01594>
- [127] G. Wiegers, Misfit layer compounds: Structures and physical properties, *Progress in Solid State Chemistry* 24 (1) (1996) 1 – 139.  
doi:[https://doi.org/10.1016/0079-6786\(95\)00007-0](https://doi.org/10.1016/0079-6786(95)00007-0).  
URL  
<http://www.sciencedirect.com/science/article/pii/0079678695000070>
- [128] W. Jolie, J. Lux, M. Pörtner, D. Dombrowski, C. Herbig, T. Knispel, S. Simon, T. Michely, A. Rosch, C. Busse, Suppression of quasiparticle scattering signals in bilayer graphene due to layer polarization and destructive interference, *Phys. Rev. Lett.* 120 (2018) 106801. doi:10.1103/PhysRevLett.120.106801.  
URL  
<https://link.aps.org/doi/10.1103/PhysRevLett.120.106801>
- [129] W. Zhao, P. H. Tan, J. Liu, A. C. Ferrari, Intercalation of few-layer graphite flakes with fecl<sub>3</sub>: Raman determination of fermi level, layer by layer decoupling, and stability, *Journal of the American Chemical Society* 133 (15) (2011) 5941–5946, pMID: 21434632.  
arXiv:<https://doi.org/10.1021/ja110939a>, doi:10.1021/ja110939a.  
URL <https://doi.org/10.1021/ja110939a>

- [130] K. Sugawara, K. Kanetani, T. Sato, T. Takahashi, Fabrication of li-intercalated bilayer graphene, *AIP Advances* 1 (2) (2011) 022103. arXiv:<https://aip.scitation.org/doi/pdf/10.1063/1.3582814>, doi:10.1063/1.3582814. URL <https://aip.scitation.org/doi/abs/10.1063/1.3582814>
- [131] M. Hell, N. Ehlen, G. Marini, Y. Falke, B. V. Senkovskiy, C. Herbig, C. Teichert, W. Jolie, T. Michely, J. Avila, G. D. Santo, D. M. de la Torre, L. Petaccia, G. Profeta, A. Grüneis, Massive and massless charge carriers in an epitaxially strained alkali metal quantum well on graphene, *Nature Communications* 11 (1) (Mar. 2020). doi:10.1038/s41467-020-15130-1. URL <https://doi.org/10.1038/s41467-020-15130-1>
- [132] R. R. Nair, P. Blake, A. N. Grigorenko, K. S. Novoselov, T. J. Booth, T. Stauber, N. M. R. Peres, A. K. Geim, Fine structure constant defines visual transparency of graphene, *Science* 320 (5881) (2008) 1308–1308. arXiv:<https://science.sciencemag.org/content/320/5881/1308.full.pdf>, doi:10.1126/science.1156965. URL <https://science.sciencemag.org/content/320/5881/1308>
- [133] B. Pamuk, J. Baima, F. Mauri, M. Calandra, Magnetic gap opening in rhombohedral-stacked multilayer graphene from first principles, *Phys. Rev. B* 95 (2017) 075422. doi:10.1103/PhysRevB.95.075422. URL <https://link.aps.org/doi/10.1103/PhysRevB.95.075422>
- [134] J. Avila, M. C. Asensio, First nanoarpes user facility available at soleil: An innovative and powerful tool for studying advanced materials, *Synchrotron Radiation News* 27 (2) (2014) 24–30. arXiv:<https://doi.org/10.1080/08940886.2014.889549>, doi:10.1080/08940886.2014.889549. URL <https://doi.org/10.1080/08940886.2014.889549>
- [135] B. OLINGER, J. W. SHANER, Lithium, compression and high-pressure structure, *Science* 219 (4588) (1983) 1071–1072. arXiv:<https://science.sciencemag.org/content/219/4588/1071.full.pdf>, doi:10.1126/science.219.4588.1071. URL <https://science.sciencemag.org/content/219/4588/1071>
- [136] M. Hanfland, I. Loa, K. Syassen, Sodium under pressure: bcc to fcc structural transition and pressure-volume relation to 100 gpa, *Phys.*

- Rev. B 65 (2002) 184109. doi:10.1103/PhysRevB.65.184109.  
 URL <https://link.aps.org/doi/10.1103/PhysRevB.65.184109>
- [137] K. Takemura, K. Syassen, High-pressure phase transitions in potassium and phase relations among heavy alkali metals, Phys. Rev. B 28 (1983) 1193–1196. doi:10.1103/PhysRevB.28.1193.  
 URL <https://link.aps.org/doi/10.1103/PhysRevB.28.1193>
- [138] H. T. Hall, L. Merrill, J. D. Barnett, High pressure polymorphism in cesium, Science 146 (3649) (1964) 1297–1299.  
 arXiv:<https://science.sciencemag.org/content/146/3649/1297.full.pdf>,  
 doi:10.1126/science.146.3649.1297.  
 URL <https://science.sciencemag.org/content/146/3649/1297>
- [139] K. Takemura, K. Syassen, High pressure equation of state of rubidium, Solid State Communications 44 (8) (1982) 1161 – 1164.  
 doi:[https://doi.org/10.1016/0038-1098\(82\)91076-6](https://doi.org/10.1016/0038-1098(82)91076-6).  
 URL  
<http://www.sciencedirect.com/science/article/pii/0038109882910766>
- [140] H. Smith, R. Berliner, J. Jorgensen, Martensitic transformation from bcc to 9r and fcc in metallic lithium, Physica B: Condensed Matter 156-157 (1989) 53 – 55.  
 doi:[https://doi.org/10.1016/0921-4526\(89\)90584-X](https://doi.org/10.1016/0921-4526(89)90584-X).  
 URL  
<http://www.sciencedirect.com/science/article/pii/092145268990584X>
- [141] T. M. Giebultowicz, A. W. Overhauser, S. A. Werner, Direct observation of the charge-density wave in potassium by neutron diffraction, Phys. Rev. Lett. 56 (1986) 1485–1488.  
 doi:10.1103/PhysRevLett.56.1485.  
 URL <https://link.aps.org/doi/10.1103/PhysRevLett.56.1485>
- [142] I. M. Templeton, Observation of a martensitic transformation in rubidium?, Journal of Physics F: Metal Physics 12 (8) (1982) L121–L122. doi:10.1088/0305-4608/12/8/001.  
 URL <https://doi.org/10.1088/0305-4608/12/8/001>
- [143] M. S. Anderson, C. A. Swenson, Experimental equations of state for cesium and lithium metals to 20 kbar and the high-pressure behavior of the alkali metals, Phys. Rev. B 31 (1985) 668–680.  
 doi:10.1103/PhysRevB.31.668.  
 URL <https://link.aps.org/doi/10.1103/PhysRevB.31.668>

- [144] C. A. Swenson, Compression of the alkali metals to 10 000 atmospheres at low temperature, *Phys. Rev.* 99 (1955) 423–430.  
doi:10.1103/PhysRev.99.423.  
URL <https://link.aps.org/doi/10.1103/PhysRev.99.423>
- [145] M. I. McMahon, R. J. Nelmes, S. Rekhi, Complex crystal structure of cesium-iii, *Phys. Rev. Lett.* 87 (2001) 255502.  
doi:10.1103/PhysRevLett.87.255502.  
URL <https://link.aps.org/doi/10.1103/PhysRevLett.87.255502>
- [146] J. Delattre, J. Badding, Rietveld refinement of the crystal structure of cs(iv), ad-electron metal, *Journal of Solid State Chemistry* 144 (1) (1999) 16 – 19. doi:<https://doi.org/10.1006/jssc.1998.8029>.  
URL  
<http://www.sciencedirect.com/science/article/pii/S002245969898029X>
- [147] U. Schwarz, K. Takemura, M. Hanfland, K. Syassen, Crystal structure of cesium-v, *Phys. Rev. Lett.* 81 (1998) 2711–2714.  
doi:10.1103/PhysRevLett.81.2711.  
URL <https://link.aps.org/doi/10.1103/PhysRevLett.81.2711>
- [148] J. Xie, S. P. Chen, J. S. Tse, D. D. Klug, Z. Li, K. Uehara, L. G. Wang, Phonon instabilities in high-pressure bcc-fcc and the isostructural fcc-fcc phase transitions of cs, *Phys. Rev. B* 62 (2000) 3624–3629. doi:10.1103/PhysRevB.62.3624.  
URL <https://link.aps.org/doi/10.1103/PhysRevB.62.3624>
- [149] M. Sigalas, N. C. Bacalis, D. A. Papaconstantopoulos, M. J. Mehl, A. C. Switendick, Total-energy calculations of solid h, li, na, k, rb, and cs, *Phys. Rev. B* 42 (1990) 11637–11643.  
doi:10.1103/PhysRevB.42.11637.  
URL <https://link.aps.org/doi/10.1103/PhysRevB.42.11637>
- [150] Y. Xie, Y. M. Ma, T. Cui, Y. Li, J. Qiu, G. T. Zou, Origin of bcc to fcc phase transition under pressure in alkali metals, *New Journal of Physics* 10 (6) (2008) 063022. doi:10.1088/1367-2630/10/6/063022.  
URL <https://doi.org/10.1088/1367-2630/10/6/063022>
- [151] H. L. Skriver, Crystal structure from one-electron theory, *Phys. Rev. B* 31 (1985) 1909–1923. doi:10.1103/PhysRevB.31.1909.  
URL <https://link.aps.org/doi/10.1103/PhysRevB.31.1909>

- [152] N. M. Caffrey, L. I. Johansson, C. Xia, R. Armiento, I. A. Abrikosov, C. Jacobi, Structural and electronic properties of li-intercalated graphene on sic(0001), *Phys. Rev. B* 93 (2016) 195421. doi:10.1103/PhysRevB.93.195421. URL <https://link.aps.org/doi/10.1103/PhysRevB.93.195421>
- [153] K. T. Chan, J. B. Neaton, M. L. Cohen, First-principles study of metal adatom adsorption on graphene, *Phys. Rev. B* 77 (2008) 235430. doi:10.1103/PhysRevB.77.235430. URL <https://link.aps.org/doi/10.1103/PhysRevB.77.235430>
- [154] J. Liu, Q. Li, Y. Zou, Q. Qian, Y. Jin, G. Li, K. Jiang, S. Fan, The dependence of graphene raman d-band on carrier density, *Nano Letters* 13 (12) (2013) 6170–6175, pMID: 24283411. arXiv:<https://doi.org/10.1021/nl4035048>, doi:10.1021/nl4035048. URL <https://doi.org/10.1021/nl4035048>
- [155] K.-H. Jin, S.-M. Choi, S.-H. Jhi, Crossover in the adsorption properties of alkali metals on graphene, *Phys. Rev. B* 82 (2010) 033414. doi:10.1103/PhysRevB.82.033414. URL <https://link.aps.org/doi/10.1103/PhysRevB.82.033414>
- [156] L. Vitos, A. Ruban, H. Skriver, J. Kollár, The surface energy of metals, *Surface Science* 411 (1) (1998) 186 – 202. doi:[https://doi.org/10.1016/S0039-6028\(98\)00363-X](https://doi.org/10.1016/S0039-6028(98)00363-X). URL <http://www.sciencedirect.com/science/article/pii/S003960289800363X>
- [157] W. Tyson, W. Miller, Surface free energies of solid metals: Estimation from liquid surface tension measurements, *Surface Science* 62 (1) (1977) 267 – 276. doi:[https://doi.org/10.1016/0039-6028\(77\)90442-3](https://doi.org/10.1016/0039-6028(77)90442-3). URL <http://www.sciencedirect.com/science/article/pii/0039602877904423>
- [158] R. Tran, Z. Xu, B. Radhakrishnan, D. Winston, W. Sun, K. A. Persson, S. P. Ong, Surface energies of elemental crystals, *Scientific Data* 3 (1) (Sep. 2016). doi:10.1038/sdata.2016.80. URL <https://doi.org/10.1038/sdata.2016.80>
- [159] P. E. Blöchl, Projector augmented-wave method, *Phys. Rev. B* 50 (1994) 17953–17979. doi:10.1103/PhysRevB.50.17953. URL <https://link.aps.org/doi/10.1103/PhysRevB.50.17953>

- [160] J. P. Perdew, K. Burke, M. Ernzerhof, Generalized gradient approximation made simple, *Phys. Rev. Lett.* 77 (1996) 3865–3868. doi:10.1103/PhysRevLett.77.3865. URL <https://link.aps.org/doi/10.1103/PhysRevLett.77.3865>
- [161] H. J. Monkhorst, J. D. Pack, Special points for brillouin-zone integrations, *Phys. Rev. B* 13 (1976) 5188–5192. doi:10.1103/PhysRevB.13.5188. URL <https://link.aps.org/doi/10.1103/PhysRevB.13.5188>
- [162] H. Starnberg, H. Brauer, V. Strocov, Low temperature adsorption of Cs on layered TiS<sub>2</sub> studied by photoelectron spectroscopy, *Surface Science* 384 (1) (1997) L785 – L790. doi:[https://doi.org/10.1016/S0039-6028\(97\)00125-8](https://doi.org/10.1016/S0039-6028(97)00125-8). URL <http://www.sciencedirect.com/science/article/pii/S0039602897001258>
- [163] C. Murray, W. Jolie, J. A. Fischer, J. Hall, C. van Efferen, N. Ehlen, A. Grüneis, C. Busse, T. Michely, Comprehensive tunneling spectroscopy of quasifreestanding MoS<sub>2</sub> on graphene on Ir(111), *Phys. Rev. B* 99 (2019) 115434. doi:10.1103/PhysRevB.99.115434. URL <https://link.aps.org/doi/10.1103/PhysRevB.99.115434>
- [164] R. I. Woodward, R. T. Murray, C. F. Phelan, R. E. P. de Oliveira, T. H. Runcorn, E. J. R. Kelleher, S. Li, E. C. de Oliveira, G. J. M. Fechine, G. Eda, C. J. S. de Matos, Characterization of the second- and third-order nonlinear optical susceptibilities of monolayer MoS<sub>2</sub> using multiphoton microscopy, *2D Materials* 4 (1) (2016) 011006. doi:10.1088/2053-1583/4/1/011006. URL <https://doi.org/10.1088/2053-1583/4/1/011006>
- [165] S. Carlesi, A. Franchini, V. Bortolani, S. Martinelli, Cesium under pressure: First-principles calculation of the bcc-to-fcc phase transition, *Phys. Rev. B* 59 (1999) 11716–11719. doi:10.1103/PhysRevB.59.11716. URL <https://link.aps.org/doi/10.1103/PhysRevB.59.11716>
- [166] W. Martin, W. Freyland, P. Lamparter, S. Steeb, Structure and density of gold-cesium-melts. ii. neutron diffraction with molten gold-cesium-alloys, *Physics and Chemistry of Liquids* 10 (1) (1980) 61–76. arXiv:<https://doi.org/10.1080/00319108008078457>,

doi:10.1080/00319108008078457.

URL <https://doi.org/10.1080/00319108008078457>

- [167] L. Wang, I. Gutiérrez-Lezama, C. Barreteau, N. Ubrig, E. Giannini, A. F. Morpurgo, Tuning magnetotransport in a compensated semimetal at the atomic scale, *Nature Communications* 6 (1) (Nov. 2015). doi:10.1038/ncomms9892.  
URL <https://doi.org/10.1038/ncomms9892>
- [168] F. Zheng, X.-B. Li, P. Tan, Y. Lin, L. Xiong, X. Chen, J. Feng, Emergent superconductivity in two-dimensional  $\text{NiTe}_2$  crystals, *Phys. Rev. B* 101 (2020) 100505. doi:10.1103/PhysRevB.101.100505.  
URL <https://link.aps.org/doi/10.1103/PhysRevB.101.100505>
- [169] P. M. Coelho, K. Nguyen Cong, M. Bonilla, S. Kolekar, M.-H. Phan, J. Avila, M. C. Asensio, I. I. Oleynik, M. Batzill, Charge density wave state suppresses ferromagnetic ordering in  $\text{VSe}_2$  monolayers, *The Journal of Physical Chemistry C* 123 (22) (2019) 14089–14096.  
arXiv:<https://doi.org/10.1021/acs.jpcc.9b04281>,  
doi:10.1021/acs.jpcc.9b04281.  
URL <https://doi.org/10.1021/acs.jpcc.9b04281>
- [170] M. Bonilla, S. Kolekar, Y. Ma, H. C. Diaz, V. Kalappattil, R. Das, T. Eggers, H. R. Gutierrez, M.-H. Phan, M. Batzill, Strong room-temperature ferromagnetism in  $\text{VSe}_2$  monolayers on van der waals substrates, *Nature Nanotechnology* 13 (4) (2018) 289–293.  
doi:10.1038/s41565-018-0063-9.  
URL <https://doi.org/10.1038/s41565-018-0063-9>
- [171] Y. Wu, D. Mou, N. H. Jo, K. Sun, L. Huang, S. L. Bud'ko, P. C. Canfield, A. Kaminski, Observation of fermi arcs in the type-II weyl semimetal candidate  $\text{WTe}_2$ , *Phys. Rev. B* 94 (2016) 121113.  
doi:10.1103/PhysRevB.94.121113.  
URL <https://link.aps.org/doi/10.1103/PhysRevB.94.121113>
- [172] K. Deng, G. Wan, P. Deng, K. Zhang, S. Ding, E. Wang, M. Yan, H. Huang, H. Zhang, Z. Xu, J. Denlinger, A. Fedorov, H. Yang, W. Duan, H. Yao, Y. Wu, S. Fan, H. Zhang, X. Chen, S. Zhou, Experimental observation of topological fermi arcs in type-II weyl semimetal  $\text{MoTe}_2$ , *Nature Physics* 12 (12) (2016) 1105–1110.  
doi:10.1038/nphys3871.  
URL <https://doi.org/10.1038/nphys3871>

- [173] A. Sirohi, S. Das, P. Adhikary, R. R. Chowdhury, A. Vashist, Y. Singh, S. Gayen, T. Das, G. Sheet, Mixed type i and type II superconductivity due to intrinsic electronic inhomogeneities in the type II dirac semimetal PdTe<sub>2</sub>, *Journal of Physics: Condensed Matter* 31 (8) (2019) 085701. doi:10.1088/1361-648x/aaf49c. URL <https://doi.org/10.1088/2F1361-648x/2Faaf49c>
- [174] M. Yan, H. Huang, K. Zhang, E. Wang, W. Yao, K. Deng, G. Wan, H. Zhang, M. Arita, H. Yang, Z. Sun, H. Yao, Y. Wu, S. Fan, W. Duan, S. Zhou, Lorentz-violating type-II dirac fermions in transition metal dichalcogenide PtTe<sub>2</sub>, *Nature Communications* 8 (1) (Aug. 2017). doi:10.1038/s41467-017-00280-6. URL <https://doi.org/10.1038/s41467-017-00280-6>
- [175] K. Zhang, M. Yan, H. Zhang, H. Huang, M. Arita, Z. Sun, W. Duan, Y. Wu, S. Zhou, Experimental evidence for type-ii dirac semimetal in ptse<sub>2</sub>, *Phys. Rev. B* 96 (2017) 125102. doi:10.1103/PhysRevB.96.125102. URL <https://link.aps.org/doi/10.1103/PhysRevB.96.125102>
- [176] Z. Huang, W. Zhang, W. Zhang, Computational search for two-dimensional MX<sub>2</sub> semiconductors with possible high electron mobility at room temperature, *Materials* 9 (9) (2016) 716. doi:10.3390/ma9090716. URL <https://doi.org/10.3390/ma9090716>
- [177] W. Zheng, R. Schönemann, N. Aryal, Q. Zhou, D. Rhodes, Y.-C. Chiu, K.-W. Chen, E. Kampert, T. Förster, T. J. Martin, G. T. McCandless, J. Y. Chan, E. Manousakis, L. Balicas, Detailed study of the fermi surfaces of the type-ii dirac semimetallic candidates  $xte_2$  ( $x=$ pd, pt), *Phys. Rev. B* 97 (2018) 235154. doi:10.1103/PhysRevB.97.235154. URL <https://link.aps.org/doi/10.1103/PhysRevB.97.235154>
- [178] C. Xu, B. Li, W. Jiao, W. Zhou, B. Qian, R. Sankar, N. D. Zhigadlo, Y. Qi, D. Qian, F.-C. Chou, X. Xu, Topological type-ii dirac fermions approaching the fermi level in a transition metal dichalcogenide nite<sub>2</sub>, *Chemistry of Materials* 30 (14) (2018) 4823–4830. arXiv:<https://doi.org/10.1021/acs.chemmater.8b02132>, doi:10.1021/acs.chemmater.8b02132. URL <https://doi.org/10.1021/acs.chemmater.8b02132>

- [179] B. Ghosh, D. Mondal, C.-N. Kuo, C. S. Lue, J. Nayak, J. Fujii, I. Vobornik, A. Politano, A. Agarwal, Observation of bulk states and spin-polarized topological surface states in transition metal dichalcogenide dirac semimetal candidate nite<sub>2</sub>, *Phys. Rev. B* 100 (2019) 195134. doi:10.1103/PhysRevB.100.195134.  
URL <https://link.aps.org/doi/10.1103/PhysRevB.100.195134>
- [180] B. de Lima, R. de Cassia, F. Santos, L. Correa, T. Grant, A. Manesco, G. Martins, L. Eleno, M. Torikachvili, A. Machado, Properties and superconductivity in ti-doped nite<sub>2</sub> single crystals, *Solid State Communications* 283 (2018) 27 – 31.  
doi:<https://doi.org/10.1016/j.ssc.2018.08.014>.  
URL  
<http://www.sciencedirect.com/science/article/pii/S0038109818306112>
- [181] T. Li, K. Wang, C. Xu, Q. Hou, H. Wu, J.-Y. Ge, S. Cao, J. Zhang, W. Ren, X. Xu, N.-C. Yeh, B. Chen, Z. Feng, Pressure-induced superconductivity in topological type ii dirac semimetal nite<sub>2</sub> (2019). arXiv:1911.07173.
- [182] M. Qi, C. An, Y. Zhou, H. Wu, B. Zhang, C. Chen, Y. Yuan, S. Wang, Y. Zhou, X. Chen, R. Zhang, Z. Yang, Pressure-driven lifshitz transition in type-ii dirac semimetal nite<sub>2</sub>, *Phys. Rev. B* 101 (2020) 115124. doi:10.1103/PhysRevB.101.115124.  
URL <https://link.aps.org/doi/10.1103/PhysRevB.101.115124>
- [183] T. Bither, C. Prewitt, J. Gillson, P. Bierstedt, R. Flippen, H. Young, New transition metal dichalcogenides formed at high pressure, *Solid State Communications* 4 (10) (1966) 533 – 535.  
doi:[https://doi.org/10.1016/0038-1098\(66\)90419-4](https://doi.org/10.1016/0038-1098(66)90419-4).  
URL  
<http://www.sciencedirect.com/science/article/pii/0038109866904194>
- [184] P. Giannozzi, S. Baroni, N. Bonini, M. Calandra, R. Car, C. Cavazzoni, D. Ceresoli, G. L. Chiarotti, M. Cococcioni, I. Dabo, A. D. Corso, S. de Gironcoli, S. Fabris, G. Fratesi, R. Gebauer, U. Gerstmann, C. Gougoussis, A. Kokalj, M. Lazzeri, L. Martin-Samos, N. Marzari, F. Mauri, R. Mazzarello, S. Paolini, A. Pasquarello, L. Paulatto, C. Sbraccia, S. Scandolo, G. Sclauzero, A. P. Seitsonen, A. Smogunov, P. Umari, R. M. Wentzcovitch, QUANTUM ESPRESSO: a modular and open-source software project for quantum simulations of materials, *Journal of Physics:*

Condensed Matter 21 (39) (2009) 395502.  
doi:10.1088/0953-8984/21/39/395502.  
URL <https://doi.org/10.1088/0953-8984/21/39/395502>

- [185] P. Giannozzi, O. Andreussi, T. Brumme, O. Bunau, M. B. Nardelli, M. Calandra, R. Car, C. Cavazzoni, D. Ceresoli, M. Cococcioni, N. Colonna, I. Carnimeo, A. D. Corso, S. de Gironcoli, P. Delugas, R. A. DiStasio, A. Ferretti, A. Floris, G. Fratesi, G. Fugallo, R. Gebauer, U. Gerstmann, F. Giustino, T. Gorni, J. Jia, M. Kawamura, H.-Y. Ko, A. Kokalj, E. Küçükbenli, M. Lazzeri, M. Marsili, N. Marzari, F. Mauri, N. L. Nguyen, H.-V. Nguyen, A. O. de-la Roza, L. Paulatto, S. Poncé, D. Rocca, R. Sabatini, B. Santra, M. Schlipf, A. P. Seitsonen, A. Smogunov, I. Timrov, T. Thonhauser, P. Umari, N. Vast, X. Wu, S. Baroni, Advanced capabilities for materials modelling with quantum ESPRESSO, *Journal of Physics: Condensed Matter* 29 (46) (2017) 465901.  
doi:10.1088/1361-648x/aa8f79.  
URL <https://doi.org/10.1088/1361-648x/aa8f79>
- [186] J. P. Perdew, K. Burke, M. Ernzerhof, Generalized gradient approximation made simple, *Physical Review Letters* 77 (18) (1996) 3865–3868. doi:10.1103/physrevlett.77.3865.  
URL <https://doi.org/10.1103/physrevlett.77.3865>
- [187] H. J. Monkhorst, J. D. Pack, Special points for brillouin-zone integrations, *Physical Review B* 13 (12) (1976) 5188–5192.  
doi:10.1103/physrevb.13.5188.  
URL <https://doi.org/10.1103/physrevb.13.5188>
- [188] S. Baroni, P. Giannozzi, A. Testa, Green’s-function approach to linear response in solids, *Phys. Rev. Lett.* 58 (1987) 1861–1864.  
doi:10.1103/PhysRevLett.58.1861.  
URL <https://link.aps.org/doi/10.1103/PhysRevLett.58.1861>
- [189] S. Poncé, E. Margine, C. Verdi, F. Giustino, Epw: Electron–phonon coupling, transport and superconducting properties using maximally localized wannier functions, *Computer Physics Communications* 209 (2016) 116 – 133. doi:<https://doi.org/10.1016/j.cpc.2016.07.028>.  
URL  
<http://www.sciencedirect.com/science/article/pii/S0010465516302260>

- [190] P. B. Allen, R. C. Dynes, Transition temperature of strong-coupled superconductors reanalyzed, *Physical Review B* 12 (3) (1975) 905–922. doi:10.1103/physrevb.12.905.  
URL <https://doi.org/10.1103/physrevb.12.905>
- [191] G.-X. Zhang, A. M. Reilly, A. Tkatchenko, M. Scheffler, Performance of various density-functional approximations for cohesive properties of 64 bulk solids, *New Journal of Physics* 20 (6) (2018) 063020. doi:10.1088/1367-2630/aac7f0.  
URL <https://doi.org/10.1088/2F1367-2630/2Faac7f0>
- [192] G. Grüner, The dynamics of charge-density waves, *Rev. Mod. Phys.* 60 (1988) 1129–1181. doi:10.1103/RevModPhys.60.1129.  
URL <https://link.aps.org/doi/10.1103/RevModPhys.60.1129>
- [193] H. J. Keller (Ed.), *Low-Dimensional Cooperative Phenomena*, Springer US, 1975. doi:10.1007/978-1-4899-7031-2.  
URL <https://doi.org/10.1007/978-1-4899-7031-2>
- [194] P. Anderson, P. Lee, M. Saitoh, Remarks on giant conductivity in ttf-tenq, *Solid State Communications* 13 (5) (1973) 595 – 598. doi:[https://doi.org/10.1016/S0038-1098\(73\)80020-1](https://doi.org/10.1016/S0038-1098(73)80020-1).  
URL <http://www.sciencedirect.com/science/article/pii/S0038109873800201>
- [195] T. Wu, H. Mayaffre, S. Krämer, M. Horvatić, C. Berthier, W. N. Hardy, R. Liang, D. A. Bonn, M.-H. Julien, Magnetic-field-induced charge-stripe order in the high-temperature superconductor YBa<sub>2</sub>Cu<sub>3</sub>O<sub>7</sub>, *Nature* 477 (7363) (2011) 191–194. doi:10.1038/nature10345.  
URL <https://doi.org/10.1038/nature10345>
- [196] W. L. McMillan, Landau theory of charge-density waves in transition-metal dichalcogenides, *Phys. Rev. B* 12 (1975) 1187–1196. doi:10.1103/PhysRevB.12.1187.  
URL <https://link.aps.org/doi/10.1103/PhysRevB.12.1187>
- [197] M.-H. Whangbo, *Structural phase transitions in layered transition metal compounds: (physics and chemistry of materials with low dimensional structures, series a: Layered structures)*. edited by k. motizuki. reidel (kulwer), dordrecht, 1986., *Journal of Solid State Chemistry* 71 (2) (1987) 591.

doi:[https://doi.org/10.1016/0022-4596\(87\)90274-X](https://doi.org/10.1016/0022-4596(87)90274-X).

URL

<http://www.sciencedirect.com/science/article/pii/002245968790274X>

- [198] J. A. Wilson, F. J. Di Salvo, S. Mahajan, Charge-density waves in metallic, layered, transition-metal dichalcogenides, *Phys. Rev. Lett.* 32 (1974) 882–885. doi:10.1103/PhysRevLett.32.882.  
URL <https://link.aps.org/doi/10.1103/PhysRevLett.32.882>
- [199] B. Loret, N. Auvray, Y. Gallais, M. Cazayous, A. Forget, D. Colson, M.-H. Julien, I. Paul, M. Civelli, A. Sacuto, Intimate link between charge density wave, pseudogap and superconducting energy scales in cuprates, *Nature Physics* 15 (8) (2019) 771–775.  
doi:10.1038/s41567-019-0509-5.  
URL <https://doi.org/10.1038/s41567-019-0509-5>
- [200] S. W. D’Souza, A. Rai, J. Nayak, M. Maniraj, R. S. Dhaka, S. R. Barman, D. L. Schlagel, T. A. Lograsso, A. Chakrabarti, Coexistence of charge-density wave and ferromagnetism in  $\text{Ni}_2\text{MnGa}$ , *Phys. Rev. B* 85 (2012) 085123. doi:10.1103/PhysRevB.85.085123.  
URL <https://link.aps.org/doi/10.1103/PhysRevB.85.085123>
- [201] M. D. Johannes, I. I. Mazin, Fermi surface nesting and the origin of charge density waves in metals, *Phys. Rev. B* 77 (2008) 165135.  
doi:10.1103/PhysRevB.77.165135.  
URL <https://link.aps.org/doi/10.1103/PhysRevB.77.165135>
- [202] S. K. Chan, V. Heine, Spin density wave and soft phonon mode from nesting fermi surfaces, *Journal of Physics F: Metal Physics* 3 (4) (1973) 795–809. doi:10.1088/0305-4608/3/4/022.  
URL <https://doi.org/10.1088/0305-4608/3/4/022>
- [203] A. H. Castro Neto, Charge density wave, superconductivity, and anomalous metallic behavior in 2d transition metal dichalcogenides, *Phys. Rev. Lett.* 86 (2001) 4382–4385.  
doi:10.1103/PhysRevLett.86.4382.  
URL <https://link.aps.org/doi/10.1103/PhysRevLett.86.4382>
- [204] K. Tsutsumi, X-ray-diffraction study of the periodic lattice distortion associated with a charge-density wave in  $1\text{-T-VSe}_2$ , *Phys. Rev. B* 26 (1982) 5756–5759. doi:10.1103/PhysRevB.26.5756.  
URL <https://link.aps.org/doi/10.1103/PhysRevB.26.5756>

- [205] W. Jolie, T. Knispel, N. Ehlen, K. Nikonov, C. Busse, A. Grüneis, T. Michely, Charge density wave phase of  $v\text{Se}_2$  revisited, *Phys. Rev. B* 99 (2019) 115417. doi:10.1103/PhysRevB.99.115417.  
URL <https://link.aps.org/doi/10.1103/PhysRevB.99.115417>
- [206] F. J. DiSalvo, J. V. Waszczak, Magnetic studies of  $v\text{Se}_2$ , *Phys. Rev. B* 23 (1981) 457–461. doi:10.1103/PhysRevB.23.457.  
URL <https://link.aps.org/doi/10.1103/PhysRevB.23.457>
- [207] D. J. Eaglesham, R. L. Withers, D. M. Bird, Charge-density-wave transitions in  $1t\text{-VSe}_2$ , *Journal of Physics C: Solid State Physics* 19 (3) (1986) 359–367. doi:10.1088/0022-3719/19/3/006.  
URL <https://doi.org/10.1088/2F0022-3719/2F19/2F3/2F006>
- [208] S. Sahoo, U. Dutta, L. Harnagea, A. K. Sood, S. Karmakar, Pressure-induced suppression of charge density wave and emergence of superconductivity in  $1t - v\text{Se}_2$ , *Phys. Rev. B* 101 (2020) 014514. doi:10.1103/PhysRevB.101.014514.  
URL <https://link.aps.org/doi/10.1103/PhysRevB.101.014514>
- [209] K. Terashima, T. Sato, H. Komatsu, T. Takahashi, N. Maeda, K. Hayashi, Charge-density wave transition of  $1t - v\text{Se}_2$  studied by angle-resolved photoemission spectroscopy, *Phys. Rev. B* 68 (2003) 155108. doi:10.1103/PhysRevB.68.155108.  
URL <https://link.aps.org/doi/10.1103/PhysRevB.68.155108>
- [210] V. N. Strocov, M. Shi, M. Kobayashi, C. Monney, X. Wang, J. Krempasky, T. Schmitt, L. Patthey, H. Berger, P. Blaha, Three-dimensional electron realm in  $v\text{Se}_2$  by soft-x-ray photoelectron spectroscopy: Origin of charge-density waves, *Phys. Rev. Lett.* 109 (2012) 086401. doi:10.1103/PhysRevLett.109.086401.  
URL <https://link.aps.org/doi/10.1103/PhysRevLett.109.086401>
- [211] P. Chen, W. W. Pai, Y.-H. Chan, V. Madhavan, M. Y. Chou, S.-K. Mo, A.-V. Fedorov, T.-C. Chiang, Unique gap structure and symmetry of the charge density wave in single-layer  $v\text{Se}_2$ , *Phys. Rev. Lett.* 121 (2018) 196402. doi:10.1103/PhysRevLett.121.196402.  
URL <https://link.aps.org/doi/10.1103/PhysRevLett.121.196402>
- [212] A. O. Fumega, M. Gobbi, P. Dreher, W. Wan, C. González-Orellana, M. Peña-Díaz, C. Rogero, J. Herrero-Martín, P. Gargiani, M. Ilyn,

- M. M. Ugeda, V. Pardo, S. Blanco-Canosa, Absence of ferromagnetism in vse2 caused by its charge density wave phase, *The Journal of Physical Chemistry C* 123 (45) (2019) 27802–27810.  
arXiv:<https://doi.org/10.1021/acs.jpcc.9b08868>,  
doi:10.1021/acs.jpcc.9b08868.  
URL <https://doi.org/10.1021/acs.jpcc.9b08868>
- [213] P. K. J. Wong, W. Zhang, F. Bussolotti, X. Yin, T. S. Heng, L. Zhang, Y. L. Huang, G. Vinai, S. Krishnamurthi, D. W. Bukhvalov, Y. J. Zheng, R. Chua, A. T. N'Diaye, S. A. Morton, C.-Y. Yang, K.-H. Ou Yang, P. Torelli, W. Chen, K. E. J. Goh, J. Ding, M.-T. Lin, G. Brocks, M. P. de Jong, A. H. Castro Neto, A. T. S. Wee, Evidence of spin frustration in a vanadium diselenide monolayer magnet, *Advanced Materials* 31 (23) (2019) 1901185.  
arXiv:<https://onlinelibrary.wiley.com/doi/pdf/10.1002/adma.201901185>,  
doi:10.1002/adma.201901185.  
URL  
<https://onlinelibrary.wiley.com/doi/abs/10.1002/adma.201901185>
- [214] W. Yu, J. Li, T. S. Heng, Z. Wang, X. Zhao, X. Chi, W. Fu, I. Abdelwahab, J. Zhou, J. Dan, Z. Chen, Z. Li, J. Lu, S. J. Pennycook, Y. P. Feng, J. Ding, K. P. Loh, Chemically exfoliated vse2 monolayers with room-temperature ferromagnetism, *Advanced Materials* 31 (40) (2019) 1903779.  
arXiv:<https://onlinelibrary.wiley.com/doi/pdf/10.1002/adma.201903779>,  
doi:10.1002/adma.201903779.  
URL  
<https://onlinelibrary.wiley.com/doi/abs/10.1002/adma.201903779>
- [215] W. Zhang, L. Zhang, P. K. J. Wong, J. Yuan, G. Vinai, P. Torelli, G. van der Laan, Y. P. Feng, A. T. S. Wee, Magnetic transition in monolayer vse2 via interface hybridization, *ACS Nano* 13 (8) (2019) 8997–9004, pMID: 31306576.  
arXiv:<https://doi.org/10.1021/acs.nano.9b02996>,  
doi:10.1021/acs.nano.9b02996.  
URL <https://doi.org/10.1021/acs.nano.9b02996>
- [216] Y. Ma, Y. Dai, M. Guo, C. Niu, Y. Zhu, B. Huang, Evidence of the existence of magnetism in pristine VX2 monolayers (x = s, se) and their strain-induced tunable magnetic properties, *ACS Nano* 6 (2)

- (2012) 1695–1701. doi:10.1021/nn204667z.  
 URL <https://doi.org/10.1021/nn204667z>
- [217] J. He, Q. Xie, G. Xu, Confinement effect enhanced stoner ferromagnetic instability in monolayer 1t-vse2 (2020).  
 arXiv:2008.09562.
- [218] T. Yilmaz, X. Tong, Z. Dai, J. T. Sadowski, E. F. Schwier, K. Shimada, S. Hwang, K. Kisslinger, K. Kaznatcheev, E. Vescovo, B. Sinkovic, Emergent of the flat band and superstructures in the vse2 / bi2se3 system (2020). arXiv:2006.13447.
- [219] J. G. Si, W. J. Lu, H. Y. Wu, H. Y. Lv, X. Liang, Q. J. Li, Y. P. Sun, Origin of the multiple charge density wave order in 1t – vse<sub>2</sub>, Phys. Rev. B 101 (2020) 235405. doi:10.1103/PhysRevB.101.235405.  
 URL <https://link.aps.org/doi/10.1103/PhysRevB.101.235405>
- [220] P. V. C. Medeiros, S. Stafström, J. Björk, Effects of extrinsic and intrinsic perturbations on the electronic structure of graphene: Retaining an effective primitive cell band structure by band unfolding, Phys. Rev. B 89 (2014) 041407.  
 doi:10.1103/PhysRevB.89.041407.  
 URL <https://link.aps.org/doi/10.1103/PhysRevB.89.041407>
- [221] G. GROSSO, G. P. PARRAVICINI, Geometrical description of crystals: direct and reciprocal lattices, in: Solid State Physics, Elsevier, 2000, pp. 37–76. doi:10.1016/b978-012304460-0/50002-5.  
 URL <https://doi.org/10.1016/b978-012304460-0/50002-5>
- [222] A. M. Woolley, G. Wexler, Band structures and fermi surfaces for 1t-TaS<sub>2</sub>, 1t-TaSe<sub>2</sub> and 1t-VSe<sub>2</sub>, Journal of Physics C: Solid State Physics 10 (14) (1977) 2601–2616. doi:10.1088/0022-3719/10/14/013.  
 URL <https://doi.org/10.1088/2F0022-3719/2F10/2F14/2F013>
- [223] H. W. Myron, The electronic structure of the vanadium dichalcogenides, Physica B+C 99 (1) (1980) 243–249.  
 doi:10.1016/0378-4363(80)90239-9.
- [224] A. Zunger, A. J. Freeman, Electronic structure of 1t-vse<sub>2</sub>, Phys. Rev. B 19 (1979) 6001–6009. doi:10.1103/PhysRevB.19.6001.  
 URL <https://link.aps.org/doi/10.1103/PhysRevB.19.6001>

- [225] M. D. Johannes, I. I. Mazin, C. A. Howells, Fermi-surface nesting and the origin of the charge-density wave in NbSe<sub>2</sub>, Phys. Rev. B 73 (2006) 205102. doi:10.1103/PhysRevB.73.205102.  
URL <https://link.aps.org/doi/10.1103/PhysRevB.73.205102>
- [226] D. Zhang, J. Ha, H. Baek, Y.-H. Chan, F. D. Natterer, A. F. Myers, J. D. Schumacher, W. G. Cullen, A. V. Davydov, Y. Kuk, M. Y. Chou, N. B. Zhitenev, J. A. Stroscio, Strain engineering a  $4a \times \sqrt{3}a$  charge-density-wave phase in transition-metal dichalcogenide 1T-VSe<sub>2</sub>, Phys. Rev. Materials 1 (2017) 024005. doi:10.1103/PhysRevMaterials.1.024005.  
URL <https://link.aps.org/doi/10.1103/PhysRevMaterials.1.024005>
- [227] T. B. Boykin, G. Klimeck, Practical application of zone-folding concepts in tight-binding calculations, Phys. Rev. B 71 (2005) 115215. doi:10.1103/PhysRevB.71.115215.  
URL <https://link.aps.org/doi/10.1103/PhysRevB.71.115215>
- [228] T. B. Boykin, N. Kharche, G. Klimeck, M. Korkusinski, Approximate bandstructures of semiconductor alloys from tight-binding supercell calculations, Journal of Physics: Condensed Matter 19 (3) (2007) 036203. doi:10.1088/0953-8984/19/3/036203.  
URL <https://doi.org/10.1088/0953-8984/19/3/036203>
- [229] V. Popescu, A. Zunger, Extracting  $e$  versus  $\mathbf{k}$  effective band structure from supercell calculations on alloys and impurities, Phys. Rev. B 85 (2012) 085201. doi:10.1103/PhysRevB.85.085201.  
URL <https://link.aps.org/doi/10.1103/PhysRevB.85.085201>
- [230] T. Sato, K. Terashima, S. Souma, H. Matsui, T. Takahashi, H. Yang, S. Wang, H. Ding, N. Maeda, K. Hayashi, Three-dimensional fermi-surface nesting in 1t-vse2 studied by angle-resolved photoemission spectroscopy, Journal of the Physical Society of Japan 73 (12) (2004) 3331–3334.  
arXiv:<https://doi.org/10.1143/JPSJ.73.3331>,  
doi:10.1143/JPSJ.73.3331.  
URL <https://doi.org/10.1143/JPSJ.73.3331>
- [231] C. Wang, C. G. Slough, R. V. Coleman, Spectroscopy of dichalcogenides and trichalcogenides using scanning tunneling microscopy, Journal of Vacuum Science & Technology B:

Microelectronics and Nanometer Structures Processing,  
Measurement, and Phenomena 9 (2) (1991) 1048–1051.  
arXiv:<https://avs.scitation.org/doi/pdf/10.1116/1.585257>,  
doi:10.1116/1.585257.  
URL <https://avs.scitation.org/doi/abs/10.1116/1.585257>

- [232] I. Ekvall, H. E. Brauer, E. Wahlström, H. Olin, Locally modified charge-density waves in na intercalated  $vse_2$  studied by scanning tunneling microscopy and spectroscopy, *Phys. Rev. B* 59 (1999) 7751–7761. doi:10.1103/PhysRevB.59.7751.  
URL <https://link.aps.org/doi/10.1103/PhysRevB.59.7751>
- [233] Á. Pásztor, A. Scarfato, C. Barreateau, E. Giannini, C. Renner, Dimensional crossover of the charge density wave transition in thin exfoliated VSe<sub>2</sub>, *2D Materials* 4 (4) (2017) 041005.  
doi:10.1088/2053-1583/aa86de.  
URL <https://doi.org/10.1088/2F2053-1583/2Faa86de>
- [234] M. V. Berry, Quantal phase factors accompanying adiabatic changes, *Proceedings of the Royal Society of London. A. Mathematical and Physical Sciences* 392 (1802) (1984) 45–57.  
arXiv:<https://royalsocietypublishing.org/doi/pdf/10.1098/rspa.1984.0023>,  
doi:10.1098/rspa.1984.0023.  
URL  
<https://royalsocietypublishing.org/doi/abs/10.1098/rspa.1984.0023>
- [235] S. shen Chern, On the curvatura integra in a riemannian manifold, *Annals of Mathematics* 46 (4) (1945) 674–684.  
URL <http://www.jstor.org/stable/1969203>
- [236] B. A. BERNEVIG, T. L. Hughes, *Topological Insulators and Topological Superconductors*, stu - student edition Edition, Princeton University Press, 2013.  
URL <http://www.jstor.org/stable/j.ctt19cc2gc>
- [237] G. W. Semenoff, Condensed-matter simulation of a three-dimensional anomaly, *Phys. Rev. Lett.* 53 (1984) 2449–2452.  
doi:10.1103/PhysRevLett.53.2449.  
URL <https://link.aps.org/doi/10.1103/PhysRevLett.53.2449>
- [238] Y. Yao, F. Ye, X.-L. Qi, S.-C. Zhang, Z. Fang, Spin-orbit gap of graphene: First-principles calculations, *Phys. Rev. B* 75 (2007)

041401. doi:10.1103/PhysRevB.75.041401.  
 URL <https://link.aps.org/doi/10.1103/PhysRevB.75.041401>
- [239] P. Y. Yu, M. Cardona, Fundamentals of Semiconductors, Springer Berlin Heidelberg, 2010. doi:10.1007/978-3-642-00710-1.  
 URL <https://doi.org/10.1007/978-3-642-00710-1>
- [240] M. R. Zirnbauer, Riemannian symmetric superspaces and their origin in random-matrix theory, Journal of Mathematical Physics 37 (10) (1996) 4986–5018. arXiv:<https://doi.org/10.1063/1.531675>, doi:10.1063/1.531675.  
 URL <https://doi.org/10.1063/1.531675>
- [241] A. Altland, M. R. Zirnbauer, Nonstandard symmetry classes in mesoscopic normal-superconducting hybrid structures, Phys. Rev. B 55 (1997) 1142–1161. doi:10.1103/PhysRevB.55.1142.  
 URL <https://link.aps.org/doi/10.1103/PhysRevB.55.1142>
- [242] S. Ryu, A. P. Schnyder, A. Furusaki, A. W. W. Ludwig, Topological insulators and superconductors: tenfold way and dimensional hierarchy, New Journal of Physics 12 (6) (2010) 065010. doi:10.1088/1367-2630/12/6/065010.  
 URL <https://doi.org/10.1088/1367-2630/12/6/065010>
- [243] A. P. Schnyder, S. Ryu, A. Furusaki, A. W. W. Ludwig, Classification of topological insulators and superconductors in three spatial dimensions, Phys. Rev. B 78 (2008) 195125. doi:10.1103/PhysRevB.78.195125.  
 URL <https://link.aps.org/doi/10.1103/PhysRevB.78.195125>
- [244] L. Fu, C. L. Kane, Topological insulators with inversion symmetry, Phys. Rev. B 76 (2007) 045302. doi:10.1103/PhysRevB.76.045302.  
 URL <https://link.aps.org/doi/10.1103/PhysRevB.76.045302>
- [245] C. Brüne, C. X. Liu, E. G. Novik, E. M. Hankiewicz, H. Buhmann, Y. L. Chen, X. L. Qi, Z. X. Shen, S. C. Zhang, L. W. Molenkamp, Quantum hall effect from the topological surface states of strained bulk hgte, Phys. Rev. Lett. 106 (2011) 126803. doi:10.1103/PhysRevLett.106.126803.  
 URL <https://link.aps.org/doi/10.1103/PhysRevLett.106.126803>

- [246] D. M. Mahler, J.-B. Mayer, P. Leubner, L. Lunczer, D. Di Sante, G. Sangiovanni, R. Thomale, E. M. Hankiewicz, H. Buhmann, C. Gould, L. W. Molenkamp, Interplay of dirac nodes and volkov-pankratov surface states in compressively strained hgte, *Phys. Rev. X* 9 (2019) 031034. doi:10.1103/PhysRevX.9.031034. URL <https://link.aps.org/doi/10.1103/PhysRevX.9.031034>
- [247] F. Teppe, M. Marcinkiewicz, S. S. Krishtopenko, S. Ruffenach, C. Consejo, A. M. Kadykov, W. Desrat, D. But, W. Knap, J. Ludwig, S. Moon, D. Smirnov, M. Orlita, Z. Jiang, S. V. Morozov, V. Gavrilenko, N. N. Mikhailov, S. A. Dvoretiskii, Temperature-driven massless kane fermions in HgCdTe crystals, *Nature Communications* 7 (1) (Aug. 2016). doi:10.1038/ncomms12576. URL <https://doi.org/10.1038/ncomms12576>
- [248] C.-X. Liu, X.-L. Qi, X. Dai, Z. Fang, S.-C. Zhang, Quantum anomalous hall effect in  $hg_{1-y}mn_yTe$  quantum wells, *Phys. Rev. Lett.* 101 (2008) 146802. doi:10.1103/PhysRevLett.101.146802. URL <https://link.aps.org/doi/10.1103/PhysRevLett.101.146802>
- [249] J. Anversa, P. Piquini, A. Fazzio, T. M. Schmidt, First-principles study of hgte/cdte heterostructures under perturbations preserving time-reversal symmetry, *Phys. Rev. B* 90 (2014) 195311. doi:10.1103/PhysRevB.90.195311. URL <https://link.aps.org/doi/10.1103/PhysRevB.90.195311>
- [250] S. Küfner, F. Bechstedt, Topological transition and edge states in hgte quantum wells from first principles, *Phys. Rev. B* 89 (2014) 195312. doi:10.1103/PhysRevB.89.195312. URL <https://link.aps.org/doi/10.1103/PhysRevB.89.195312>
- [251] Wu, Shu-Chun, Yan, Binghai, Felser, Claudia, Ab initio study of topological surface states of strained hgte, *EPL* 107 (5) (2014) 57006. doi:10.1209/0295-5075/107/57006. URL <https://doi.org/10.1209/0295-5075/107/57006>
- [252] A. Svane, N. E. Christensen, M. Cardona, A. N. Chantis, M. van Schilfhaarde, T. Kotani, Quasiparticle band structures of  $\beta$ -hgs, hgse, and hgte, *Phys. Rev. B* 84 (2011) 205205. doi:10.1103/PhysRevB.84.205205. URL <https://link.aps.org/doi/10.1103/PhysRevB.84.205205>

- [253] J. P. Perdew, Density functional theory and the band gap problem, *International Journal of Quantum Chemistry* 28 (S19) (1985) 497–523. arXiv:<https://onlinelibrary.wiley.com/doi/pdf/10.1002/qua.560280846>, doi:10.1002/qua.560280846.  
URL <https://onlinelibrary.wiley.com/doi/abs/10.1002/qua.560280846>
- [254] N. N. Berchenko, M. V. Pashkovskii, Mercury telluride—a zero-gap semiconductor, *Soviet Physics Uspekhi* 19 (6) (1976) 462–480. doi:10.1070/pu1976v019n06abeh005265.  
URL <https://doi.org/10.1070/2Fpu1976v019n06abeh005265>
- [255] S. Groves, W. Paul, Band structure of gray tin, *Phys. Rev. Lett.* 11 (1963) 194–196. doi:10.1103/PhysRevLett.11.194.  
URL <https://link.aps.org/doi/10.1103/PhysRevLett.11.194>
- [256] T. Harman, W. Kleiner, A. Strauss, G. Wright, J. Mavroides, J. Honig, D. Dickey, Band structure of hgte and hgte-cdte alloys, *Solid State Communications* 2 (10) (1964) 305 – 308. doi:[https://doi.org/10.1016/0038-1098\(64\)90531-9](https://doi.org/10.1016/0038-1098(64)90531-9).  
URL <http://www.sciencedirect.com/science/article/pii/0038109864905319>
- [257] M. Cardona, N. E. Christensen, G. Fasol, Relativistic band structure and spin-orbit splitting of zinc-blende-type semiconductors, *Phys. Rev. B* 38 (1988) 1806–1827. doi:10.1103/PhysRevB.38.1806.  
URL <https://link.aps.org/doi/10.1103/PhysRevB.38.1806>
- [258] J. Autschbach, Perspective: Relativistic effects, *The Journal of Chemical Physics* 136 (15) (2012) 150902. arXiv:<https://doi.org/10.1063/1.3702628>, doi:10.1063/1.3702628.  
URL <https://doi.org/10.1063/1.3702628>
- [259] L. Liu, W. Leung, Transport property of zero-gap semiconductors under tensile stress, *Phys. Rev. B* 12 (1975) 2336–2345. doi:10.1103/PhysRevB.12.2336.  
URL <https://link.aps.org/doi/10.1103/PhysRevB.12.2336>
- [260] C. I. Fornari, P. H. O. Rappl, S. L. Morelhão, T. R. F. Peixoto, H. Bentmann, F. Reinert, E. Abramof, Preservation of pristine bi2te3 thin film topological insulator surface after ex situ mechanical removal of te capping layer, *APL Materials* 4 (10) (2016) 106107.

arXiv:<https://doi.org/10.1063/1.4964610>, doi:10.1063/1.4964610.

URL <https://doi.org/10.1063/1.4964610>

- [261] J. P. Perdew, A. Zunger, Self-interaction correction to density-functional approximations for many-electron systems, *Phys. Rev. B* 23 (1981) 5048–5079. doi:10.1103/PhysRevB.23.5048. URL <https://link.aps.org/doi/10.1103/PhysRevB.23.5048>
- [262] R. Sakuma, C. Friedrich, T. Miyake, S. Blügel, F. Aryasetiawan, *gw* calculations including spin-orbit coupling: Application to hg chalcogenides, *Phys. Rev. B* 84 (2011) 085144. doi:10.1103/PhysRevB.84.085144. URL <https://link.aps.org/doi/10.1103/PhysRevB.84.085144>
- [263] S. L. Dudarev, G. A. Botton, S. Y. Savrasov, C. J. Humphreys, A. P. Sutton, Electron-energy-loss spectra and the structural stability of nickel oxide: An lsd+u study, *Phys. Rev. B* 57 (1998) 1505–1509. doi:10.1103/PhysRevB.57.1505. URL <https://link.aps.org/doi/10.1103/PhysRevB.57.1505>
- [264] F. Tran, P. Blaha, Accurate band gaps of semiconductors and insulators with a semilocal exchange-correlation potential, *Phys. Rev. Lett.* 102 (2009) 226401. doi:10.1103/PhysRevLett.102.226401. URL <https://link.aps.org/doi/10.1103/PhysRevLett.102.226401>
- [265] F. Tran, P. Blaha, K. Schwarz, Band gap calculations with becke-johnson exchange potential, *Journal of Physics: Condensed Matter* 19 (19) (2007) 196208. doi:10.1088/0953-8984/19/19/196208. URL <https://doi.org/10.1088/0953-8984/19/19/196208>
- [266] A. V. Krukau, O. A. Vydrov, A. F. Izmaylov, G. E. Scuseria, Influence of the exchange screening parameter on the performance of screened hybrid functionals, *The Journal of Chemical Physics* 125 (22) (2006) 224106. doi:10.1063/1.2404663. URL <https://doi.org/10.1063/1.2404663>
- [267] N. Orlowski, J. Augustin, Z. Gołacki, C. Janowitz, R. Manzke, Direct evidence for the inverted band structure of hgte, *Phys. Rev. B* 61 (2000) R5058–R5061. doi:10.1103/PhysRevB.61.R5058. URL <https://link.aps.org/doi/10.1103/PhysRevB.61.R5058>

- [268] F. m. c. Virost, R. Hayn, M. Richter, J. van den Brink, Engineering topological surface states: Hgs, hgse, and hgte, *Phys. Rev. Lett.* 111 (2013) 146803. doi:10.1103/PhysRevLett.111.146803.  
URL <https://link.aps.org/doi/10.1103/PhysRevLett.111.146803>
- [269] S. Oehling, M. Ehinger, T. Gerhard, C. R. Becker, G. Landwehr, M. Schneider, D. Eich, H. Neureiter, R. Fink, M. Sokolowski, E. Umbach, Termination, surface structure and morphology of the molecular beam epitaxially grown hgte(001) surface, *Applied Physics Letters* 73 (22) (1998) 3205–3207.  
arXiv:<https://doi.org/10.1063/1.122719>, doi:10.1063/1.122719.  
URL <https://doi.org/10.1063/1.122719>
- [270] N. Marzari, A. A. Mostofi, J. R. Yates, I. Souza, D. Vanderbilt, Maximally localized wannier functions: Theory and applications, *Rev. Mod. Phys.* 84 (2012) 1419–1475. doi:10.1103/RevModPhys.84.1419.  
URL <https://link.aps.org/doi/10.1103/RevModPhys.84.1419>
- [271] N. Marzari, D. Vanderbilt, Maximally localized generalized wannier functions for composite energy bands, *Phys. Rev. B* 56 (1997) 12847–12865. doi:10.1103/PhysRevB.56.12847.  
URL <https://link.aps.org/doi/10.1103/PhysRevB.56.12847>
- [272] A. A. Mostofi, J. R. Yates, G. Pizzi, Y.-S. Lee, I. Souza, D. Vanderbilt, N. Marzari, An updated version of wannier90: A tool for obtaining maximally-localised wannier functions, *Computer Physics Communications* 185 (8) (2014) 2309 – 2310.  
doi:<https://doi.org/10.1016/j.cpc.2014.05.003>.  
URL <http://www.sciencedirect.com/science/article/pii/S001046551400157X>
- [273] M. P. L. Sancho, J. M. L. Sancho, J. M. L. Sancho, J. Rubio, Highly convergent schemes for the calculation of bulk and surface green functions, *Journal of Physics F: Metal Physics* 15 (4) (1985) 851–858. doi:10.1088/0305-4608/15/4/009.  
URL <https://doi.org/10.1088/2F0305-4608/2F15/2F4/2F009>
- [274] A. Damascelli, Probing the electronic structure of complex systems by ARPES, *Physica Scripta T109* (2004) 61.  
doi:10.1238/physica.topical.109a00061.  
URL <https://doi.org/10.1238/2Fphysica.topical.109a00061>

- [275] G. Dresselhaus, Spin-orbit coupling effects in zinc blende structures, *Phys. Rev.* 100 (1955) 580–586. doi:10.1103/PhysRev.100.580.  
URL <https://link.aps.org/doi/10.1103/PhysRev.100.580>
- [276] M. Cardona, N. E. Christensen, G. Fasol, Terms linear in  $k$  in the band structure of zinc-blende-type semiconductors, *Phys. Rev. Lett.* 56 (1986) 2831–2833. doi:10.1103/PhysRevLett.56.2831.  
URL <https://link.aps.org/doi/10.1103/PhysRevLett.56.2831>
- [277] P. Capper, J. Garland (Eds.), *Mercury Cadmium Telluride*, Wiley, 2010. doi:10.1002/9780470669464.  
URL <https://doi.org/10.1002/9780470669464>
- [278] G. Kresse, J. Hafner, Ab initio molecular dynamics for liquid metals, *Phys. Rev. B* 47 (1993) 558–561. doi:10.1103/PhysRevB.47.558.  
URL <https://link.aps.org/doi/10.1103/PhysRevB.47.558>
- [279] G. Kresse, J. Hafner, Ab initio molecular-dynamics simulation of the liquid-metal–amorphous-semiconductor transition in germanium, *Phys. Rev. B* 49 (1994) 14251–14269. doi:10.1103/PhysRevB.49.14251.  
URL <https://link.aps.org/doi/10.1103/PhysRevB.49.14251>
- [280] P. Leubner, Strain-engineering of the topological insulator hgte, doctoralthesis, Universität Würzburg (2017).
- [281] M. A. Berding, W. D. Nix, D. R. Rhiger, S. Sen, A. Sher, Critical thickness in the HgCdTe/CdZnTe system, *Journal of Electronic Materials* 29 (6) (2000) 676–679. doi:10.1007/s11664-000-0204-3.  
URL <https://doi.org/10.1007/s11664-000-0204-3>
- [282] Q. Wu, S. Zhang, H.-F. Song, M. Troyer, A. A. Soluyanov, Wanniertools : An open-source software package for novel topological materials, *Computer Physics Communications* 224 (2018) 405 – 416. doi:<https://doi.org/10.1016/j.cpc.2017.09.033>.  
URL <http://www.sciencedirect.com/science/article/pii/S0010465517303442>
- [283] F. Schindler, Z. Wang, M. G. Vergniory, A. M. Cook, A. Murani, S. Sengupta, A. Y. Kasumov, R. Deblock, S. Jeon, I. Drozdov, H. Bouchiat, S. Guéron, A. Yazdani, B. A. Bernevig, T. Neupert, Higher-order topology in bismuth, *Nature Physics* 14 (9) (2018)

918–924. doi:10.1038/s41567-018-0224-7.  
URL <https://doi.org/10.1038/s41567-018-0224-7>

- [284] F. Schindler, A. M. Cook, M. G. Vergniory, Z. Wang, S. S. P. Parkin, B. A. Bernevig, T. Neupert, Higher-order topological insulators, *Science Advances* 4 (6) (2018) eaat0346. doi:10.1126/sciadv.aat0346.  
URL <https://doi.org/10.1126/sciadv.aat0346>